Universidade de Aveiro
2018

Departamento de Eletrónica, Telecomunicações e Informática

ANA RITA NAIA BASTOS

Fotónica sustentável: circuitos de ótica integrada para comunicações óticas e sensores baseados em híbridos orgânico-inorgânicos

Green photonics: photonic integrated circuits for optical communications and sensing based on organic-inorganic hybrids

Universidade de Aveiro
2018

Departamento de Eletrónica, Telecomunicações e Informática

ANA RITA NAIA BASTOS

Fotónica sustentável: circuitos de ótica integrada para comunicações óticas e sensores baseados em híbridos orgânico-inorgânicos

Green photonics: photonic integrated circuits for optical communications and sensing based on organic-inorganic hybrids

Tese apresentada à Universidade de Aveiro para cumprimento dos requisitos necessários à obtenção do grau de Doutor em Telecomunicações, realizada sob a orientação científica do Doutor Mário José Neves de Lima, Professor Auxiliar na Universidade de Aveiro, e da Doutora Maria Rute de Amorim e Sá Ferreira André, Professora Associada com Agregação na Universidade de Aveiro.

Trabalho desenvolvido no âmbito do projeto CICECO-Instituto de Materiais de Aveiro, POCI-01-0145-FEDER-007679 (UID/CTM/50011/2013), e Instituto de Telecomunicações (UID/EEA/50008/2013), financiado por fundos nacionais através do FCT/MEC e cofinanciado pelo FEDER sob o acordo PT2020. A autora agradece o apoio financeiro concedido pela FCT através da bolsa PD/BD/105859/2014, e à Fundação Calouste Gulbenkian pelo "Prémio de Estímulo à Investigação 2015" (Procº 141767).

Dedico este trabalho aos meus pais.

o júri

presidente

Prof. Doutor João de Lemos Pinto
Professor Catedrático da Universidade de Aveiro

Prof. Doutor José Manuel Marques Martins de Almeida
Professor Associado c/ Agregação da Universidade de Trás-Os-Montes e Alto Douro

Prof. Doutor Henrique Manuel de Castro Faria Salgado
Professor Associado da Universidade do Porto

Prof. Doutora Ana Maria de Matos Charas
Investigadora Principal do Instituto de Telecomunicações de Lisboa

Prof. Doutor Paulo Miguel Nepomuceno Pereira Monteiro
Professor Associado da Universidade de Aveiro

Prof. Doutor Maria Rute de Amorim e Sá Ferreira André
Professora Associada c/ Agregação da Universidade de Aveiro

agradecimentos / acknowledgements

O trabalho apresentado nesta dissertação resulta da colaboração de várias pessoas e instituições.
Em primeiro, gostaria de agradecer aos meus orientadores Professor Doutor Mário Lima pela oportunidade, e à Professora Doutora Maria Rute André pela motivação e apoio constantes indispensáveis e fundamentais para o desenvolvimento e conclusão deste trabalho. Sem o seu apoio nada disto seria possível.
Ao Professor Doutor Paulo André quero agradecer por todo o incentivo, acompanhamento, disponibilidade e suporte científico que foram essenciais durante este percurso.
Pela ajuda nas diferentes etapas do trabalho e pela sua disponibilidade, devo, também, um agradecimento ao Professor Doutor Luís Carlos.
Agradeço ao Doutor Carlos Vicente por todo o apoio, motivação e partilha de conhecimento essenciais para o desenvolvimento desta dissertação.
À Professora Doutora Rachel Evans agradeço a sua disponibilidade, colaboração, e por ceder os materiais baseados em di-ureasils dopados com polímeros conjugados.
Ao Doutor Lianshe Fu, pela síntese dos materiais (di-ureasils e tri-ureasils), e ajuda na análise e interpretação dos resultados de caracterização estrutural.
Ao Doutor Ali Shahpari pelo auxílio no laboratório de comunicações óticas.
Ao Professor Doutor Enrique Rodríguez-Castellón pelas medidas de XPS e ajuda na análise dos respetivos dados.
Ao Doutor Nuno João Silva agradeço a colaboração na preparação da amostra de E. Coli para a caracterização do biosensor.
Agradeço, também, aos meus colegas do grupo Phantom-G, do Instituto de Telecomunicações e do MAP-Tele pela ajuda, companheirismo e bom ambiente durante o desenvolvimento deste trabalho.
Aos Professores do programa doutoral MAP-Tele por todo o ensinamento e enquadramento na área das Telecomunicações essenciais para o início desta dissertação.
À Fundação para a Ciência e Tecnologia, e à Fundação Calouste Gulbenkian pela ajuda financeira.
Ao CICECO Aveiro Institute of Materials, Instituto de Telecomunicações, Departamento de Eletrónica, Telecomunicações e Informática, e Departamento de Física agradeço por me terem proporcionado todos os meios físicos para a concretização deste trabalho de doutoramento. Neste contexto, agradeço, também, ao pessoal técnico destas instituições pelo apoio que sempre me disponibilizaram.
Um enorme obrigado, a todos os meus amigos, que ao longo deste percurso foram sempre uma fonte de força, alegria e energia na minha vida.
O agradecimento mais importante é dirigido aos meus pais por serem os melhores do mundo, e por me apoiarem e encorajarem em todos os meus projetos, incondicionalmente. Agradeço também aos meus avós pela presença e carinho contínuo.
E por fim, a ti Tiago Paixão, pelo companheirismo, paciência, força e motivação diária que deste durante estes anos. Obrigado por estares sempre presente.

A todos, muito obrigado.

Palavras-chave

híbridos orgânico-inorgânicos, escrita direta por radiação *laser*, guia de onda, circuito de ótica integrada, nova geração de redes óticas de acesso, biosensor.

resumo

O presente trabalho tem como objetivos a produção e caracterização de circuitos de ótica integrada (OI) eficientes e de baixo custo, no contexto dos requisitos de fotónica sustentável, nomeadamente na área das comunicações óticas e dos sensores. Para isso, híbridos orgânico-inorgânicos (di-ureiasil e tri-ureiasil), dopados com propóxido de zircónio estabilizado com ácido metracrílico, foram sintetizados pela metodologia sol-gel, à temperatura ambiente, como guias de onda planares processados na forma de monólitos, com forma e tamanho controlados, ou filmes de espessura variável (10^{-5}-10^{-6} m), em substratos vítreos e de silício oxidado. Estes materiais exibem propriedades óticas estáveis e ajustáveis, estabilidade mecânica e térmica resultantes da sinergia entre os componentes orgânicos e inorgânicos. A sua principal propriedade é o fácil controlo das propriedades óticas devido à inerente flexibilidade dos materiais que são auto-padronizados pela escrita direta por radiação ultravioleta (UV), e o controlo do índice de refração por dopagem química.

A influência de diferentes concentrações de aglomerados de zircónio (20-60 mol%) na estrutura local dos di-ureails e tri-ureasils foi analisada através de difração de raio-X, ressonância magnética nuclear dos átomos de ^{13}C e ^{29}Si, espectroscopia de infravermelho por transformada de Fourier, espectroscopia Raman por transformada de Fourier e análise termogravimétrica. As características óticas relevantes para aplicações em OI foram determinadas, revelando coeficientes de atenuação aceitáveis (~1-5 dB·cm^{-1}) para circuitos de baixas dimensões, e baixas perdas de inserção devido à similaridade entre os índices de refração do dispositivo-fibra (1,49-1,52). Tomando partido da fotossensibilidade do material, foi utilizada a escrita direta por radiação UV para padronizar a arquitetura ótica desejada na superfície de híbridos orgânico-inorgânicos.

No que respeita às comunicações óticas, foram produzidos dispositivos passivos e ativos: controlador de polarização termo-ótico para monitorizar o estado de polarização de um sinal ótico, apresentando um coeficiente de retardamento linear de 17±1 °/°C; um acoplador híbrido de 90° para demodular uma transmissão de quadratura de chaveamento de fase com 20 Gb/s em 40 km de fibra, resultando numa penalidade de potência de 2,5 dB comparativamente à configuração sem fibra; um modulador de fase eletro-ótico baseado num interferómetro Mach-Zehnder (MZI) com uma diferença de potencial para uma variação de fase de π de 2,9±0,3 V; amplificador ótico na região espectral do azul para comunicações óticas no visível com uma eficiência máxima de ganho ótico de 1,62±0,02 cm·μJ^{-1}.

Na área dos sensores, o desenvolvimento de biosensores portáteis de baixo custo baseados em OI para dispositivos é de grande interesse. Sendo assim, um biosensor baseado na arquitetura de um MZI foi produzido para monitorizar a concentração de bactérias num meio líquido, apresentando uma sensibilidade de 2×10^{-4} RIU e um limite de deteção de 2,0 pg·mm^{-3}.

keywords

organic-inorganic hybrids, direct *laser* writing, waveguide, photonic integrated circuit, next generation of optical access network, biosensor.

abstract

The present work aims the production and characterization of cost-effective photonic integrated circuits (PICs) to encounter green photonics goals, namely in the optical communications and sensing fields. Therefore, organic-inorganic hybrids (di-ureasil and tri-ureasil), doped with zirconium propoxide stabilized with methacrylic acid, were synthesized by the versatile sol-gel methodology, at room temperature, as planar waveguides processed in the form of monoliths, with controlled shape and size, and films with variable thickness (10^{-5}-10^{-6} m) in vitreous or silicon oxide substrates. They exhibit stable and tunable properties, mechanical and thermal stability resulting from the synergy between the organic and inorganic counterparts. Their main feature is the heavily facilitated control of the surface optical properties by the inherent flexibility offered by these materials that are easily self-patterned by direct UV *laser* writing, and the refractive index tuning through chemical doping.

The influence of different concentrations of zirconia-based clusters (20-60 mol%) in the local structure of di-ureasils and tri-ureasils was studied through X-ray diffraction, nuclear magnetic resonance of ^{13}C and ^{29}Si atoms, infrared spectroscopy by Fourier transform, Raman spectroscopy by Fourier transform and thermogravimetry analysis. The relevant optical features for applications in PICs were determined, showing acceptable attenuation values (~1-5 dB·cm^{-1}) for low dimension circuits, and reduced insertion losses arising from the fibre-device similar refractive index (1.49-1.52). Taking advantage of the material photosensibility, direct UV *laser* writing was used to pattern the desired optical architecture on the surface of organic-inorganic hybrids.

In what concerns optical communications, passive and active devices were produced: a thermo-optic integrated variable wave plate device to control the state of polarization of an optical signal, showing a linear retardation coefficient of 17±1 °/°C; a 90° hybrid coupler to demodulate a 20 Gb/s quadrature phase shift keying transmission over 40 km of fibre, yielding a 2.5 dB power penalty, relatively to back-to-back; an electro-optic phase modulator based on a Mach-Zehnder interferometer (MZI) with a voltage shift required for a π phase change of 2.9±0.3 V; an optical amplifier in the blue spectral region for visible light communications with a maximum optical gain efficiency of 1.62±0.02 cm·μJ^{-1}.

In the sensing field, the development of portable low-cost PICs based biosensors for lab-on-a-chip devices are of great interest. Thus, a biosensor based on an MZI was produced to monitor the growing concentration of bacteria in a liquid medium, presenting a sensitivity of 2×10^{-4} RIU and limit of detection of 2.0 pg·mm^{-3}.

CONTENTS

ACRONYMS

AFM	Atomic force microscope
ASE	Amplified spontaneous emission
BER	Bit error rate
BPM	Beam propagation method
CPE	Conjugated polyelectrolyte
CVD	Chemical vapour deposition
DFA	Doped fibre amplifier
DSC	Differential scanning calorimetry
DWDM	Dense wavelength division multiplexing
d-UPTES	Di-ureapropyltriethoxysilane
EDFA	Erbium doped fibre amplifier
EO	Electro-optic
EVM	Error vector magnitude
FT	Fourier transform
FT-IR	Fourier transform infrared spectroscopy
FWHM	Full width at half maximum
F8DP	Poly(9,9-dioctylfluorene-co-9,9-di(4-methoxy)phenylfluorene
HD-FEC	Hard-decision forward error correction
ICPTES	3-isocyanatopropyltriethoxysilane
IQM	In-phase and quadrature modulator
IR	Infrared
ITO	Indium tin oxide
Laser	Light amplification by stimulated emission of radiation
LB	*Lysogeny* broth
LED	Light emitting diode
LO	Local oscilator
LOD	Limit of detection
MBE	Molecular beam epitaxy
MMI	Multimode interference
MZI	Mach-Zehnder interferometer
NGOA	Next generation of optical access
NIR	Near infrared
OCR	Optical coherent receiver
OSA	Optical spectrum analyser
PBS-PFP	Poly[9,9-bis(4-sulfonylbutoxyphenyl) fluorene-2,7-diyl-*alt*-1,4-phenylene]

PCD	Polarization controller device
PD	Photodiode
PDM	Polarization division multiplexing
PFO	Polydioctylfluorene
PIC	Photonic integrated circuit
PM	Polarization maintaining
PMMA	Poly(methyl methacrylate)
PON	Passive optical network
POP	Polyoxypropylene
QAM	Quadrature amplitude modulation
QPSK	Quadrature phase shift keying
SEM	Scanning electronic microscope
SOA	Semiconductor optical amplifier
SOP	State of polarization
SSMF	Standard single mode fibre
TE	Transverse electric
TEOS	Tetraethoxysilane
TGA	Thermogravimetric analysis
THF	Tetrahydrofuran
TM	Transverse magnetic
TO	Thermo-optic
t-UPTES	Tri-ureapropyltriethoxysilane
UV	Ultraviolet
VLC	Visible light communication
VOA	Variable optical attenuator
VSL	Variable stripe length
XPS	X-ray photoelectron spectroscopy
XRD	X-ray diffraction
XT	Crosstalk

SYMBOLS

α	Optical losses
β	Propagation constant
β_a	Propagation constant of the anti-symmetric mode
β_s	Propagation constant of the symmetric mode
γ	Fibre rotator angle
Γ	MZI transfer function
δ	Retardance
Δabs	Absorption coefficient variation
Δb_T	Thermally induced birefringence variation
$\Delta\delta$	Retardance phase shift of the optical signal
$\Delta\theta$	Phase difference between the QPSK and the LO signals
Δn	Refractive index contrast induced by UV radiation
Δn_{EO}	Refractive index variation induced by electro-optic effect
Δn_F	Biosensor sensitivity
Δn_{RS}	Difference between the effective refractive index of the reference and the sensing MZI arms
Δn_{MZI}	Difference between the effective refractive index of the MZI arms
ΔPM	Power meter measurement error
ΔT	Temperature variation
$\Delta\phi_{MZI}$	Phase shift of the optical signal in the MZI arm
$\Delta\Phi$	Phase deviation
η_G	Optical gain efficiency
λ	Wavelength
λ_{em}	Emission wavelength
λ_{exc}	Excitation wavelength
$\lambda_{1,2}$	Boundaries of the relevant spectral range in the wavelength units
ϕ	Phase variation of the electric field
ϕ_A and ϕ_B	Volume fractions of the two components A (LB medium) and B (*E. coli* cells)
Ω	Solid angle defined by the output side of the amplifier and the slit on the sample surface
A_{sp}	Spontaneous emission rate
b_0	Initial birefringence of the planar waveguide
c	Condensation degree
C	*E. coli* cells concentration
C_0	Initial *E. coli* cells concentration
d	Electrodes distance

dn/dt	Thermo-optic coefficient
$d_{i\text{-}s}$	Inter-siliceous domain structural mean distance
$d\text{-}Si$	Intra-siliceous domain structural mean distance
$d\text{-}Zr$	Inter-Zr clusters characteristic distance
E	Electric field
E_{in}	Input electric filed
E_{LO}	Local oscillator electric field
$E_{MZI1,2}$	Electric field at the MZI arm 1 and 2
E_{out}	Output electric field
E_p	Photon energy
E_s	Quadrature phase shift keying signal electric field
$E_{1,2,3,4}$	Electric field at the output port number 1, 2, 3 and 4 in the 90° hybrid coupler
G	Optical gain
I_{ASE}	Amplified spontaneous emission intensity
I_c, I_s	Ellipsometric parameters
I_{in}	Input intensity
I_I	Photocurrent of the in-phase component
I_{out}	Output intensity
I_Q	Photocurrent of the quadrature phase component
J_{sp}	Density of the amplified spontaneous emission
k	Wavenumber
k_c	Coupling coefficient
K_c	Couple factor
k_T	Thermal linear retardation coefficient
k_0	Wavenumber in free space
$\overline{k}$	Reference wavenumber
L	Stripe length
$L_{coupler}$	Length of the coupling region
L_H	Heater length in the wave plate device
L_{MZI}	Length of the Mach-Zehnder interferometer arm
M_R	Muller matrix
n	Refractive index
n_A and n_B	Refractive indexes of component A (LB medium) and B (*E. coli* cells)
n_{ch}	Channel waveguide refractive index
n_{EC}	*E. coli* cell refractive index
n_F	Fluid refractive index
n_{fats}	Refractive index of the fats and proteins left form the LB medium
n_{LB}	LB medium refractive index
n_R	MZI reference arm refractive index

n_S	MZI sensing arm refractive index
n_{TE}	Refractive index for the TE mode
n_{TM}	Refractive index for the TM mode
N	Number of *E. coli* cells
N_L	Number of levels in the IQ constellation
N_0^*	Excited state population density
P_{in}	Input optical power
P_{chi}	Output optical power in channel *i* of the 90° hybrid coupler
P_{LO}	Local oscillator optical power
P_{out}	Output optical power
Q^m	Q^m-type environments $Si(OSi)_{4-m}(OH)_m$ for m = 1, 2, 3 and 4
R	Photodiode responsivity
R'	Alkyl group
r_{33}	Electro-optic coefficient
S	Stokes parameters of the final state of polarization
S_i	Stokes parameters of the initial state of polarization
S_0, S_1, S_2, S_3	Stokes parameters
T1	Temperature for solvent evaporation
T1-T2	Temperature range for the organic component degradation
T^m	T^m environments of m=1 $R'Si(OSi)_-(OR)$, m=2 $R'Si(OSi)_2(OR)$ and m=3 $R'Si(OSi)_3$ organosiloxane entities
u	Slowly varying electric field
V	Applied voltage
V_{cell}	Volume of a single *E. coli* cell
V_{EC}	Volume of *E. coli* cells in the fluid
V_{total}	Fluid total volume
V_π	Voltage shift required for a phase change of π between the optical signal in the two MZI arms
W	Lambert function
x_c	Centre position in X-ray diffractogram
EtOH	Ethanol
d-$U_{600}ZB$	Di-ureasil where *B* indicates the molar concentration of ZPO added (20, 40 or 60 mol%)
HCl	Hydrochloric acid
t-U_YZB	Tri-ureasil where *Y* is the average molecular weight of the tri-ureasil (440, 3000 or 5000), and *B* indicates the molar concentration of ZPO added (20, 40 or 60 mol%)
ZPO	Zirconium propoxide
ZPO-McOH	Zirconium propoxide stabilized with methacrylic acid clusters

CHAPTER 1

FRAMEWORK AND MOTIVATION

1.1 INTRODUCTION

Photonics is the science and technology that study the generation, manipulation, transmission, and detection of electromagnetic radiation [1], offering solutions in several areas, such as information technology [2], health care and life sciences [3], sensing [4], lighting [5], and space technology [6]. Some forecasts predict a long-term growth of photonics and light-based technologies, where industrial production will be revolutionized creating 1 million jobs by 2030 [7]. Photonics is considered a competitive global market that is worth 447 billion euros in 2015, and it is growing by 7.5 % per year, expecting to reach 615 billion euros by 2020 [7]. This growth is driven by ubiquitous applications of photonics, illustrated in Figure 1.1, where the main ones are information technology, displays and photovoltaic technology.

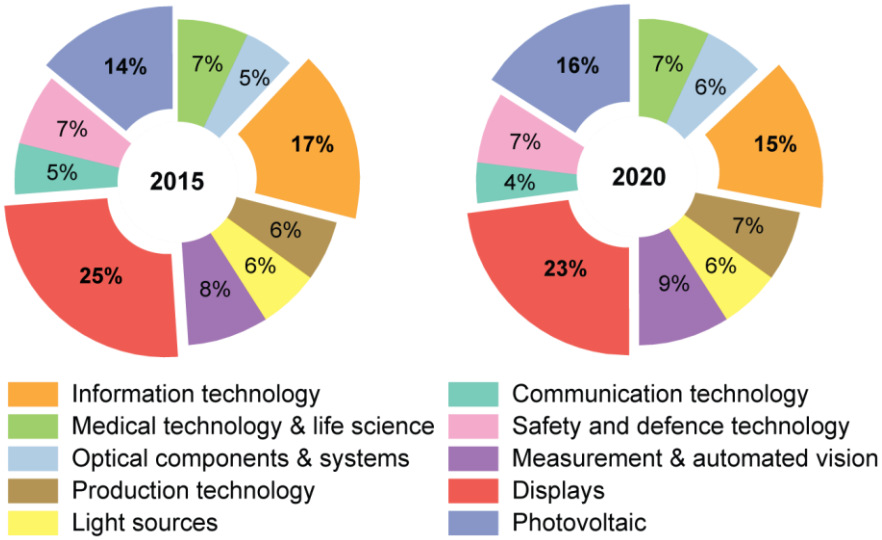

Figure 1.1 Global photonic market in 2015 and the predicted one for 2020. Adapted from [8].

In the recent years, there has been much attention given to environmental issues [9], bringing into question the viability of future products and services [10]. Until 2030, the European Commission have committed to ensure the long-term sustainability by reducing 40 % greenhouse gas emissions, and 27 % of the total energy used [11]. To prevent potentially tragic environmental, economic and geopolitical consequences, green technologies are being encourage for the energy-hungry industrial sectors [12]. To respond to this necessity in the area of photonics it emerged a new and crucial sector known as green photonics, which predicted growth rate is 19.6 % per year [10]. This energy-efficient technology includes any device or process that uses photonics in a sustainable way [13], yielding an environmentally sustainable outcome and improve public health. The areas of impact in green photonics are photovoltaics, solid-state lighting, optical communications and sensing, with the common goals of generate/conserve energy, cut greenhouse emissions and reduce pollution [14]. In this dissertation, the optical communications and sensing fields were addressed.

In what concerns optical communications, efforts are direct towards new energy-efficient communication technologies to answer the today-ever increasing traffic demand for high capacity optical access networks [15]. Also, to prevent the strangle of communication growth by an energy and space bottleneck, innovative and miniaturize optical components with low power consumption, and low production and maintenance costs are required, in parallel with low-cost and room temperature processing methods.

In the sensing field, the development of biosensors has acquired extreme importance for highly sensitive and fast pathogen detection, with a wide range of applications, such as drug discovery, diagnosis, food safety and processing, environmental monitoring, defence and security [16]. Therefore, it is important to develop cost-effective, portable, precise and powerful analytical tools for biological sensing elements [17].

Taking these requirements into account, this dissertation focus on the optical communications and sensing fields, particularly in the development of miniaturized optical components with low energy consumption and low production cost to encounter green photonics goals. To accomplish this goal, siliceous based organic-inorganic hybrids, namely di-ureasils and tri-ureasils materials, will be developed and characterized, as novel photonic integrated circuit (PIC) substrates. Following the work developed in PICs based on di-ureasils [18], this well-known material will be used to produce new devices with different designs and applications. Also, organic-inorganic hybrids with different ramification and polymer

molecular weight (tri-ureasils) will be developed and characterized to tune the optical and thermal properties through changes in the molecular structure.

1.2 OPTICAL COMMUNICATIONS

1.2.1 PASSIVE OPTICAL COMPONENTS

To respond the traffic demands growth, network operators continue to seek solutions to improve the transmission capacity of optical access networks [15]. There is already a common understanding that fibre-to-the-home is the solution capable of meeting this demand [2]. As the cost of an overall access network is supported by the end users, the technology used for this application is highly cost-sensitive. Thus, the most attractive optical access architecture is the passive optical network (PON), in which the overall complexity and energy cost is minimised by employing passive devices in the optical distribution network to provide broadband access to the subscribers [19].

Recently, the next generation of optical access networks (NGOA) is being developed to meet the future requirements of users and network operators [20]. To fulfil the flexibility requirements, cost and scalability, it is important to combine technologies and innovations, as coherent optical systems [21], which have been well established as the technology of choice for high transmission capacity and high bitrate communications [22]. These systems have an intrinsic high-spectral efficiency achieved by advanced modulation formats [23], that can encode the information in the amplitude, phase and polarization of an optical signal [24,25]. The most common modulation schemes are the quadrature amplitude modulation (QAM), quadrature phase shift keying (QPSK) and polarization division multiplexing (PDM) [26–28]. Considering the feasibility for high data rates and the increase of spectral efficiency, the QPSK modulation scheme and PDM were addressed, which require polarization controlling devices (PCDs), phase modulators and demodulators.

Polarization controlling device

The coherent detection with PDM is one of the most popular modulation schemes [29], because it can duplicate the transmission capacity, as different signals can be transmitted over orthogonal states of polarization (SOP) [30]. To multiplexed the signals in two polarization fields, it is required to control the optical signals SOP [31], which is performed by PCDs. These devices can be based on linear polarizers, wave plates or polarization splitters/combiners. Typically, these building block elements are obtained using birefringent

crystals, such as quartz, MgF_2 or CdS [32], or liquid crystals [33], which have the drawback of not being compact. Since flexible and compact solutions with low-cost and low power consumption are needed for a scalable implementation of PCDs, one effective solution is PICs [34–36]. Integrated variable wave plates have been demonstrated with $LiNbO_3$ [34], liquid crystals [35] and silicon-based waveguides [36]. As these devices involve complex production processes, the need of a simple and low-cost integrated wave plate is still an open issue to encounter green photonics. Therefore, thermal-actuated wave plates are a good solution for cost-effective PCDs. To improve the device performance, the following material requirements should be considered: thermal stability, refractive index similar to the one in optical fibres, and high thermo-optic coefficient.

Phase modulator

The most common modulator for coherent systems is the Mach-Zehnder Interferometer (MZI) [37]. This device splits a beam into two parts, shifts the phase of one with respect to the other and then recombines them [38]. Currently, the modulators are based on the electro-optic effect, where the phase shift is induced by an applied electric field in one of the MZI arms. Consequently, the output intensity varies due to the interference between the signals on the two arms, and the result transfer function has the form of a sinusoid due to the constructive and destructive interferences. In order to improve the device response and to decrease the operation energy cost, a high electro-optic coefficient, and a low voltage shift required for a phase change of π between the optical signal in the two arms of the MZI, are required.

Phase demodulator

If the transmitted optical signal is modulated in phase, the receiver must have a device that extracts the signal phase components. As an illustrative example, the demodulation of a QPSK signal will be addressed. In the QPSK modulation scheme one symbol represents two bits, by encoding the data in the in-phase (I) and quadrature (Q) phase components of an optical signal [26]. To demodulate a QPSK signal, a 90° hybrid coupler combined with balanced photodiodes (PDs) is often used, Figure 1.2. This device separates the I and Q phase components of the signal as a result of the interference generated by a local oscillator (LO) [39]. The balanced detector in the upper branches measures the real part of the input data signal (I phase component, Figure 1.2), and in the lower branches, which have a 90° phase delay, it measures the imaginary part (Q phase component, Figure 1.2) [40].

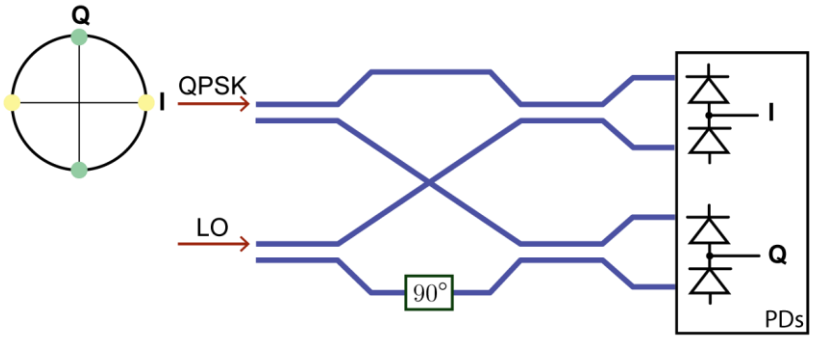

Figure 1.2 Scheme of a coherent receiver for a QPSK signal modulation, using an optical 90° hybrid coupler.

1.2.2 ACTIVE OPTICAL COMPONENTS

In optical communications, active devices such as optical sources, amplifiers and detectors, are also required. In this dissertation, the optical amplification was addressed, and an optical amplifier was fabricated. This device amplifies an optical signal directly, without the need to first convert it to an electrical signal [41]. There are several physical mechanisms that can be used to amplify radiation, as stimulated emission (e.g. doped fibre amplifiers and bulk *lasers* [42]), amplified spontaneous emission (e.g. random *lasers* [43]), electron-hole recombination (e.g. semiconductor optical amplifiers [44]), and Raman scattering (e.g. Raman amplifiers [45]).

In fibre optical communications, due to the ever-increasing number of nodes in a network, signal amplification becomes essential. As the input signal is split, it is required to maintain the signal strength throughout all the network [46]. For low-cost micro amplifiers on the access network, Erbium-doped fibre amplifier (EDFA) are by far the most used fibre amplifier, as they provide an efficient amplification in the infrared spectral region [46], which is the working spectral region in fibre optical communications.

In what concerns visible light communications (VLC), it is required a high efficiency optical amplifier in the visible spectral range. Taking advantage of the fast-switching characteristic of commercial light-emitting diodes (LEDs), they can be used as a wireless signal transmitter to transfer information at rates up to Gigabits per second [47], without losing their illumination functionality [48]. White LEDs can be produced in two ways: a combined red-green-blue LED module, or alternatively a blue-LED coated with a phosphor colour converter [49]. The white-emitting LEDs is the simpler variant for VLC, because the receiver only needs a photodiode and, optionally, an optical band pass filter for the spectral region between 430 nm and 485 nm [50]. In order to increase the signal-to-noise ratio at the VLC receiver, it is required to amplify the blue component of the transmitting signal, which can be achieved through a compact and cost-effective optical amplifier in this spectral region.

1.3 SENSING

In the sensing field, there are several techniques to detect and quantify biological elements as electrochemical [51], colony biomass measurements [52], direct counts (e.g., using optical microscopy and flow cytometry) and optical measurements (e.g., using optical fibres [53,54] or optical circuits [55]).

The optical biosensors are a powerful alternative to conventional analytical techniques [56], allowing an easy-to-use, fast, portable, multiplexed, high specificity, sensitivity and cost-effective diagnosis [17]. These biosensors can be tailored for the detection of specific pathogens (e.g. bacteria or virus), by simply measuring an optical property, such as refractive index or SOP. Therefore, several devices can be implemented for biosensing, as interferometers [57], micro-ring resonators [58], waveguide-coupled surface plasmon resonance [59], and planar directional couplers [60], making them ideal for lab-on-a-chip applications. The detection principle is based on the evanescent field detection. In this case, a bio-receptor layer is immobilized onto the surface of a waveguide, and the exposure to the partner analyte produces a biomolecular interaction affecting the guiding properties of the waveguide (refractive index) [61]. The variation of the refractive index can be correlated with the concentration of the analyte and with the affinity constant of the interaction [61].

For these applications, the experimental measurements are based on benchtop instruments with a relatively large footprint, which commonly require sample handling, that can be particularly cumbersome when pathogenic or anaerobic microorganisms are the targets of the measurement operation [62]. These facts pose a challenge to the scientific community, as there is the need to develop compact optical devices easily operated on bench and laminar flow chambers or in the field, in order to determine the concentration of biological elements.

In this context, to develop optical devices for optical communications and sensing applications, PICs are an excellent cost-effective solution [63]. Therefore, in this dissertation, PICs were produced and characterized for optical communications and sensing applications, considering green photonics goals.

1.4 PHOTONIC INTEGRATED CIRCUITS

Photonic integrated circuits have attracted a lot of interest as they contain several optical components in a single chip (all-in-one package), reducing the size, weight, power consumption, and the cost of optical-to-electrical-to-optical conversions [63]. The interest in

PICs is also justified by other advantages, such as minimum number of optical fibre connections, high sensitivity, and electromagnetic immunity [64].

The evolution of the PICs level of integration is illustrated in Figure 1.3, suggesting that photonic integration is taking a similar development path to microelectronics (Moore's law [65]), probably driven by the same improvements in the processing equipment [66].

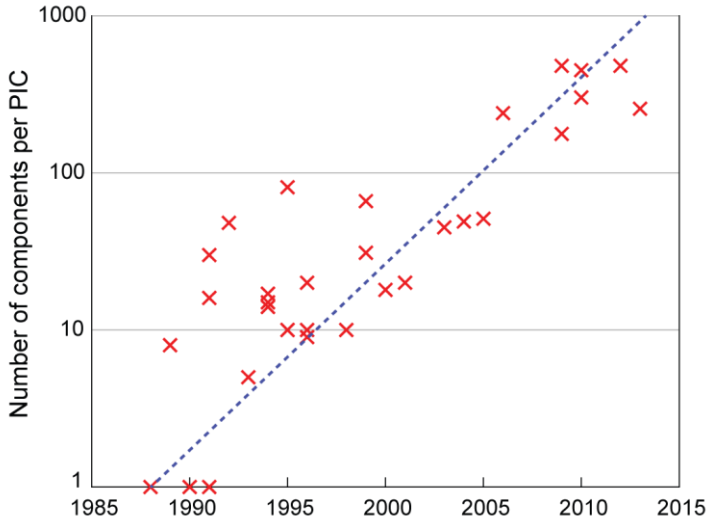

Figure 1.3 Development of PICs complexity measured as the number of components per chip. The dashed line represents the trend. Adapted from [66].

Despite similarities in the development, unlike electronic integration where silicon is the dominant material, there is no clear winner yet in the materials used to fabricate PICs. As a result, there are as many production technologies as applications, e.g. light sources are mostly manufactured using III–V semiconductor-related materials [67,68], modulators have been dominated by lithium niobate ($LiNbO_3$) [38], but gradually overtaken by indium phosphide (InP) [69] and silicon [70] based platforms, which also arise as the main platforms for passive optical devices.

The InP semiconductor provides a platform for complete monolithic integration of passive and active functions [66] operating in the 1300-1600 nm spectral range [69]. Nonetheless, InP is characterized by high attenuation values (5 $dB \cdot cm^{-1}$) and high refractive index (3.10 at 1550 nm), allowing more compact devices, but due to the refractive index mismatch between the InP-based PIC and the optical fibre, the insertion losses are significant (10 dB [71]).

The silicon platform is widely used for passive PICs, due to its low propagation losses (0.1 $dB \cdot cm^{-1}$ [72]), similar refractive index to optical fibres (1.44-1.47 at 1550 nm) which reduces the insertion losses (<0.5 dB [73]), and enables co-integration of photonics with transistor-based electronics [74]. In silicon-based photonics, the typical platform is the

silicon-on-insulator, where the majority of optical components are constructed on the silicon device layer [75]. In order to enhanced the material functionality, it can be integrated with other materials, as III-V semiconductor that provide active optical functionalities as gain, photodetection, and phase/amplitude modulation [76].

Recently, TriPleX™ platform have attracted a lot of attention [77], due to its low propagation loss (5×10^{-4} dB·cm^{-1} [78]) and low insertion losses (<0.5 dB [79]). The waveguide is made of silicon nitride (Si_3N_4) surrounded by silicon oxide (SiO_2) [78,79]. The Si_3N_4 is characterized by a large refractive index (1.99 at 1550 nm) enabling the production of more compact devices [80].

To compare the commercial platforms for PICs, Table 1.1 shows their strengths and weakness for different applications. As it can be observed, the silicon offers a better performance for modulators, detectors (photodiodes), and passive components, due to its low radiation losses. On the contrary, the InP platform is preferred to design active devices, as *lasers*, modulators and amplifiers, but it has poor passive optical components [81].

Table 1.1 Performance classification for PIC platforms to operate selected devices. Adapted from [81].

	Performance		
Devices	InP	Si	TriPleX™
Passive components	●	●●	●●●
Lasers	●●●	○	○
Modulators	●●●	●●	●
Optical amplifiers	●●●	○	○
Detectors	●●●	●●●	○

● modest ●● good ●●● very good ○ challenging

For all these platforms, the main costs arise from two independent aspects: the material processing and device fabrication. The material synthesis and processing are based on complex, expensive and high-temperature physical methods, as chemical vapour deposition (CVD) and molecular beam epitaxy (MBE) techniques. The device patterning is performed by a sequence of photolithography and etching techniques. The photolithography is a microfabrication process that pattern a circuit using radiation to transfer the geometric pattern from a photomask to a light-sensitive chemical (photoresist) [82]. The etching is used to chemically remove layers from the surface of a wafer during manufacturing. The quality of the PIC will depend on the mask, the photolithography resolution, the photoresist material, and the etching process [75]. Therefore, the production of PICs based on these materials is

considered complex and expensive, which are drawbacks to develop cost-effective devices. In the point of view of sustainability, these platforms also present drawbacks in the carbon footprint associated with deployment, manufacturing and recycling issues [83].

In this context, there is still a pertinent issue in the area of materials, which needs to combine the relevant optical features for the PIC operation [13]. As it is expected that concepts like sustainability, cost-effectiveness and eco-friendly became key driving factors to develop PICs, an opportunity is provided to new multifunctional materials. To meet green photonics goals, organic-inorganic hybrids are good candidates, as they are produced from high-purity and bio-degradable available precursors under ambient conditions, which is a relevant parameter from the energetic point of view. Contrarily to that found in other optical polymers, the organic-inorganic hybrids are self-patternable, which means that the refractive index is ultraviolet (UV) tunable without the need of adding photoinitiators (e.g. benzyldimethylketal, α-Aminoketone, Bis Acyl Phosphine), decreasing the precursor cost and processing time. Therefore, direct UV *laser* writing can be used to pattern the desired optical architecture, which is a competitive method comparing with photolithographic methodologies, that require chemical post-treatment and mask technology [84,85].

1.5 ORGANIC-INORGANIC HYBRIDS

Flexible and compact solutions with low-cost and low power consumption are required for a scalable implementation of PICs solutions. Sol-gel derived organic-inorganic hybrid materials emerge as one effective answer for these requirements [86]. These materials have the organic and inorganic components connected at molecular scale, combining the relevant features of each one, in particular the thermal and mechanical resistance of the inorganic counterpart, and the processing flexibility of the organic counterpart. Moreover, organic-inorganic hybrids can be processed either as transparent monoliths (with the desired shape) or thin, transparent, and uniform films with controlled thickness.

Planar and channel waveguides are the most reported and simpler optical components implemented in organic-inorganic hybrids. An overview of their main optical features (refractive index and attenuation coefficient values) is presented in Table 1.2. As observed, the main organic-inorganic materials used in PICs are the ORMOCER®, 3-methacryloxypropyltrimethoxysilane (MAPTMS), di-ureasil, 3-glycidoxypropyltrimethoxysilane (GPTMS), and the 3-aminopropyltriethoxysilane (APTES).

To control and modify the refractive index of organic-inorganic hybrids the most employed materials are zirconium (Zr) and titanium (Ti) alkoxides.

Table 1.2 Optical propertied (refractive index and attenuation coefficient) of selected organic-inorganic hybrids.

Hybrid	Wavelength (nm)	Refractive index	Attenuation coefficient (dB/cm)	Ref.
ORMOCER®	850	1.528	0.07	[87]
	1310	1.418-1.545	<0.02-0.44	[85,88]
	1550	1.508	0.1-0.6	[89,90]
MAPTMS-ZrO_2	543.5	1.5031-1.5143	-	[91]
	640	1.56-1.66	1.6-4.2	[89]
di-ureasil-ZPO-McOH	532	1.5028-1.5361	-	[92]
	632.8	1.4999-1.5103	2.0-3.0	
	1550	1.4840-1.4933	1.0-1.3	
MAPTMS-di-ureasil-ZrOMc	632.8	1.5111-1.5246	0.4-1.5	[91,93]
	1310	1.42	0.13	
	1550	1.490-1.509	0.6-1.1	
MAPTMS-ZrOMc	543.5	1.6280-1.7822	-	[93,94]
	1310	-	1	
	1550	1.5050-1.5090	1.6	
SUNCONNECT®	589.3	1.6	-	[95]
	832	1.592	-	[96,97]
	1550	-	0.43-0.45	
Fluorinated MAPTMS	1550	1.48-1.52	0.1	[98]
TEOS-PVP-TiO_2	633	1.39-1.65	<0.62	[99]
TEOT-APTES-TiO_2	632.8	1.6154-1.7608	1.88	[100,101]
	1550	1.5855-1.7072	0.5	
GPTMS-TiO_2	488	1.52-1.56	<0.5-8	[102,103]
	1593	1.5061-1.5072	1.6-6.6	[103]
GPTMS-TiO_2-azodye	-	-	0.8	[104]
GPTMS-TEOS-ZrO_2	543.5	1.5007-1.5302	<0.5	[102,105]
	633	1.52-1.56		
Fluorinated PMMA	1550	1.571	-	[106]
GTMS-APTES	1310	1.568	0.56	[107]
ChG glass		2.7	6.0	[108]
SU-8 2005	1550	1.5821	0.8	[109]
PMMA-GMA		1.4798	2.8	[110]

ORMOCER®: Organic Modified Ceramic – trademark from Fraunhofer ISC;
MAPTMS: 3-Methacryloxypropyltrimethoxysilane; TEOS: Tetraethoxysilane;
PVP: polyvinylpyrrolidone; APTES: 3-aminopropyltriethoxysilane;
GPTMS: 3-glycidoxypropyltrimethoxysilane; PMMA: poly(methyl methacrylate);
GTMS: (3-Glycidyloxypropyl)Trimethoxysilane; ChG: chalcogenide; GMA: glycidyl methacrylate.

Comparing with pure organic-based materials, the enhanced mechanical and photostability provided by the inorganic skeleton yield long-term stability of the optical features [111], in particular, siloxane-based organic-inorganic hybrids, namely di-ureasils. This material

combines acceptable attenuation values (~1-5 $dB \cdot cm^{-1}$ at 1550 nm [86]) for low dimension circuits, with reduced insertion losses arising from the fibre-device similar refractive index (~1.49), and thermal stability (up to 250 °C [86]). The di-ureasil structure is approximated to a dipodal one with the inorganic components (siliceous skeleton) connected by the organic component. One of the main features of this material is the easily refractive index control through chemical and physical means. The di-ureasil refractive index can be tuned by doping the material with zirconium propoxide ($Zr(OPr^n)_4$, ZPO) and methacrylic acid (McOH), Figure 1.4(a). Also, as the di-ureasil is UV self-patternable, a variation of refractive index is observed when the material is exposed to UV radiation, Figure 1.4(b).

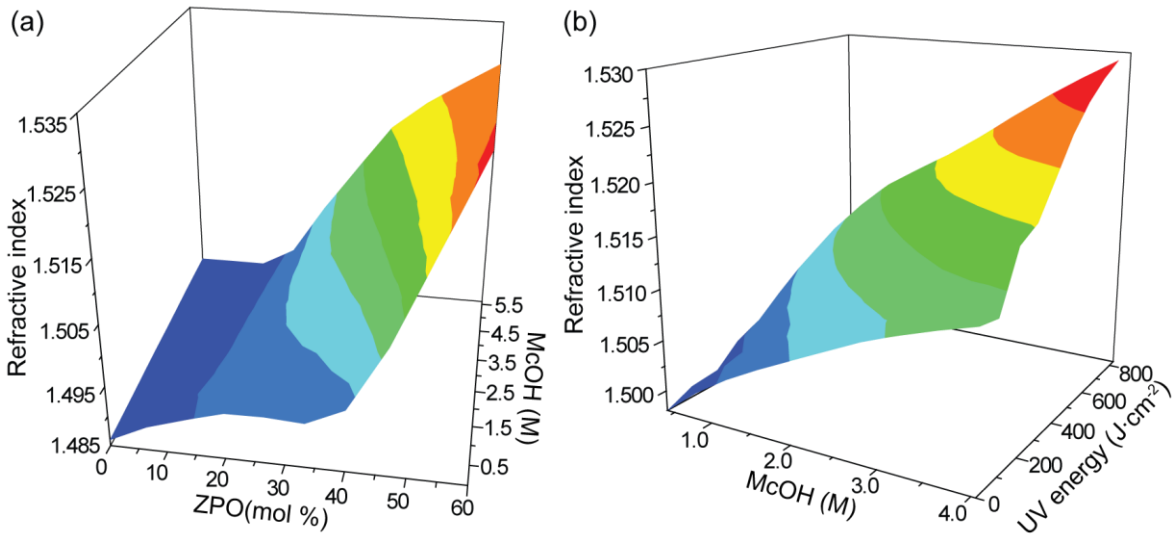

Figure 1.4 Refractive index variation at 635 nm of di-ureasil hybrids as function of (a) ZPO and McOH concentrations, and (b) UV energy that the material was exposed. Adapted from [111].

Taking into account the optical properties required for PICs, the di-ureasil doped with 40 mol% ZPO and a ZPO:McOH molar ratio of 1:2 shows the best compromise between transparency and photosensibility [111], clearly evidenced in the fabrication of distinct optical devices [86,111–115].

Exploiting the advantages of siloxane-based organic-inorganic hybrids, and based on the past experience of di-ureasil doped with 40 mol% ZPO to produce optical devices, in this dissertation, cost-effective PICs with different designs were produced using this material, for optical communications and sensing applications to encounter green photonics goals.

To verify the opportunity to extend the range of refractive index, decrease the optical losses and improve the thermal stability, it was studied the possibility to tune these features through the material molecular structure, namely the ramification and the polymer molecular weight. Thus, tri-ureasils organic-inorganic hybrids with different polymer molecular weights

were synthesized and characterized for the first time. Also, the zirconium propoxide concentration in the tri-ureasils, and the UV exposure were considered as a technique to change the optical features in these new materials.

1.6 ORIGINAL CONTRIBUTIONS

This dissertation was developed under the scope of two main institutions, Instituto de Telecomunicações and CICECO - Aveiro Institute of Materials at University of Aveiro. Therefore, taking advantage of each institution, this work covers several scientific fields, with the aim of producing cost-effective PICs with different designs based on organic-inorganic hybrids incorporating zirconia-based clusters, and new solutions for light amplification and biosensing.

The devices fabricated are based on di-ureasil organic-inorganic hybrids, which is a well-known material, exhibiting stable and tunable relevant properties, namely mechanical, thermal and size control resulting from the synergy between the organic and inorganic (silicon-based) counterparts. This material was synthetized at room temperature by the versatile sol-gel method. Furthermore, this material has a heavily facilitated control of the surface optical properties by its inherent flexibility, and it is easily self-patterned by UV exposure. These cost-effective aspects are certainly absent in the case of the current used platforms (InP, silicon-on-insulator, TriPleX™) which are fabricated by complex, expensive and high-temperature physical methods.

The proposed devices were produced using the di-ureasil, and they were subject to experimental validation. The main contributions of this can be summarized as follows:

- Synthesis and processing (thin films and monoliths) of di-ureasil incorporating zirconia-based clusters;
- Optical characterization of the material by prism coupling and spectroscopic ellipsometry.
- Development and experimental validation of a thermal actuated wave plate, with electrodes heaters based on nickel-chromium (Ni-Cr) and silver (Ag) materials.
- Development of a 90° hybrid coupler, which was validated through a demodulation of a 20 Gb/s QPSK transmission performed over 40 km (G.652 fibre).
- Development and experimental validation of an electro-optic modulator based on a MZI.

- Collaboration with Professor Rachel Evans, from Department of Materials Science & Metallurgy, University of Cambridge, United Kingdom, in the development of di-ureasil doped with a blue-emitting poly(fluorene) conjugated polyelectrolyte, namely, poly[9,9-bis(4-sulfonylbutoxyphenyl) fluorene-2,7-diyl-*alt*-1,4-phenylene] (PBS-PFP).
- Proposal of di-ureasil doped with PBS-PFP material to be implemented as an optical amplifier for VLC. Photoluminescent spectroscopy, photoluminescent quantum yield, spectroscopic ellipsometry, and the variable stripe length gain measurements were performed to demonstrate the feasibility of the proposed material for optical amplification.
- Development and experimental validation of a MZI biosensor to monitor the growing concentration of bacteria in a liquid medium.

In addition, other relevant contributions were produced through the study of new and innovative organic-inorganic hybrid materials for PICs, known as tri-ureasils. On contrary to the di-ureasils, these new materials have a tripodal ureasil structure, and they were never implemented in PICs. Therefore, it is important to study their local structure and optical features. The main contributions of this can be summarized as follows:

- Synthesis and processing (thin films and monoliths) of tri-ureasil with different polymer molecular weights and doped with different zirconia-based clusters concentration.
- Local structure characterization through X-ray diffraction (XRD), nuclear magnetic resonance (NMR) for the ^{29}Si and ^{13}C atomic nucleus, Fourier-transform infrared spectroscopy (FT-IR), and Fourier transform Raman spectroscopy (FT-Raman).
- Experimental validation of the materials thermal stability by thermogravimetric analysis (TGA) and differential scanning calorimetry (DSC).
- Production of planar and channel waveguides by direct writing by UV *laser*.
- Optical characterization through prism coupling, spectroscopic ellipsometry and UV-Vis-NIR spectroscopy to obtain the refractive index and attenuation coefficients, which are relevant features to choose the most suitable material for a specific application in the future.

Concluding, this dissertation proposes cost-effective PICs based in organic-inorganic hybrids for green photonics. To approve the proposed devices, each contribution has been

subject of experimental validation and peer reviews by the international scientific community. The resulting scientific outputs are listed below.

Awards

- "Prémio de Estímulo à Investigação", Calouste Gulbenkian Foundation (2015).

Scientific communications

- A. R. N. Bastos, C. M. S. Vicente, L. Fu, L. D. Carlos, M. Lima, P. S. André, R. A. S. Ferreira, "Revisiting thermal-actuated integrated optics devices based on organic-inorganic hybrids", 17th*International Conference on Transparent Optical Networks*, invited oral presentation, Budapest, Hungary (2015).
- A. R. N. Bastos, C. M. S. Vicente, L. D. Carlos, M. Lima, P. S. André, R. A. S. Ferreira, "Development of a low cost coherent receiver", *Jornadas CICECO*, poster presentation, Aveiro, Portugal (2016).
- A. R. N. Bastos, C. M. S. Vicente, L. D. Carlos, M. Lima, P. S. André, R. A. S. Ferreira, "Development of a low cost coherent receiver", 40th *Workshop on Compound Semiconductor Devices and Integrated Circuits held in Europe*, oral presentation, Aveiro, Portugal (2016).
- A. R. N. Bastos, C. M. S. Vicente, L. D. Carlos, M. Lima, P. S. André, R. A. S. Ferreira, "Flexible 90° hybrid coupler for coherent optical systems", 18th*International Conference on Transparent Optical Networks*, invited oral presentation, Trento, Italy (2016).
- A. R. N. Bastos, C. M. S. Vicente, L. D. Carlos, M. Lima, P. S. André, R. A. S. Ferreira, "Development of an Integrated Optical Demodulator for Coherent Systems", II *Jornadas Nacionais de Caracterização de Materiais*, poster presentation, Aveiro, Portugal (2017).
- A. R. N. Bastos, A. Shahpari, L. D. Carlos, M. Lima, P. S. André, R. A. S. Ferreira, "Performance assessment of a QPSK coherent demodulator based on organic-inorganic hybrids", 19th*International Conference on Transparent Optical Networks*, invited oral presentation, Girona, Spain (2017).
- A. R. N. Bastos, A. Shahpari, L. D. Carlos, M. Lima, P. S. André, R. A. S. Ferreira, "A Cost-Effective demodulator for the Next Generation of Optical Access Networks Receivers", *Conference on Lasers and Electro-Optics Conference*, poster presentation, San Jose, California, USA (2018).
- A. R. N. Bastos, A. Shahpari, L. D. Carlos, M. Lima, P. S. André, R. A. S. Ferreira, "Green photonic integrated circuit for the next generation of optical access network", *Jornadas CICECO*, poster presentation, Aveiro, Portugal (2018).

- A. R. N. Bastos, C. M. S. Vicente, M. Lima, P. S. André, R. A. S. Ferreira, "Electro-optic organic-inorganic hybrids for signal modulation", 20th *International Conference on Transparent Optical Networks*, invited oral presentation, Bucharest, Romania (2018).

Scientific papers

- A. R. N. Bastos, C. M. S. Vicente, R. Oliveira-Silva, N. J. O. Silva, M. Tacão, J. P. Costa, M. Lima, P. S. André, R. A. S. Ferreira, "Integrated Optical Mach-Zehnder Interferometer Based on Organic-Inorganic Hybrids for Photonics-on-a-chip Biosensing Applications", *Sensors* **18**, 840 (2018).
- A. R. Frias, E. Pecoraro, S. F. H. Correia, L. M. G. Minas, A. R. Bastos, S. García-Revilla, R. Balda, S. J. L. Ribeiro, P. S. André, L. D. Carlos and R. A. S. Ferreira, "Sustainable luminescent solar concentrators based on organic–inorganic hybrids modified with chlorophyll", *Journal of Materials Chemistry A* **6**, 8712-8723 (2018).
- Ana R. N. Bastos, Barry McKenna, Mário Lima, Paulo S. André, Luís D. Carlos, Rachel C. Evans and Rute A. S. Ferreira, "Flexible optical amplifier for Visible Light Communications based in organic-inorganic hybrids", *ACS Omega* **3**, 13772−13781 (2018).
- A. R. N. Bastos, A. Shahpari, M. Lima, P. S. André, R. A. S. Ferreira, "Green photonics integrated circuit for NGOA coherent receivers", *submitted.*
- A. R. Bastos, P. S. André, R. A. S. Ferreira, L. D. Carlos, 'Organic–Inorganic Hybrids Towards Photonic Integrated Circuits For Green Photonics", in Sol-gel derived optical and photonic materials, edited Alex Martucci, L. Santos and Rocio Hernandez, *Wiley, John Wiley & Sons*, to be published in 2020.

1.7 THESIS OUTLINE

To accomplish the established research objectives, this document is divided in 8 chapters, where it is demonstrated the potential of organic-inorganic hybrids in the green photonics fields, namely in optical communications and sensing. After this introductory chapter, which illustrates the optical components required for the next generation of optical communications and biosensing, considering green photonics goals, it follows an overview of the PICs technology, focusing on the propagation fundaments in channel waveguides, and operation principles of passive (MZI and 3-dB directional optical coupler) and active (optical amplifier) devices.

Chapter 3 presents the synthesis and processing techniques used to produce organic-inorganic hybrids. The local structure characterization of the materials is also addressed in this chapter, with experimental results of XRD, NMR, FT-IR and FT-Raman. The thermal properties of the materials were studied through TGA and DSC measurements.

The characterization of the relevant optical features to develop PICs is provided in Chapter 4, where the refractive index dispersion curves and absorption spectra performed through prism coupling, spectroscopic ellipsometry and UV-Vis-NIR absorption spectroscopy are addressed. The photosensibility of the hybrids and the mechanism used to change locally the refractive index are also discussed.

The devices developed for optical communications during this dissertation are addressed in Chapters 5 and 6, which contain the experimental details, results and discussion for passive and active devices, respectively. Taking advantage of the know-how in the optimized PICs fabrication, a MZI was produced to demonstrate a lab-on-a-chip biosensor, which is detailed in Chapter 7.

Finally, the main conclusions, and some future work proposals are summarized in Chapter 8.

CHAPTER 2

INTEGRATED OPTICS FUNDAMENTS

This chapter addresses the concept of integrated optics and the principles behind radiation guidance in channel waveguides, which are the fundaments of PICs. In particular, the optical losses, and the principle of operation of MZIs, 3-dB directional couplers and optical amplifiers will be described in detail.

2.1 PHOTONIC INTEGRATED CIRCUITS TECHNOLOGY

Integrated optics aims at producing the so-called PICs or planar lightwave circuits. As in micro-electronics, in PICs a broad range of functionalities is realised from a set of basic building blocks. By connecting these building blocks in different numbers and topologies, it is possible to develop a large variety of circuits and systems. The building blocks can be categorized as active and passive devices. As examples, active components include *lasers*, optical amplifiers, and detectors, whereas passive components are related to waveguides, couplers, filters and (de)multiplexers. Figure 2.1 illustrates examples of basic PICs building blocks.

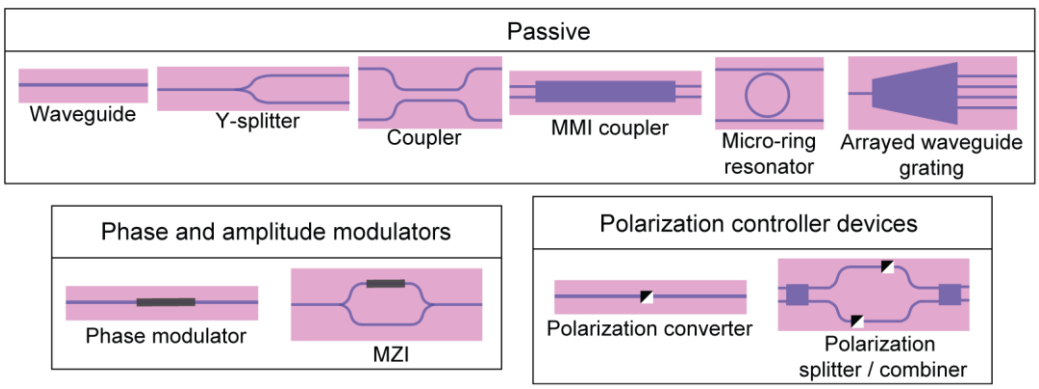

Figure 2.1 Schematic examples of functionalities that can be attained in generic PIC technology.

The most elementary component is the channel waveguide, which could be linear or with curvatures, allowing the optical signal to be guided between two points in the optical circuit. The combination of waveguides with different dimensions (width and length) can yield more complex and versatile components, such as couplers, Y-splitters, multi-mode interference (MMI) couplers, micro-ring resonators, and arrayed waveguide gratings. In addition, other basic building blocks are necessary for manipulating the phase, amplitude and the polarization of the optical signal, to support a broad range of functionalities. The most common structure for phase and amplitude modulators is the MZI combined with electro-optic (EO) or thermo-optic (TO) effects to perform the signal modulation function. The polarization controller devices allow the signal transmission to have a well-defined state of polarization.

The first application for PICs was in the area of optical communications, despite the evolution in other fields such as sensing, biomedical and photonic computing [64,116]. For sensing, the PICs make use of interaction between the radiation and various environmental factors of physical nature, like temperature, pressure, radiation, toxins and pollutants [117]. Therefore, this sensors convert the variation of the measured quantity into a variation of radiation parameters like intensity, resonant wavelength or phase shift [118]. In what concerns optical communications, PICs can provide devices operating with higher transmission rates, with the possibility to encode the information in the optical signal amplitude, phase and polarization, and to implement spectral multiplexing. The operation spectral range of interest is the near infra-red (NIR), due to the low absorption losses in optical fibres in this spectral region. However, some properties in optical circuits can produce optical losses and limit the optical signal propagation. Therefore, it is required to understand how the radiation is guided in a specific PIC structure.

2.2 CHANNEL WAVEGUIDES

2.2.1 RADIATION GUIDANCE

To propagate radiation in a waveguide it is required to confine the optical signal in this structure. Since, the waveguide dimensions are in the same order of magnitude as the optical signal wavelength, the propagation cannot be explained by geometrical optics. Therefore, to analyse the propagation in channel waveguides it is used, generally, analytical or numerical techniques [119]. For a uniform structure, it is required to determine its mode distribution and its associated propagation constant β. Then, for a given geometry, it is important to determine the behaviour of the optical signal propagation. The solution to these problems can be found

by solving Maxwell's equations in the domain subjected to the boundary conditions dictated by the geometries [120]. For uniform structures, a number of methods have been developed and implemented, as the Marcatili method, effective index method, finite-element method, and finite-difference method [121]. For non-uniform structures, the commonly used approaches are the beam propagation method (BPM) [122] and the finite-difference time-domain method [123].

In this dissertation, to optimize the devices geometry it was used the BPM method to analyse the optical signal propagation. This method solves problems of guided-wave propagation, and tt was first introduced by Feit and Fleck [124] who employed this technique to calculate the propagation and mode properties in optical fibres. Since then, many other wave guiding structures, such as tapers, Y-junctions, bends, gratings, waveguide crossings, EO modulators, fibre couplers, and nonlinear directional couplers have been modelled and analysed by BPM [121]. This approach is based on the approximation of the exact wave equation for monochromatic waves and the numerical solution of the resulting equations.

In the basic form of BPM, the electric field is represented as a scalar value instead of a vector value. Therefore, the polarization effects are neglected, and the propagation is assumed to be paraxial (i.e. confined to a narrow range of angles). The scalar field assumption allows the wave equation to be written in the form of the Helmholtz equation for monochromatic waves:

$$\nabla^2\phi(x,y,z)+k(x,y,z)^2\phi=0\cdot \tag{2.1}$$

where the scalar electric field is written as $E(x, y, z) = \phi(x, y, z)e^{-\omega t}$, and $k(x, y, z) = k_0 n(x, y, z)$ is the spatially dependent wavenumber, with k_0 as the wavenumber in free space. It can be seen that the refractive index distribution $n(x, y, z)$ defines the geometry of the problem [119].

For typical guided wave, the phase variation due to propagation along the guided axis (i.e. the z axis) gives a rapid variation in the field ϕ. To improve the technique efficiency, this rapid phase variation is removed from the problem with the introduction of a slowly varying field u:

$$\phi(x,y,z)=u(x,y,z)e^{i\bar{k}z}\cdot \tag{2.2}$$

where $\bar{k}$ is the reference wavenumber, a constant representing the average phase variation of the field ϕ. This approximation can only be applied to paraxial fields (i.e. the field is propagating mainly along the z axis).

Combining Equation (2.1) and Equation (2.2), the following equation for the slowly varying field arises:

$$\frac{\delta^2 u}{\delta x^2}+\frac{\delta^2 u}{\delta y^2}+\frac{\delta^2 u}{\delta z^2}+2i\bar{k}\frac{\delta u}{\delta z}+u(k^2-\bar{k}^2)=0\cdot \tag{2.3}$$

Assuming that the variation u with z is slow, the second derivative term in z can be neglected through the paraxial approximation, which reduces the problem from a second-order boundary value problem requiring eigenvalue analysis, to a first-order initial value one that can be simply solved by integration. By eliminating the second derivative, the reflections (i.e. backward travelling wave solutions) cannot be accurately modelled based on this approach. Equation (2.3) then becomes:

$$\frac{i}{2\bar{k}}\left(\frac{\delta^2 u}{\delta x^2}+\frac{\delta^2 u}{\delta y^2}+u(k^2-\bar{k}^2)\right)=\frac{\delta u}{\delta z}\cdot \tag{2.4}$$

which is the basic BPM equation in three dimensions. This basic form of BPM models the continuous wave optical fields propagating in the z-direction. By discretizing the cross-section of a waveguide structure into grid points, the cross-sectional profile is calculated through one "slice" at a time using Equation (2.4) in the z-direction, with each successive slice being mathematically dependent on the current slice. This process is repeated until the wave has propagated through the entire structure [119].

The basic BPM theory may be extended in many ways to address the above-mentioned limitations. For example, vector BPM calculations may be performed by incorporating the polarization effects. Wide-angle BPM calculations [125] may be performed to address the paraxial restrictions on the basic BPM. The paraxial limitations may be reduced by incorporating the effects of the second order derivative according to the different degrees of approximation. Lastly, bidirectional BPM [126] may also be incorporated to handle simultaneous propagation along the negative z axis based on a transfer matrix approach.

Besides these analyses, it is also important to consider the attenuation mechanisms that limits the optical signal propagating in a PIC, namely the optical signal propagation losses based on radiation, absorption, and scattering.

2.2.2 PROPAGATION LOSSES

The losses by radiation occur due to the proximity of the refractive index values of the waveguide and these of the substrate/superstrate, leading to similar propagation constants. In these situations, there is a fraction of the guided mode energy that is lost in the substrate and

superstrate, Figure 2.2. For channel waveguides with a low refractive index contrast ($<10^{-2}$ [127]) between the waveguide and the surrounds of the film, part of the guided mode is lost in the film. The energy of the guided mode lost is known as the evanescent field (yellow region, Figure 2.2).

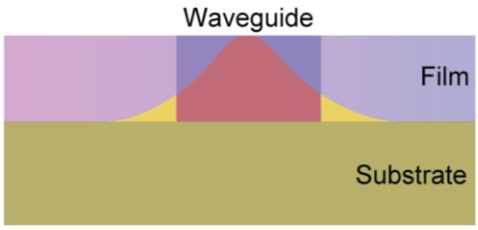

Figure 2.2 Illustration of an electromagnetic field distribution in a channel waveguide, where the yellow regions correspond to the evanescent field.

A common requirement in PICs is the ability to guide radiation through a bend, for example to establish links between different devices on a chip. However, any curvature in a waveguide leads to additional loss [128]. The radius of curvature affects the guided mode profile, because the propagated mode centre is shifted to the outer part of the waveguide-film interface as shown in Figure 2.3 [121]. In this case, when the curvature changes, a modal transition loss occurs because the modal profile is not centred in the waveguide, and the energy distribution in the waveguide-film interface is larger than in a linear waveguide. This will increase the propagated mode sensibility to any imperfection in the waveguide-film interface, increasing the radiation losses [121]. Therefore, the bend loss is very dependent on the confinement offered by the waveguide. For low refractive index contrast ($<10^{-2}$ [127]), the confinement is poor, so bends must be shallow (~50 mm for sol-gel materials), limiting the device packaging density considerably [128].

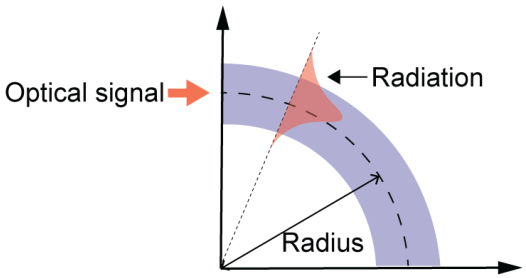

Figure 2.3 Illustration of radiation losses in a waveguide curvature.

Another relevant mechanism for optical losses occurs when the material absorbs radiation (absorption losses). In particular, in what concerns organic-based materials (as in the present case) the major challenge in the synthesis of organic-inorganic hybrid materials for PICs is to reduce the number of oscillators (e.g. OH, CH, NH and CO groups), because they absorb

radiation in the NIR spectral region [129]. Although relevant, this aspect was not focused as only low dimension circuits were considered.

The scattering losses are due to defects in the film-substrate and film-superstrate interfaces, or in the waveguide. The potential defects in waveguides can be: porosity, fissures, particles, surface and substrate roughness [130], Figure 2.4. The existence of particles can result from the thin films deposition process. Therefore, this process should be done in a cleanroom, minimizing the presence of particles. The fissures can be minimized by optimizing the thermal treatment of the film.

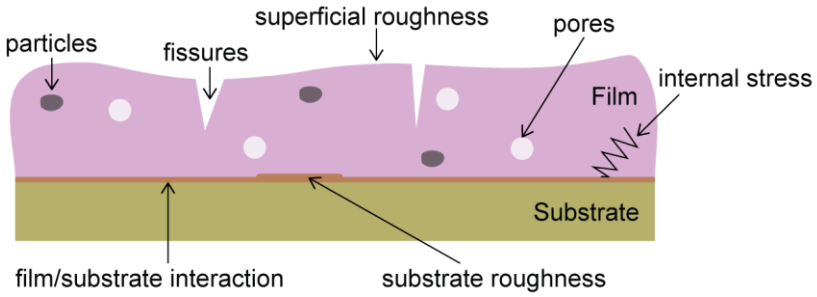

Figure 2.4 Illustration of defects in a waveguide responsible for scattering losses. Adapted from [18].

Concluding, to optimize the performance of a PIC, it is required to consider its geometry, due to the propagation losses. In parallel, the materials chemical design and processing are also relevant to decrease the contribution of absorption and scattering losses. The design of optimized circuits requires also a detailed understanding of the various factors that affect the device operation.

2.3 PASSIVE DEVICES: PRINCIPLE OF OPERATION

2.3.1 MACH-ZEHNDER INTERFEROMETER

In the early optical systems, the intensity modulation and direct detection systems were used, in which *lasers* were modulated directly by combining the data signal with the bias of the *laser* diode [26]. The advantages of this modulation system are its simplicity, and the receiver sensitivity independence of the carrier phase and the state of polarization of the incoming signal. However, for data rates higher than 1-2 Gb/s, the complex dynamics of the coupling of electrons and photons within the *laser* cavity cause undesirable frequency variations, known as chirp [131], which causes signal distortion as it propagates on the optical fibre. Therefore, for high data rates a better option is the external modulation. In this scheme, the *laser* operates on a constant bias producing a continuous narrow line width, and the data is imposed on the optical carrier by an external modulator [132].

The optical amplitude modulator is one of the simplest devices, which can be controlled, for instance, by an external source, or through changes in the effective index of the superstrate, using, for example, a MZI structure, Figure 2.5. A MZI exploits the phase difference between two optical signals, to interfere destructively or constructively, and thus producing an amplitude modulated signal at the output. The input waveguide is split into two waveguide interferometer arms. By applying an effect (e.g. electro-optic or thermo-optic) that will induce a phase shift for the wave passing through one of the arms, and recombining the signals of both arms, the phase difference between the two waves is converted to an amplitude modulation [67].

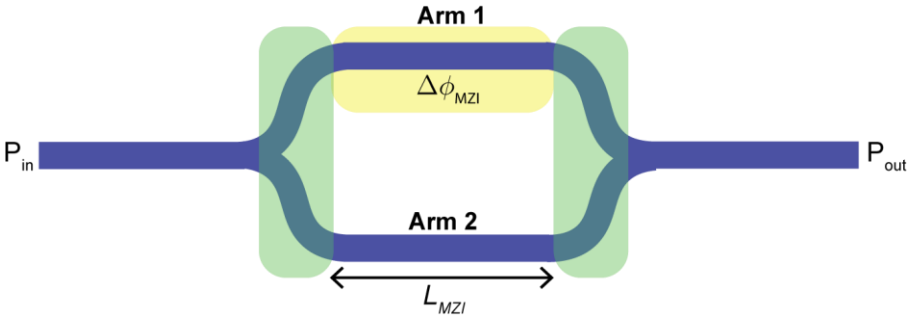

Figure 2.5 Scheme of a MZI, where L_{MZI} is the arm length, the green region are the Y-junctions, and the yellow region is the arm with an induced phase shift, $\Delta\phi_{MZI}$.

This device consists of one phase modulator and one ordinary channel waveguide (or two integrated phase modulators), and two Y-junctions, one at the input for splitting the signals and another at the output to combine them. The input Y-junction splits the power equally into two branches to give fields E_{MZI1} and E_{MZI2}, in the two arms of the interferometer. Then, an external source in one of the branches introduces a phase shift in the optical signal ($\Delta\phi_{MZI}$) [133]:

$$E_{MZI1} = \frac{E_{in}}{2} e^{i\Delta\phi_{MZI}}$$
$$E_{MZI2} = \frac{E_{in}}{2} \tag{2.5}$$

where E_{in} is the input field. By combining the two fields in the output Y-junction, the output field E_{out} is described by

$$E_{out} = E_{MZI1} + E_{MZI2} = \frac{E_{in}}{2}\left(1 + e^{i\Delta\phi_{MZI}}\right) = E_{in}\cos\left(\frac{\Delta\phi_{MZI}}{2}\right)e^{i\Delta\phi_{MZI}/2}. \tag{2.6}$$

Therefore, the optical output power will be

$$P_{out} = \frac{|E_{out}|^2}{2} = P_{in}\cos\left(\frac{\Delta\phi_{MZI}}{2}\right)^2 = \frac{1}{2}P_{in}\left(1+\cos(\Delta\phi_{MZI})\right). \tag{2.7}$$

whose output transfer function is characterized by a sinusoidal function.

The $\Delta\phi_{MZI}$ is induced by a variation of the effective index in the MZI arm 1 (Figure 2.5), and it is described by

$$\Delta\phi_{MZI} = \left(\frac{2\pi \, \Delta n_{MZI} \, L_{MZI}}{\lambda} \right). \tag{2.8}$$

where Δn_{MZI} is the refractive index change, and λ is the wavelength of the propagating signal. As already mentioned, this change could be induced by an external source (thermo-optic or electro-optic effect) or the change of superstrate environment in the MZI arm. The first one could be applied for modulation, and the last one as a sensor.

2.3.2 3-DB OPTICAL DIRECTIONAL COUPLER

Directional couplers are passive devices that couple a defined amount of the optical power in a waveguide enabling the signal to be used in another circuit [134]. A 3-dB directional coupler is designed to split power equally between two ports. This device is highly desirable for many applications in optical communications [135], as power combiner/dividers, add–drop multiplexers, and switches [136].

The operation principle of a directional coupler is based on the energy transfer between adjacent waveguide cores. In Figure 2.6 it is illustrated a double input and double output device constituted by three main parts: two transition regions (orange area, Figure 2.6) and one coupling region (green area, Figure 2.6). The transition regions make the connection to and from the coupling region, whose gap between the waveguides should be large enough to guarantee no coupling. The region where the coupling occurs consists of two monomode waveguides that are closely placed in parallel. An array of two waveguides supports two modes (known as super-modes): a symmetric and an anti-symmetric mode. When radiation is launched into one of the waveguides it excites a linear combination of the super-modes.

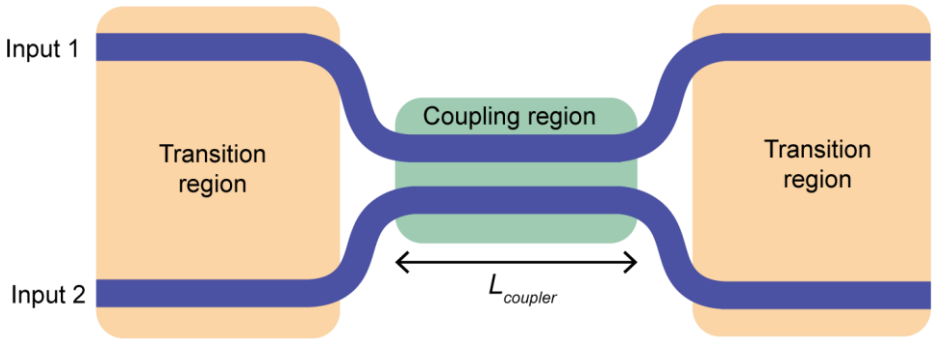

Figure 2.6 Scheme of a directional coupler, where $L_{coupler}$ is the coupling length.

The symmetric and antisymmetric modes have different propagation constants, so along the distance of propagation the system develops a phase difference between them, leading to cancellation in one waveguide and addition on the other at certain positions. Therefore, there is a power transfer from one waveguide to another. As, this phase difference between the modes is periodic, a periodic exchange of power between the waveguides occurs along the propagation length.

In the case of a symmetric coupler formed by two identical waveguides, the transfer matrix of the device can be described as,

i) for the amplitude

$$\begin{bmatrix} A_1(L_{coupler}) \\ A_2(L_{coupler}) \end{bmatrix} = \begin{bmatrix} \cos(k_c L_{coupler}) & i\sin(k_c L_{coupler}) \\ i\sin(k_c L_{coupler}) & \cos(k_c L_{coupler}) \end{bmatrix} \begin{bmatrix} A_1(0) \\ A_2(0) \end{bmatrix}. \tag{2.9}$$

ii) for the electric field

$$\begin{bmatrix} E_1(L_{coupler}) \\ E_2(L_{coupler}) \end{bmatrix} = \begin{bmatrix} \sqrt{i-K_c} & i\sqrt{K_c} \\ i\sqrt{K_c} & \sqrt{i-K_c} \end{bmatrix} \begin{bmatrix} E_1(0) \\ E_2(0) \end{bmatrix}. \tag{2.10}$$

where k_c is the coupling coefficient that measures the strength of coupling and is given by [137]

$$k_c = \frac{\beta_s - \beta_a}{2}. \tag{2.11}$$

where β_s and β_a are the propagation constants of the symmetric and anti-symmetric mode of the individual waveguides, respectively, and K_c is the couple factor that varies from 0 to 1 specifying the amount of power that is transferred from one waveguide to the other.

If only the first input is excited, one can conclude that [137]

$$\begin{aligned} P_1(L_{coupler}) &= A^2 \cos^2(k_c L_{coupler}) \\ P_2(L_{coupler}) &= A^2 \sin^2(k_c L_{coupler}) \end{aligned}. \tag{2.12}$$

By analysing Equations (2.12), it is relatively easy to control the amount of power that is transferred from one waveguide to the other. For example, for a 3-dB coupler, the coupling length should be $\pi/4k_c$.

In this dissertation, the 3-dB coupler was implemented for a homodyne coherent receiver based on a 90° hybrid coupler which separates the IQ components of the encoded signal with the interference between the QPSK modulated signal (E_S) and the local oscillator signal (E_{LO}). This device is characterized by four 3-dB directional couplers and an additional 90° phase delay in one of the branches [138], as depicted in Figure 2.7.

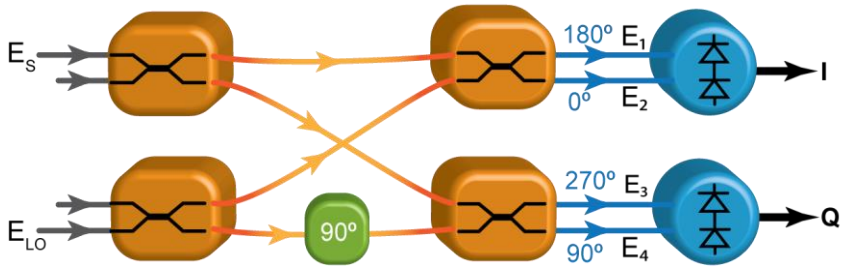

Figure 2.7 Schematic representation of a coherent receiver with balanced photodiodes to extract the IQ components. E_S is the modulated signal field, E_{LO} is the LO field, and $E_{1\text{-}4}$ are the signal field at the output port 1-4, respectively.

The interference will generate different responses at each output port (output 1-4), that can be calculated through Equation (2.13) [39].

$$\begin{bmatrix} E_1 \\ E_2 \\ E_3 \\ E_4 \end{bmatrix} = \frac{1}{2}\begin{bmatrix} 1 & -1 \\ -j & -j \\ -j & 1 \\ -1 & j \end{bmatrix} \cdot \begin{bmatrix} E_s \\ E_{LO} \end{bmatrix}. \tag{2.13}$$

where E_s is the normalized signal field, E_{LO} is the normalized LO field, and $E_{1\text{-}4}$ are the normalized signal field at the output port 1-4, respectively. Detecting $E_{1\text{-}2}$ with the one pair of balanced diodes and $E_{3\text{-}4}$ with another one, the photocurrents (I_I and I_Q) that give the information about the I and Q phase components, respectively, are:

$$\begin{aligned} I_I &= R \cdot \sqrt{P_{in}} \cdot \sqrt{P_{LO}} \cdot \cos(\Delta\theta) \\ I_Q &= R \cdot \sqrt{P_{in}} \cdot \sqrt{P_{LO}} \cdot \sin(\Delta\theta) \end{aligned} \tag{2.14}$$

where R is the photodiodes responsivity, P_{in} and P_{LO} are the signal input and LO optical power, respectively, and $\Delta\theta$ is the phase difference between the E_s and E_{LO}.

2.4 Active devices: principle of operation

Among several active optical devices, such as optical sources, amplifiers and detectors, in this dissertation it was focus the optical amplification. Therefore, in this section, the principle of operation of different optical amplifiers will be described.

2.4.1 Optical amplifier

In access networks, such as PONs where an optical signal is divided among many users, it is required to compensate the signal-splitting losses. This requirement is also applied to point-to-point optical fibre links, due to the scattering and absorption losses mechanisms in an optical fibre which cause a progressive attenuation of the optical signals. Therefore, the signals

need to be amplified so that the receiver can properly interpret them, making optical amplifiers indispensable components in high-performance optical communication links. There are different physical mechanisms that can be used to amplify an optical signal, as electron-hole recombination (semiconductor optical amplifiers, SOAs), stimulated emission in the amplifier's gain medium (doped fibre amplifiers, DFAs), stimulated Raman scattering (Raman amplifiers), and amplified spontaneous emission (ASE).

The SOAs are amplifiers in which the gain medium is a semiconductor [139], that can be easily integrated on the same substrate as other optical devices and circuits. The SOA principle of operation is similar to the one of *laser* diodes, where an external current injection is the pumping method used to create the population inversion needed for the operation of the gain mechanisms. Takin as an example the travelling wave SOA, the optical signal travels through the device only once, in contrast to a *laser* where the optical signal makes many passes through the lasing cavity. During this passage the signal emerges intensified at the end of the device. These amplifiers are typically based on III-V compound semiconductors such as GaAs/AlGaAs, InP/InGaAs, InP/InGaAsP and InP/InAlGaAs, operating at signal wavelengths between 850 nm and 1600 nm and generating up to 30 dB gain [140].

The DFAs are optical amplifiers that use a doped optical fibre as a gain medium. The amplification is achieved by stimulated emission of photons from dopant ions in the fibre, using a pump *laser*. The pumping excites the ions into a higher energy from where they can decay via stimulated emission of a photon at the signal wavelength [140]. The most common DFA is the erbium one (EDFA), where the core of a silica fibre is doped with trivalent erbium ions, and it is efficiently pumped with a *laser* at a wavelength of 980 nm or 1480 nm, exhibiting a gain in the 1550 nm region [41].

A Raman amplifier makes use of the transmission fibre itself as the amplification medium, and it is based on the stimulated Raman scattering effect. This effect is due to an interaction between the optical energy field and the vibration modes of the lattice structure in a material. The principle of operation is based on an atom absorbing a photon at one energy, and then releases another photon at a lower energy. The energy difference between the absorbed and the released photons leads to a phonon, which is a vibration mode of the material. The power transfer results in an increasing wavelength shift of 80 to 100 nm, known as the Stokes shift. For example, pumping at 1450 nm will lead to a signal gain at approximately 1530 to 1550 nm [140].

In the ASE, the gain medium is optically pumped to produce a population inversion, resulting in a diffuse fluorescence emission. The devices that uses this technique are random *lasers*, which operate when multiple radiation scattering in the disordered materials lets the gain surpass the loss [141]. Since, these *lasers* do not require rigorous resonant cavities, issues like miniaturization and cost are no longer a problem. Since the experimental breakthrough by Lawandy et al. [142], efforts have been made to produce random lasing actions in diversified material from inorganic [143] to organic [144] or even bio-material [145].

CHAPTER 3

ORGANIC-INORGANIC HYBRIDS

In this chapter, the synthesis and processing of organic-inorganic hybrid materials used as substrates for PICs are discussed.

Based on past experience and featuring the development of innovative materials with enhanced and tunable optical properties for PICs, two families of organic-inorganic hybrids were prepared, namely di-ureasils and tri-ureasils. These materials were prepared by sol-gel method and doped with different concentrations of zirconium propoxide ($Zr(OPr^n)_4$, ZPO) and methacrylic acid (McOH) to control the refractive index. The dopants used in the preparation of the doped materials will be named hereafter as ZPO-McOH. To quantify the amount ratio between Zr and Si atoms, X-ray photoelectron spectroscopy (XPS) measurements were done. The synthesis and doping were conducted in collaboration with Doctor Lianshe Fu, Principal Researcher at Physics Department and CICECO-Institute of Materials Aveiro from University of Aveiro.

The effect of different polymer molecular weights and different concentrations of ZPO-McOH in the local structure of tri-ureasils is fundamental to understand how it will interfere in the relevant physical properties (refractive index and absorption coefficient), and consequently to choose the best one for a specific application, and to a given device design. As these materials are amorphous, it is required to use several techniques to characterize the local structure of the organic and inorganic components. Through the analysis of experimental results obtained from XRD, and NMR for the ^{29}Si atomic nucleus, it was studied the materials inorganic component. To analyse the organic component, it was considered the experimental results obtained from XRD, NMR ^{13}C atomic nucleus, FT-IR, and FT-Raman. To analyse the materials thermal stability, TGA and DSC measurements were performed. The experimental details of these techniques are present in Annex A.

Featuring active optical devices, the di-ureasil was doped with a conjugated polyelectrolyte (CPE), whose materials processing was performed in straight collaboration with Professor Rachel Evans, from Department of Materials Science & Metallurgy, University of Cambridge, United Kingdom.

3.1 SOL-GEL METHOD

The development of new materials combining different components in one system is one of the most expanding fields in materials chemistry [146]. In particular, the polyvalent synthetic conditions offered by sol-gel process, such as low temperature processing and shaping, high-purity and availability precursors, and sample homogeneity, allow the synthesis of multifunctional organic-inorganic hybrids structures.

The sol-gel technique is based on the formation of a colloidal suspension (sol), and on the gelation of the suspension to form a three-dimensional network (gel) [147]. The preparation of the materials can be summarized in the following steps (Figure 3.1):

- mixture of reagents to form the sol;
- synthesis of the material from hydrolysis and partial condensation;
- aging;
- drying.

While the above steps are common to most of the sol-gel processes, the nature of the specific reactions involved in hydrolysis and condensation reactions differ between the various types of precursors [148]. Because of their high reactivity with water, metal alkoxides Si(OR), where R represents the alkyl group, in particular Tetraethoxysilane (TEOS), are the most widely used precursors in the sol–gel process [149].

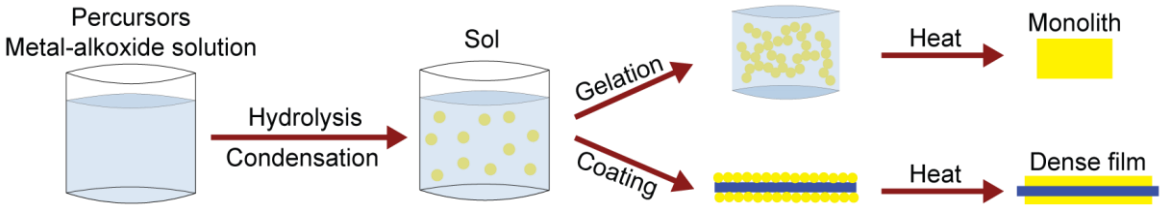

Figure 3.1 Scheme of sol-gel process evolution.

The hydrolysis reaction occurs when the water molecules react with the precursor, and removes the alkoxides group (-OR), replacing it with the hydroxyl group (-OH) and forming the silonal groups (Si-OH) [147]:

$$Si(OR)_n + H_2O \rightarrow Si(OH)(OR)_{n-1} + SiOH \quad (3.1)$$

Through condensation reaction, the silanol groups, formed during the hydrolysis, react to produce siloxane bonds (Si-O-Si) and alcohol (3.2) or water (3.3). During the condensation process, the siloxane bonds increase leading to bridging and aggregation of the individual molecules in the sol. Gel formation occurs when these aggregates start forming the networks.

$$\text{Si-OR} + \text{Si-OH} \rightarrow \text{Si-O-Si} + \text{ROH} \quad (3.2)$$

$$\text{Si-OH} + \text{Si-OH} \rightarrow \text{Si-O-Si} + \text{H}_2\text{O} \quad (3.3)$$

Aging is the process where condensation continues with the gel network, often shrinking it and resulting in expulsion of the solvent [148]. The drying is performed by heating the material to remove the solvents, shrinking the whole system. Depending on the process used to dry the material, the result can be a monolith (bulk) or film. Figure 3.2 illustrates the most relevant properties of the sol-gel method for commercial applications. In this dissertation, di-ureasils and tri-ureasils organic-inorganic hybrids were prepared using this versatile method.

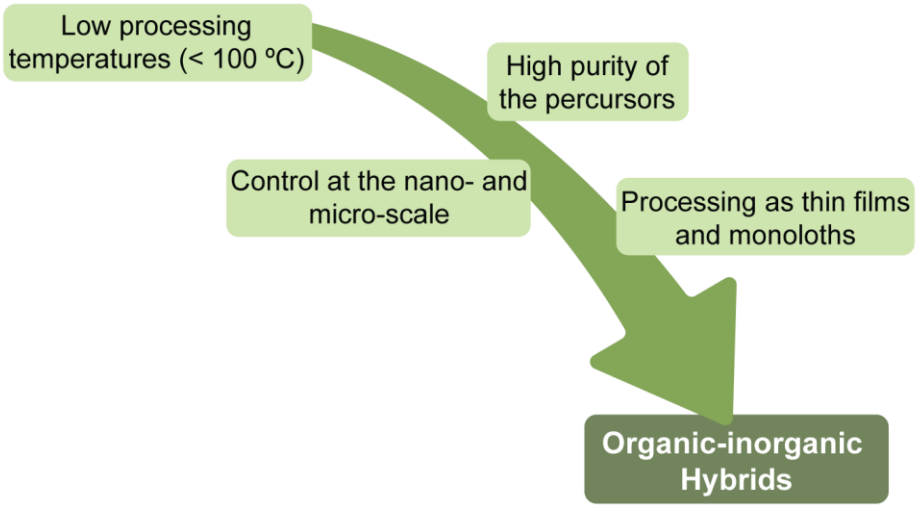

Figure 3.2 Scheme of sol-gel method key factors.

3.2 DI-UREASIL AND TRI-UREASILS SYNTHESIS AND PROCESSING

3.2.1 NON-DOPED DI-UREASIL

Materials

Double functional diamine Jeffamine ED-600® with average molecular weight of ~600 g·mol^{-1} was purchased from Fluka Company. Isocyanate group of an alkoxysilane precursor (3-isocyanatopropyltriethoxysilane, ICPTES 95 %) was obtained from Aldrich. The tetrahydrofuran (THF, 99 %) is commercially available at Sigma–Aldrich. High-purity distilled water was used throughout experiments. The chemical structure for ED-600 is shown in Figure 3.3.

Preparation of di-ureasil organic-inorganic hybrid materials [150]

The organic-inorganic hybrid designated as di-ureasil is composed of polyether-based chains grafted at both ends to a siloxane backbone through urea functionalities [113]. The di-ureasil is designated as d-U_{600}, where d indicates di (both ends of the polymer chain are covalently bond to the siliceous-based domains), U originates from the word "urea" and 600, indirectly indicates the length of the oligopolyoxyethylene chains. The urea linkages were formed between the terminal ED-600 and the ICPTES, molar ratio ICPTES:ED-600=2:1. The resulting mixture was further refluxed for 24 h (at around 75 °C). The solvent THF was evaporated under vacuum to afford the non-hydrolysed precursor di-ureapropyltriethoxysilane, d-UPTES(600). The scheme of the precursor d-UPTES(600) synthesis is presented in Figure 3.3.

For the synthesis of d-U_{600}, a certain amount of precursor d-UPTES(600) was mixed with ethanol (EtOH, Sigma–Aldrich), and stirred at room temperature for 10 minutes. The diluted Hydrochloric acid (HCl) aqueous solution was added to speed up the hydrolysis and condensation reaction, with a molar ratio of d-UPTES(600): H_2O = 1:9. The resulting sol was further stirred at room temperature for some time, transferred to a mould, and placed in an oven at 45 °C for 24 h.

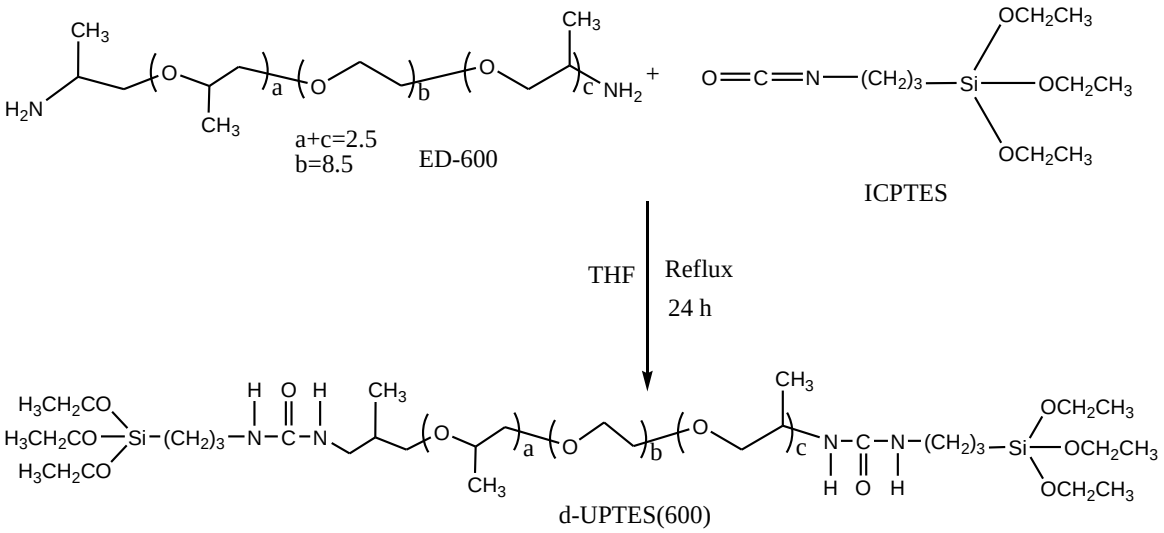

Figure 3.3 Schematic representation of the synthesis of the non-hydrolysed precursor, d-UPTES(600).

3.2.2 NON-DOPED TRI-UREASILS

Materials

Trifunctional primary amines Jeffamine® T-403, T-3000 and T-5000 with average molecular weights of approximately 440, 3000 and 5000 $g \cdot mol^{-1}$, denoted as T-403, T-3000 and T-5000, respectively, were purchased from Huntsman Company. 3-Isocyanateproplytriethoxysilane (ICPTES, 95 %, Aldrich) was obtained from Aldrich. Hydrochloric acid (HCl, Aldrich), EtOH and THF are all commercially available. High-purity distilled water was used throughout experiments. The structures for T-403, T-3000 and T-5000 are shown in Figure 3.4 and 3.5.

Preparation of tri-ureasils organic-inorganic hybrid materials

The preparation of tri-ureasils t-U_Y, where t indicates tri (branched tripodal structure), U originates from the word "urea" and *Y* = 440, 3000 and 5000, indirectly indicates the length of the oligopolyoxyethylene chains, involves two steps: the synthesis of precursor t-UPTES(*Y*), and the hydrolysis/polycondensation of the precursor in the presence of an HCl aqueous solution, Figure 3.4 and 3.5. A certain amount of T-403 (T-3000 or T-5000) was mixed with THF thoroughly under stirring. The ICPTES was added dropwise to this solution, with a molar ratio of T-403 (T-3000 or T-5000) : ICPTES = 1:3. The resulting mixture was further refluxed for 24 h (at around 75 °C). The solvent THF was evaporated under vacuum to afford the precursors t-UPTES(*Y*), *Y* = 440, 3000 and 5000 for starting materials T-403, T-3000 and T-5000, respectively.

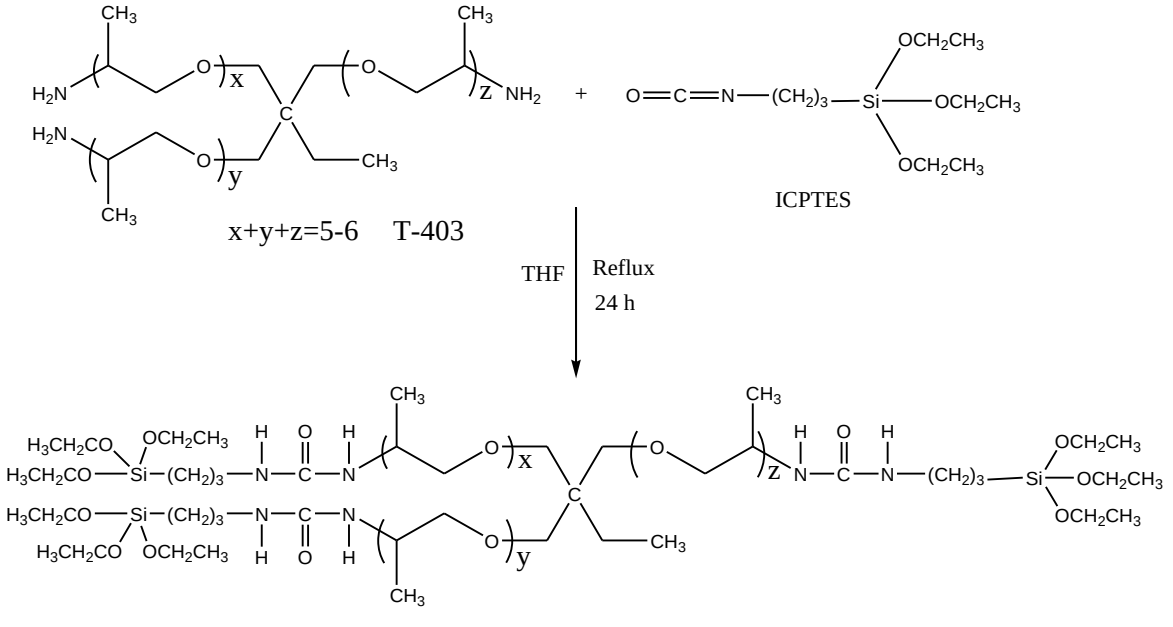

Figure 3.4 Schematic representation of the synthesis of the non-hydrolysed precursor, t-UPTES(440).

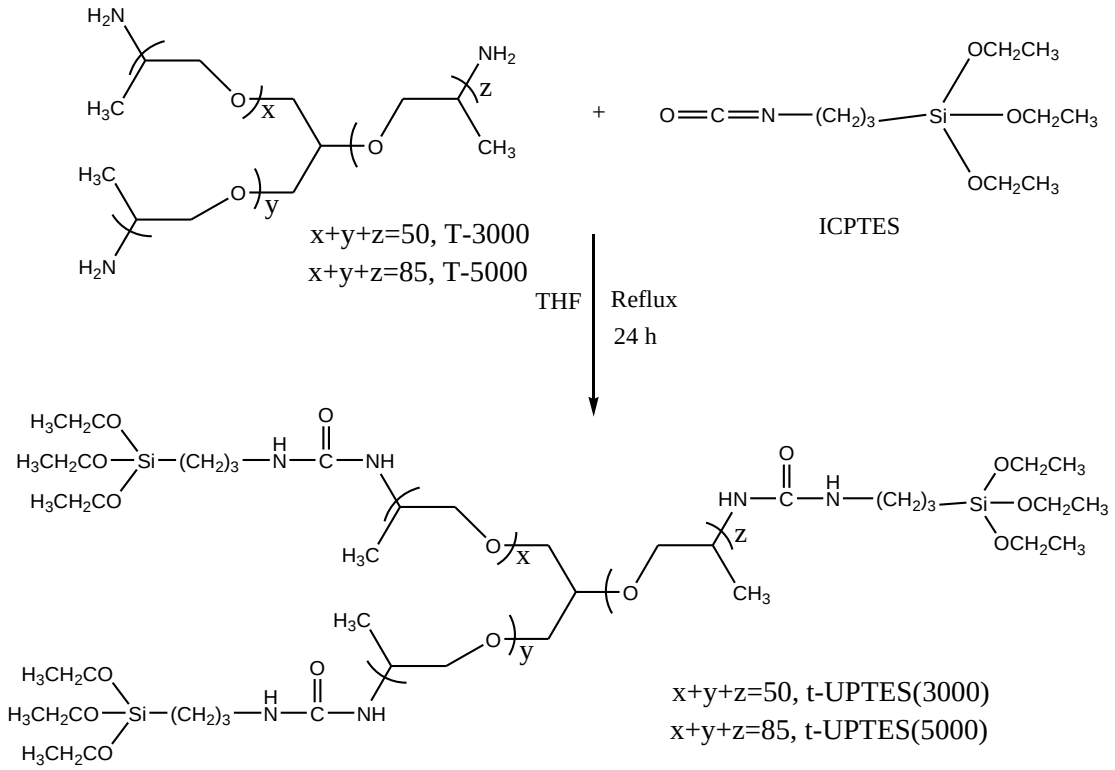

Figure 3.5 Schematic representation of the synthesis of the non-hydrolysed precursor, t-UPTES(Y) where Y= 3000 and 5000.

For the synthesis of tri-ureasils t-U_Y (Y = 440, 3000 and 5000), a certain amount of precursor t-UPTES(Y) was mixed with EtOH, and stirred at room temperature for 10 minutes. The diluted HCl aqueous solution was added to speed up the hydrolysis and condensation reaction, with a molar ratio of t-UPTES(Y) : H_2O = 1:9. The resulting sol was further stirred at room temperature for some time, transferred to a mould, and placed in an oven at 45 °C for 24 h. The resultant tri-ureasils were designated as t-U_{440}, t-U_{3000} and t-U_{5000} for starting materials T-403, T-3000 and T-5000, respectively.

3.2.3 DI-UREASIL AND TRI-UREASILS MODIFIED BY ZIRCONIUM PROPOXIDE AND METHACRYLIC ACID

To control the refractive index, different quantities of zirconium propoxide (ZPO, 20-60 mol%) and McOH, with a ZPO:McOH molar ratio of 1:2, were added to the non-doped hybrid materials. The dopant used was obtained by mixing ZPO solution in PrOH (Fluka, 2.23 mol/L) and McOH (CH_2=C(CH_3)C(=O)OH, Fluka, 11.67 mol/L), Figure 3.6, at room temperature with a molar ratio ZPO:McOH of 1:2, and stirred for 0.5 h. Then, the ZPO-McOH solution was added to the non-doped hybrids, and the solution is stirred for more 0.5 h.

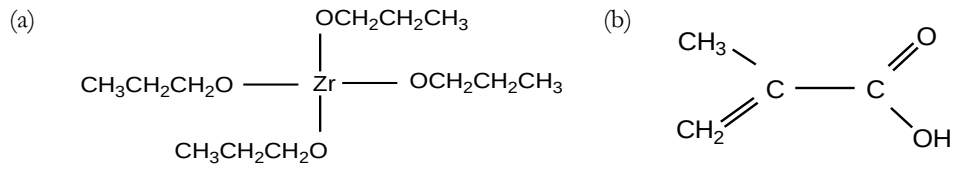

Figure 3.6 Molecular structures of the (**a**) ZPO and (**b**) McOH.

Table 3.1 lists the doping parameters. The doped samples will be henceforth identified as t-U_YZ*B*, where *B* indicates the molar concentration ratio between the ZPO and Si (20, 40 or 60 mol%). For comparison purposed and to, simultaneously, develop PICs, the di-ureasil doped with 40 mol% [ZPO]/[Si] and a ZPO:McOH molar ratio of 1:2, denominated as d-U_{600}Z40, was also prepared.

For the electro-optic phase modulator, an indium tin oxide (ITO) coated glass substrate was used, due to its electrical conductivity (resistance of 16 $\Omega \cdot cm^{-2}$ [151]), and optical transparency [152]. As, ITO substrate has a refractive index of ~1.5 [153], the amount of ZPO added in the d-U_{600} was varied within 20 to 60 mol%, to tune the refractive index to values above to that of ITO. These samples will be henceforth identified as d-U_{600}Z*B*.

Table 3.1 Amount of ZPO and McOH added in the doping of selected di-ureasil and tri-ureasils. The amount of the respective precursor was 3 g. The final concentration of ZPO is also indicated.

Sample designation	ZPO (mL)	McOH (mL)	[ZPO]/[Si] (mol%)	Processing method
d-U_{600}Z20	0.615	0.233	20	
d-U_{600}Z40	1.640	0.620	40	
d-U_{600}Z60	3.691	1.400	60	
t-U_{440}Z20	0.850	0.330	20	
t-U_{440}Z40	2.280	0.870	40	
t-U_{3000}Z20	0.270	0.100	20	Film/Monolith
t-U_{3000}Z40	0.720	0.270	40	
t-U_{3000}Z60	1.620	0.620	60	
t-U_{5000}Z20	0.180	0.067	20	
t-U_{5000}Z40	0.470	0.180	40	
t-U_{5000}Z60	1.050	0.400	60	

The di-ureasils and tri-ureasils were processed as monoliths with controlled shape, and deposited as thin films in glass or Si/SiO_2 substrates, Figure 3.7. In particular, the monoliths were produced by solvent-cast: first, the material was deposited in a polypropylene mould and dried in an oven at 80 °C during 3 days until gelation occurs and the material becomes solid

and easily released from the mould. The monoliths were used in the local structure characterization.

The thin films deposition is performed via spin-coating (SPIN150-NPP APT) at 1000 rpm for 60 s. The films were dried at 50 °C for 12 h for complete solvent removal. For optical characterization (spectroscopic ellipsometry, prism coupling and UV-Vis-NIR absorption spectroscopy), the organic-inorganic hybrids were deposited in a borosilicate glass substrate (Nexterion Slide Glass B, refractive index of 1.47140 at 587.6 nm [154]). The materials were also deposited in oxidized silicon wafers (SQI, 2" prime wafers) with silica thickness of 1.00±0.05 μm and 5.00±0.25 μm, for ellipsometric measurements and to fabricate PICs, respectively.

Figure 3.7 Photographs of the flexible d-U_{600}Z40 (**a**) monoliths; and thin films deposited in (**b**) borosilicate glass and (**c**) oxidized silicon wafer. The scale bars represent 1 cm.

To quantify the Zr/Si molar ratio in the doped samples, XPS spectra were obtained, Figure 3.8. Through the analysis of Zr 3*d*, Zr 4*p*, Si 2*s* and Si 2*p* signals, the estimated Zr/Si molar ratio values were 0.48±0.05, 0.38±0.05 and 0.66±0.05 for d-U_{600}Z40, t-U_{440}Z40 and t-U_{5000}Z60, respectively, which is in good agreement with that estimated based on the synthesis conditions.

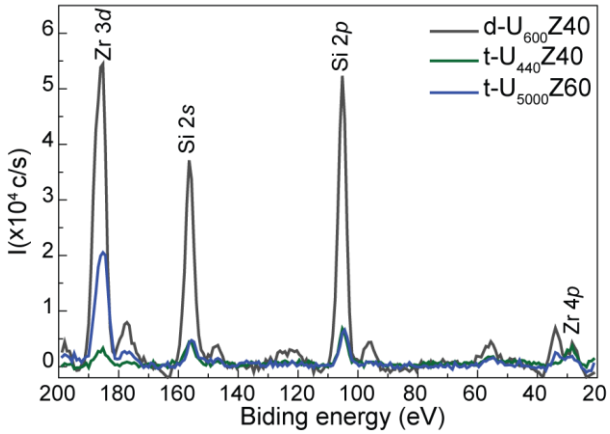

Figure 3.8 XPS spectra for d-U_{600}Z40, t-U_{440}Z40 and t-U_{5000}Z60.

Model Compounds

In addition to the latter precursor solution, a McOH free compound (designated as ZPO) was prepared just by hydrolysis and condensation of $Zr(OPr^n)_4$. Due to its high reactivity, $Zr(OPr^n)_4$ can absorb water from the air (typically about 50 % moisture) and consequently readily hydrolyse and condensate quickly, forming a white powder [113].

3.2.4 DI-UREASIL DOPED WITH POLY[9,9-BIS(4-SULFONYLBUTOXYPHENYL) FLUORENE-2,7-DIYL-*ALT*-1,4-PHENYLENE]

Materials

Jeffamine ED-600®, ICPTES, EtOH (HPLC grade), and HCl (37 % Puriss) were purchased from Sigma Aldrich and were used as received. THF (99.9 %) was obtained from Fischer Scientific and used as received.

Poly[9,9-bis(4-sulfonylbutoxyphenyl) fluorene-2,7-diyl-*alt*-1,4-phenylene] (PBS-PFP, Figure 3.9) with an average number molecular weight (Mn) of 6500 g·mol^{-1} determined by gel permeation chromatography (~740 g·mol^{-1} repeat units), was synthesized as previously reported [155].

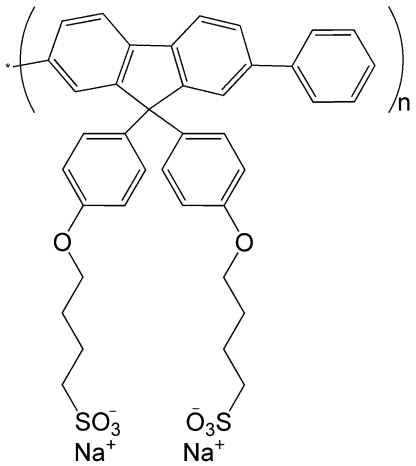

Figure 3.9 Molecular structures of the PBS-PFP.

Synthesis and Processing of PBS-PFP-di-ureasils

PBS-PFP-di-ureasil composites were prepared via direct insertion method. This method involves the preparation of a d-UPTES precursor solution, which was described in detail in the previous section. The non-doped di-ureasil sample is obtained by addition of ethanol (0.409 ml, 7 mmol), HCl (0.5 M, 0.040 ml) and H_2O (0.095 ml, 5.3 mmol) to the d-UPTES solution, which triggers the acid catalysed sol-gel reaction. This corresponds to a ratio of 1 ICPTES:2.3 EtOH:1.8 H_2O:0.006 HCl molar equivalents. The solution was stirred for 5 min before being poured into a polyurethane mould which was then covered with Parafilm. After 24 hr, the Parafilm was pierced to encourage slow evaporation of the solvent. The non-doped sample was then placed in the oven at 40 °C for 48 hr to complete the drying process which produced a free-standing, transparent monolith. In the direct insertion method, a fixed volume of PBS-PFP stock solution is mixed with the d-UPTES precursor solution prior to condensation of the silica network. The samples in this series are designated as PBS*x*, Table 3.2. Notably, once incorporated, the polymer is physically retained within the di-ureasil network [155].

Table 3.2 Composition, processing method and thickness of PBS-PFP-di-ureasils prepared in this study. [PBS-PFP] is the concentration of the stock PBS-PFP solution (in μM repeat units, r.u.), that is added to the d-UPTES. The weight percent (wt%) of polymer incorporated was estimated from [PBS-PFP] and the resultant mass of the dry PBS-PFP-di-ureasil. The monoliths thickness was determined using a digital capiller, and the thickness of the thin films was measured using a Filmetrics F20 thin film analyser.

Sample designation	[PBS-PFP] (μM r.u.)	PBS-FTP (wt%)	Processing method	Spin rate (rpm)	Thickness* (mm)
d-U_{600}-M	-	-	Monolith	-	2.9 ± 0.1
PBS1-M	4.7	1.2×10^{-3}		-	2.7 ± 0.1
PBS2-M	9.8	1.3×10^{-3}		-	3.1 ± 0.1
PBS3-M	98.4	1.2×10^{-2}		-	3.2 ± 0.1
d-U_{600}	-	-	Film	10 000	0.82×10^{-5}
PBS4-F	90	2.5×10^{-2}		8 000	3.28×10^{-5}
PBS5-F	790	0.2		8 000	1.62×10^{-5}
PBS6-F	790	0.2		10 000	1.8×10^{-5}

* The thickness values depend on the spin rate, time of spinning, viscosity, and the amount of material deposited on the substrate.

The PBS-PFP-di-ureasil were processed as monoliths with controlled shape, and deposited as thin films in Si/SiO_2 substrates (SiO_2 thickness of 300 nm), Figure 3.10. The monoliths were prepared as previously reported [155]. The thin films were prepared by spin-coating immediately upon addition of the gelation reagents. The spin rate was varied to change the film thickness, Table 3.2.

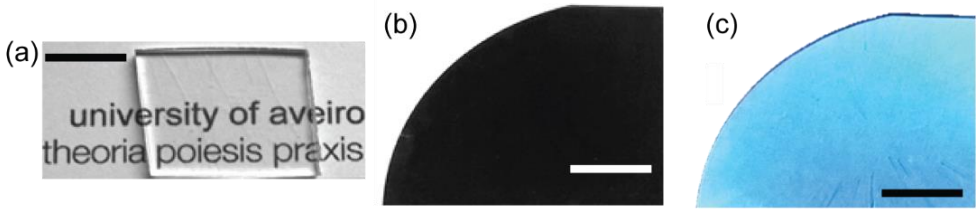

Figure 3.10 Photographs of the (**a**) PBS3-M monolith, and PBS6 film (**b**) taken under daylight and (**c**) UV radiation (365 nm). The scale bars represent 1 cm.

3.3 LOCAL STRUCTURE AND THERMAL PROPERTIES

3.3.1 X-RAY DIFFRACTION (XRD)

The knowledge of the materials local structure is fundamental to understand how the ramification, polymer molecular weight and the doping affects the material properties. Therefore, to first analyse the effect of these parameters on the organic-inorganic hybrids, XRD measurements were performed. Figure 3.11(a) shows the diffractograms for the non-doped hybrids, where broad bands, typical of amorphous materials, can be observed. Through the XRD diffractograms, the structural unit distance d_x can be estimated using the Bragg Law, Equation (3.4) [156].

$$2d_x \sin(\theta) = m' \lambda_{CuK\alpha}. \tag{3.4}$$

where θ is the scattering angle, m' the diffraction order, and $\lambda_{CuK\alpha}$ is the incident radiation wavelength (1.54 Å). The error associated to the d_x calculation, Δd_x, was obtained through Equation (3.5).

$$\Delta d_x = \frac{\lambda_{CuK\alpha} \cos(\theta)}{2\,\mathrm{sen}^2(\theta)} \Delta\theta. \tag{3.5}$$

where $\Delta\theta$ is the scattering angle resolution (7×10^{-4} rad).

The diffractograms for the non-doped hybrids are dominated by a broad component (full width at half maximum, FWHM, 9.8−10.8 Å) centred at ~20 ° (peak 3), ascribed to the presence of amorphous siliceous domains [156,157]. The respective structural unit distance was measured through Equation (3.4), showing an intra-domain characteristic structural mean distance (*d-Si*) values of 4.2±0.1 Å for d-U_{600}, 4.3±0.1 Å for t-U_{440}, and 4.4±0.1 Å for t-U_{3000} and t-U_{5000}. As previously observed [113], these value are similar to those reported for vitreous SiO_2 (4.2 Å) [158] and larger than the Si−O (1.62 Å), O−O (2.65 Å), and Si−Si (3.12 Å) distances, pointing out that for d-U_{600} and the selected tri-ureasils, the basic period is well beyond the first few near-neighbour distances [156,157]. The second-order diffraction of this peak appears as a broad weak hump between 35 °and 50 ° [156].

In addition, a shoulder is also detected in all patterns between 11 ° and 15 ° (peak 2), ascribed to an intra-siloxane domains in-plane [156], ordering with a characteristic distance around 7.3±0.1 Å for d-U_{600}, 7.1±0.1 Å for t-U_{440}, 6.3±0.1 Å for t-U_{3000} and 6.1±0.1 Å for t-U_{5000}.

The low-angle region (2θ<7 °) was further inspected for the d-U_{600} and t-U_{5000} revealing a main peak (peak 1, amplified region of the d-U_{600} pattern of Figure 3.11(a)) centred at ~3.4 ° and at ~1.9 °, respectively, assigned to the spatial correlation between the siliceous domains embedded in a polymer-rich medium [157,159]. This assignment was based on the fact that the peak position shifts to lower angles with the increase of the polymer molecular weight [159]. From the peak maximum position, an average inter-siliceous domain distance ($d_{i\text{-}s}$) was estimated (Equation 3.4), yielding values of 26.0±0.5 Å and 46.0±0.6 Å for d-U_{600} and t-U_{5000}, respectively. Based on the previous results the local structure of the non-doped hybrids may be illustrate as in Figure 3.11(b).

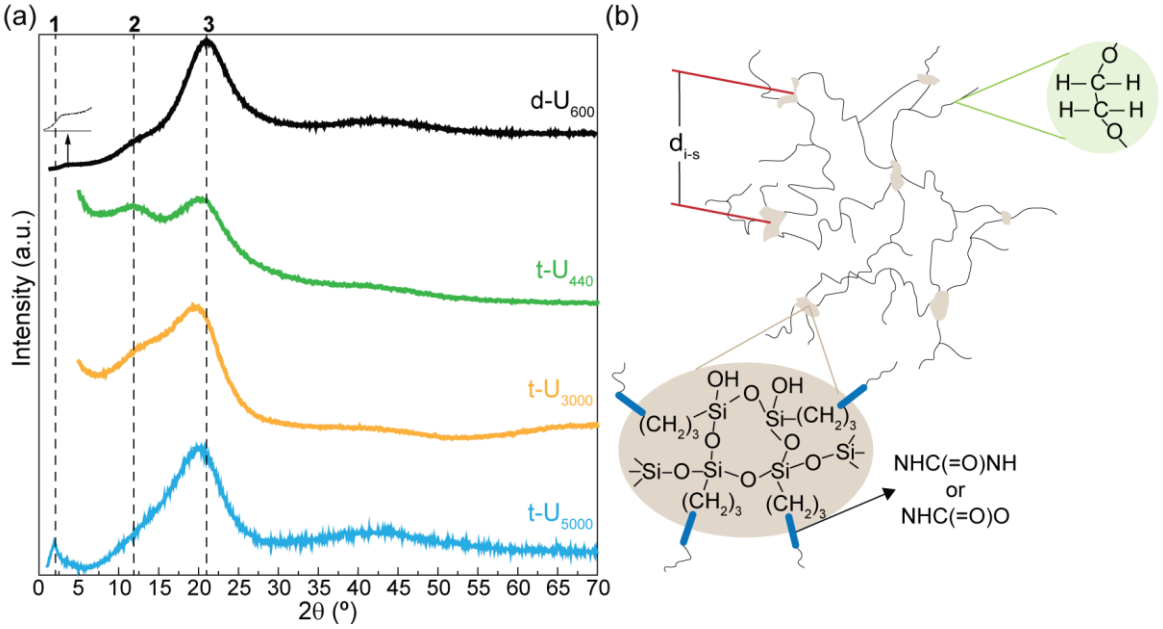

Figure 3.11 (**a**) X-ray diffraction patterns of non-doped di-ureasil and tri-ureasils. The inset shows a magnification (× 100) of the low-angle region for the d-U_{600}. 1, 2 and 3 represent the peak 1 (1.9 °), peak 2 (12 °) and peak 3 (21 °), respectively. (**b**) Scheme of the tri/di-ureasils morphology. $d_{i\text{-}s}$ is the distance between the siliceous domain.

To analyse the doping effect on the local structure, Figure 3.12 shows the diffractograms for the ZPO model composite and doped hybrids. The ZPO diffraction pattern exhibits three broad bands around 30 °, 50 ° and 60 °, corresponding to the tetragonal zirconia (ZrO_2) features [160]. In the low-angle region, the peak observed around 5.6 ° is associated to an inter-Zr clusters characteristic distance (*d-Zr*) of 15.9±0.3 Å [113]. The diffractograms of the doped materials showed two broad bands centred at ~6 ° (peak 4) and ~20 ° (peak 5) corresponding to the same broad peaks from the ZPO and the non-doped samples, respectively. Therefore, these peaks are associated with *d-Si* and *d-Zr*, revealing that the doping of the hybrid with ZPO-McOH preserves the individual order of the components based in silica and zirconium, Table 3.3.

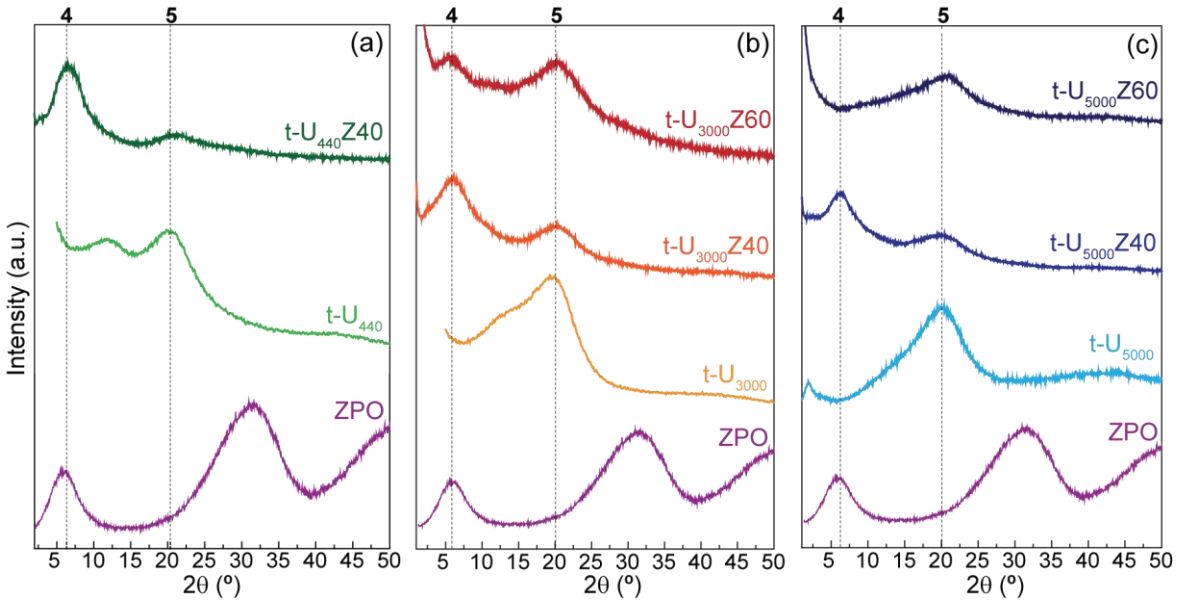

Figure 3.12 X-ray diffraction patterns of non-doped and doped (**a**) t-U_{440} (**b**) t-U_{3000}, and (**c**) t-U_{5000}, where 1 and 2 represent the peak 4 (6 °) and peak 5 (20 °), respectively.

Comparing the *d-Si* values, it is verified that they are analogous to that found for the non-doped material. However, upon increasing the ZPO concentration, *d-Zr* approximated to the value found for ZPO (15.9±0.3 Å). This behaviour can be rationalized by a structural model where for high ZPO concentration, segregation of the individual components occurs and *d-Zr* approaches the value characteristic of ZPO model compound. This indicates that the Si- and Zr-based networks are inter-constrained. Comparing, the *d-Zr* values for the same amount of ZPO but in different tri-ureasils (shadow lines in Table 3.3), it was verified that for a higher polymer molecular weight (t-U_{3000}Z40 and t-U_{5000}Z40) the *d-Zr* value is higher, suggesting a higher accommodation of the ZPO clusters in the network.

Table 3.3 Structural distances and central position (x_c) for intra-siliceous domains and inter-Zr clusters.

Sample designation	Siliceous domains		Inter-Zr clusters	
	x_c (°)	*d-Si* (Å)	x_c (°)	*d-Zr* (Å)
ZPO	-	-	5.6	15.9±0.3
d-U_{600}	20.97	4.2±0.1	-	-
t-U_{440}	20.36	4.3±0.1	-	-
t-U_{440}Z40	21.55	4.1±0.2	6.5	13.6±0.3
t-U_{3000}	19.96	4.4±0.1	-	-
t-U_{3000}Z40	20.20	4.4±0.3	6.2	14.3±0.3
t-U_{3000}Z60	20.21	4.4±0.3	5.6	15.6±0.3
t-U_{5000}	20.00	4.4±0.3	-	-
t-U_{5000}Z40	20.40	4.3±0.3	6.3	14.0±0.3
t-U_{5000}Z60	20.88	4.3±0.3	-	-

3.3.2 NUCLEAR MAGNETIC RESONANCE (NMR)

As the inorganic component of the material is silicon-based, ^{29}Si NMR measurements were performed to study the chemical environments around the silicon atoms. The ^{29}Si NMR spectra of the non-doped materials are depicted in Figure 3.13, exhibiting broad signals around −52, −58 and −67 ppm, which are characteristic of T^1 R'Si(OSi)$_2$(OR), T^2 R'Si(OSi)$_2$(OR) and T^3 R'Si(OSi)$_3$ organosiloxane entities, respectively, where R' represents an alkyl group [113]. For tri-ureasils, the signals between −90 and −130 ppm are assigned to a Q^m-type environments (Si(OSi)$_{4-m}$(OH)$_m$) (m=1, 2, 3 and 4) [161], indicating partial cleavage of the Si−C bonds during the synthesis, that emerge due to the pre-hydrolysis of the precursor, similar to that found before [162,163]. The peak assignment and the population of the various silicon sites are given in Table 3.4. In all the samples, the signals from T^2 and T^3 sites are clearly dominant indicating that the condensation process favours branched structures instead of linear segments.

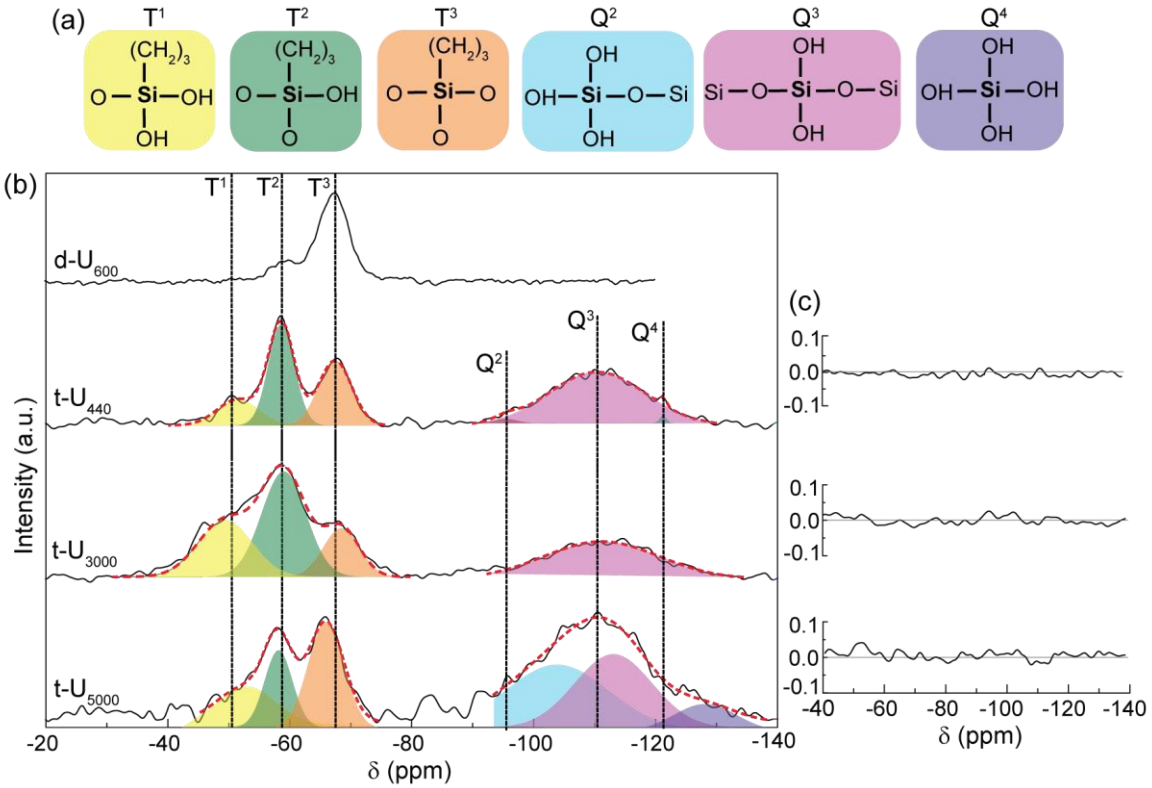

Figure 3.13 (**a**) Scheme of the T^m and Q^m Si-local environments. (**b**) ^{29}Si NMR spectra of the non-doped di-ureasil and tri-ureasils materials. The shadow areas indicate the T^m and Q^m local environments best fit using a Gaussian function, and the red dots are the cumulative fit (r^2>0.9). (**c**) Fit regular residual plot.

To estimate the condensation degree (*c*), the deconvolutions were carried out in the regions of T^m and Q^m. However, since the Q^m environments correspond to Si bonds after the cleavage

of the Si−C bond, which does not reside in the functional material, *c* was calculated according to Equation (A.1), Table 3.4. Considering only the T^m environments, the *c* values obtained were 96.0, 72.6, 73.0 and 73.5 % for d-U_{600}, t-U_{440}, t-U_{3000} and t-U_{5000}, respectively. The tri-ureasils *c* values are lower than those for d-U_{600}, because the relative population of T^3 sites decreases while the percentage of T^2 sites increases and T^1 terminal units are observed, demonstrating the existence of less compact silicate structures in tri-ureasils.

Table 3.4 Chemical shift (T^m or Q^m, ppm), integrated area (I, %) and *c* (%) values of T^m and Q^m environments in the ^{29}Si spectra for selected materials.

Sample designation	T^1	I_{T1}	T^2	I_{T2}	T^3	I_{T3}	Q^2	I_{Q2}	Q^3	I_{Q3}	Q^4	I_{Q4}	*c*
d-U_{600}	0.0	0.0	−59.5	13.0	−67.4	87.0							96.0
t-U_{440}	−51.5	9.8	−58.6	23.6	−67.4	19.2	−95.6	1.0	−110.4	46.0	−121.2	0.4	72.6
t-U_{440}Z20	−51.7	19.0	−59.8	23.4	−68.1	23.6					−111.8	34.0	69.0
t-U_{440}Z40	−56.8	4.7	−59.4	9.0	−66.7	25.8					−110.9	60.5	84.5
t-U_{3000}	−48.8	23.0	−58.7	35.1	−68.5	12.6	0.0	0.0	−111.1	29.3	0.0	0.0	73.0
t-U_{3000}Z20	−52.6	7.2	−59.0	18.1	−67.1	15.3					−110.1	59.4	73.3
t-U_{3000}Z40	−50.7	2.2	−58.9	18.1	−67.8	23.2					−110.3	56.5	82.3
t-U_{3000}Z60	−52.1	2.9	−57.7	11.9	−67.4	27.4					−110.5	57.8	85.9
t-U_{5000}	−52.8	10.2	−58.2	10.1	−65.9	18.1	−103.8	29.9	−113.1	26.5	−128.1	5.2	73.5
t-U_{5000}Z20	0.0	0.0	−59.0	9.8	−67.3	13.5					−110.3	76.7	84.1
t-U_{5000}Z40	−53.0	1.0	−58.5	6.2	−67.4	26.0					−112.3	66.8	91.8
t-U_{5000}Z60	−54.4	1.0	−58.8	12.7	−62.2	26.0					−112.7	60.3	87.6

For the doped materials, the NMR spectra (Figure 3.14) exhibit three distinct broad peaks, approximately, at −52, −59, and −67 ppm, ascribed to the above-mentioned T^m environments. Also, Q^m-type environments are observed, which does not reside in the functional material, as explained above. Upon varying the ZPO concentration, it can be infer that with the presence of Zr-clusters, an increase of T^3 sites population and a decrease of T^2 and T^1 sites occurs, resulting in higher *c* values (Table 3.4). Thus, with Zr-clusters, a slightly constrain of the siliceous network formation occurs, leading to less branched arrangements for the siliceous backbone domains with the respect to the non-doped samples.

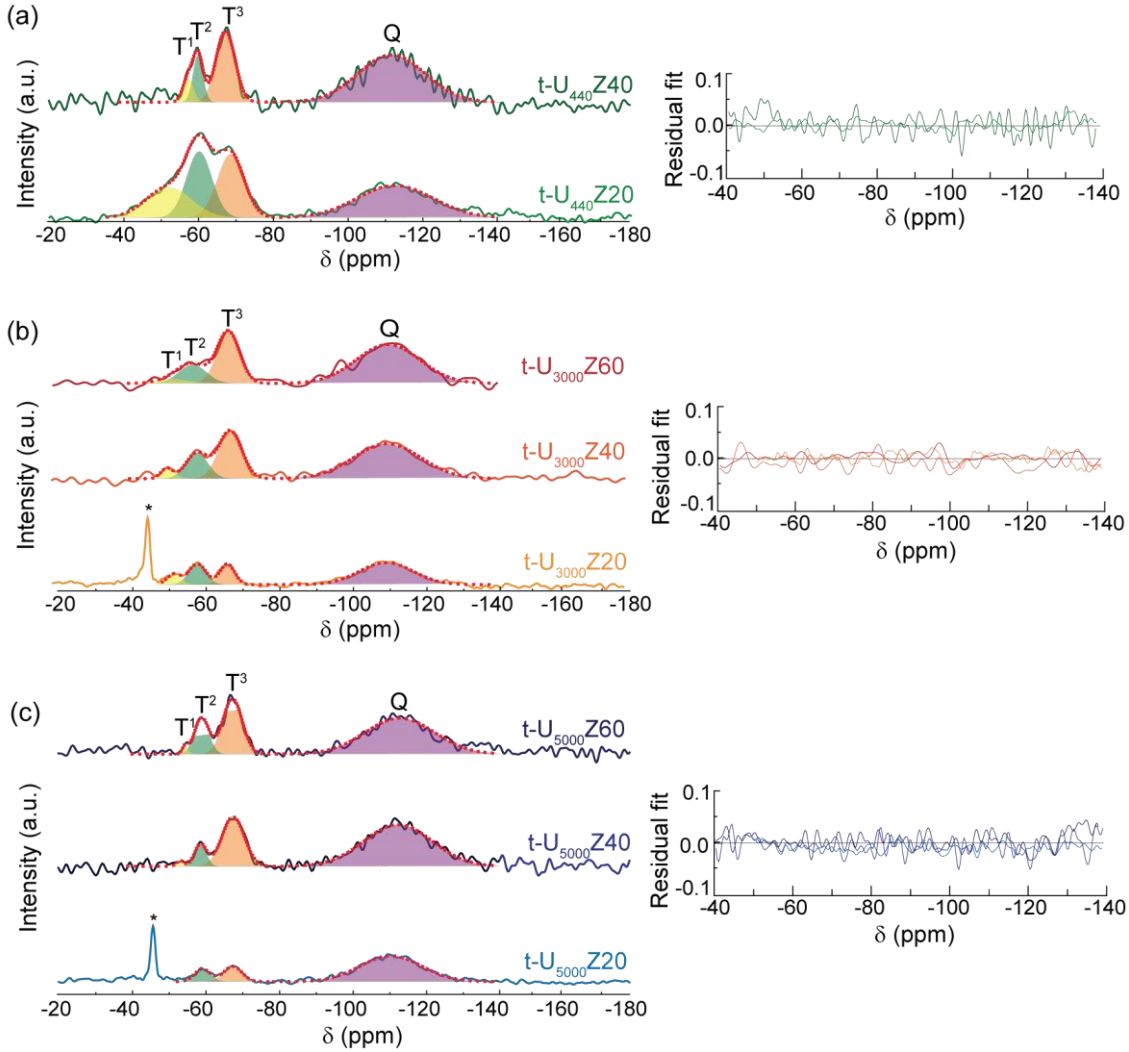

Figure 3.14 (**a**) ^{29}Si NMR spectra (left) of doped (**a**) t-U_{440} (**b**) t-U_{3000}, and (**c**) t-U_{5000}; the shadow areas indicate the T^m and Q^m local environments best fit using a Gaussian function, and the red dots are the cumulative fit (r^2>0.9). Star symbols corresponds to the T^0 environment of the non-hydrolysed precursor. Fit regular residual plot (right).

The NMR technique was also used to describe the materials organic component, by solid state ^{13}C NMR spectra, Figure 3.15. These spectra are dominated by two peaks located at

75.5 ppm and 73.5 ppm ascribed to the methane and methylene groups of the polyoxypropylene (POP) polymer chains, respectively. For the tri-ureasils materials, an intense peak at 17.7 ppm appears due to the methyl groups of the oxypropylene repeat units [164]. The broad, ill-defined signal at ~159 ppm is associated to the urea carbonyl groups [156]. The peak around 43 ppm is characteristic of the $(CH_2)_3$ aliphatic chains [156]. The peaks at 43.5, 24.7 and 10.2 ppm are due to different CH_2 moieties in spectrum of t-U_{440}. The absence of these peaks in spectra of t-U_{3000} and t-U_{5000} indicates the lower ratios of urea contents in these two tri-ureasils. For the doped samples, it is verified an intensity increase of the peaks at ~18.5 ppm, ascribed to the groups present in the ZPO-McOH complex [165].

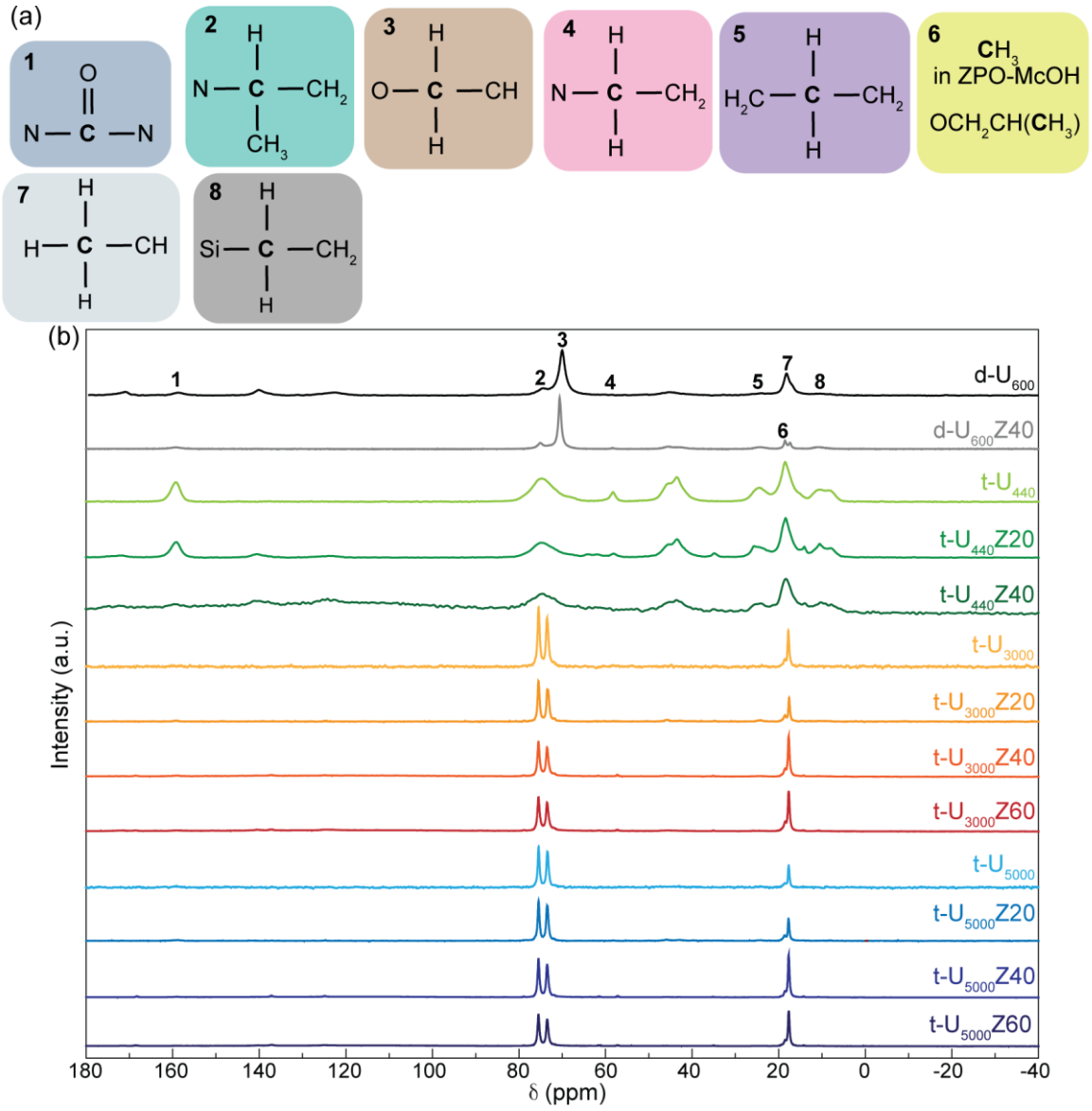

Figure 3.15 (**a**) Tentative representation of the peak assignment groups: (1) N(C̲O)N (2) C̲H(CH3)CH2 (3) CH(CH3)C̲H2 (4) NC̲H2CH2CH2Si (5) NCH2C̲H2CH2Si (6) OCH2CH(C̲H3) and C̲H3 in ZPO-McOH (7) CH(C̲H3)CH2 (8) NCH2CH2C̲H2Si. (**b**) Solid state ^{13}C NMR spectra for selected materials.

In the overall results for the doped samples, no significant differences are discerned in the solid state ^{13}C NMR spectra, suggesting that the zirconia-based clusters do not significantly interact with the polyether chains. Therefore, NMR data reinforces the inter-constraining between the Zr- and Si-based phases mentioned above. Table 3.5 lists the peaks assignments identified for each sample.

Table 3.5 Chemical shift and the respective assignment of the solid state ^{13}C NMR spectra for selected materials.

Sample designation	Chemical shift (ppm)							
	1	2	3	4	5	6	7	8
d-U_{600}	159.4	75.1	70.6	45.8	24.3	18.5	17.4	11.1
d-U_{600}Z40	159.5	75.1	70.6	45.8	-	18.7	17.6	-
t-U_{440}	159.2	75.1	72.0	43.5	24.4	-	18.8	10.2
t-U_{440}Z20	159.2	74.8	72.1	43.5	24.1	18.3	-	10.5
t-U_{440}Z40	159.7	74.5	72.1	43.6	24.0	18.3	-	10.3
t-U_{3000}	-	75.4	73.4	-	-	-	17.7	-
t-U_{3000}Z20	159.2	75.5	73.5	45.8	24.7	18.5	17.6	10.7
t-U_{3000}Z40	159.0	75.5	73.5	45.8	23.8	18.6	17.7	10.7
t-U_{3000}Z60	158.9	75.5	73.5	45.9	24.5	18.5	17.7	10.7
t-U_{5000}	-	75.4	73.4	-	-	-	17.6	-
t-U_{5000}Z20	159.3	75.5	73.5	-	-	18.6	17.7	-
t-U_{5000}Z40	158.7	75.5	73.5	45.9	24.2	18.5	17.7	10.8
t-U_{5000}Z60	-	75.5	73.5	46.0	24.1	18.5	17.7	10.8

(**1**) N(C̲O)N (**2**) C̲H(CH_3)CH_2 (**3**) CH(CH_3)C̲H_2 (**4**) NC̲$H_2CH_2CH_2Si$ (**5**) $NCH_2C̲H_2CH_2Si$ (**6**) $OCH_2CH(C̲H_3)$ and C̲H_3 in ZPO-McOH (**7**) CH(C̲H_3)CH_2 (**8**) $NCH_2CH_2C̲H_2Si$

3.3.3 FOURIER-TRANSFORM INFRARED SPECTROSCOPY (FT-IR)

In order to study the vibrational properties of the organic component of di-ureasils and tri-ureasils, the FT-IR spectra were recorded, Figure 3.16. This technique allows to analyse the organic component and cross-linkages of the hybrid materials. The dominant bands appear around 1200 to 1050 cm^{-1} being characteristic of the vibrations from the skeleton COC stretching (ν_{COC}) modes. The broad ν_{COC} envelope displays a peak at ~1110 cm^{-1} (peak 6) and a shoulder around 1149 cm^{-1} (peak 5), assigned to the ν_{COC} mode and CH_2 rocking modes, respectively [157]. The band at 1452 cm^{-1} (peak 3) is attributed to the CH_2 scissoring vibration, whereas the peak at 1370 cm^{-1} (peak 4) is assigned to the vibration from CH_2 wagging [166].

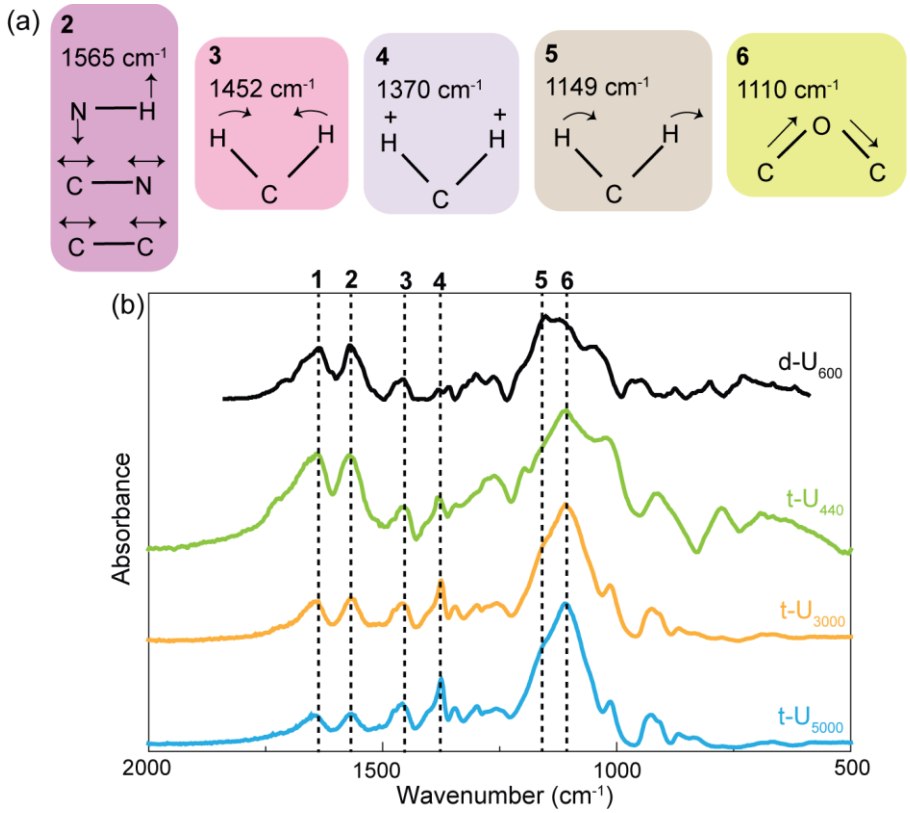

Figure 3.16 (**a**) Tentative representation of the vibration modes assigned to each peak. Peak **1** is a combination of vibration modes that are represented in Figure 3.17. (**b**) FT-IR spectra in the region of 2000–500 cm^{-1} for selected materials.

The band observed between 1900 to 1500 cm^{-1} (Figure 3.17), termed as "amide I" mode, is mainly associated with the C=O stretching vibration [167]. Thus, it indicates that the starting amine group from the diamine/triamine reacted with ICPTES and the urea-linkages in the materials are formed. For the non-doped tri-ureasils, the intensity ratios between the peak at 1110 cm^{-1} and the band at 1640 cm^{-1} (peak 1) are 0.68, 0.29 and 0.21 for t-U_{440}, t-U_{3000} and t-U_{5000}, respectively. This indicate that in t-U_{440} the urea-linkages concentration is higher than those for t-U_{3000} and t-U_{5000}.

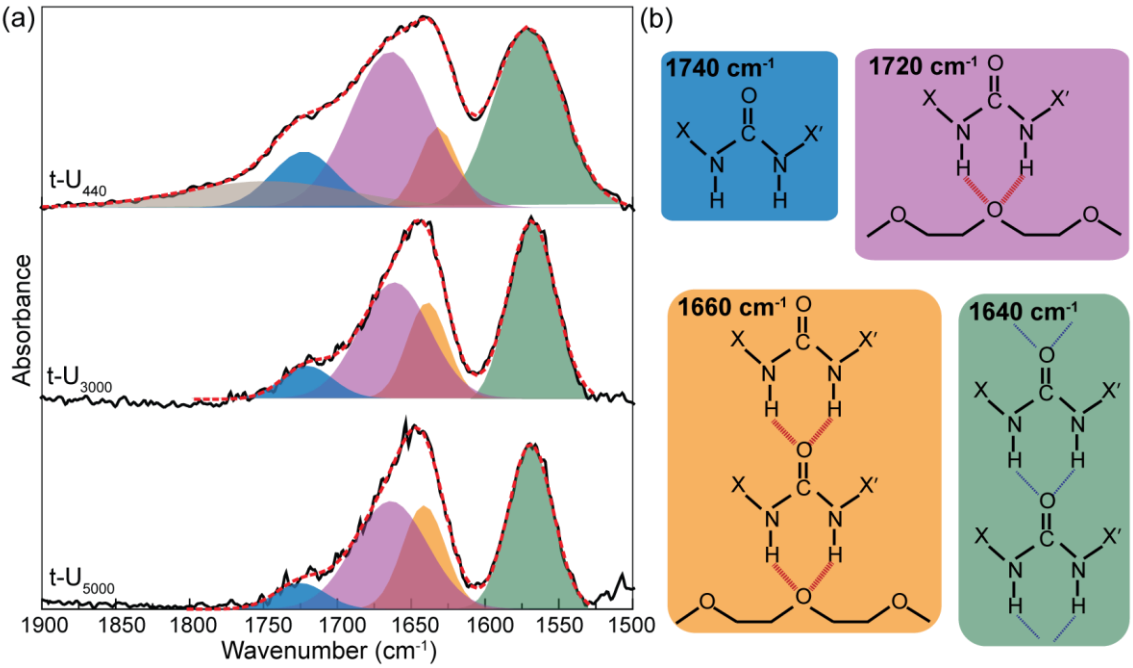

Figure 3.17 (**a**) FT-IR spectra in the region of 1900–1500 cm^{-1} with the fit using a multi-Gaussian function of "amide I" and "amide II" modes of non-doped tri-ureasils (r^2>0.9). (**b**) Tentative representation of the hydrogen-bonded associations present in the tri-ureasils, where X and X' represent the alkyl group of the hybrid structure.

The band around 1565 cm^{-1} (peak 2) is associated with the "amide II" mode, which has a mixed contribution of the N−H in-plane bending, C−N and C−C stretching vibrations [167]. To analyse the "amide I" and "amide II" bands, spectral deconvolutions were carried out between 1900 and 1500 cm^{-1} using a sum of Gaussian bands, Figure 3.17. The band positions and their relative ratios are summarized in Table 3.6.

Table 3.6 Band positions (wavenumber) and intensity ratios between them of "amide I" and "amide II" regions for the non-doped tri-ureasils.

Sample designation	**"Amide I" Wavenumber (cm^{-1})/ratio (%)**				**"Amide II" Wavenumber (cm^{-1})**
t-U_{440}	1747/19	1722/15	1661/53	1632/13	1571
t-U_{3000}	-	1720/12	1661/60	1639/28	1568
t-U_{5000}	-	1725/10	1664/58	1641/32	1569

The "amide I" bands are located at 1720 and 1660 cm^{-1}, ascribed to C=O groups of disordered hydrogen-bonded POP/urea aggregates. The band around 1640 cm^{-1} is assigned to C=O groups included in significantly more ordered hydrogen-bonded urea/urea aggregates [168]. For all tri-ureasils, the main components are attributed to the C=O groups of disordered hydrogen-bonded POP/urea aggregates. On the other hand, the band at

~1750 cm^{-1} observed in t-U_{440} is produced by "free" urea groups that do not participate in any hydrogen-bonding interactions, due to the higher ratio of urea moieties and less ratio of hydrogen-bonded urea/urea aggregates in this material. For the "amide II" mode, the peak positions are around 1570 cm^{-1} for the tri-ureasils, which is similar to the results obtained from the literatures [169,170].

The FT-IR spectra of the doped samples are present in Figure 3.18. After the incorporation of the ZPO, the position of the 1640 cm^{-1} peak (peak 1) remains constant, indicating that the urea–urea aggregates are unaffected as the ZPO concentration increases. The bands at 1423 cm^{-1} (peak 2), also detected in the infrared spectrum of the Z1:1 compound, can be assigned to the $\nu_s COO^-$ mode [171]. The band centred at 663 cm^{-1} (peak 3) is allocated to the Zr−O stretching vibration mode [172].

Also, it is not present the characteristic band of McOH aggregates formed via hydrogen bond, which typically occurs at 1728 cm^{-1}. Therefore, it is possible to conclude that the McOH is not free in the material because it totally reacted. The absorption typical for Zr−O−Zr bonds (~851 cm^{-1} [173]) does not appears in the spectra, suggesting a favouring of homocondensation in relation to heterocondensation.

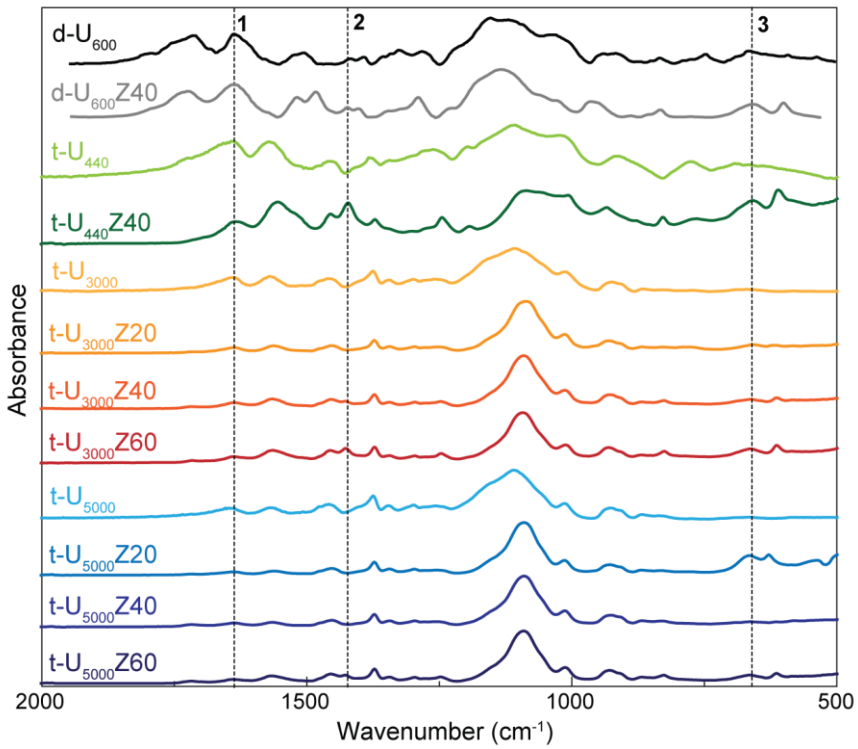

Figure 3.18 FT-IR spectra of the selected materials, where 1, 2 and 3 represent the peak 1 (1640 cm^{-1}), peak 2 (1423 cm^{-1}) and peak 3 (663 cm^{-1}), respectively.

3.3.4 FOURIER TRANSFORM RAMAN SPECTROSCOPY (FT-RAMAN)

FT-Raman spectroscopy is a complementary technique to the FT-IR presented in Section 3.3.3, that was used to analyse the organic component of the hybrid materials. Figure 3.19 shows the normalized FT-Raman spectra for the non-doped and doped materials. In all the spectra the dominant spectral event is associated with a band around 1455 cm^{-1} (peak 2) which is ascribed to the CH_2 scissoring [174]. The intensity order in the amide I and amide II regions for the non-doped tri-ureasils is t-U_{440} > t-U_{3000} > t-U_{5000}, which can be rationalized by the higher proportion of urea groups in t-U_{440} than those in t-U_{3000} and t-U_{5000}. This conclusion is also supported by the above FT-IR analysis, Figure 3.17.

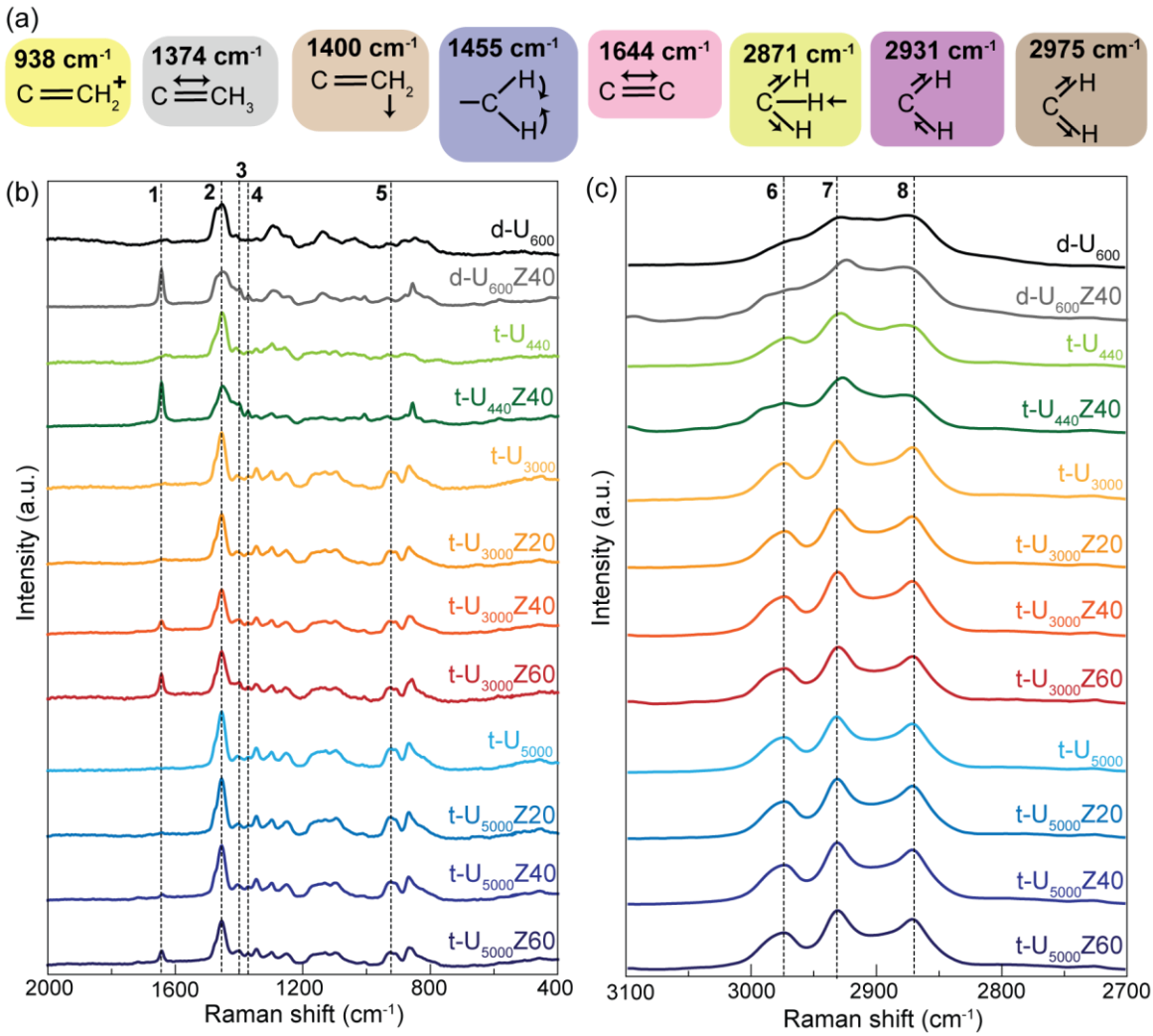

Figure 3.19 (**a**) Tentative representation of the vibration modes assigned to each peak. FT-Raman spectra in the region of (**b**) 2000–400 cm^{-1}, and (**c**) 3100–2700 cm^{-1} for selected materials. 1, 2, 3, 4, 5, 6, 7 and 8 represent the peak 1 (1644 cm^{-1}), peak 2 (1455 cm^{-1}), peak 3 (1400 cm^{-1}), peak 4 (1374 cm^{-1}), peak 5 (938 cm^{-1}), peak 6 (2871 cm^{-1}), peak 7 (2931 cm^{-1}) and peak 8 (2975 cm^{-1}), respectively.

For the doped samples, a band at ~1644 cm^{-1} (peak 1) appeared, and it is ascribed to the stretching vibration mode of C=C [113], which intensity increases with the ZPO concentration. The infrared characteristic bands of the methacrylate groups at 1374 cm^{-1} (peak 4) and 1400 cm^{-1} (peak 3) are visible in all the spectra, and correspond to the stretching vibration mode of C−CH_3 and to the deformation vibration mode of C=CH_2 [175]. The band centred at 938 cm^{-1} (peak 5) is attributed to the wagging vibration mode of C=CH_2 [113].

In Figure 3.19(c) the region between 3100 and 2800 cm^{-1} is presented. All the curves present three bands at 2871 (peak 6), 2931 (peak 7) and 2975 cm^{-1} (peak 8) assigned to the CH_2 symmetric and asymmetric, and CH_3 asymmetric stretching νC–H modes [176].

3.3.5 THERMOGRAVIMETRIC ANALYSIS (TGA) AND DIFFERENTIAL SCANNING CALORIMETRY (DSC)

To use organic-inorganic hybrids as PIC substrates, another important property that should be considered is the thermal stability. Therefore, it was studied through the interpretation of TGA and DSC data from around 20 to 800 °C, Figure 3.20. All the TGA curves show a three-stage decomposition process. The first weight loss (~1.0 %) occurs before 140 °C (T1), and it is attributed to the evaporation of residual solvent EtOH and/or water. Further weight loss between 140 and 445 °C is due to the removal of Jeffamine moieties [170]. The final weight changes above 445 °C (T2) involve the losses of remaining organic components.

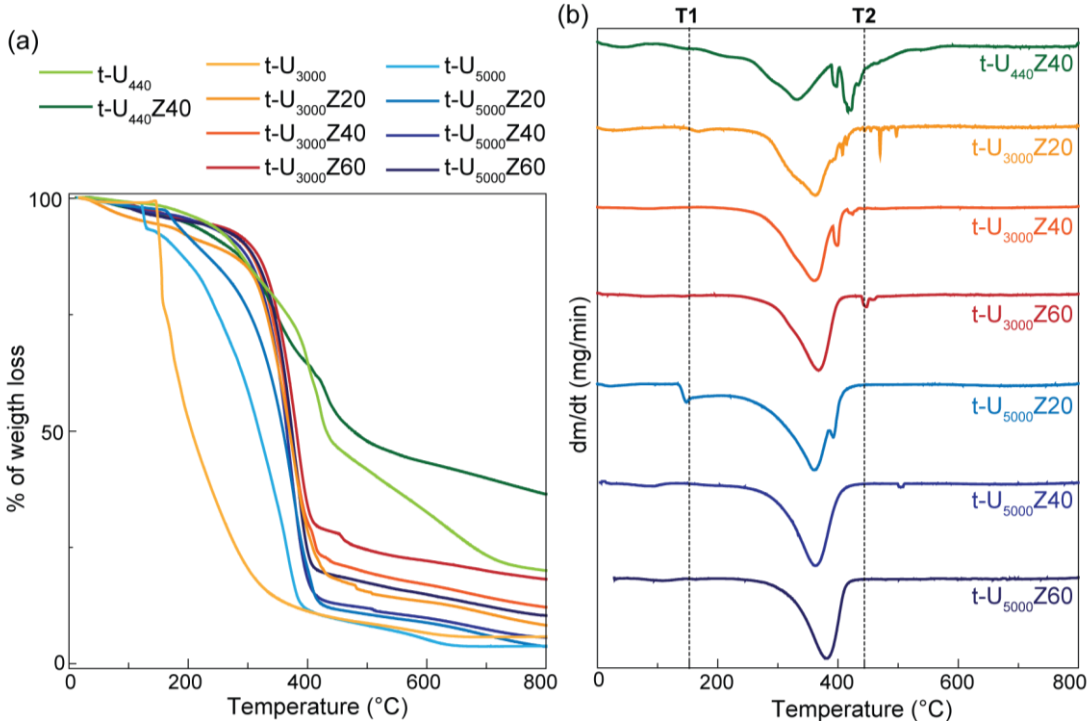

Figure 3.20 (**a**) Thermogravimetric curves, and (**b**) differential thermogravimetry of the non-doped and doped tri-ureasils, where T1 and T2 corresponds to 140 °C and 445 °C.

Table 3.7 presents the weight loss percentage associated to each thermic event, described above. Comparing the results for the non-doped samples, a higher weight loss (~38 %) is verified for higher polymer molecular weight, due to a higher organic degradation. With the addition of ZPO to the matrix, it was observed a decrease of weight loss (~16 %), suggesting that the occurrence of ZPO in the hybrid matrix is beneficial in the thermal stability point of view.

Table 3.7 Weight loss percentage associated to a temperature of 140 °C and 445 °C in selected materials.

Sample designation	Temperature (°C)		
	20-140	**140-445**	**445-800**
t-U_{440}	1.4	51.3	27.2
t-U_{440}Z40	3.1	42.3	18.2
t-U_{3000}	0.9	89.2	4.1
t-U_{3000}Z20	5.4	76.2	10.1
t-U_{3000}Z40	3.7	74.6	9.5
t-U_{3000}Z60	2.4	69.4	10.1
t-U_{5000}	6.9	83.3	5.96
t-U_{5000}Z20	2.4	85.8	8.1
t-U_{5000}Z40	3.3	83.7	7.3
t-U_{5000}Z60	3.8	77.2	8.7

Concerning the technological application of ZPO modified tri-ureasils, for the fabrication of thermo-optic devices, the materials are thermally stable up to 150 °C, a value significantly higher than the glass transition temperatures of some conventional optical polymers, such as poly(methyl methacrylate), polystyrene and poly(carbonate) (105, 100 and 145 °C, respectively [12]), employed in integrated optics. Also, these values meet the thermal standards under the reliability of PICs (up to +70 °C [178]).

3.4 CONCLUSIONS

Homogeneous di-ureasils and tri-ureasils organic-inorganic hybrids doped with methacrylate modified Zr based oxo-clusters were prepared. The structural features of these hybrids were discussed based on XRD, ^{29}Si and ^{13}C NMR, FT-IR, and FT-Raman.

From XRD, Si and Zr- based nanobuilding structural units were identified, showing that the individual order of the components based in Si and Zr were preserved even with the doping of the hybrid. It was also verified that for higher polymer molecular weight the

ZPO-McOH clusters have a higher accommodation in the network. The ^{29}Si NMR results showed that the degree of condensation of tri-ureasils is lower than the one in di-ureasil materials, due to the existence of less compact silicate structures in tri-ureasils. Adding ZPO, the degree of condensation increases, due to the constrain of the siliceous network formation, and, consequently, a less branched arrangements for the siliceous backbone domains. For the doped samples, no significant differences were observed in the solid state ^{13}C NMR spectra, suggesting that the zirconia-based clusters do not significantly interact with the hybrid.

The absence of Zr−O−Zr bonds and different coordination modes for the methacrylate groups were the main results obtained by FT-IR and FT-Raman measurements. These observations also support a structural model where the Si- and Zr-based networks are inter-constrained, because the Zr-based clusters are embedded in the polymeric phase between the siliceous domains. Based on these results and the tri-ureasils local structure illustrated in Figure 3.11(b), when the ZPO is added into the hybrid the structure model is expected to be similar to the one in Figure 3.21. Through the TGA and DSC data, it was demonstrated that the materials are thermal stable up to 150 °C, which meet the thermal standards under the reliability of PICs (up to +70 °C [178]).

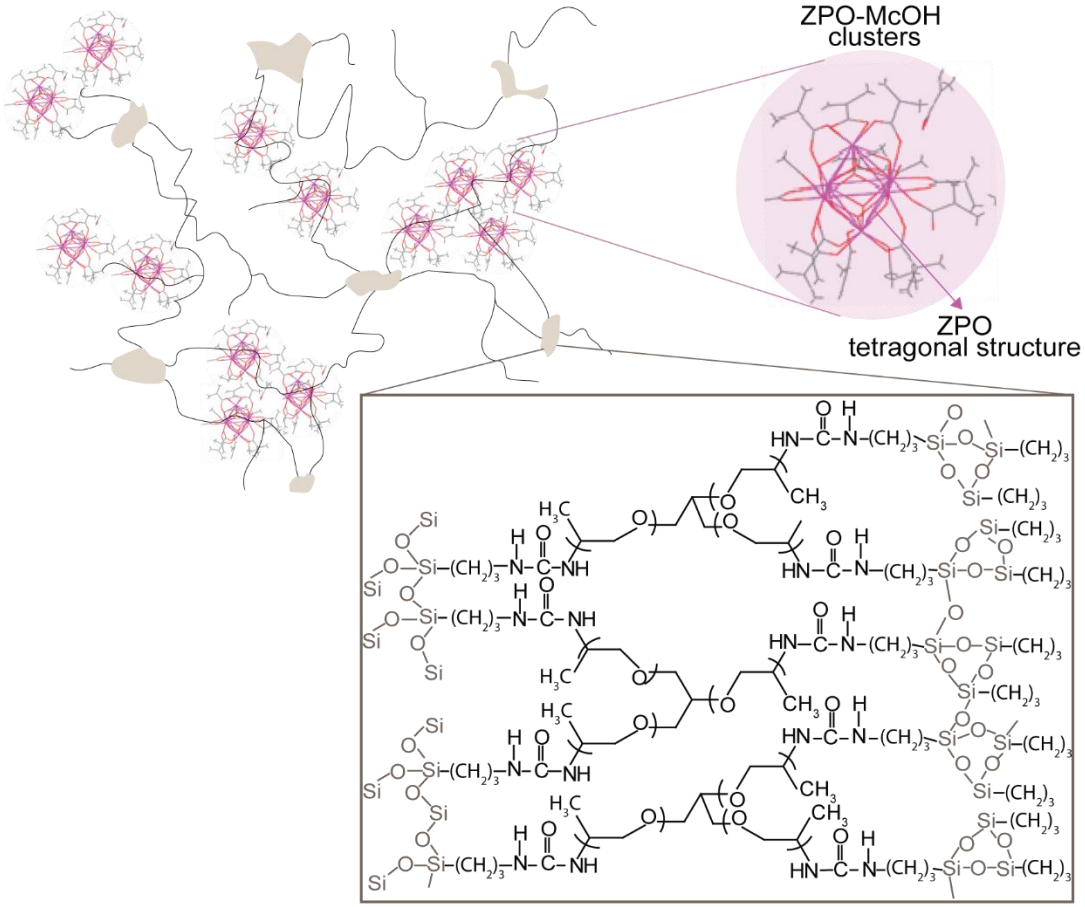

Figure 3.21 Scheme of the di/tri-ureasils doped with ZPO-McOH morphology.

CHAPTER 4

OPTICAL CHARACTERIZATION AND UV *LASER* PATTERNING

Refractive index and attenuation coefficient are relevant parameters for PICs applications. Therefore, in this chapter, the optical features of tri-ureasils with different polymer molecular weight and different ZPO-McOH concentrations are discussed through the experimental results acquired from prism coupling, spectroscopic ellipsometry, and UV-Vis-NIR absorption spectroscopy. For these analysis, planar waveguides were produced by processing the tri-ureasils materials as thin films deposited in borosilicate glass substrates via spin-coating. As the d-U_{600}Z40 will be implemented as a PIC substrate, it was processed as thin films in Si/SiO_2 substrates (1.00±0.05 μm of SiO_2 thickness) for ellipsometry measurements.

The refractive index variation upon UV exposure was quantified and the mechanisms behind it are discussed. The UV patterning methodology was the direct UV *laser* writing.

4.1 PLANAR WAVEGUIDES

4.1.1 UV-VIS-NIR ABSORPTION SPECTROSCOPY

To produce PICs based on organic-inorganic hybrids, it is important to quantify its intrinsic absorption in the operation spectral region (NIR). Also, to produce PICs using the direct writing by UV *laser*, it is also required to quantify the material absorption in the UV spectral region. Therefore, UV-Vis-NIR absorption spectroscopy was used to obtain the absorption coefficient spectra for selected samples upon varying the ZPO-McOH concentration, Figure 4.1. The experimental details are described in Annex B.1.

The materials are transparent for wavelengths between 300 nm and 800 nm. In the NIR spectral region, absorption arises from the presence of C−H and C=O groups, and the Si−OH groups. As observed in the ^{13}C and ^{29}Si NMR, the relative amount of C−H and C=O groups and Si−OH group increases with the ZPO-McOH concentration, thus higher absorption coefficient values are expected in the samples with higher ZPO-McOH concentration. Comparing the tri-ureasils polymer weight, it can be observed that the absorption decreases for higher polymer weights, which occurs due to the relative amount of the Si−OH group that also decreases (4.7, 2.2 and 1.0 %, for t-U_{440}Z40, t-U_{3000}Z40 and t-U_{5000}Z40, respectively). Table 4.1 shows the experimental absorption coefficient at 1550 nm, which presents an increase of absorption coefficient with the ZPO-McOH concentration and the decrease of absorption coefficient with the polymer weight, as expected by the NMR results.

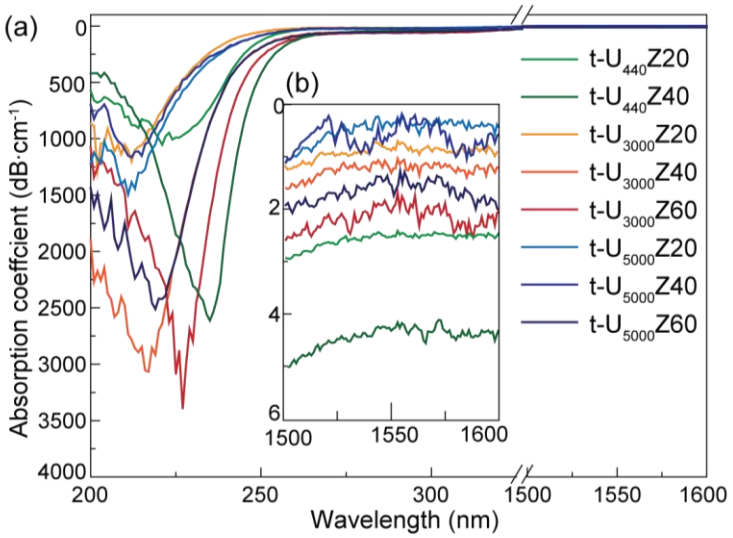

Figure 4.1 (**a**) UV-Vis-NIR absorption coefficient spectral dependence of selected materials. The inset show a magnification of the (**b**) NIR spectral region.

As the photopolymerization process depends on the material ability to absorb UV radiation, it is also important to analyse the absorption coefficient in this spectral region. In all the samples, a main component is observed between 200 and 275 nm, also present in the non-doped samples, ascribed to oxygen related defects in the silica-based skeleton, and urea groups [111].

Adding the ZPO-McOH, the C=C bonds from the methacrylate group contribute to an extra absorption around 250 nm. Therefore, there is a general increase in the UV absorption for a higher ZPO-McOH concentration, Table 4.1.

Table 4.1 Absorption coefficient values of selected hybrids at 250, 635 and and 1550 nm.

Sample designation	Absorption coefficient (dB·cm^{-1})		
	250 nm	635 nm	1550 nm
t-U$_{440}$Z20	130	1.8	2.5
t-U$_{440}$Z40	424	2.1	4.3
t-U$_{3000}$Z20	52	1.1	1.0
t-U$_{3000}$Z40	193	1.2	1.3
t-U$_{3000}$Z60	272	1.8	2.1
t-U$_{5000}$Z20	85	1.2	0.8
t-U$_{5000}$Z40	83	1.2	0.7
t-U$_{5000}$Z60	191	1.5	1.9

4.1.2 PRISM COUPLING CHARACTERIZATION

As mentioned in Section 2.2, the optical losses in PICs can be caused by other features besides the material absorption. To understand the main source of propagation loss in planar waveguides based on organic-inorganic hybrids, the attenuation coefficient was evaluated through light scattering measurements, using the prism coupler technique, Annex B.2. The attenuation coefficients were measured for a wavelength of 532 nm and 635 nm, yielding optical loss values between 1-3 dB·cm^{-1} (Table 4.2), which are acceptable values for low dimension circuits. The results obtain for the attenuation coefficient at 635 nm are ~0.3 dB higher than the absorption values, showing that the main source of attenuation is the material absorption.

Table 4.2 Attenuation coefficient measured for selected hybrids.

Sample designation	Attenuation coefficient (dB·cm^{-1})	
	532 nm	635 nm
t-U$_{440}$	2.4 ± 0.6	1.9 ± 0.2
t-U$_{440}$Z20	2.6 ± 0.5	2.1 ± 0.3
t-U$_{440}$Z40	2.7 ± 0.8	2.3 ± 0.3
t-U$_{3000}$	2.0 ± 0.6	1.6 ± 0.7
t-U$_{3000}$Z20	2.1 ± 0.9	1.4 ± 0.1
t-U$_{3000}$Z40	2.3 ± 0.2	1.6 ± 0.1
t-U$_{3000}$Z60	2.4 ± 0.1	2.1 ± 0.1
t-U$_{5000}$	1.1 ± 0.2	1.2 ± 0.1
t-U$_{5000}$Z20	1.4 ± 0.6	1.4 ± 0.1
t-U$_{5000}$Z40	1.9 ± 0.7	1.5 ± 0.1
t-U$_{5000}$Z60	1.9 ± 0.4	1.7 ± 0.1

To further characterize the optical features of these materials, the refractive index and thickness values were also calculated using the prism coupling technique, which experimental details are described in Annex B.2. An increase of the refractive index as a function of the

zirconium content is verified (Table 4.3) due to the relative decrease of the polymeric fraction, relative to the Zr content [179], which also occurs in related zirconium containing organic-inorganic hosts [91,105]. The thickness values were also obtained, yielding values between 6-18 μm, which are in agreement with the ones measured by spectroscopic ellipsometry.

Table 4.3 Refractive index and thickness values obtained through prism coupling for selected hybrids.

Sample designation	Refractive index				Thickness (μm)	
	532 nm	635 nm	980 nm	1550 nm		Ellipsometry
t-U_{440}	1.5112 ± 0.0004	1.5030 ± 0.0006	1.4501 ± 0.0005	1.4981 ± 0.0002	18.2±0.3	16.418±0.010
t-U_{440}Z20	1.5178 ± 0.0002	1.5149 ± 0.0013	1.5047 ± 0.0004	1.5039 ± 0.0002	16.0±0.3	17.650±0.002
t-U_{440}Z40	1.5206 ± 0.0018	1.5185 ± 0.0001	1.5108 ± 0.0002	1.5069 ± 0.0003	8.3±0.3	11.001±0.005
t-U_{3000}	1.5121 ± 0.0005	1.5077 ± 0.0015	1.4998 ± 0.0009	1.4982 ± 0.0002	17.5±0.1	16.370±0.002
t-U_{3000}Z20	1.5161 ± 0.0004	1.5108 ± 0.0014	1.5051 ± 0.0004	1.5030 ± 0.0003	9.1±0.2	11.250±0.003
t-U_{3000}Z40	1.5220 ± 0.0008	1.5150 ± 0.0012	1.5107 ± 0.0002	1.5048 ± 0.0001	5.8±0.3	4.962±0.004
t-U_{3000}Z60	1.5300 ± 0.0002	1.5200 ± 0.0002	1.5120 ± 0.0006	1.5100 ± 0.0004	10.8±0.1	8.752±0.007
t-U_{5000}	1.5140 ± 0.0004	1.5117 ± 0.0002	1.5058 ± 0.0012	1.5012 ± 0.0007	17.5±0.2	16.920±0.004
t-U_{5000}Z20	1.5232 ± 0.0008	1.5185 ± 0.0015	1.5098 ± 0.0005	1.5060 ± 0.0007	8.0±0.1	10.970±0.003
t-U_{5000}Z40	1.5293 ± 0.0003	1.5203 ± 0.0002	1.5150 ± 0.0002	1.5090 ± 0.0001	6.7±0.3	5.872±0.002
t-U_{5000}Z60	1.5352 ± 0.0006	1.5302 ± 0.0007	1.5241 ± 0.0001	1.5176 ± 0.0001	6.0±0.1	7.227±0.004

4.1.3 SPECTROSCOPIC ELLIPSOMETRY

The refractive index was also quantified by spectroscopic ellipsometry (Annex B.3). The measured ellipsometric parameters I_s and I_c, and the respective fit for the non-doped and doped tri-ureasils are represented in Figure 4.2-4.4. The structure model in Figure B.6(a) was used to fit the experimental data.

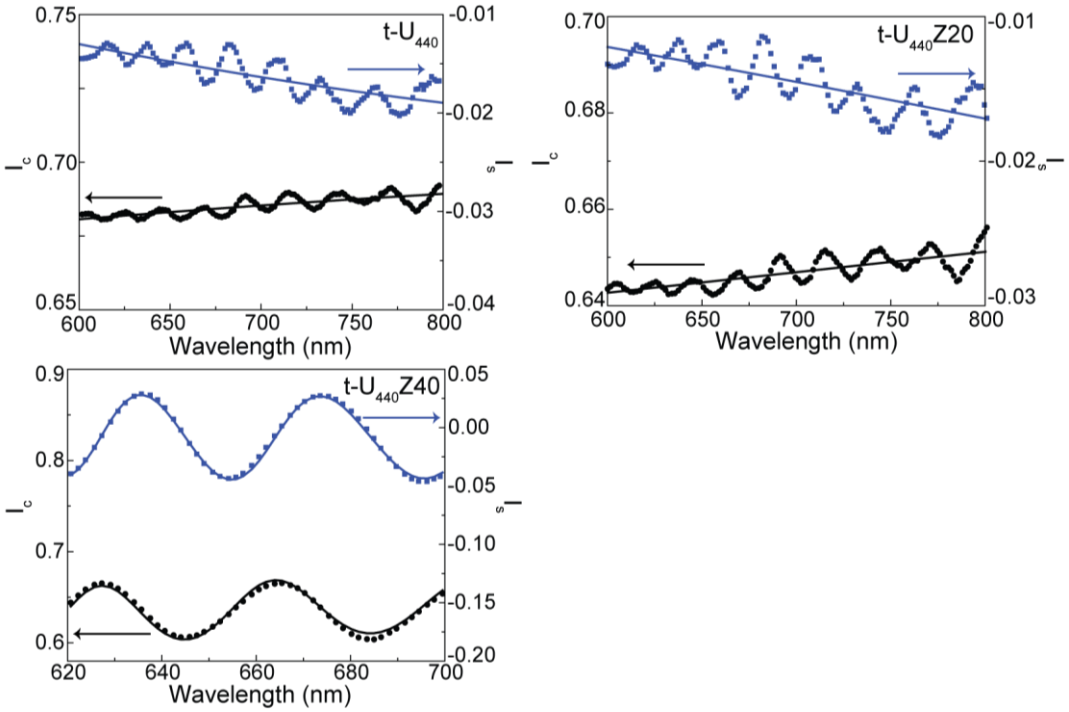

Figure 4.2 Ellipsometric parameters I_C (black) and I_S (blue) measured for non-doped and doped t-U_{440}. The solid lines correspond to the data best fit (r^2>0.9).

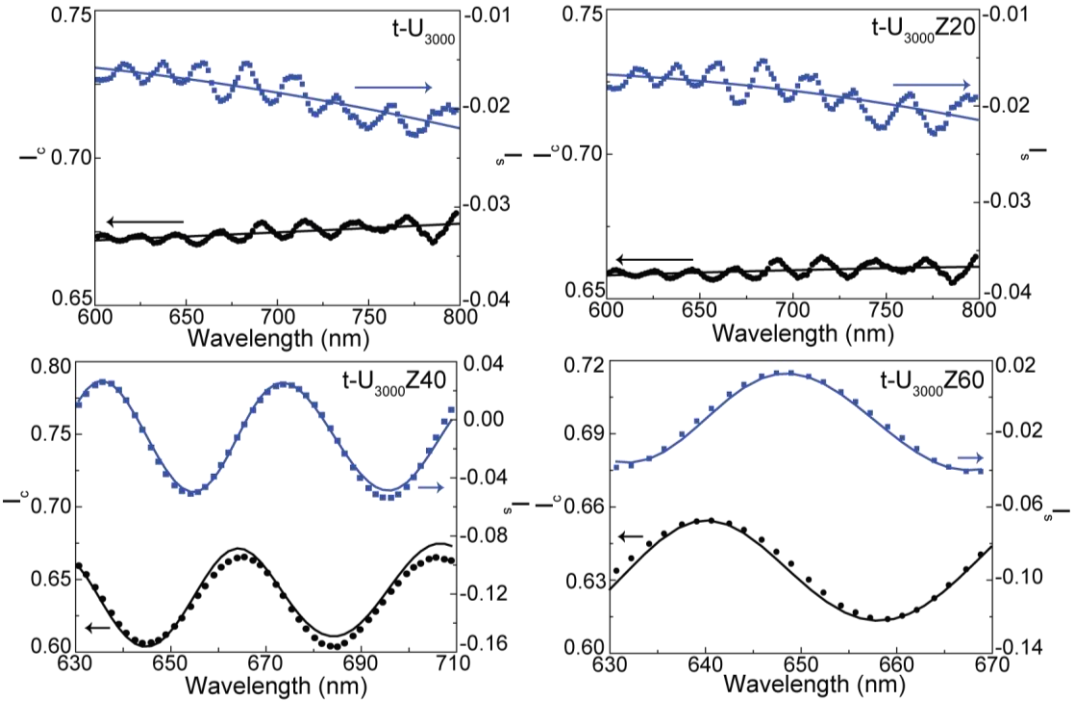

Figure 4.3 Ellipsometric parameters I_C (black) and I_S (blue) measured for non-doped and doped t-U_{3000}. The solid lines correspond to the data best fit (r^2>0.9).

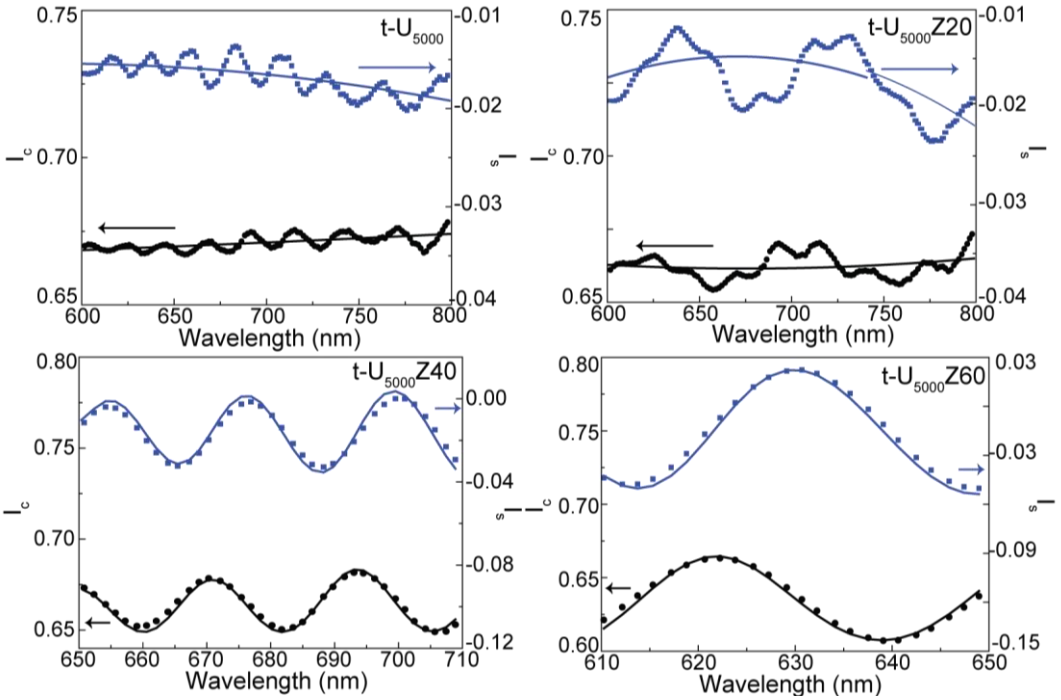

Figure 4.4 Ellipsometric parameters I_C (black) and I_S (blue) measured for non-doped and doped t-U$_{5000}$. The solid lines correspond to the data best fit (r^2>0.9).

The calculated dispersion curves are shown in Figure 4.5, revealing that the refractive index increases with the ZPO-McOH concentration, as observed in the prism coupling technique and in the di-ureasils family (Figure 1.4). The refractive index values also showed an increase for tri-ureasils with higher polymer molecular weight. This can be related to the higher relative amount of silica in the materials with lower polymer molecular weight, leading to a refractive index value similar to the one in silica (1.45 at 1550 nm [136]) in the materials with lower polymer molecular weight.

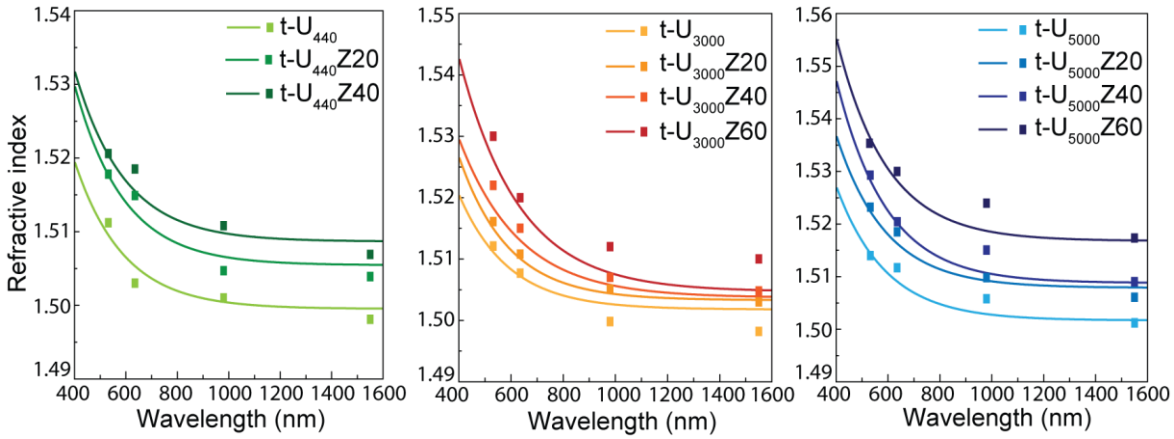

Figure 4.5 Dispersion curves (line) and refractive index values (points) obtained by spectroscopic ellipsometry and prism coupling, respectively.

4.2 CHANNEL WAVEGUIDES

4.2.1 PHOTOSENSIBILITY IN ORGANIC – INORGANIC HYBRIDS

The UV photosensibility of organic-inorganic hybrids is an essential requirement to pattern channel waveguides, because it allows to permanent change locally the refractive index using UV radiation. This feature can be found both in inorganic (silicates) and organic (polymers) materials [180]. During UV exposure, two main mechanisms may occur: thermal excitation and electronic excitation. In the thermal excitation, the local temperature at the surface increases, leading to densification effects. The electronic excitation leads to an activation of the organic (decomposition of the metal-organic bonds) and inorganic (rearrangement and reduction of bonds) components. Therefore, the response of a hybrid material to UV radiation is dependent on both the organic and inorganic counterparts.

The absorption coefficient values of selected samples showed an increase with ZPO-McOH concentration, as mentioned in Section 4.1.1. In the non-doped samples, the UV absorption can be related to its Si−O−Si bonding and the amine (nitrogen containing non-bonding pairs of electrons) and carbonyl (containing C=O bonding) of the urea group. With the increase of ZPO-McOH concentration, the UV absorption increases due to the C=C contribution, arising from the methacrylate group.

Under UV exposure, the di-ureasils and tri-ureasils surface undergoes a volume contraction leading to densification, which results from the local UV-induced polymerization. After UV exposure, the intensity of the C=C groups stretching vibration in the methacrylate moieties decreases, confirming the UV photopolymerization of the methacrylate groups [113]. Because of the hybrids' surface polymerization and densification, the Zr aggregates are dragged toward the interior of the waveguide region, which are responsible for a refractive index increase in the region underneath the exposed area, where the waveguide region is formed. Therefore, the refractive index can be tuned through chemical (ZPO-McOH concentration) and physical (UV exposure) means.

The variation of the refractive index is related to the variation of the absorption coefficient through the Kramers-Kronig relation, Equation (4.1), which establishes a direct proportionality between the refractive index variation and the absorption coefficient [181].

$$\Delta n = \frac{1}{2\pi}\int_{\lambda_1}^{\lambda_2} \frac{\Delta abs(\lambda')}{1-\frac{\lambda'^2}{\lambda^2}}\, d\lambda'. \tag{4.1}$$

where λ_1 and λ_2 are the boundaries of the relevant spectral range, λ is the wavelength, which the refractive index is calculated, Δn is the refractive index variation and Δabs is the absorption coefficient variation. Due to this effect, the organic-inorganic hybrids are photosensitive. Taking advantage of the UV photosensibility, an UV *laser* was used to pattern the organic-inorganic hybrids surface, using the experimental set-up described in Annex C. To morphologically and optically characterized the channel waveguides, optical microscopy, ellipsometry and optical mode field measurements were performed.

4.2.2 OPTICAL MICROSCOPY

To characterize the morphology of produced planar and channel waveguides, scanning electronic microscopy (SEM) and atomic force microscopy (AFM) were used, Annex A.7 and A.8, respectively. Figure 4.6(a-d) shows SEM images of a d-U_{600}Z40 film cross section deposited in Si/SiO_2 substrate (SiO_2 thickness of 1.00±0.05 μm) and borosilicate glass substrate. The images reveal a smooth film surface, with film thickness around 9.40±0.05 μm, 7.00±0.05 μm, 0.85±0.05 μm, and 7.80±0.05 μm for Figure 4.6(a-d) respectively.

The surface of the film was investigated by AFM. Figure 4.6(e-f) shows the surface of the d-U_{600}Z40 film, revealing also a smooth surface without fissures and defects. The average roughness value obtained was 0.65±0.05 nm, pointing out that surface light scattering in the film layer is minimized.

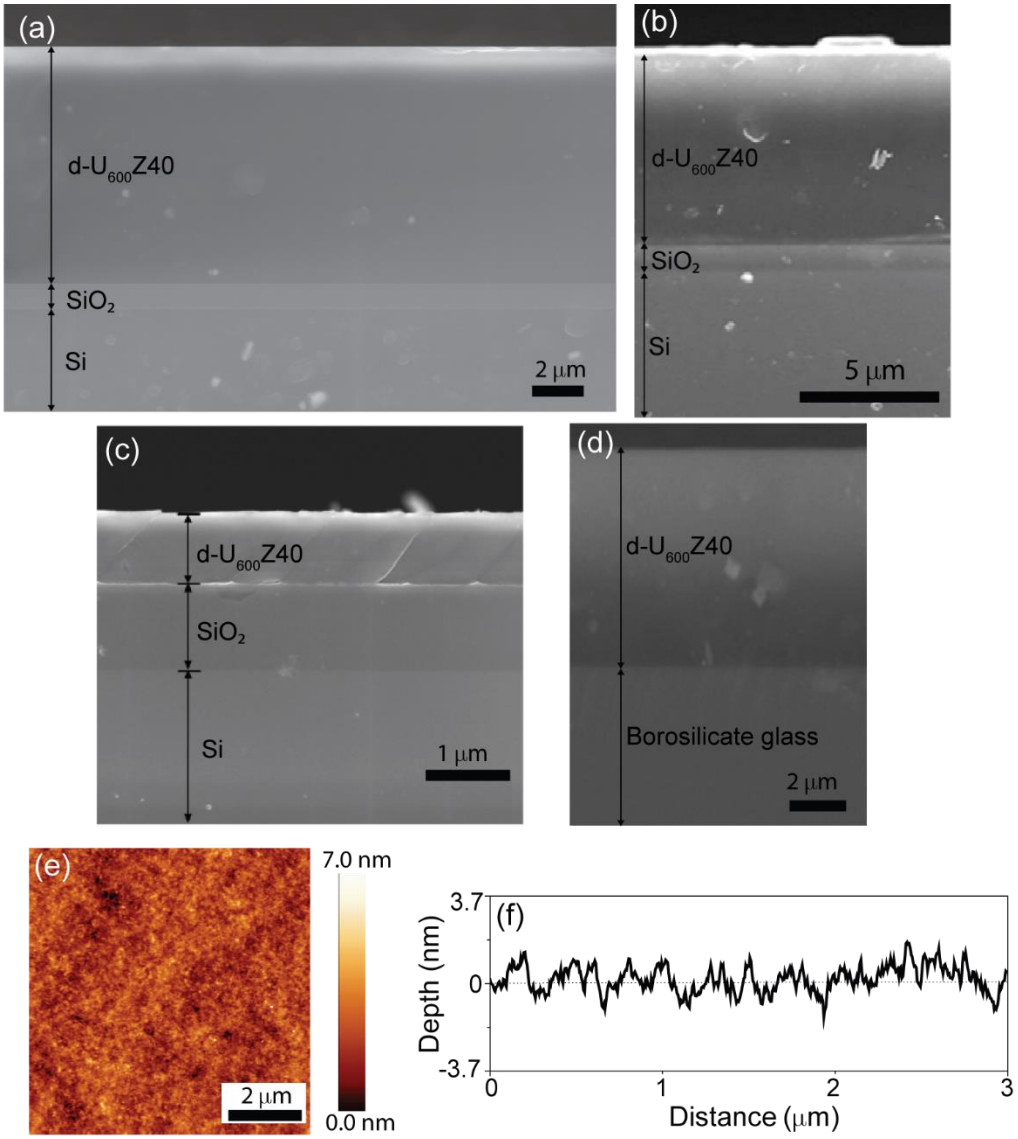

Figure 4.6 SEM images of the d-U_{600}Z40 film cross section deposited in (**a-c**) Si/SiO_2 substrate and (**d**) borosilicate glass substrate. (**e**) AFM topography image of the d-U_{600}Z40 film surface, and (**f**) the respective AFM cross section profile. (b, e) are adapted from [182] and (c) from [183].

The SEM and AFM images, and the respective cross section, of a channel waveguide written on the d-U_{600}Z40 film surface by UV *laser* direct writing are shown in Figure 4.7. The patterned region exposed to UV radiation shows a surface depression with a Gaussian shape arising from the beam spatial distribution, as previously reported [113]. This patterned region has dimensions (width × depth) of 40.0±0.5 μm × 70±1 nm, and results from the local UV polymerization, leading to material densification, inducing a positive refractive index contrast between the exposed and non-exposed regions [183].

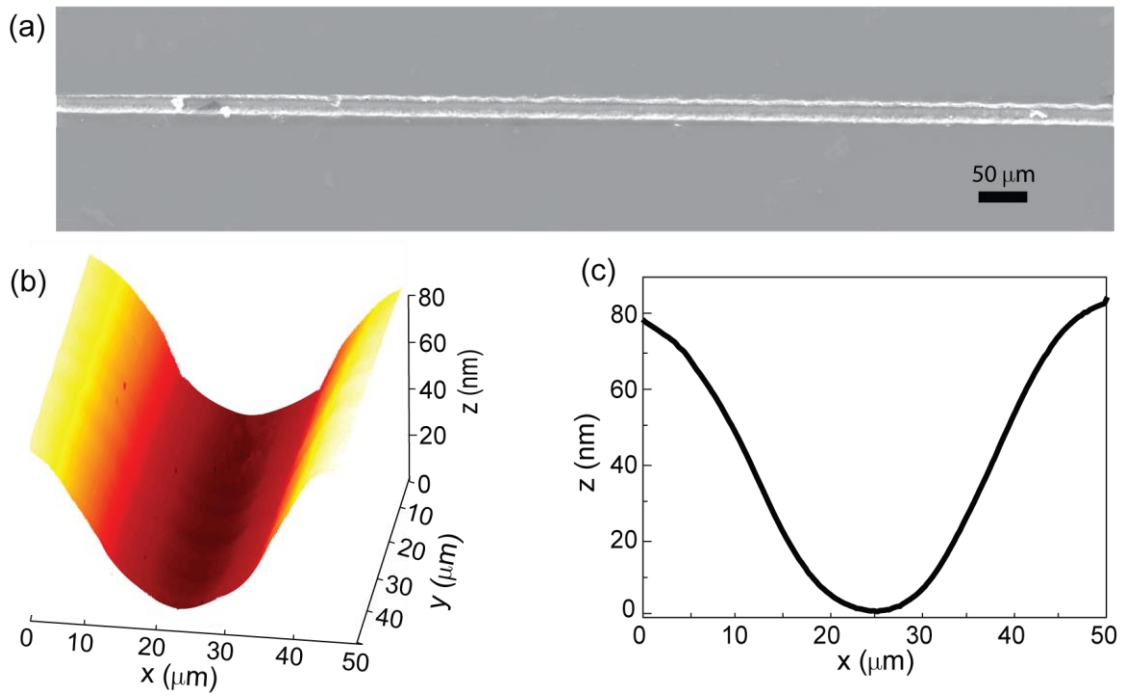

Figure 4.7 (**a**) SEM and (**b**) AFM topography images. (**c**) AFM cross section profile of the channel waveguide written on the d-U_{600}Z40 surface with a UV energy around 3 μJ·pulse^{-1}.

4.2.3 SPECTROSCOPIC ELLIPSOMETRY

To quantify the refractive index contrast induced by UV exposure, spectroscopic ellipsometry measurements were performed in the non-exposed and exposed regions. The experimental details for these measurements are detailed in Annex B.3. For this analysis, the material was processed as thin films deposited in Si/SiO_2 substrates (silica thickness of 1.00±0.05 μm), and exposed to the UV *laser* with 900 Hz and 3 μJ·pulse^{-1} as mentioned in Annex C. The layered structure with Si/SiO_2 substrate and the Cauchy model mentioned in Annex B.3 were considered in the ellipsometric data analysis to describe the refractive index for both regions. Figures 4.8(a-b) show the experimental ellipsometric parameters I_s and I_c, and the respective fit. The degree of polarization is represented in Figure 4.8(e), which compares the depolarization spectra for the non-exposed and exposed regions. As the degree of polarization is very close to the unit, it reveals a very small depolarization effect, which indicates a poor effect of the surface features in the ellipsometric analysis [183].

The resulting dispersion curves are shown in Figure 4.8(f), revealing a positive refractive index contrast between the exposed and non-exposed regions of $\Delta n \sim (5.0 \pm 0.5) \times 10^{-3}$, induced by the UV *laser* exposition with an energy of 3 μJ·pulse^{-1}. The film thickness estimated was 9.386±0.002 μm, which is in good agreement with that found by SEM, Figure 4.6(a).

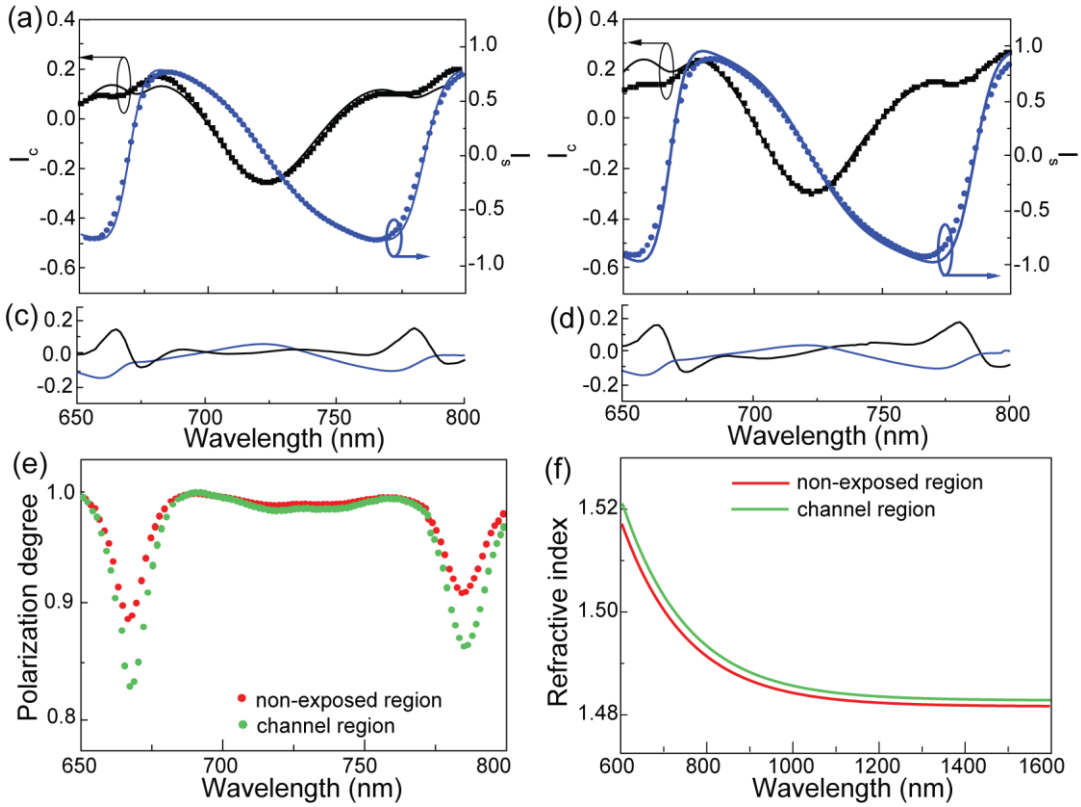

Figure 4.8 Ellipsometric parameters I_S (blue) and I_C (black) measured in the (**a**) non-exposed region and (**b**) channel waveguide written by UV *laser* direct writing. The solid lines correspond to the data best fit (r^2>0.98), and (**c**, **d**) are the respective fit residual plots. (**e**) Experimental depolarization spectra in the non-exposed and channel regions. (**f**) Dispersion curves obtained for the non-exposed and channel waveguide regions in the d-U_{600}Z40 film.

4.2.4 Optical mode field

As previous observed, under UV exposure the organic-inorganic hybrid refractive index changes, resulting in a positive refractive index contrast between the exposed and non-exposed regions. Taking advantage of the tri-ureasils UV absorption, several channel waveguides were written on the surface of doped tri-ureasil films deposited in borosilicate glass, using the UV *laser* direct writing process described in Annex C.1. After the writing process, the samples were cleaved with a diamond scribe to allow fibre butt coupling.

To get further insight into the mechanisms behind the radiation propagation in these materials, the characterization of the mode field distribution is required. Therefore, near-field measurements were performed in the IR spectral region (1550 nm) to characterize the guided modes intensity profile in each waveguide output. The experimental details are detailed in Annex B.4. For all the channel waveguides written on the surface of doped tri-ureasils, propagation was attained. Figure 4.9 shows the mode field profiles at each output, and the bi-dimensional intensity profile, which is well modelled by a Gaussian function, in a good agreement with monomode propagation.

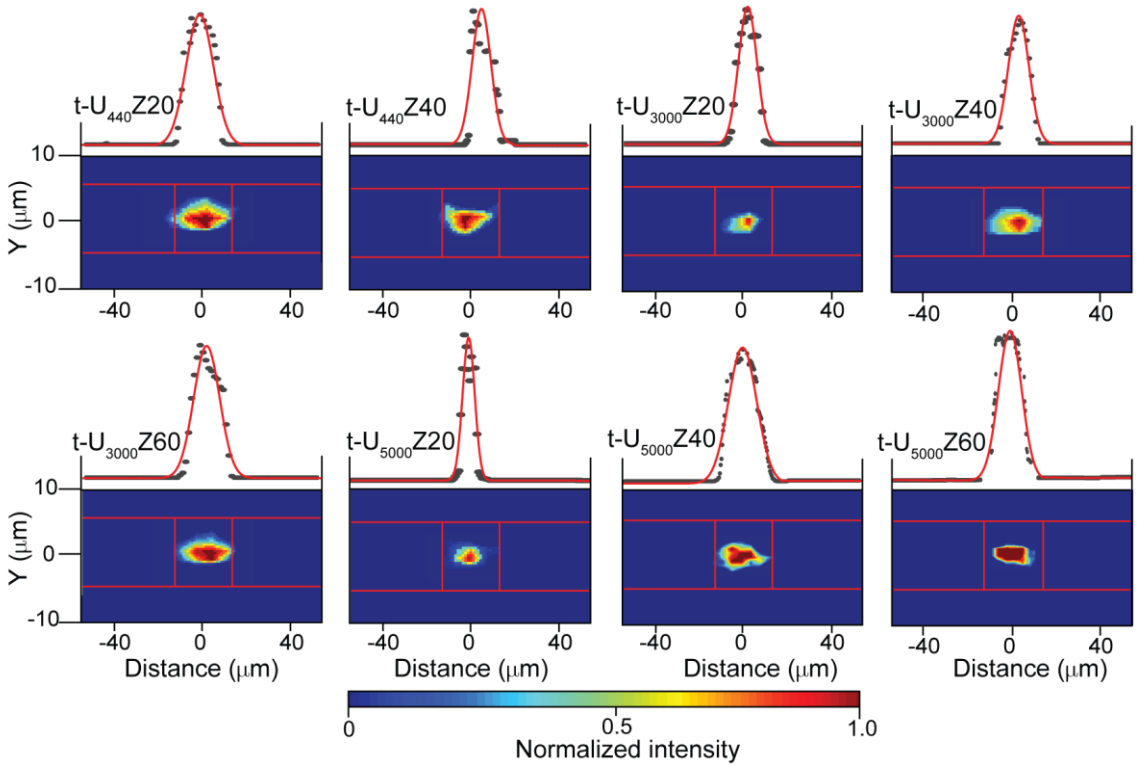

Figure 4.9 Mode field profiles and intensity profile of the predominant mode (solid line corresponds to the data best fit, r^2>0.98, using a Gaussian function) measured at the waveguide output written by UV *laser* in selected materials.

The UV pulse energy used to write the waveguides is presented in Table 4.4, with the FWHM values of the guided mode estimated through the data best fit to a single Gaussian function (Figure 4.9). The variation observed in the FWHM values is mainly due to the film thickness, ZPO-McOH concentration, and the pulse energy. As the *laser* focal point in the film changes with the film thickness, the width of the channel waveguides will differ, and, consequently, the FWHM of the guided mode will vary.

Table 4.4 Pulse energy used to write the waveguides on the surface of selected doped tri-ureasils, and the FWHM of the intensity profile Gaussian fit at each output waveguide.

Sample designation	Pulse energy* (μJ·pulse^{-1})	FWHM (μm)
t-U$_{440}$Z20	3.6	16.7±0.5
t-U$_{440}$Z40	2.9	14.4±0.4
t-U$_{3000}$Z20	2.5	10.3±0.1
t-U$_{3000}$Z40	2.2	15.9±0.2
t-U$_{3000}$Z60	2.8	20.6±0.2
t-U$_{5000}$Z20	3.5	7.9±0.2
t-U$_{5000}$Z40	3.2	31.8±0.9
t-U$_{5000}$Z60	3.0	28±1

* The error is estimated to be 3 % of the measured value.

4.3 CONCLUSIONS

As illustrated in Chapter 1 (Figure 1.4), it was already demonstrated that the refractive index in di-ureasil is easily tuned through chemical (ZPO concentration) and physical (UV dose) parameters. Here, it was demonstrated that the refractive index is also tuned by the Jeffamine structure and polymer molecular weight, without losing the thermal stability.

Planar and direct UV written channel waveguides with low losses in the visible and in the IR spectral region were prepared using tri-ureasil organic-inorganic hybrids doped with ZPO-McOH. In the relevant NIR spectral region (1550 nm), the refractive index values vary between 1.4981±0.0002 and 1.5176±0.0001 (Figure 4.10), and the attenuation coefficient is around 1.2±0.1 and 2.3±0.3 $dB \cdot cm^{-1}$.

In the UV spectral region, the materials present high absorption coefficients (> 50 $dB \cdot cm^{-1}$), mainly due to the Si−O−Si bonding (non-doped samples), and the C=C bonds present in the methacrylate group (doped samples). Due to this high absorption, under UV exposure, the material surface undergoes a volume contraction leading to densification, which results from the local UV-induced polymerization. Consequently, the refractive index is permanently change in the exposed region. Thus, the refractive index can be tuned through chemical (ZPO concentration) and physical (UV exposure) means. Taking advantage of the easily tuning of the refractive index, channel waveguides were pattern through direct UV writing on the doped materials surface, which can support guided modes at 1550 nm. The results obtained show that these materials have a high potential to develop passive and active integrated optical devices.

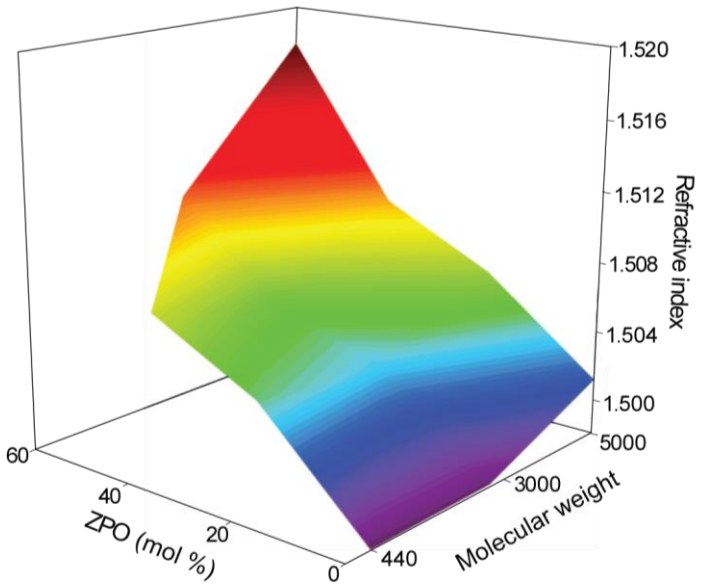

Figure 4.10 Refractive index variation at 1550 nm of tri-ureasil hybrids as a function of the polymer molecular weight and the ZPO-McOH concentration.

CHAPTER 5

PASSIVE DEVICES

In this chapter, the fabrication and characterization of the proposed passive devices are presented, namely a TO integrated variable wave plate device, a 90° hybrid coupler, and an EO modulator. The devices were produced by patterning a channel waveguides through direct UV *laser* writing on the surface of di-ureasil films, as described in Annex C.

The integrated TO variable wave plate is characterized by a linear waveguide written on the surface of d-U_{600}Z40 films. The di-ureasil TO coefficient was measured, yielding a value of $-(4.9\pm0.5)\times10^{-4}$ °C^{-1} at 1550 nm. The waveguide temperature was tuned through a heater of Ni-Cr or Ag stripe, inducing an optical phase retardation between the transverse electric (TE) and transverse magnetic (TM) modes, resulting in a controllable wave plate. A maximum phase retardation of 77 ° was achieved for a waveguide induced temperature increase of 5 °C above room temperature, with a power consumption of 0.4 W, with a Ni-Cr stripe heater of 10 mm length. The thermal linear retardation coefficient was calculated to be 19±1 °/°C. For a Ni-Cr stripe length of 20 mm, a thermal linear retardation coefficient of 44±1 °/°C was obtained, and the total thermal induced birefringence variation calculated was 3.9×10^{-5}. For the TO variable wave plate with an Ag electrode heater, a maximum phase shift of 54 ° was achieved for an electrical power consumption of 0.03 W. The thermal linear retardation coefficient was estimated to be 17±1 °/°C. These results led to the following publication: A. R. N. Bastos, *et. al*, ICTON 2015.

Foreseen an application on coherent optical systems, a 90° hybrid 2×4 coupler based on self-patternable d-U_{600}Z40 films was fabricated. The 90° hybrid coupler was incorporated with balanced photodiodes, resulting in an optical coherent receiver with capacity to extract the IQ

phase components of an optical signal. The device performance was assessed through the demodulation of a 20 Gb/s QPSK transmission performed over 40 km (G.652 fibre) and in back-to-back, yielding a 2.5 dB power penalty, unequivocally demonstrating the feasibility of the proposed PIC to be used as coherent receiver on NGOA. These results led to the publication of four scientific contributions: A. R. N. Bastos, *et. al*, WOCSDICE 2016; A. R. N. Bastos, *et. al*, ICTON 2016; A. R. N. Bastos, *et. al*, ICTON 2017; and A. R. N. Bastos, *et. al*, CLEO 2018.

Featuring electro-optic applications, such as telecommunications switching devices for coherent optical systems, the EO coefficient (r_{33}) was measured by an interferometric methodology for the d-U_{600}Z60 material, yielding a value of 39.9±0.5 pm/V. The voltage shift required for a phase change of π between the optical signal in the two arms of the MZI (V_π) was 2.9±0.3 V, which resemble to those reported for $LiNbO_3$ and silicon-based materials, highlighting the potential of di-ureasils for this application. These results led to the publication of one scientific contribution: A. R. N. Bastos, *et. al*, ICTON 2018.

5.1 THERMO-OPTIC VARIABLE WAVE PLATE

The recent developments in multiplexing formats, such as PDM, led to an increase of the data transmission capacity, by exploring the control of the optical signals SOP, as mentioned in Chapter 1. To implement this advanced format, PCDs containing building block elements are required. Since compact solutions with low-cost and low power consumption are needed, an integrated variable wave plate device based on the TO effect was fabricated, taking advantage of the large TO coefficient (dn/dT) of sol-gel derived siloxanes. Also, these organic-inorganic hybrid materials were considered particularly suitable to fabricate passive [184], active [185] and thermal actuated [186] devices, being thermally more stable and exhibiting higher glass transition and degradation temperatures than that observed in polymers.

The TO variable wave plate produced is based on a linear waveguide written on the surface of di-ureasil films. The TO actuation was performed by applying an electrical current on an electrode heater. Two different approaches were followed to produce the heater, one with a Ni-Cr stripe electrode heater placed on the top of the thin film, and another one with Ag electrode placed bellow the thin film. Both electrodes are parallel to the waveguide propagation direction. This device allowed the optical signal SOP to be thermally modulated and measured simultaneously on a waveguide produced with sol-gel technology.

5.1.1 EXPERIMENTAL DETAILS

Thermo-optic variable wave plate fabrication based on d-U_{600}Z40

The d-U_{600}Z40 was synthetized as mentioned in Section 3.2, and the channel waveguides were patterned on the film surface deposited in oxidized silicon wafers, following the procedure described in Annex C.

The waveguide thermal actuation was performed using a Ni-Cr or Ag stripe electrode heaters. The Ni-Cr stripe electrode heater (Driver-Harris, Nichrome 80, 800×150 μm^2) was placed on the top of the d-U_{600}Z40 film, with two different stripe lengths (L_H), 10.0±0.5 mm and 20.0±0.5 mm. The Ag electrode heater (thickness of 500±50 nm) with a L_H of 10 mm was deposited on top of the SiO_2 substrate with an inkjet materials printer (Dimatix, DMP-2831, resolution of 10-30 μm) from Instituto de Telecomunicações - Lisboa. Then, the d-U_{600}Z40 was deposited on top of the metallic Ag thin layer, leaving the electrodes contacts without the hybrid material on top. In these electrode heaters, an electrical current (Thurlby Thandar PL320QMD) was applied using current probes from (Wentworth Laboratories, PVX-400), to induce a temperature variation on the waveguide. The temperature was measured using a thermal camera (FLIR Systems, ThermaCamTM i50) with sensitivity of ±0.1 °C, Figure 5.1(a). The camera temperature profiles resulted from an average of five consecutive thermal images, considering the emissivity of the hybrid material as 0.40 [86].

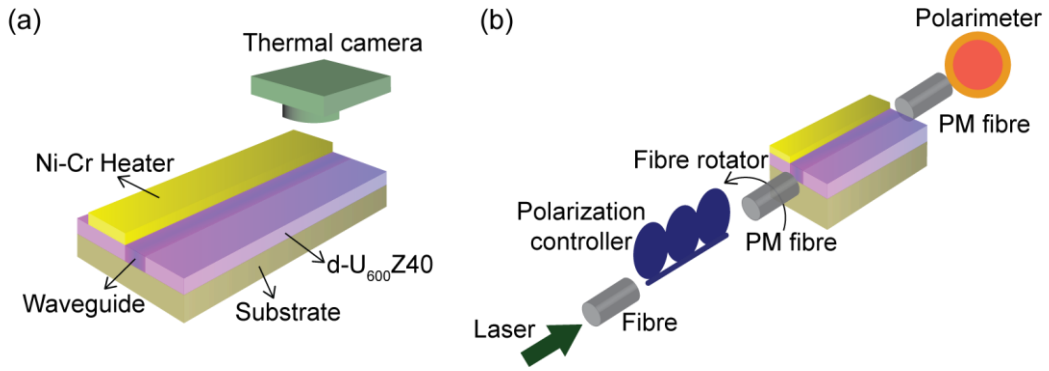

Figure 5.1 Scheme of the experimental set-up used for the measurement of (**a**) the temperature on the waveguide and (**b**) thermally induced variations of the state of polarization on the waveguide.

Refractive index measurements

The refractive index and thickness measurements were performed in the films deposited on borosilicate glass, using the prism coupling system at 1550 nm mentioned in Annex B.2. The refractive index values were measured for the TE and TM modes as a function of the film temperature, enabling TO coefficient calculation. The temperature was changed above room

temperature, between 20-45 °C with a step of 5 °C. For each temperature-*laser* polarization pair, three measurements were done, and the average value was considered.

State of polarization measurements on the TO variable wave plate

The optical characterization of the TO variable wave plate intended to measure the variation of the optical signal SOP with respect to the temperature variation. The SOP measurements were performed with a *laser* operating at 1550 nm (EXFO, IQ2400 WDM *Laser* Source) injected from a pigtailed polarization maintaining (PM) single mode optical fibre (Thorlabs, P1-1550PM-FC-1) into the waveguide, by aligning the PM fibre with one positioning system (Thorlabs, Nanomax-TS) containing a fibre rotator (Thorlabs, HFR007). The optical signal at the waveguide output was aligned using the above-mentioned positioning system, with a PM fibre connected to a polarimeter (Thorlabs, PAX5710IR3-T) with an external sensor head (Thorlabs, PAN5710IR3), Figure 5.1(b). The data acquisition was done with a sampling time of 30 ms. The SOP measurements started by imposing the initial SOP at the output of the waveguide, by adjusting the polarization controller. Then, the waveguide was thermally actuated by increasing the temperature of the waveguide, and the variation of the optical signal SOP was collected.

5.1.2 Results and discussion

Optical properties

Figure 5.2 shows the effective refractive index dependence with temperature of d-U_{600}Z40, for TE and TM modes, at 1550 nm. At room temperature the effective refractive index values are 1.5055±0.0006 and 1.5054±0.0003 for TE and TM modes, respectively, on a film with a thickness of 11.6±0.1μm. The initial birefringence of the planar waveguide defined as ($b_0 = n_{TE} - n_{TM}$) takes the value of (1.0±0.2)×10^{-4}. This initial value of birefringence is similar to that reported for other hybrid materials, such as diphenylsilanodiol with 3-(methoxysilyl)propylmethacrylate and perfluoroalkylsilane [187] or polymers, such as poly(methyl methacrylate) (PMMA), polystyrene and benzocyclobutane [188]. This birefringence is expected to occur [91], due to the amorphous nature of the di-ureasils [113], and the in-plane stress on the film, induced during the spin-coating process [189].

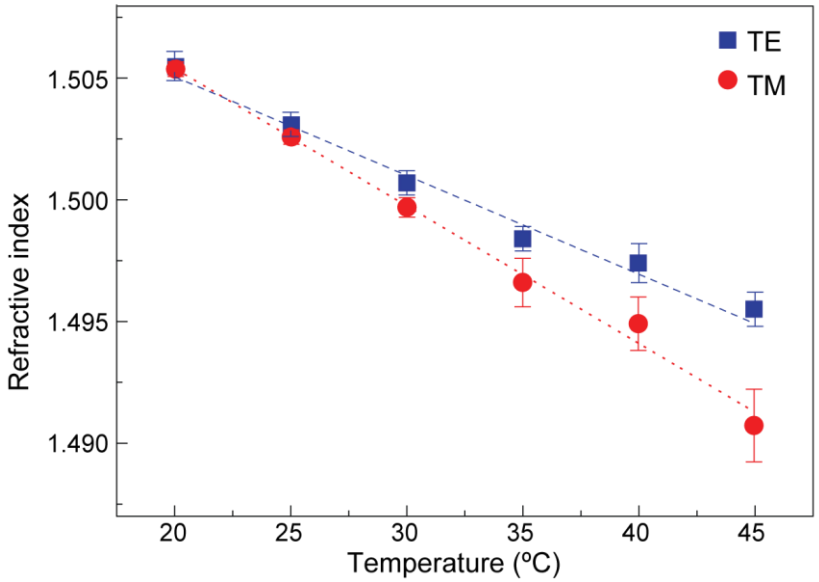

Figure 5.2 Refractive index as function of the temperature for TE (□) and TM (○) modes. The dashed lines correspond to the data best linear fit (r^2>0.98).

Upon increasing the temperature, the refractive index values decrease, revealing a linear behaviour and yielding TO coefficient values for TE and TM modes of $-(4.1\pm0.3)\times10^{-4}\,°C^{-1}$ and $-(5.6\pm0.1)\times10^{-4}\,°C^{-1}$, respectively. Comparing these values to those known for organic-inorganic hybrids and polymers (Table 5.1), they are higher, pointing out di-ureasils as competitive materials for TO devices operating with low power consumption.

Table 5.1 TO coefficients of selected polymers and organic-inorganic hybrids at 1550 nm. The methodology used to estimate the TO coefficients is also indicated.

Material		$dn/dT \times 10^{-4}$ (°C^{-1})	Methodology
Polymers	PMMA	− 1.3 [190] − 1.05 [191]	Ellipsometry
	Poly(ethyl methacrylate)	− 1.10 [190]	
	Poly(carbonate)	− 0.9 [190] − 1.06 [192]	Ellipsometry Prism coupler
	Cycloaliphatic acrylate	−2.8 [193]	Ellipsometry
	Polystyrene	− 1.2 [190]	
	Silicone	− 3.1 [190] − 2.5 [194]	Prism coupler on device
	Epoxy SU-8 2000	− 1.87 [195]	Prism coupler
	Benzocyclobutane	− 0.8 [196]	
	PMMA	− 1.20 [197]	
	Azopolymers of DR1/PMMA	−1.2 [198]	
	Azo-nitrobenzothiazole polyimide	−1.46 [199]	
	DR1 polyimide	−1.33 [199]	
	tB-PEEK	−1.0 [200]	
Organic-inorganic hybrids	d-U_{600}Z40	− 4.1 − 5.6	
	ORMOCER®	− 2.0 [85]	
	IPG®	− 3.0 [201]	
	MAPTMS	− 1.44 [202]	
	MAPTMS+TMOS	− 1.94 [203]	
	MAPTMS+PTMS+MTMS	− 2.4 [204]	
	TMOS+MTMS+DMDMS	−1.1 [205]	Refractometer

tB-PEEK: tert-butyl poly(etheretherketone); ORMOCER®: Organic Modified Ceramic – trademark of Fraunhofer ISC; IPG=inorganic polymer glass; MAPTMS: 3-Methacryloxypropyltrimethoxysilane; TMOS: tetrametilortossilicato; PTMS: phenyltrimethoxysilane; MTMS: methyltrimethoxysilane; DMDMS: dimethyldimethoxysilane.

Waveguide TO variable wave plate characterization

The interpretation of thermally induced variations of an optical signal SOP occurring after the waveguide propagation can be done by the Muller matrix formalism, $[S]=[M_R][S_i]$ in which the final SOP (S) is dependent of the initial one (S_i) and on the properties of the waveguide (M_R). The vector $[S] = [S_0, S_1, S_2, S_3]$ is represented on the Poincaré sphere through the Stokes parameters S_0, S_1, S_2 and S_3, where S_0 is the intensity of the optical signal, S_1 the difference between the horizontal (H) and vertical (V) linearly polarized intensity components, S_2 the difference between the intensity of the linearly polarized components oriented at ±45 °, and S_3 the difference between right (R) and left (L) circular components intensity. For

simplification, it is assumed that the Stokes vector is normalized, (S_0=1). On the Poincaré sphere the linear SOP (the polarization plane is constant along the propagation) are represented along the equator line, while the circular SOP (the polarization plane rotates along the propagation and the intensity of the vertical and horizontal components are equal) on the poles, intermediates SOP are designed as elliptical and are represented in the upper/lower hemispheres.

Considering the TO waveguide as a linear birefringence medium with fast axis aligned with the fibre rotator angle (γ), and retardance (δ) the waveguide Muller matrix, M_R, can be defined as [32],

$$M_R = \begin{bmatrix} 1 & 0 & 0 & 0 \\ 0 & \cos^2(2\gamma)+\sin^2(2\gamma)\cos(\delta) & \cos(2\gamma)\sin(2\gamma)(1-\cos(\delta)) & -\sin(2\gamma)\sin(\delta) \\ 0 & \cos(2\gamma)\sin(2\gamma)(1-\cos\delta) & \sin^2(2\gamma)+\cos^2(2\gamma)\cos(\delta) & \cos(2\gamma)\sin(\delta) \\ 0 & \sin(2\gamma)\sin(\delta) & -\cos(2\gamma)\sin(\delta) & \cos(\delta) \end{bmatrix} \tag{5.1}$$

with $\delta = k_T \Delta T$, where k_T is the thermal linear retardation coefficient and ΔT is the temperature variation. The retardance phase shift of the optical signal ($\Delta\delta$), acquired from travelling through the actuated waveguide of length L_H, can also be defined as,

$$\Delta\delta = \frac{2\pi}{\lambda} L_H \Delta b_T \tag{5.2}$$

where λ is the wavelength of the optical signal and Δb_T is the thermally induced birefringence variation.

The evolution of SOP at the output for temperature variations in the range $0<\Delta T<5$ °C is represented on the Poincaré sphere, for waveguides with Ni-Cr and Ag electrodes, Figure 5.3. From these results, a SOP change induced by an increase of temperature can be infer, visualized by the paths taken in the Poincaré sphere.

Figure 5.3(a) shows the SOP transition for the wave plate based on a 10 mm Ni-Cr stripe. Two distinct initial SOPs were taken, namely, right circular (RC) and linear horizontal (H). When the waveguide temperature increased, the RC state changes to an approximately linear state of +45 °, (path i). When the horizontal linear state is imposed, there is no variation in the state of polarization with the temperature, due to the fact that the plane of polarization is aligned with the fast axis of the waveguide. After adjusting the fibre rotator for an angle of 45 ° in relation to the principal axes of the waveguide, and controlling the SOP of the input optical signal, the state is tuned from linear horizontal to an approximately left circular SOP (path ii).

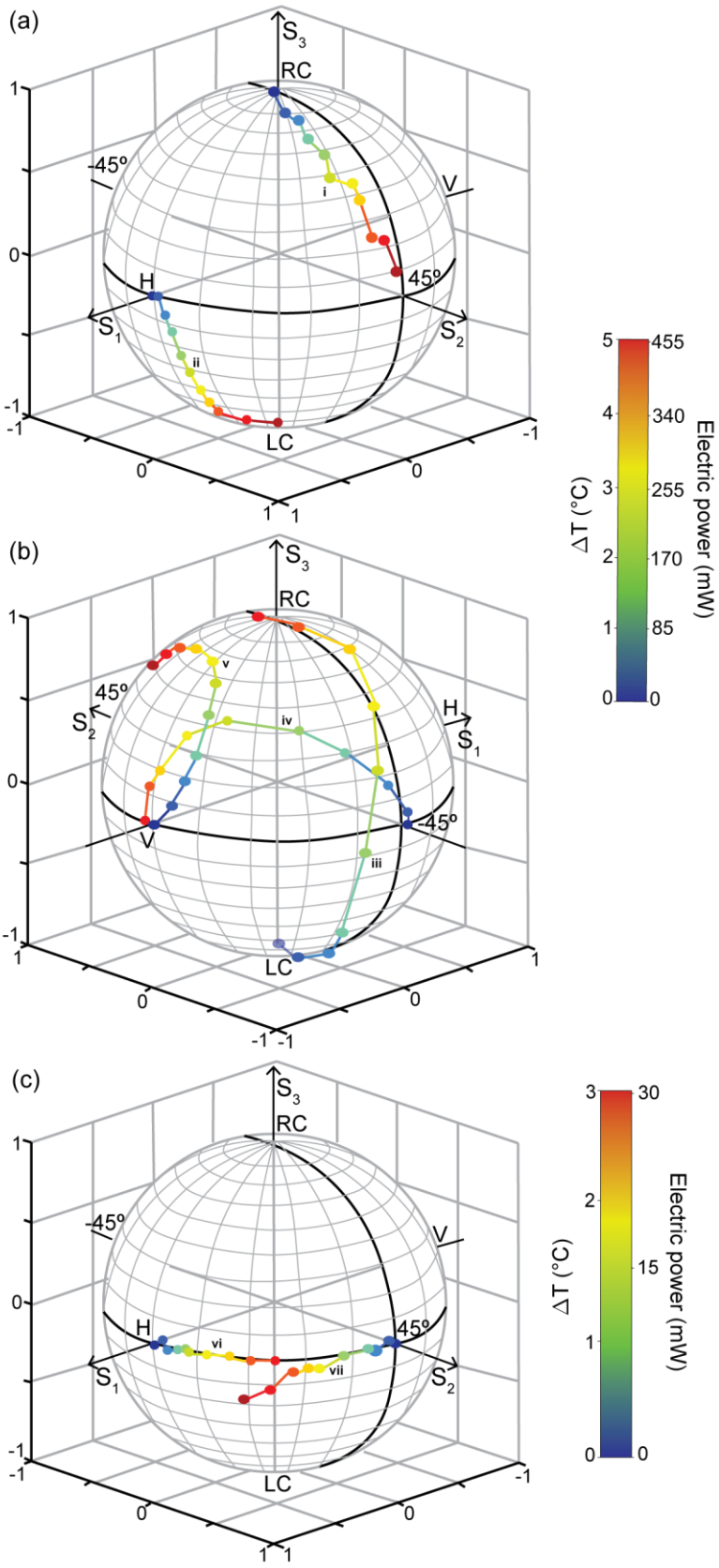

Figure 5.3 Poincaré sphere illustrating the evolution of the Stokes parameters S_1, S_2 and S_3 of the optical signal with the temperature variation in the waveguides induced by a Ni-Cr electrode heater with a length of (**a**) 10 mm and (**b**) 20 mm; and (**c**) by an Ag electrode heater. The temperature variations were **i**) 5.0 °C, **ii**) 4.2 °C, **iii**) 4.8 °C, **iv**) 4.7 °C, **v**), **vi**) and **vii**) 3 °C.

If $S_1 \approx 0$ (path i) and $S_2 \approx 0$ (path ii), it is possible to estimate the average thermal linear retardation coefficient of the waveguide as a function of the temperature variation, yielding a mean value of $k_T = 19 \pm 1$ °/°C. The maximum phase shift achieved was $\Delta\delta = 77 \pm 2$ ° for an electrical power consumption of 0.4 W. The total thermal induced birefringence variation calculated, from Equation (5.2), was $\Delta b_T = (3.3 \pm 0.2) \times 10^{-5}$, which is higher than the reported for thermally induced birefringence of PMMA [206]. Similar values for the phase shift ($\Delta\delta = 90°$) were obtained with periodic poled $LiNbO_3$ [34,207] and silica waveguides [208]. However, the characteristics of these devices led to higher electrical applied fields in the case of the periodic poled $LiNbO_3$ (3-4 kV/cm) and to relative larger power consumption (0.500 W) for the thermo-actuated silica waveguides. The obtained phase shift value of 77±2 ° obtained with d-U_{600}Z40 is also higher than that proposed in a liquid crystal-based fibre device ($\Delta\delta = 60°$), at 200 V [209]. Liquid crystal-based wave plates inserted as arrays on an optical chip yielded a maximum phase shift of 540 ° at 5 V but require a complex process to insert the liquid crystals arrays into the chip. On a TO actuated wave plate developed with perfluorinated acrylate waveguides, a 180° phase shift was attained with a power consumption of 0.073 W [210].

Figure 5.3(b) illustrates the results for a Ni-Cr heater with 20.0±0.5 mm length. It was observed a transformation between circular SOP, namely from L circular to R circular (path iii) performed without any rotation of the fibre holder in relation with the principal axis of the waveguide. For transformations between linear SOP, −45° to V (path iv) and V to +45º (path v) the measurement was performed with a rotation of the PM fibre of +22.5° and −22.5°, respectively. If $S_1 \approx 0$ (path iii) and $S_3 \approx 0$ (path iv and v), it is possible to estimate the average thermal linear retardation coefficient of the waveguide as a function of the temperature variation, yielding a mean value of $k_T = 44 \pm 1$ °/°C. The maximum phase shift achieved was $\Delta\delta = 180 \pm 2$ ° for an electrical power consumption of 0.4 W. The total thermal induced birefringence variation calculated, from Equation (5.2), was $\Delta b_T = (3.9 \pm 0.1) \times 10^{-5}$, similar to the values obtained with a smaller Ni-Cr stripe.

For the TO variable wave plate with an Ag electrode heater, the evolution of SOP at the output for temperature variations in the range $0 < \Delta T < 3$ °C is represented in Figure 5.3(c). From the results, also a SOP change is verified with the increase of temperature, visualized by the paths vi and vii. Path vi illustrates the transformation between linear H to linear 22.5° linear SOP, and path vii corresponds to the change from 45° to an elliptical SOP. Both

measurements were performed without any rotation of the fibre holder in relation with the principal axis of the waveguide. As $S_3 \approx 0$, the average thermal linear retardation coefficient as a function of the temperature was estimated, yielding a mean value of $k_T = 17 \pm 1\ °/°C$. The maximum phase shift achieved was $\Delta\delta = 54 \pm 2\ °$ for an electrical power consumption of 0.03 W. The total thermal induced birefringence variation calculated, from Equation (5.2), was $\Delta b_T = (2.32 \pm 0.02) \times 10^{-5}$. In this case, the power consumption is lower than the one with Ni-Cr electrodes, because with the electrodes above the film, the heat dissipates more easily than with the electrodes bellow the film.

Concluding, the TO variable wave plates produced allowed the polarization control of an optical signal, with higher Δb_T and thermal linear retardation values than the ones for PMMA, demonstrating the potential of di-ureasils as a cost-effective solution for PCDs.

5.2 90° HYBRID COUPLER

One way to allow high quality NGOA is the employment of coherent optical systems, as they enable large data rates, due to the intrinsic high-spectral efficiency [22]. As mentioned in Chapter 1, this technology allows a variety of advanced modulation formats, as QPSK, which requires a phase demodulator in the coherent receiver. In what concerns PICs deployment, demodulators based on $LiNbO_3$ [211], silicon [70], and InP [69] have been reported previously. Nevertheless, the complex and expensive production, and recycling processes for these platforms are still drawbacks. Therefore, exploiting the advantages of di-ureasil organic-inorganic hybrids, a QPSK demodulator based on the 90° hybrid coupler geometry was produced and characterized. The 90° hybrid coupler was incorporated with balanced photodiodes to extract the IQ phase components.

5.2.1 90° HYBRID COUPLER ARCHITECTURE

Considering the 90° hybrid coupler principle of operation described in Section 2.3.2, the device geometry optimization was performed recurring to the beam propagation method using a commercial numerical simulator (OptiBPM Designer® 9.0). The optimization intends to maximize the performance, i.e. the input-output transfer function dependence with the phase of the incoming signal. A typical structure model for di-ureasil based devices, was considered, consisting on a three layers stack (substrate, di-ureasil layer and air). The thickness and refractive index values for the di-ureasil layer are around 11.0 μm and 1.48, respectively, and for the oxidized silicon wafer layer are 5.0±0.25 μm and 1.45 (in accordance to the manufacture), respectively. The UV patterned channel was modelled using a rectangular profile core waveguide with a width of 10.0 μm and a spatial uniform refractive index of $n_{ch} = n+\Delta n$, where n is the di-ureasil refractive index and Δn is the refractive index variation induced by the UV *laser* exposure. It was considered a typical maximum value for Δn of 5.0×10^{-3} [183]. The Δn and the dimension values were experimentally verified by spectroscopic ellipsometry and microscopic analysis, respectively, as noticed in Section 4.2.

The optical signal transmission through the device was obtained for phase differences ($\Delta\theta$) between the local oscillator (LO) and the QPSK signal of {0°, 90°, 180°, 270°}. Figure 5.4 shows that propagation is attained at each output port, according to the phase differences between the two inputs (QPSK and LO signals). Therefore, this 90° hybrid coupler provides a selective intensity output as function of the incident phase, being able to demodulate a QPSK signal, as intended.

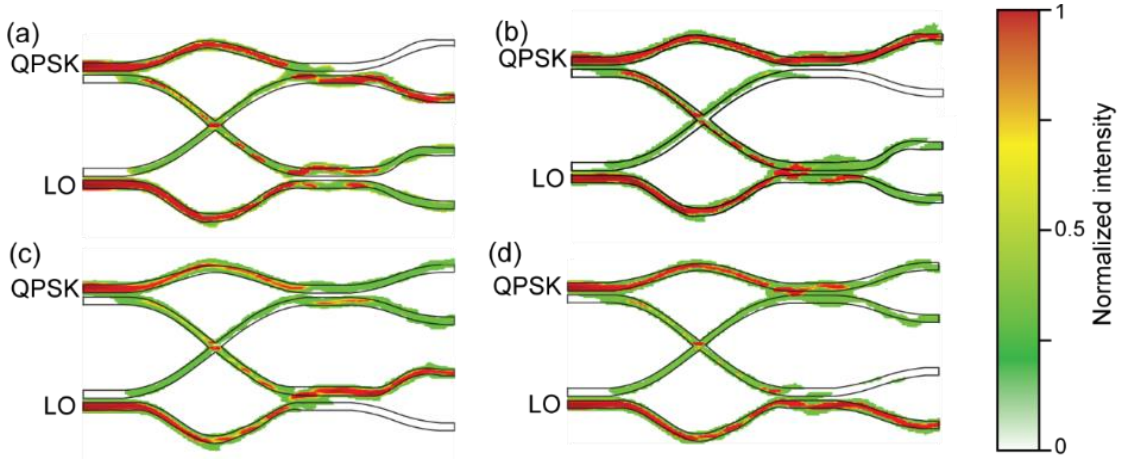

Figure 5.4 Scheme of the geometry and simulated transmission characteristics of the proposed device for Δθ values of (**a**) 0°, (**b**) 180°, (**c**) 270° and (**d**) 90°. The amplitude for the LO signal was set to be identical to the data signal.

The 90° hybrid coupler final design consists of four (2×2) directional couplers with a coupling interaction length of 3×10^3 μm and a waveguide gap of 30 μm, resulting in a coupling ratio of −3 dB. The 2×2 couplers are connected with two inputs and four outputs (designated as ch1-4) with a length of 10^3 μm and a gap between them of 125 μm, Figure 5.5(a). The 90° phase delay is imposed on the waveguide of ch4.

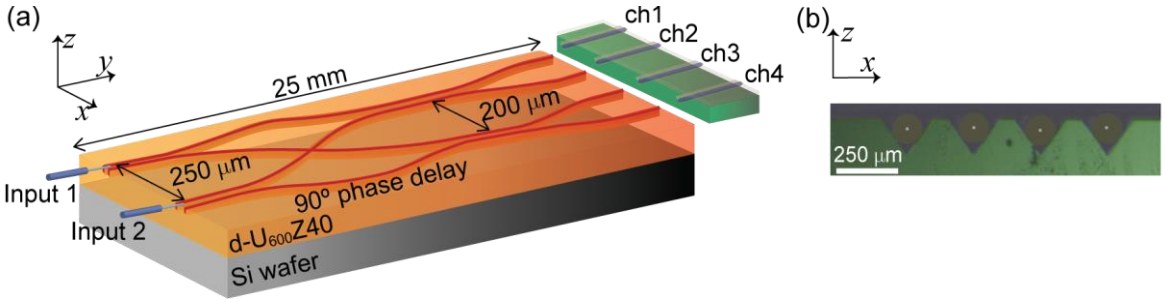

Figure 5.5 (**a**) Scheme of the 90° hybrid coupler structure. (**b**) Scheme and optical microscopy images of the V-groove used to align the waveguides with the output optical fibre.

5.2.2 EXPERIMENTAL DETAILS

Morphological characterization

Optical microscopy measurements were performed using a microscope set-up (Leica DM750 M) with an incorporated HD video camera (ICC50HD, resolution 2048×1536 pixels). The device images were acquired using an eyepiece of 20× (HI PLAN 20, NA=0.4).

Optical characterization to assess the receiver performance

In order to assess the device performance, the experimental set-ups demonstrated in Figure 5.6 were implemented. The optical signal from a semiconductor *laser* emitting at 1550 nm

(JDSU, CQF413) was divided (input 1 and input 2, Figure 5.6) using a beam splitter, and they were connected to polarization controllers.

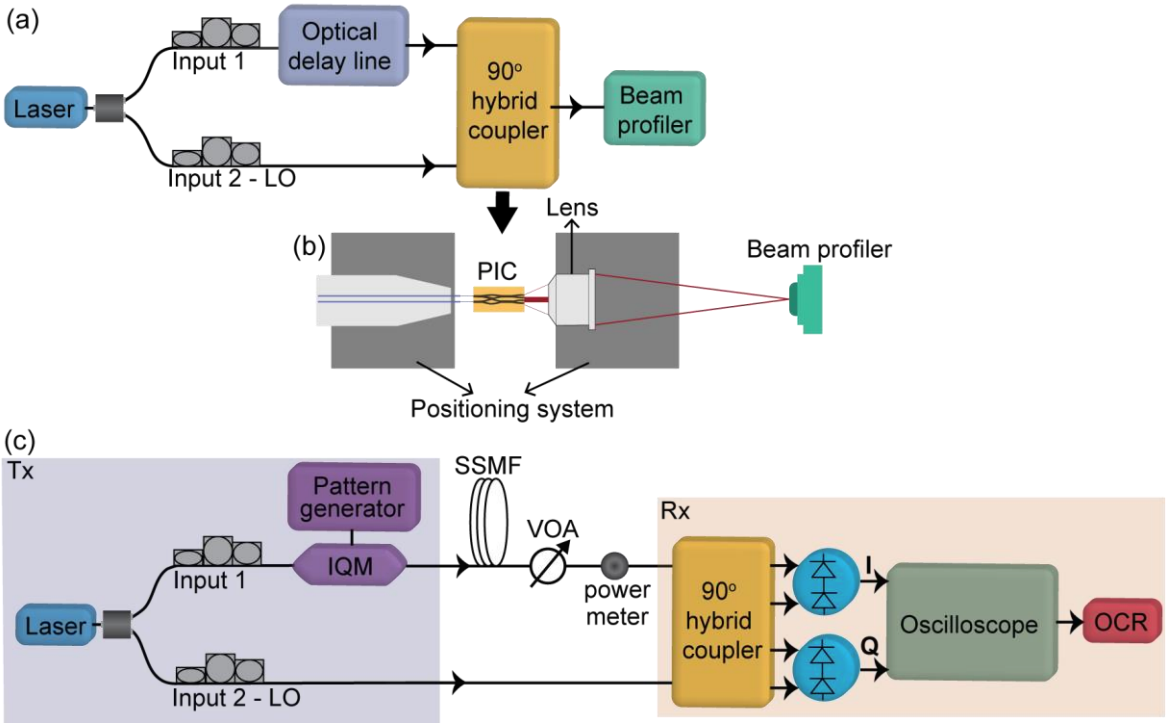

Figure 5.6 Schematic representation of the experimental set-up for the: (**a**) mode field profile measurements, and (**b**) alignment system, (**c**) QPSK signal demodulation performance assessment, where Tx and Rx are the transmitter and receiver systems, respectively.

In the experimental set-up of Figure 5.6(a), the PIC response as function of the relative phase difference ($\Delta\theta$) between the two inputs optical signals was attained. To perform these measurements, the mode field profiles at each output port were measured, and an optical delay line was used to control the optical signal phase of the input 1. Then the input signals were injected into the PIC, using a positioning system (Thorlabs, Nanomax-TS). The mode field profiles at the output channels were focused into a beam profile analyser (Newport LPB-1), using the above-mentioned positioning system and a 10× microscope objective (Newport, M-10X), Figure 5.6(b). The mode field profile at each output (ch1-4) was fitted using a single Gaussian function. The output power at the four channels was also measured for a spectral range between 1540-1560 nm (Nettest, OSICS-ECL).

In the experimental set-up of Figure 5.6(c), the optical signal in input 1 was modulated with an IQ optical modulator (IQM), using a 20 Gb/s data sequence from a bit pattern generator with a bit sequence of ($2^{12}-1$). The skew was minimized through a pre-distortion in the IQM in order to obtain the lowest bit error rate (BER) possible at the receiver. The input signals were injected into the device, using the above-mentioned positioning system, and the outputs

were aligned to four fibres V-groove array (Figure 5.5(b)), connected to a balanced diode system. The electric signal was digitalized by a 50 GSa/s real-time oscilloscope (Agilent 86100A), connected to the optical coherent receiver analyser (OCR) via Ethernet.

The coherent receiver analyse is a digital signal processing software used to analyse the transmission, and includes a normalization and clock, frequency and phase recovery subsystems. The normalization block controls the electrical amplitude fluctuations, due to the optical amplitude fluctuations. Since, the symbol rate of the transmitted symbol may not match an exact integer multiple of the receiver analogic to digital converter clock, an estimation of the ideal sampling instant is required. For this, a digital recovery clock subsystem is used, which interpolate the signal and resample it in the best symbol instant. To estimate the frequency of the modulated signal, a differential phase method was used. The phase recovery is performed using a "Viterbi and Viterbi" algorithm [212,213], to compensate some frequency shift occurred between the received signal and the LO, and *laser* phase noise variation over the time. After all these blocks, the software calculated the error vector magnitude (EVM), BER and the eye diagram to analyse the signal quality.

The device was tested in back-to-back configuration and after propagation in 40 km of standard single mode optical fibre (SSMF, G.652), which is a typical reach distance for access network scenarios. A variable optical attenuator (VOA) and a power meter was used to sweep and measure the input optical in order to characterize the receiver sensitivity.

5.2.3 RESULTS AND DISCUSSION

The optical microscope image of a 90° hybrid coupler patterned on a d-$U_{600}Z40$ film surface is shown in Figure 5.7. It can be observed that the device structure is in agreement with the simulated one.

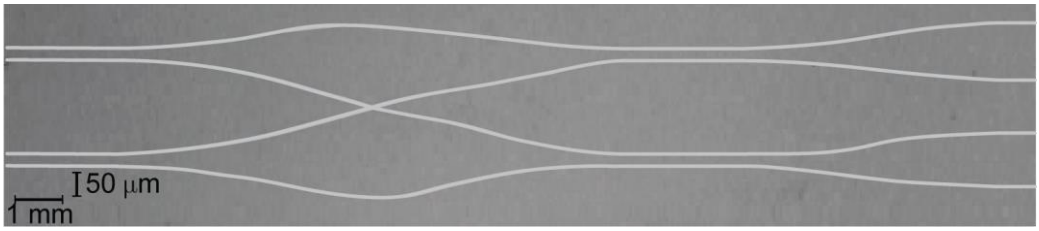

Figure 5.7 Optical microscope image showing the device structure written in the di-ureasil surface deposited over the Si/SiO_2 substrate.

Through near-field measurements, the characterization of the guided modes intensity profile for two optical signals (1550 nm) injected in input 1 and input 2 with relative phase, $\Delta\theta$, between 0 and 270° was performed. For the entire $\Delta\theta$ range, propagation in the waveguide

was attained and it was verified an input-output port transfer function dependence on the selected Δθ of the incoming radiation, as expected by the simulations presented above. Figure 5.8 shows the mode field profiles at each output, when Δθ = {0°, 90°, 180°, 270°}, and its bi-dimensional intensity profile, which is well modelled by a Gaussian function, in a good agreement with the single mode propagation predicted.

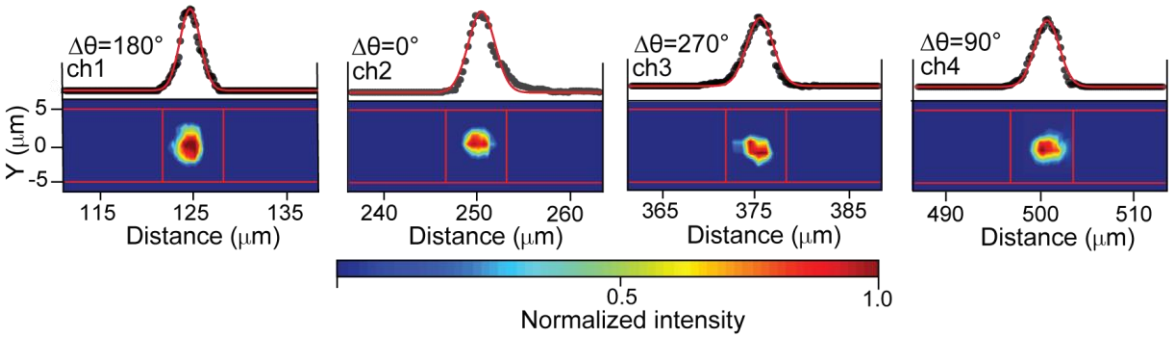

Figure 5.8 Mode field profiles and intensity profile of the predominant mode (solid line corresponds to the data best fit, $r^2 > 0.98$, using a Gaussian function) measured at the selected 90° hybrid coupler output ports when an optical signal (1550 nm) was injected in the two inputs with phase differences (Δθ) between 0 and 270°.

The excess loss (EL) and crosstalk (XT) of the hybrid coupler were deduced by comparing the optical power of each branch. An optical signal with −5.00 dBm±0.05 dB of power was inserted in the device input, and the outputs signals were aligned to four fibres V-groove array and connected to a power meter (OPM4-4D). The excess loss was extracted, using Equation (5.3)

$$EL = 10\log_{10}\left(\frac{P_{in}}{\sum_{i=1}^{4} P_{ch_i}}\right). \tag{5.3}$$

where P_{in} is the signal optical power, and P_{chi} is the output power in channel i, yielding a value of 3.8±0.3 dB. In the literature, it was found smaller values only for InP (0.2 dB [214]) and silicon (0.5 dB [215]) based devices. For polymer-based PICs, the excess loss values are larger (4.0 dB [216], 5.2 dB [217] and 7.0 dB [218]), due to the fibre chip coupling. As the absorption losses is typical between 1 dB·cm^{-1} and 5 dB·cm^{-1}, the expected minimum excess loss value is around 2.5 dB, which is accordance with the experimental one.

The crosstalk was determined for each output port, j, using Equation (5.4) yielding to a mean value of −8.6±1.5 dB.

$$XT_j = 10\log_{10}\left(\frac{\sum_{i\neq j} P_{ch_i}}{P_{ch_j}}\right). \tag{5.4}$$

To analyse the spectral bandwidth of the proposed device, the wavelength dependence of the output power at the in-phase and quadrature channels was determined, Figure 5.9. The power of each balanced photodiodes (I and Q channel) was measured, and it was observed a bandwidth of operation around 5 nm (in accordance with simulated results), I_Q>0.9 and I_I<0.1, suitable for dense wavelength division multiplexing (DWDM) systems, covering several channels.

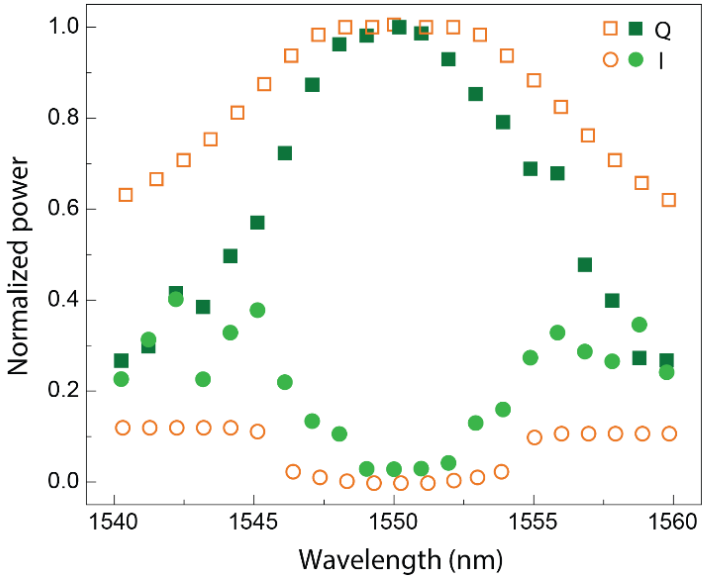

Figure 5.9 Experimental (full symbols) and simulated (open symbols) normalized power in the in-phase (circles) and quadrature (squares) channels of the proposed 90° hybrid coupler.

To further evaluate the device performance, a 20 Gb/s QPSK signal was demodulated as function of the input signal power (–35 dBm≤ P_{in} ≤–5 dBm). All the measurements were performed for 15 devices produced in the same conditions. The final results are an average of the values acquired for each device. The experimental IQ components were compared with the ideal ones through the calculation of EVM and phase deviation (ΔΦ) figures of merit which provide insight into the quality of the demodulated signal. The EVM corresponds to the average distance between the ideal and experimental symbols [219]. The ΔΦ (°) is the average difference between the transmitted and received signal vector angle. The EVM values were obtained for 2048 recovered symbols, over 3 independent measurements.

The constellation and eye diagrams for each configuration and for an input power of ~−20 dBm are shown in Figure 5.10. The experimental constellation diagram for the back-to-back configuration reveals a lower dispersion (~10 %) around the ideal values, compared with that found for the propagation in 40 km of fibre, due to the dispersion inherent to the propagation in the fibre. Concerning the eye diagrams, in the configuration with 40 km of fibre, the jitter (time taken in the crossing regions) is 25 % higher when compared to back-to-back, due to the fibre dispersion.

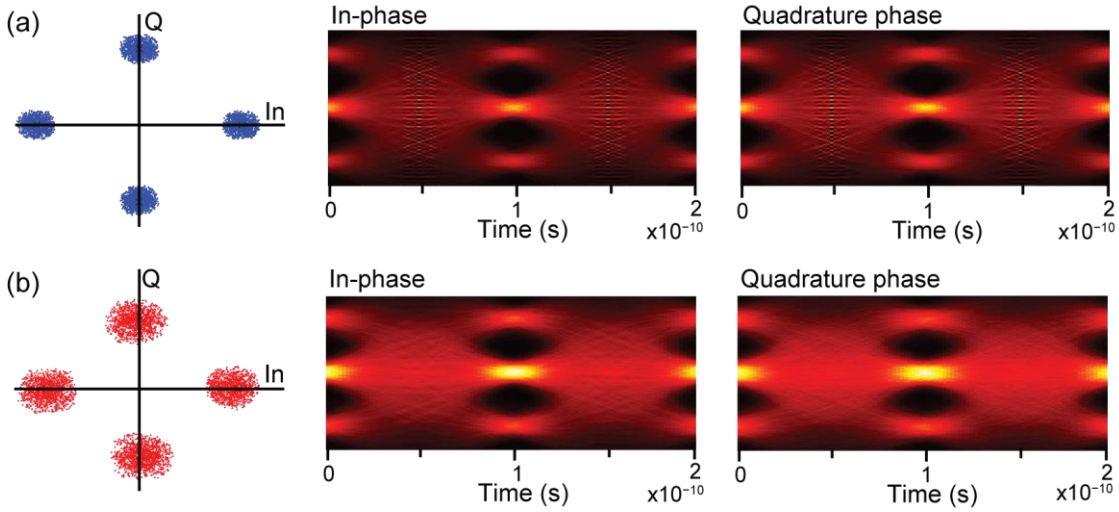

Figure 5.10 Constellation (left) and eye (right) diagrams for signal input power equal to −20 dBm for (**a**) back-to-back and (**b**) 40 km propagation over G.652; in the constellation, the crosses represent the ideal points.

To better compare the device performance, the variation of EVM as a function of P_{in} is shown in Figure 5.11(a). For high input power, the EVM approach to a minimum value of ~−19 dB, which can be ascribed to the evanescent field crosstalk (XT) between waveguides. As the EVM is dependent on the bitrate, the comparison with the literature should take this aspect into consideration. For an analogous bitrate, the value here reported is better than that reported for QPSK demodulators based in silicon (−17.7 dB [220]), Table 5.2. The $\Delta\Phi$ obtained is ~2 °, which is comparable to the values obtained for silicon (2 ° [221]) and polymer (2.5 ° [217]) based devices, and lower than those reported for InP-based ones (5 ° [138]), Table 5.2, demonstrating the quality of the patterning process. The higher value of $\Delta\Phi$ obtained was ~7 °, however a small percentage of experimental symbols were taken in to consideration (< 5 %).

The signals BER values for the back-to-back configuration and after 40 km of G.652 propagation, were estimated based on Equation (5.5) [222].

$$BER = \frac{(1-N_L^{-1})}{\log_2(N_L)} erfc\left(\sqrt{\frac{3\log_2(N_L)}{(N_L^{\,2}-1)}\frac{\sqrt{2}}{EVM^2\log_2(M)}}\right). \quad (5.5)$$

where N_L is the number of levels in the IQ constellation ($\log_2$M), yielding to BER values within (10^{-12}-10^{-2}), Figure 5.11(b). To further quantify the performance, a BER limit of 3.8×10^{-3} (corresponding to the 7 % hard-decision forward error correction, HD-FEC [223]) was considered as a threshold limit [224]. As demonstrated in Figure 5.11, the proposed device is able to operate below this limit, with a power penalty of 2.5 dB relatively to back-to-back.

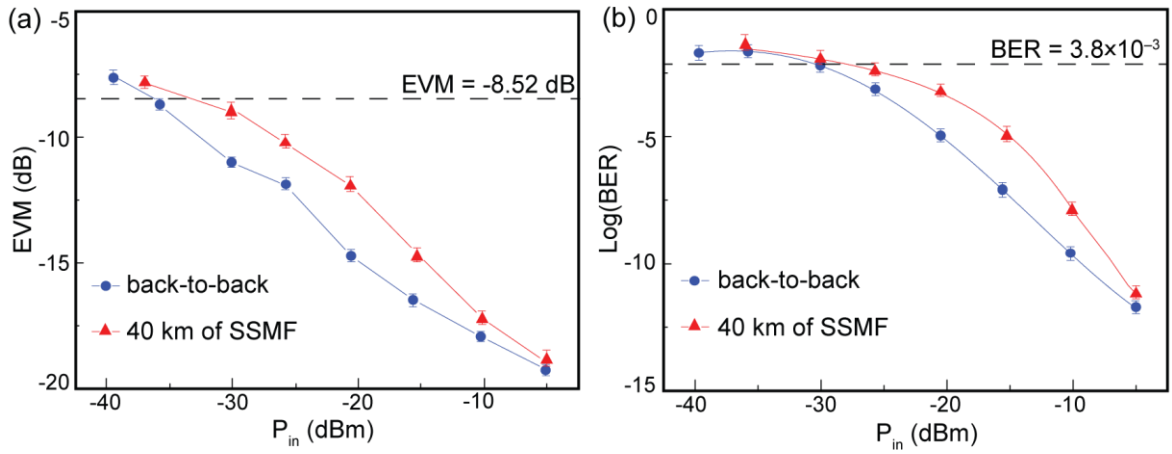

Figure 5.11 Experimental (**a**) EVM and (**b**) BER as function of the input power in the coherent receiver in back-to-back (blue) and over 40 km of G.652 (red) for 20 Gb/s QPSK transmission. The solid lines are visual guides and the dashed line corresponds to the HD-FEC limit.

Similarly, to that found for EVM, the power penalty depends on the bitrate. Due to the lack of quantitative results in the literature, the power penalty was compared with similar coherent receivers but applied for long-haul networks. Enhanced performances were only obtained for InP (1.3 dB [225]) and polymer (1.2-1.7 dB [217]) based devices tested for bitrates higher than 50 Gb/s. As power penalty increases with the bitrate, it can be assumed that these devices should also have a lower power penalty in the same test conditions of the proposed device. Nonetheless, these devices present a more complex and expensive production, due to photolithography and CVD processes, Table 5.2.

The performance of such optimized device unequivocally demonstrates the feasibility of the proposed cost-effective PIC coherent receiver to be used in NGOA.

Table 5.2 Figures of merit for EVM, power penalty and phase deviation of selected optical coherent receivers. The method used to fabricate the device and the attained refractive index contrast (Δn) are also indicated.

Network		Material	Production	Device	Δn	Bitrate (Gb/s)	BER	EVM (dB)	Power penalty (dB)	ΔΦ (°)	Ref.
	Access/Short-haul	di-ureasil	Direct writing	90° hybrid couplers	5×10^{-3}	20	10^{-3}	−19	2.5 for 40 km	2	this work
		InP	MOCVD	2×4 MMI	-	-	-	-	-	5	[226]
		Silicon based	PECVD	2 coupled 2×2 MMI	10^{-2}	40	-	-	-	2	[221]
			Photolithography	2×4 MMI	0.4	20	-	−17.7	-	-	[220]
		InP		Tapered 2×4 MMI	0.1	-	-	-	-	5	[138]
	Metro/Long-haul	Polymer		2×4 MMI 2×2 MMI	-	112	10^{-3}	-	1.3 for 100 km	3	[216]
				4 coupled 2×2 MMI	-	56-112	10^{-3}	-	1.2-1.7 for 110 km	2.5	[217]
		InP		2×4 MMI	-	160	10^{-3}	-	<1 for 610 km	5	[224]
					-	112	10^{-3}	−12.3	1.3 for 100 km	-	[225]

5.3 ELECTRO-OPTIC MODULATION

The modulation of an optical signal is one of the basic functions required in PICs [227,228], which implies an induced change in the optical field (amplitude or phase), that may be achieved by changing the refractive index value of the waveguide. Currently, the main modulators are based on the EO effect, wherein the refractive index variation (Δn_{EO}) is induced by the application of an electric field. The linear relation between Δn_{EO} and the applied electric field is designated as the Pockels effect [229]. This effect occurs for instance, in $LiNbO_3$ [38], semiconductors (gallium arsenide – GaAs), and in other non-centrosymmetric media (polymers containing organic molecules [230]), providing high bandwidth, strict linear modulation, and high-quality optical signals suitable for advanced modulation formats [231]. Nonetheless, this technology has several limitations like high-cost, large ecological footprint and limited ability for monolithic integration in PICs [232]. Therefore, the EO effect in di-ureasils hybrids was analysed through a MZI patterned on d-U_{600}Z60. The device performance was assessed through the estimation of the r_{33}, and V_π figures of merit.

5.3.1 EXPERIMENTAL DETAILS

Fabrication of the EO-MZI device

As mentioned in Section 1.5, the refractive index values increase with the amount ZPO in di-ureasils, namely between 1.4830±0.0003 (d-U_{600}Z20) to 1.5180±0.0002 (d-U_{600}Z60), at 980 nm. As the more concentrated di-ureasil film (d-U_{600}Z60) is characterised by a refractive index larger than that of ITO, it was selected for the EO-MZI device.

The EO-MZI fabrication process is characterized by four stages, as illustrated in Figure 5.12(a). First, the silver ink (Eletrolube, ESCP50G) deposition was performed through drop-cast to fabricate one electrode in a section of the ITO substrate (Xinyan Technology, XY07S). Then, the d-U_{600}Z60 was deposited by spin-coating and the MZI structure was patterned through direct *laser* writing, as described in Annex C. The MZI structure is formed by two symmetric Y-junctions, one that equally splits the input optical signal, and another one that combines the signal after traversing the two arms, Figure 5.12(b). The input/output waveguide has 5×10^{-3} m length, and the two parallel arms have a 2.5×10^{-4} m gap and a 5×10^{-3} m length. The final step is the production of a second electrode in one of the MZI arms with the same silver ink deposition process. Finally, the ITO substrate was cleaved to allow fibre butt coupling in the device, and the electric wires were fused to the electrodes.

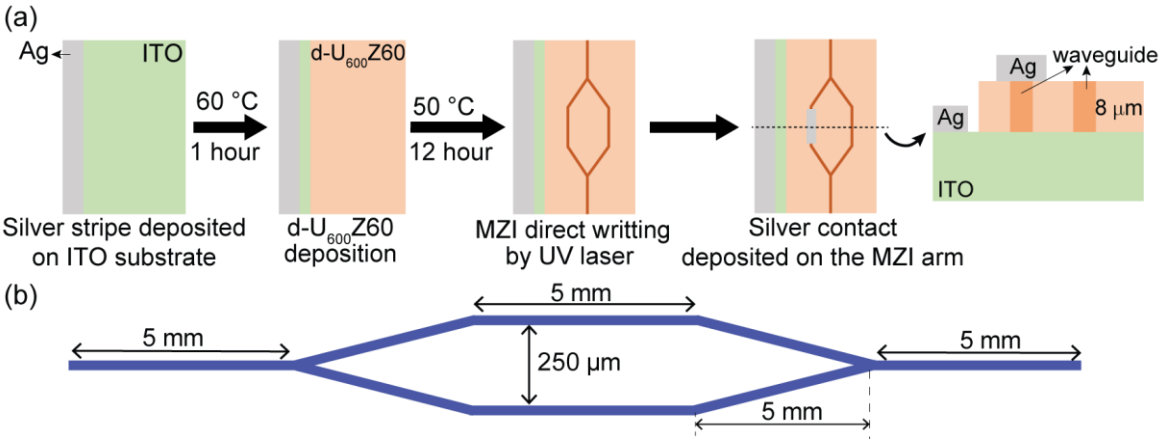

Figure 5.12 (**a**) Schematic representation of the fabrication process. (**b**) General view and detailed dimensions of the MZI structure.

Spectroscopic ellipsometry

The ellipsometry measurements were performed in a spectroscopic ellipsometer, as described in Annex B.3. The theoretical model used is characterized by four-layered system incorporating two layers for the substrate, the organic-inorganic hybrid layer and air as ambient medium, Figure B.6(b).

Electro-optic characterization

The optical power at the MZI output was acquired for an applied voltage around 10 V and an electric current of 3×10^{-2} A. A pigtailed *laser* operating at 980 nm (Agere Systems, SL980S33C) was connected to a single mode optical fibre, which was placed on a positioning system (Thorlabs, Nanomax-TS) used to couple the signal into the MZI. The waveguide output was aligned, using the above-mentioned fibre alignment system, with a monomode polarization maintaining fibre connected to a power meter (AFL Global, Noyes OPM4). The waveguide EO actuation was performed through a variable voltage source (Thurlby Thandar PL320QMD), using current probes from Wentworth Laboratories (PVX-400) placed on the top of the electrodes. The experimental set-up is demonstrated in Figure 5.13.

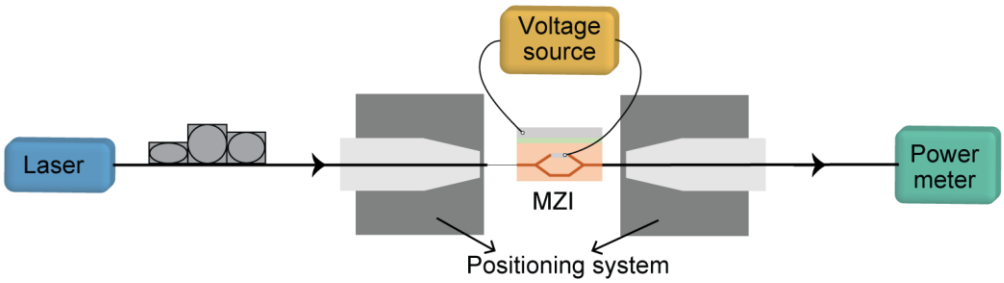

Figure 5.13 Schematic representation of the experimental set-up for the electro-optic characterization.

5.3.2 RESULTS AND DISCUSSION

Through spectroscopic ellipsometry, the d-U_{600}Z60 dispersion curve was obtained, Figure 5.14(a), revealing a refractive index larger than that of ITO, as expected.

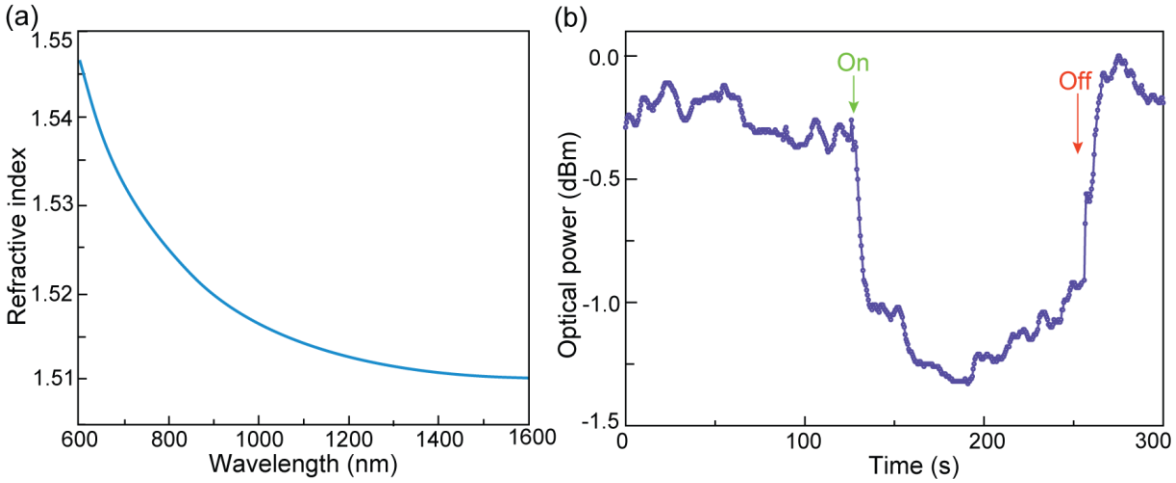

Figure 5.14 (**a**) Dispersion curves of the d-U_{600}Z60. (**b**) Optical output power for the MZI patterned in the d-U_{600}Z60.

To characterize the EO-MZI performance, the output optical power was measured as function of the time, Figure 5.14(b). After signal stabilization (~−0.3 dBm), a voltage of 10 V was applied for 2 minutes, leading to an optical power decrease of ~0.6 dB. After turning off the electric voltage, the optical power increase to its initial value. The MZI transfer function, Γ(dB), is related to the refractive index change (Δn_{EO}) by Equation (5.6),

$$\Gamma(dB) = 10 \times \log_{10}\left[\frac{1}{2}\left(1+\cos\left(\frac{2\pi \cdot \Delta n_{EO} \cdot L_{MZI}}{\lambda}\right)\right)\right]. \quad (5.6)$$

where λ is the wavelength and L_{MZI} is the arm length [61]. Based on Equation (5.6), the induced refractive index change, due to the EO effect, was estimated as $(4.27\pm0.03)\times10^{-5}$. Considering the Pockels effect, the EO coefficient (r_{33}) can be calculated using Equation (5.7)

$$\Delta n_{EO} = -\frac{1}{2} r_{33} n^3 \frac{V}{d}. \quad (5.7)$$

where n is the d-U_{600}Z60 refractive index (1.5180±0.0002, Figure 5.14(a)), and d is the electrodes distance (16.4±0.1 μm) [233], yielding a r_{33}=39.9±0.5 pm/V. Larger or analogous values were only achieved for $LiNbO_3$ and silicon-based devices (Table 5.3), pointing out the potential of the di-ureasil based PIC. Another performance figure of merit is the voltage shift (V_π) required to displace from constructive to destructive interference (change the cosine argument of Equation (5.6) from 0 to π), yielding a value of 2.9±0.3 V. Also, the product

$V_\pi \cdot L_{MZI}$=15.0±0.2 V·mm is often used as figure of merit. The obtained value is analogous to those achieved by $LiNbO_3$ and silicon-based devices, whose production is more complex and expensive. Nonetheless, smaller values could be achieved by improving the MZI structure (lower L_{MZI}).

Table 5.3 EO coefficient (r_{33}), V_π, and $V_\pi \cdot L_{MZI}$ of selected MZI devices.

Material	r_{33} (pm/V)	V_π (V)	$V_\pi \cdot L_{MZI}$ (V·mm)	Ref
d-U_{600}Z60	39.9±0.5	2.9±0.3	15.0±0.2	this work
Silicon-organic hybrid	-	1.6	1	[234]
Silicon with plasmonic phase shifters	-	-	0.05	[235]
$LiNbO_3$	28-34	-	-	[236]
Silicon	-	-	15-20	[237]
	122	-	-	[232]
	-	3.1	18.5	
	-	12	24	[238]
	-	5.2	21	
InP	-	-	0.73	[239]

5.4 CONCLUSIONS

The implementation of an integrated thermally controlled wave plate, using UV *laser* patterned channel waveguides in the surface of organic-inorganic di-ureasil hybrids was demonstrated. The hybrid material is thermally stable up to 250 °C and exhibits a large TO coefficient of $-(4.9\pm0.5)\times10^{-4}$ °C^{-1}. By increasing the waveguide temperature up to 5 °C (above room temperature) it is possible to control the phase shift up to 77±2 ° with the Ni-Cr heater. The average thermal linear retardation coefficient of the wave plate was estimated to be 19±1 °/°C and the thermally induced birefringence variation was $\Delta b_T=(3.3\pm0.2)\times10^{-5}$, which are higher than the figure of merit known for PMMA, placing di-ureasils as potential low-cost solution for the fabrication of polarization controlling devices. By increasing the Ni-Cr stripe length, a thermal linear retardation coefficient of 44±1 °/°C was obtained, and the total thermal induced birefringence variation calculated was $(3.9\pm0.1)\times10^{-5}$. The power consumption was reduced by placing the electrodes bellow the hybrid film in order to minimize the heat dissipation, showing a maximum phase shift of 54±2 ° achieved for an electrical power consumption of 0.03 W. The thermal linear retardation coefficient estimated was 17±1 °/°C. Moreover, the integrated optics example discussed here can be extended to

other polymer-based materials and the performance can be improved (response time of ~10^{-3} s) by the use of lithographic processes to build the heating element.

A cost-effective coherent receiver based on a 90° hybrid coupler, patterned by direct UV *laser* writing on the surface of di-ureasil films was demonstrated. The functionality of the PIC was shown in a test-in-bed configuration with 20 Gb/s QPSK over 40 km G.652. The proposed 90° hybrid exhibited a phase deviation of 2 ° and an excess loss of 3.8±0.3 dB. An EVM minimum value of −19 dB was attained with a power penalty of 2.5 dB relatively to back-to-back, for a BER of 3.8×10^{-3}. The comparison of those values with the ones attained for InP and silicon-based devices, shows the potential of integrated organic-inorganic hybrid to become key building blocks for PIC based demodulators. Furthermore, since this device functionality extracts IQ components and has an operation bandwidth of 5 nm, it demonstrates its capability to operate with other multi-level amplitude and phase shift keying modulation schemes, as M-QAM, and with DWDM systems.

Envision the implementation of a low-cost optical modulator, measurements were performed in an EO-MZI device, manufactured with direct UV *laser* patterned method on the surface of organic-inorganic hybrid films. The measured parameters, r_{33} (39.9±0.5 pm/V), V_π (2.9±0.3 V) and $V_\pi \cdot L$ (15.0±0.2 V·mm) fit the figures of merit of analogous devices based on $LiNbO_3$ and silicon, envisaging promising cost-effective alternatives to the current MZI devices.

CHAPTER 6

ACTIVE DEVICES

Visible light communications (VLC) based on white light-emitting diodes (LEDs) are emerging as a low-cost and energy-efficient alternative solution to wireless communications. As white LEDs use a combination of a long-lived yellow emission combined with the faster response of a blue-emitting LED (peaking at ~460 nm), VLC technology requires amplification of the blue component to improve the signal-to-noise ratio.

In this chapter, it is described the fabrication and characterization of planar and channel waveguides based on a blue-emitting poly(fluorene) conjugated polyelectrolyte, namely, poly[9,9-bis(4-sulfonylbutoxyphenyl)fluorene-2,7-diyl-*alt*-1,4-phenylene] (PBS-PFP) incorporated into di-ureasil organic-inorganic hybrids for optical amplification in VLC. Taking advantage of the di-ureasil host as an UV self-patternable material, UV *laser* direct writing was used to pattern channel waveguides with a larger refractive index (0.09) compared with the non-exposed region. The material synthesis and the channel waveguides patterning were described in Section 3.2 and Annex C, respectively. The channel waveguides enable confinement and guidance of the PBS-PFP emission with a maximum optical gain efficiency value of 1.62±0.02 $cm \cdot \mu J^{-1}$. This value is among the best figures of merit known for polymeric materials with additional advantages added by the di-ureasil hybrid host, establishing the proposed approach as a promising cost-effective solution for optical amplification in VLC. These results led to the publication of one scientific contribution: Ana R. N. Bastos, *et. al*, ACS Omega (2018).

6.1 INTRODUCTION

Recent advances in LED technology have created a new generation of energy-efficient light sources that look set to revolutionize the indoor lighting market [240]. Modern LEDs can be rapidly modulated, presenting opportunities for their future application in VLC, in which the LED simultaneously functions as both a light source and wireless signal transmitter to transfer information at rates up to Gigabits per second [47]. While inorganic materials have traditionally dominated the fields of solid-state lighting and optical communications, organic materials are rapidly emerging as alternatives for applications where inorganics are not ideally suited, such as those requiring large active areas, colour tunability or mechanical flexibility [241]. The wide scale commercial availability of organic light-emitting diodes is a prime example of how these key attributes can be successfully leveraged [242,243].

White LEDs for VLC can be produced in two ways: a combined red-green-blue LED module, or alternatively a blue-LED coated with a phosphor colour converter [49]. Conjugated polymers (CPs) have recently been successfully implemented as organic colour converters to replace traditional inorganic phosphor coatings [244–246]. High photoluminescence quantum yields (PLQY), tunable emission colours and in particular sub-nanosecond emission lifetimes make CPs attractive for this purpose, since these features enable higher communication bandwidths to be attained than for conventional inorganic phosphors which emit in the micro-millisecond regime [247]. Conjugated polymers have also been used to prepare free-standing polymer membrane *lasers* [248] or have been doped within polymer organic fibres or slab waveguides to generate waveguide modulators [249] and optical amplifiers [250–253]. The latter operation is important for VLC since an optical amplifier is usually required to enhance the blue component of the transmitting signal [47].

Despite the ease of processability, simultaneous control of both the morphology and electronic properties remains a significant challenge for conjugated polymers. Optical loss mechanisms such as singlet-state annihilation and charge generation are mediated by inter-chain coupling [254], which becomes exacerbated upon transfer to the solid-state. Strategies for the control of intermolecular interactions, whilst maintaining or even enhancing the optical properties in the solid-state are thus highly desirable. It was recently shown that the incorporation of CPs into organo-silica hybrid polymers known as ureasils is an effective approach to minimize inter-chain interactions leading to highly emissive solid-state materials [155,255]. Moreover, ureasils are intrinsically photoluminescent, emitting in the purple-blue spectral region with a lifetime of nano-microseconds [256,257] and have a reasonable

refractive index (~1.5 [86]), which enables them to be used as waveguides for optical amplification [258], high-rejection optical filters [111] and luminescent solar concentrators [176,259–262]. Electronic coupling between the CP and the di-ureasil, combined with the formation of isolated polymer domains, leads to the creation of localized radiative trap sites which relax with a PLQY of >60 % [155].

Inspired by these results, the combination of a short-lived CP, coupled with the waveguide characteristics of the di-ureasil, could deliver a fast response optical amplifier, suitable for VLC. To minimize spectral losses, the blue-emitting PBS-PFP was chosen, which exhibits good spectral overlap with the di-ureasil and shows thermally-assisted population of radiative trap sites [155].

6.2 EXPERIMENTAL DETAILS

6.2.1 PHOTOLUMINESCENCE SPECTROSCOPY

The emission and excitation spectra were recorded at room temperature using a Fluorolog3® Horiba Scientific (Model FL3-2T) spectroscope, with a modular double grating excitation spectrometer (fitted with 1200 grooves·mm^{-1} grating blazed at 330 nm) and a TRIAX 320 single emission monochromator (fitted with 1200 grooves·mm^{-1} grating blazed at 500 nm, reciprocal linear density of 2.6 nm·mm^{-1}), coupled to a R928 photomultiplier (visible measurements), using the front face acquisition mode. The excitation source was a 450 W Xe arc lamp. The emission spectra were corrected for detection and optical spectral response of the spectrofluorimeter and the excitation spectra were corrected for the spectral distribution of the lamp intensity using a photodiode reference detector.

6.2.2 EMISSION QUANTUM YIELD

The emission quantum yield values were measured at room temperature using a C9920-02 Hamamatsu system. The method is accurate within 10 %.

6.2.3 VARIABLE STRIPE LENGTH GAIN MEASUREMENTS

The optical gain was measured using the variable stripe length (VSL) method by implementing the experimental set-up represented in Figure 6.1. A narrow stripe on the sample surface was optically excited and the amplified spontaneous emission (ASE) signal intensity (I_{ASE}) was collected from the edge of the sample as a function of the stripe length (L)

[263]. In order to have a narrow stripe on the sample surface with a variable length, a slit (aperture of 1.5×10^{-3} m) and a movable shutter connected to two translation stages (Thorlabs, 13 mm) were used, allowing the stripe length to be controlled within the limits $0 \leq L \leq 2.5$ ($\times10^{-2}$ m). To detect the I_{ASE}, an optical fibre (Quartz fibre, SMA MMF) and a spectrometer (MAYA Pro 2000, OceansOptics) were used. The emission spectra were acquired with an integration time of 5 s and 15 scans excited with a UV pump (Vilber VL-6.LC) emitting at 365 nm.

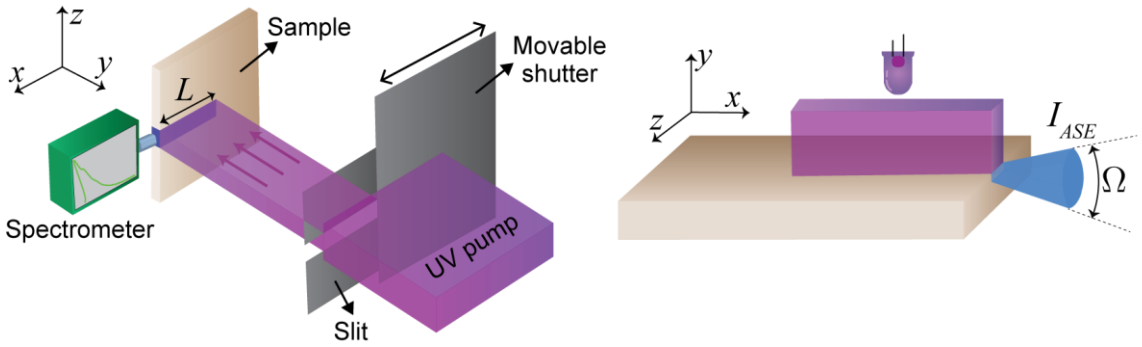

Figure 6.1 Schematic representation of the experimental set-up used for the VSL measurements.

6.2.4 Optical net gain measurements

The optical net gain of the channel waveguide was measured in the spectral domain for a continuous wave diode *laser* emitting at 450 nm (Roithner LD 450-1600MG). The *laser* signal was coupled to an optical fibre aligned with the channel waveguide using a positioning system (Thorlabs, Nanomax-TS). The propagated signal was collected at the channel output using the above-mentioned positioning system and spectrometer, with an integration time of 10^{-2} s and an average of 5 scans.

The net gain was also measured in the time domain using a modulated optical signal, pulsed with a mechanical chopper (MC1F10HP, Thorlabs), Figure 6.2. For this characterization, the waveguide output optical signal was aligned to a photodiode (DET 210, Thorlabs), connected to an oscilloscope (MSO7014B, Agilent Technologies). These measurements were performed under daylight, and for two independent optical pumping (UV excitation) configurations: i) externally to the channel using an UV pump (VL-6.LC, Vilber) as an external waveguide perpendicular pumping architecture, or ii) with an optical signal from a UV emitting diode (MCLS LED 365, Ocean Optics), injected in the channel input as a co-propagation pumping architecture. This pumping solution provides a compact and integrated system.

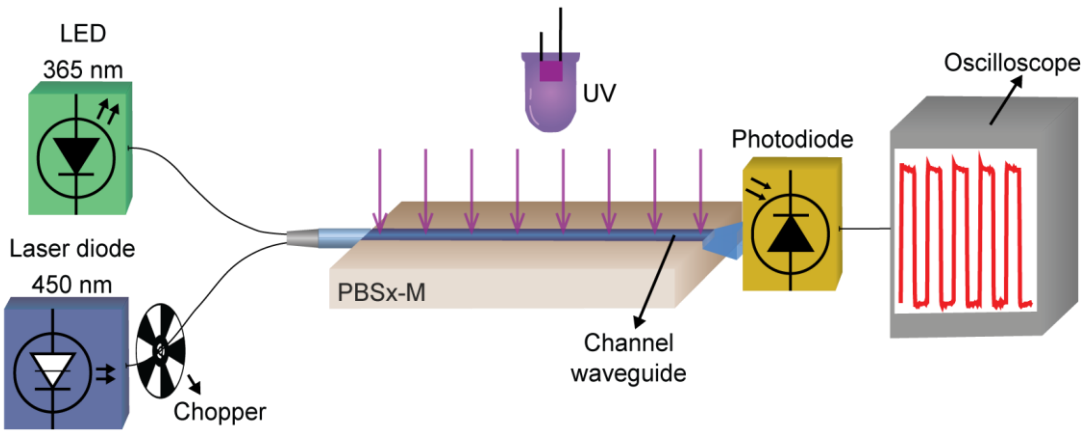

Figure 6.2 Scheme of the experimental set-up used to measure the net gain with a modulated optical signal for the two pumping strategies (external perpendicular or co-propagating).

6.3 RESULTS AND DISCUSSION

Monolithic PBS-PFP-di-ureasils are flexible, transparent under daylight, and exhibit an intense blue emission under UV radiation (365 nm), as shown in Figure 6.3(a). The transparency was quantified by the measurement of the absorption coefficient from the UV-Vis absorption spectra that comprise a main absorption band in the UV region (250-325 nm), assigned to the d-U_{600} host [157], Figure 6.3(b), with a maximum absorption coefficient of ~8.5 cm^{-1}. After doping with PBS-PFP, although the host-related absorption band still dominates the spectra, absorption coefficient decreases to around ~6.7 cm^{-1} and ~4.5 cm^{-1} for PBS-1-M and PBS3-M, respectively. Moreover, upon increasing the PBS-PFP concentration, a new band peaking at 380 nm appears, which is ascribed to the poly(fluorene) absorption [264]. For all samples, for wavelengths longer than 400 nm, absorption coefficient is very low (<0.1 cm^{-1}), providing transparency under daylight.

Upon excitation at 365 nm, PBS-PFP-di-ureasil monoliths reveal a structured emission band between 390-550 nm, Figure 6.3(c), which is characteristic of the vibronic relaxation of the poly(fluorene) excited singlet state [260]. However, the contribution of the intrinsic emission of the d-U_{600} [157] to the spectrum cannot be neglected as it also occurs in the same spectral region, Figure 6.3(c). Comparing the emission spectra of the samples processed as monoliths with those in films, Figure 6.3(d), whereas for the low-concentrated film (PBS4-F), they resemble those of the monoliths, the emission spectra of the more concentrated films (PBS5-F e PBS6-F) are shifted to the blue, revealing additional variations in the relative intensity of the vibronic progression components. In any case, as desirable for VLC, the blue emission of the PBS-PFP-di-ureasils overlaps that of the InGaN-based LED used to produce the commercial solid state lighting LEDs, whose white light results from the mixture of the

blue emission arising from high efficiency LEDs and yellow-emitting YAG:Ce phosphor [265].

The contribution of both the d-U_{600} and PBS-PFP excited states to the observed blue emission is also inferred from the excitation spectra monitored around 435 nm, Figure 6.3(e,f). The spectra are dominated by a band between 300-450 nm, assigned to overlapping contributions from PBS-PFP and the d-U_{600} host, and a weaker component around 275 nm. However, variations in the relative intensity and bandwidth of the peaks are observed as a function of the PBS-PFP wt%. As noted above for the more concentrated films, their excitation spectra differ from that of the monoliths and the low-concentrated film. These observations can be attributed to a combination of factors. Firstly, the processing methodology used can lead to distinct kinetic control of the sol-gel process, in particular differences in the gelation times (hours for the bulk and seconds for the films), which is known to modulate the degree of organization of the d-U_{600} host material [266–268]. Thus, the monolithic and film samples are both expected to provide a distinct host environment for the PBS-PFP chains. Secondly, while PBS-PFP is soluble in dilute solutions of mixed polar solvents (such as the THF/water mixture used to prepare the samples), it tends to form dispersions of supramolecular aggregates in pure water [269,270]. Thus, preferential evaporation of THF during the gelation and drying processing steps will gradually induce a local concentration gradient in the samples, leading to an increasingly more aqueous environment in which chain entanglements will be favoured. This process will occur more rapidly for the films and for samples with a higher PBS-PFP wt%, although electrostatic/polar interactions with di-ureasil and other siliceous hosts have been shown to control the extent of aggregation of conjugated polymers at the organic-inorganic interface [260,271,272]. From Figure 6.3(e,f), at the lowest PBS-PFP concentration in both the film (PBS4-F) and monolith (PBS1-M) samples, the excitation and emission spectra are reminiscent of well-dissolved PBS-PFP chains, with some excitation of the PBS-PFP emission arising from energy transfer from the d-U_{600} host [155]. As the concentration is increased in the monoliths (e.g. PBS3-M), the excitation spectrum indicates an increase in the electronic interaction between the host-guest species, while the band broadening and change in vibronic structure in the emission spectrum suggest increasing aggregation of the PBS-PFP chains. In the film samples, the effect of aggregation becomes even more apparent, with the red-shift in the emission band and change in the relative intensity of the vibronic peaks indicative of self-absorption (usually designated as inner-filter effect) [273].

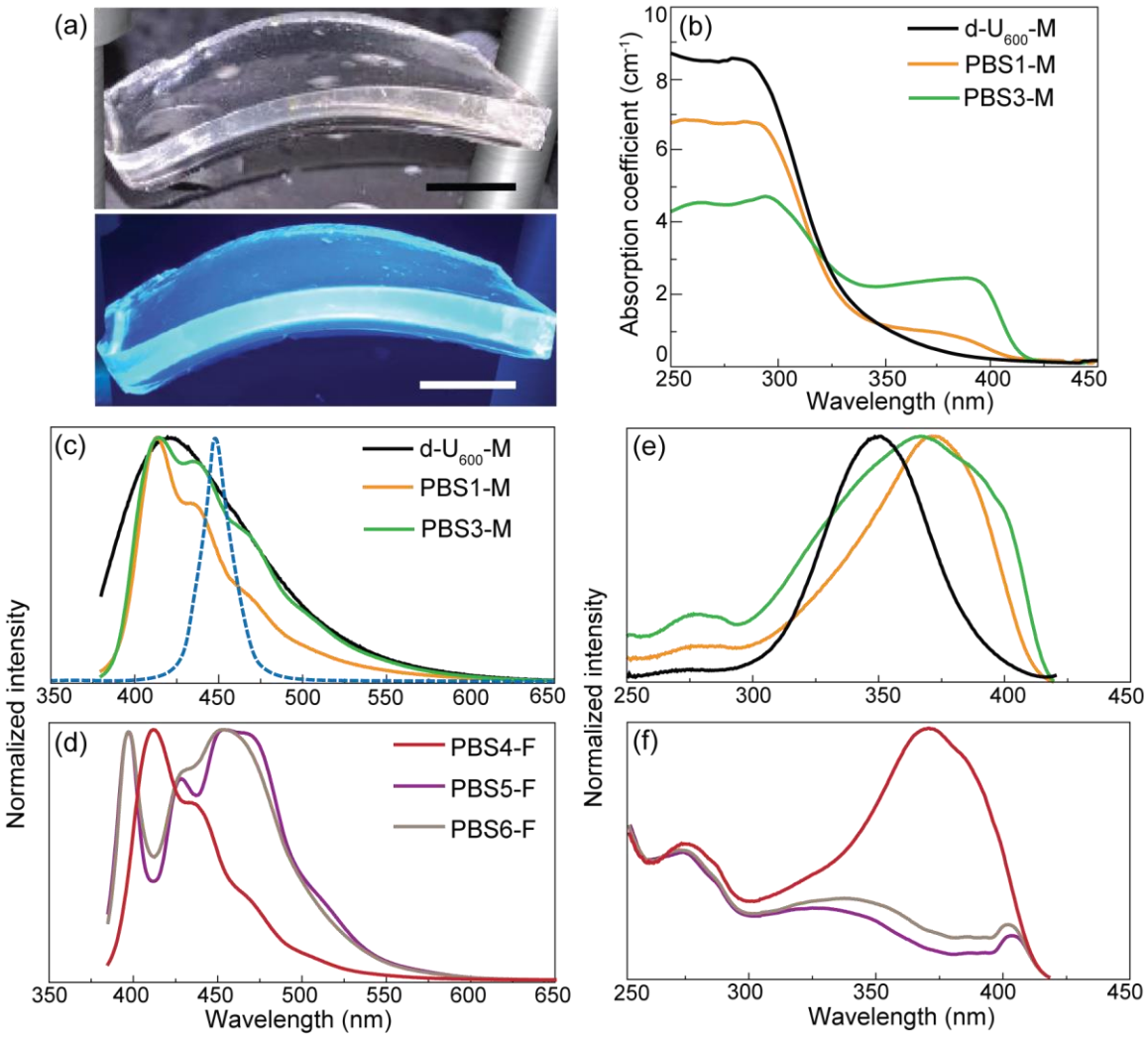

Figure 6.3 (**a**) Photographs of the flexible PBS3-M monolith taken under daylight (top) and UV radiation 365 nm (bottom). The scale bars represent 1 cm. (**b**) UV-Vis absorption coefficient spectral dependence for monoliths and the parent d-U_{600} host. (**c**,**d**) Emission spectra excited at 365 nm, and (**e**,**f**) the corresponding excitation spectra monitored at 435 nm for monoliths (M) and films (F). The dashed line represents the typical emission of the commercial InGaN-based LED used to produce the commercial solid state lighting LEDs [274]. The spectra of PBS2-M were omitted as it resembles that of PBS1-M.

The emission quantum yield values obtained on excitation at 365 nm are shown in Table 6.1 and reveal a significant increase as a function of increasing PBS-PFP wt%, reaching 0.411±0.005, 0.493±0.005 and 0.759±0.008 for PBS1-M, PBS2-M and PBS3-M, respectively. Independently of the concentration, the films reveal lower quantum yield values in comparison with that found for the monoliths, despite the same trend of increase being observed with the PBP-PFP wt%, achieving a maximum value of $(0.110\pm0.001)\times10^{-2}$ for PBS6-F. The non-doped d-U_{600} monolith exhibits an emission quantum yield of 0.179±0.002, which is in good agreement with previously reported values [155]. The increase in quantum yield with the concentration reflects the significant contribution of the PBS-PFP to the

photoluminescence as the host reveals intrinsically lower values. This enhanced quantum yield in the blue spectral region renders it easier to excite the samples using commercial UV emitting LEDs, showing the potential of the material to be integrated with VLC as an optical amplifier.

Table 6.1 Sample composition and emission quantum yield values for PBS-di-ureasils. The weight percent of polymer incorporated was estimated from [PBS-PFP] and the resultant mass of the dry PBS-PFP-di-ureasil. M and F denote monolith and film samples, respectively.

Sample	wt% PBS-PFP	Thickness (mm)	Emission quantum yield*
d-U(600)-M	0	2.9±0.1	0.179
PBS1-M	1.2×10^{-3}	2.7±0.1	0.411
PBS2-M	1.3×10^{-3}	3.1±0.1	0.493
PBS3-M	1.2×10^{-2}	3.2±0.1	0.759
d-U(600)-F	0	0.8×10^{-3}	0.001
PBS4-F	2.5×10^{-2}	3.3×10^{-3}	0.004
PBS5-F	0.2	1.6×10^{-3}	0.010
PBS6-F	0.2	1.8×10^{-3}	0.011

* The error is estimated to be 10 % of the emission quantum yield value

In order to further characterize the optical features of these materials, the refractive index was monitored by spectroscopic ellipsometry, as described in Annex B.3. The theoretical model represented in Figure B.6(b) was used for the thin film samples, and the direct inversion technique was implemented for the monoliths. The measured ellipsometric parameters I_c and I_s, and the respective fit are represented in Figure 6.4.

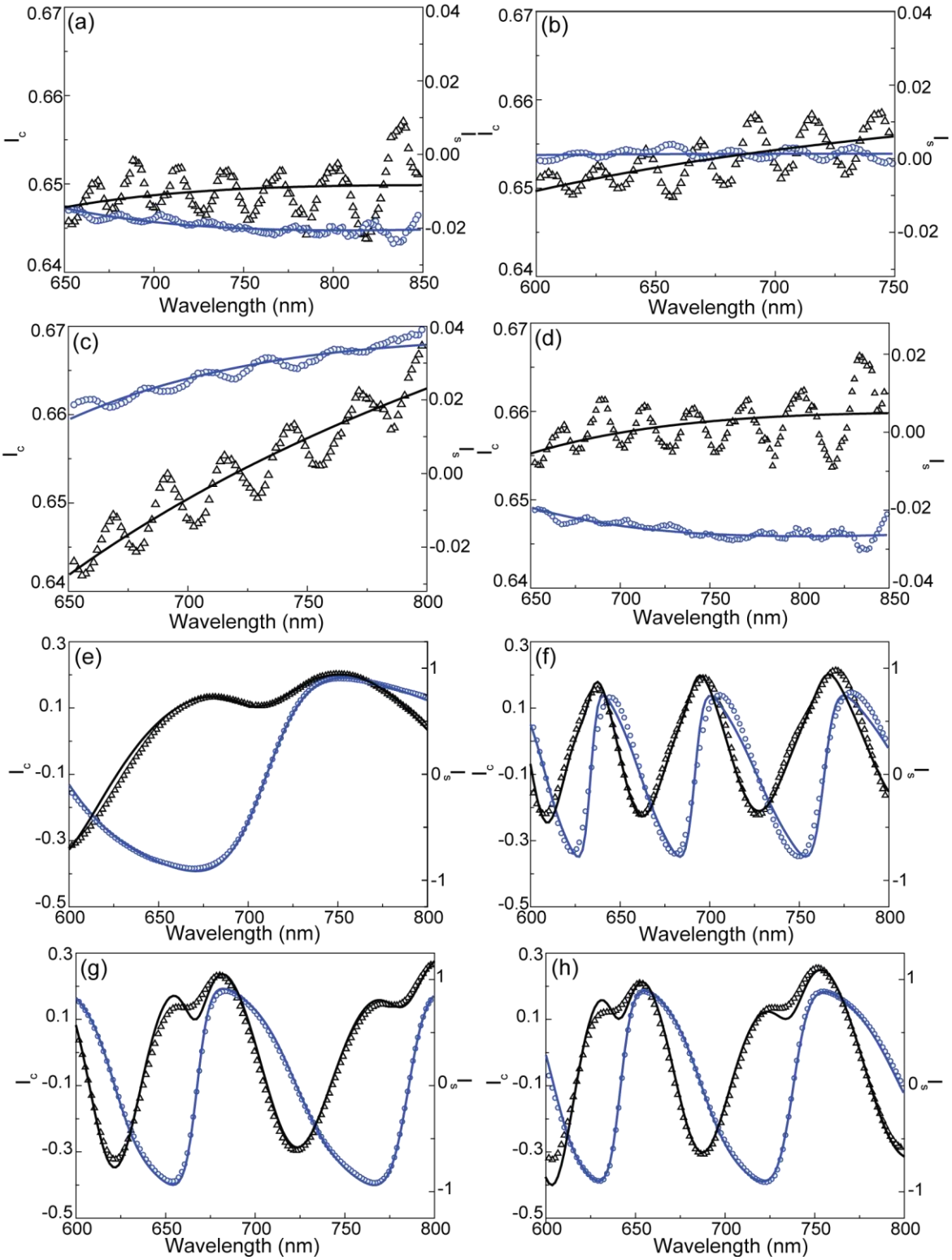

Figure 6.4 Ellipsometric parameters I_c (black triangles) and I_s (blue circles) measured for (**a**) d-U_{600}-M; (**b**) PBS1-M; (**c**) PBS2-M; (**d**) PBS3-M; (**e**) d-U_{600}-F; (**f**) PBS4-F; (**g**) PBS5-F; and (**h**) PBS6-F. The solid lines represent the data best fit (r^2>0.9).

The resulting dispersion curves are represented in Figure 6.5 and show that the refractive index increases with the PBS-PFP wt%, yielding a refractive index difference at 450 nm of +0.01 between PBS3-M and d-U_{600}, and +0.02 between PBS6-F and d-U_{600}. The refractive index increase upon addition of PBS-PFP is expected as conjugated polymers are known to have a refractive index value larger than 1.6 [275], which is a higher value than that of the non-doped d-U_{600} [86,276].

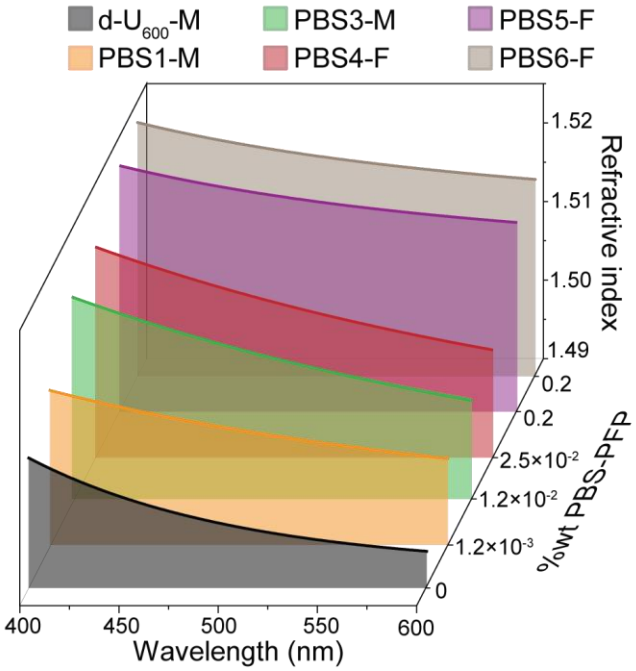

Figure 6.5 Optical properties of pristine PBS-PFP-di-ureasils. Dispersion curves for pristine monolithic and film samples. The curve of PBS2-M was omitted as it resembles that of PBS1-M.

One of the advantages of using the di-ureasil organic-inorganic hybrid as a host is the possibility to locally control the refractive index through UV exposure by direct writing with a UV pulsed *laser* (see Chapter 4). Taking this feature into account, the refractive index was studied as a function of the UV pulsed *laser* energy ($\mu J \cdot pulse^{-1}$) through ellipsometric measurements in the exposed regions. The measured ellipsometric parameters I_s and I_c, and the respective fit are represented in Figure 6.6-6.8.

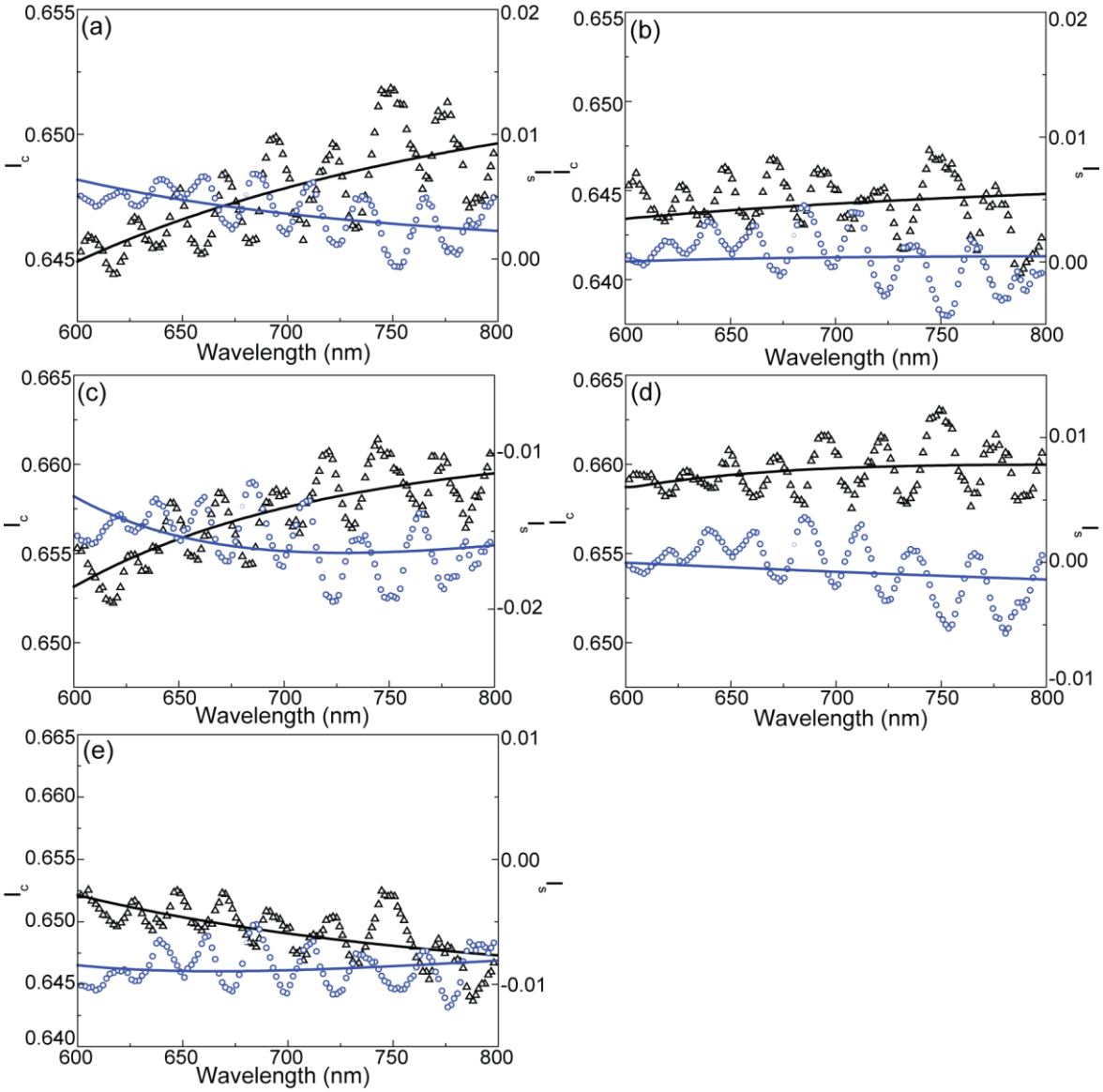

Figure 6.6 Ellipsometric parameters I_c (black triangles) and I_s (blue circles) measured in PBS1-M in the regions exposed to UV radiation with energy of (**a**) 30; (**b**) 60; (**c**) 80; (**d**) 100; (**e**) 120 μJ·pulse^{-1}. The solid lines represent the data best fit (r^2>0.9).

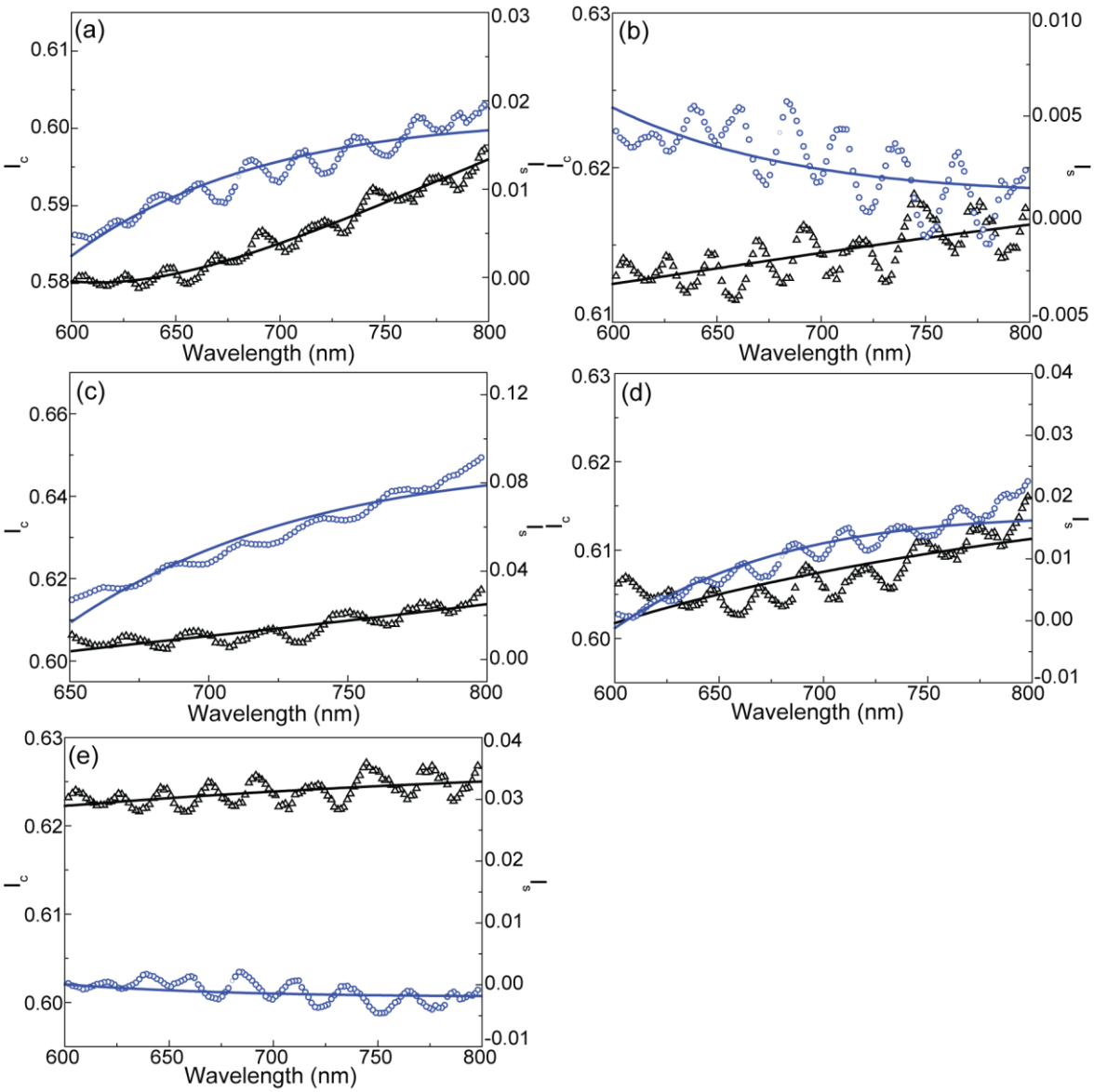

Figure 6.7 Ellipsometric parameters I_c (black triangles) and I_s (blue circles) measured in PBS2-M in the regions exposed to UV radiation with energy of (**a**) 30; (**b**) 60; (**c**) 80; (**d**) 100; (**e**) 120 μJ·pulse^{-1}. The solid lines represent the data best fit (r^2>0.9).

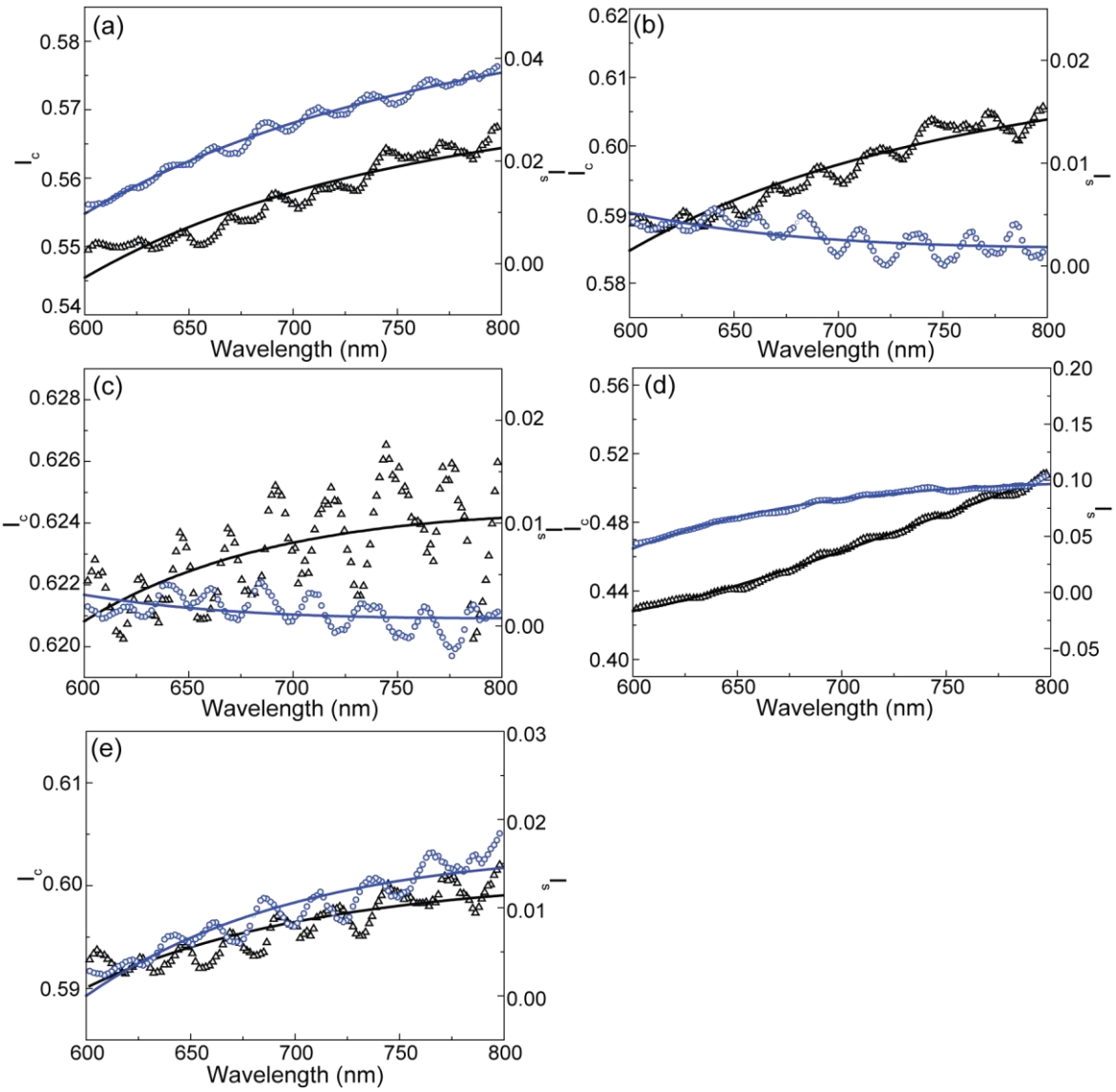

Figure 6.8 Ellipsometric parameters I_c (black triangles) and I_s (blue circles) measured in PBS3-M in the regions exposed to UV radiation with energy of (**a**) 30; (**b**) 60; (**c**) 80; (**d**) 100; (**e**) 120 μJ·pulse^{-1}. The solid lines represent the data best fit (r^2>0.9).

The dispersion curves measured in the exposed regions are represented in Figure 6.9, revealing a refractive index increase with the UV energy used in the exposition, indicating that the polymer addition did not affect the UV self-pattern properties of the di-ureasil host. A positive refractive index contrast between the exposed and non-exposed regions (Δn) was observed, yielding a maximum Δn of +0.09, at 450 nm, for an UV energy of ~120 μJ·pulse^{-1} in PBS3-M. The dispersion curves for the exposed regions in PBS1-M and PBS2-M also reveal a positive refractive index contrast, yielding a maximum value for Δn of +0.03 and +0.05 at 450 nm, respectively. Thus, the PBS-PFP-based di-ureasils refractive index can be is easily

tuned through chemical (PBS-PFP doping) and physical (UV exposure) parameters, in which the UV exposed region can be assumed to behave as channel waveguides.

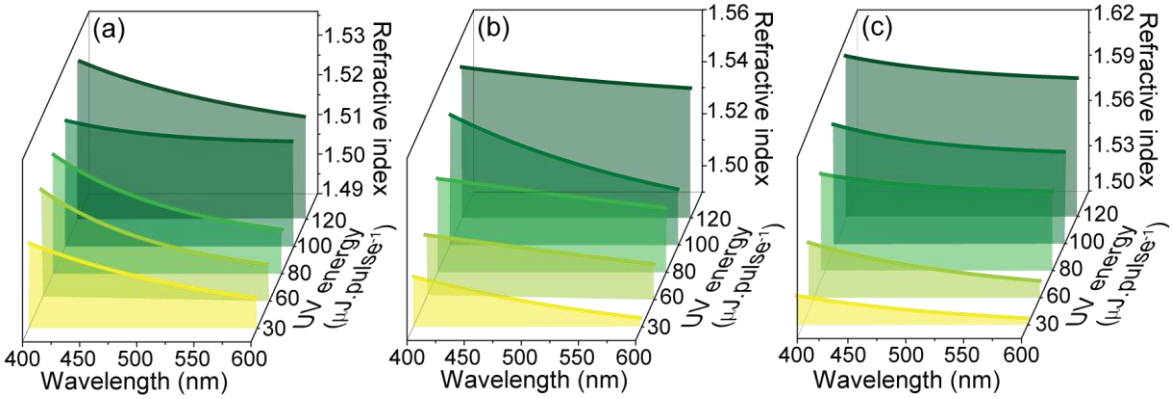

Figure 6.9 Optical properties of UV exposed PBS-PFP-di-ureasils. Dispersion curves for channel waveguides in (**a**) PBS1-M, (**b**) PBS2-M and (**c**) PBS3-M as function of the *laser* pulse energy used in the writing system (30-120 μJ·pulse^{-1}).

Then, using UV *laser* writing, channel waveguides were patterned on the surface of the monoliths, yielding a length around 2×10^{-2} m and a width of ~2.00×10^{-4} m. An optical microscope image of a channel waveguide written with 120 μJ·pulse^{-1} on the PBS3-M surface, under UV illumination is shown in Figure 6.10. Note that the monoliths, without UV exposure, behave as planar waveguides, where the propagation occurs without lateral confinement.

Figure 6.10 Optical microscope image taken under UV radiation (365 nm), showing the channel waveguide written with 120 μJ·pulse^{-1} on the PBS3-M surface.

Since the PBS-PFP-based di-ureasils materials have a high PLQY, and show a positive Δn, the optical gain was measured by applying the VSL technique in the planar and channel waveguides. The emission spectra were acquired for a stripe length range between 0.0 and 2.5×10^{-2} m, with a step of 5×10^{-4} m. Figure 6.11-14 show the ASE spectra for the planar and channel waveguides written on PBS1-M, PBS2-M, and PBS3-M, respectively.

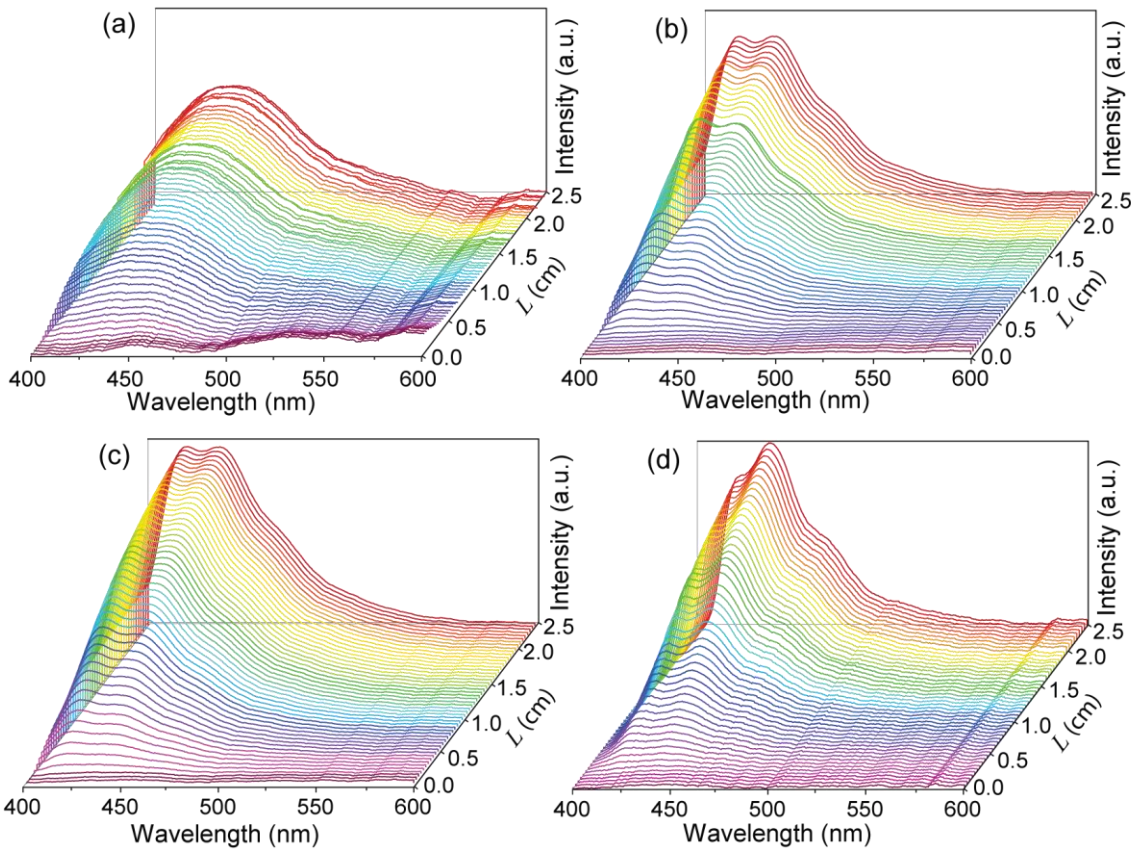

Figure 6.11 Emission spectra for different stripe lengths in the planar waveguide (**a**) d-U_{600}-M, (**b**) PBS1-M, (**c**) PBS2-M and (**d**) PBS3-M.

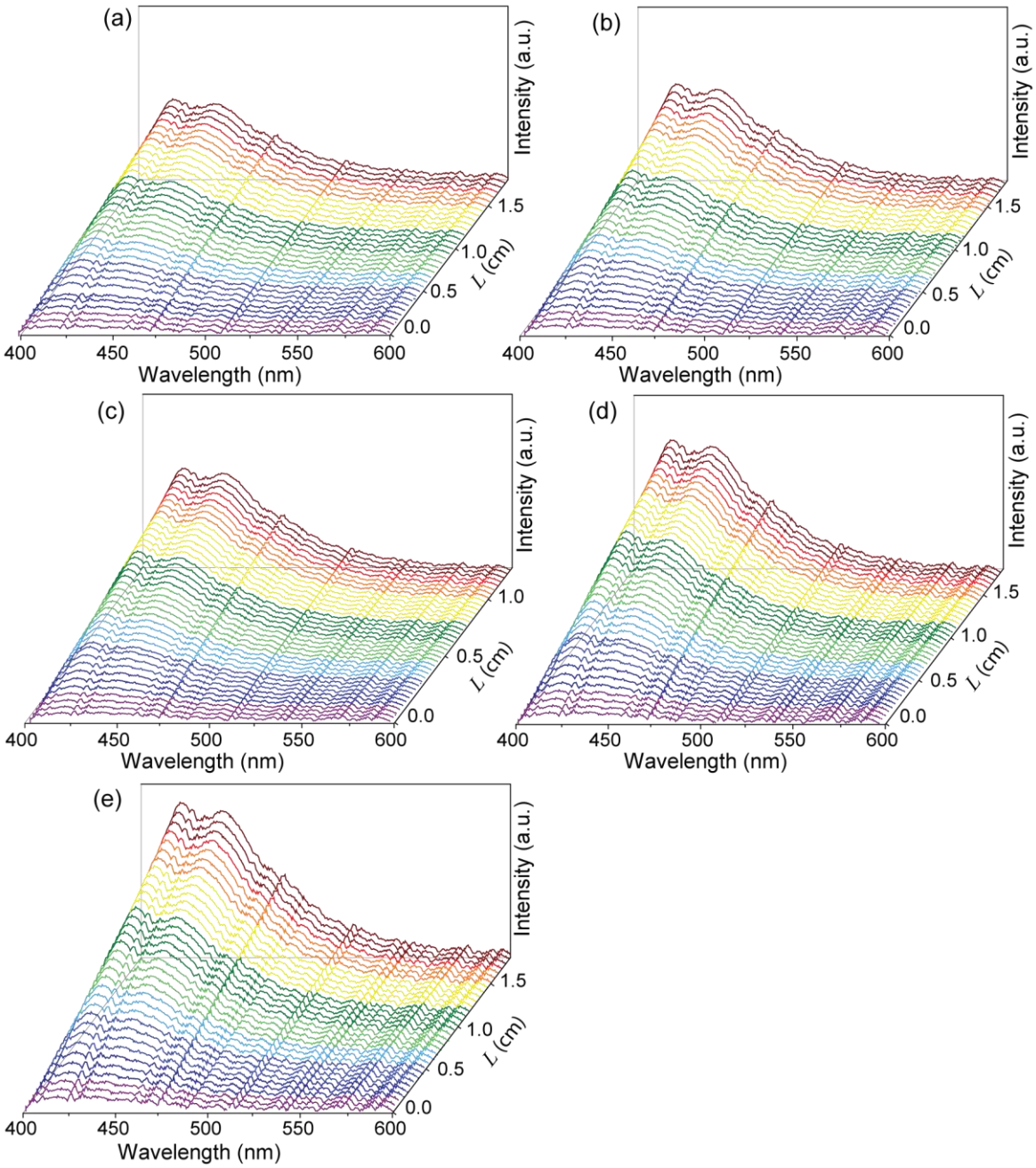

Figure 6.12 Emission spectra for different stripe lengths PBS1-M in the regions exposed to UV radiation with energy of (**a**) 30; (**b**) 60; (**c**) 80; (**d**) 100; (**e**) 120 μJ·pulse^{-1}.

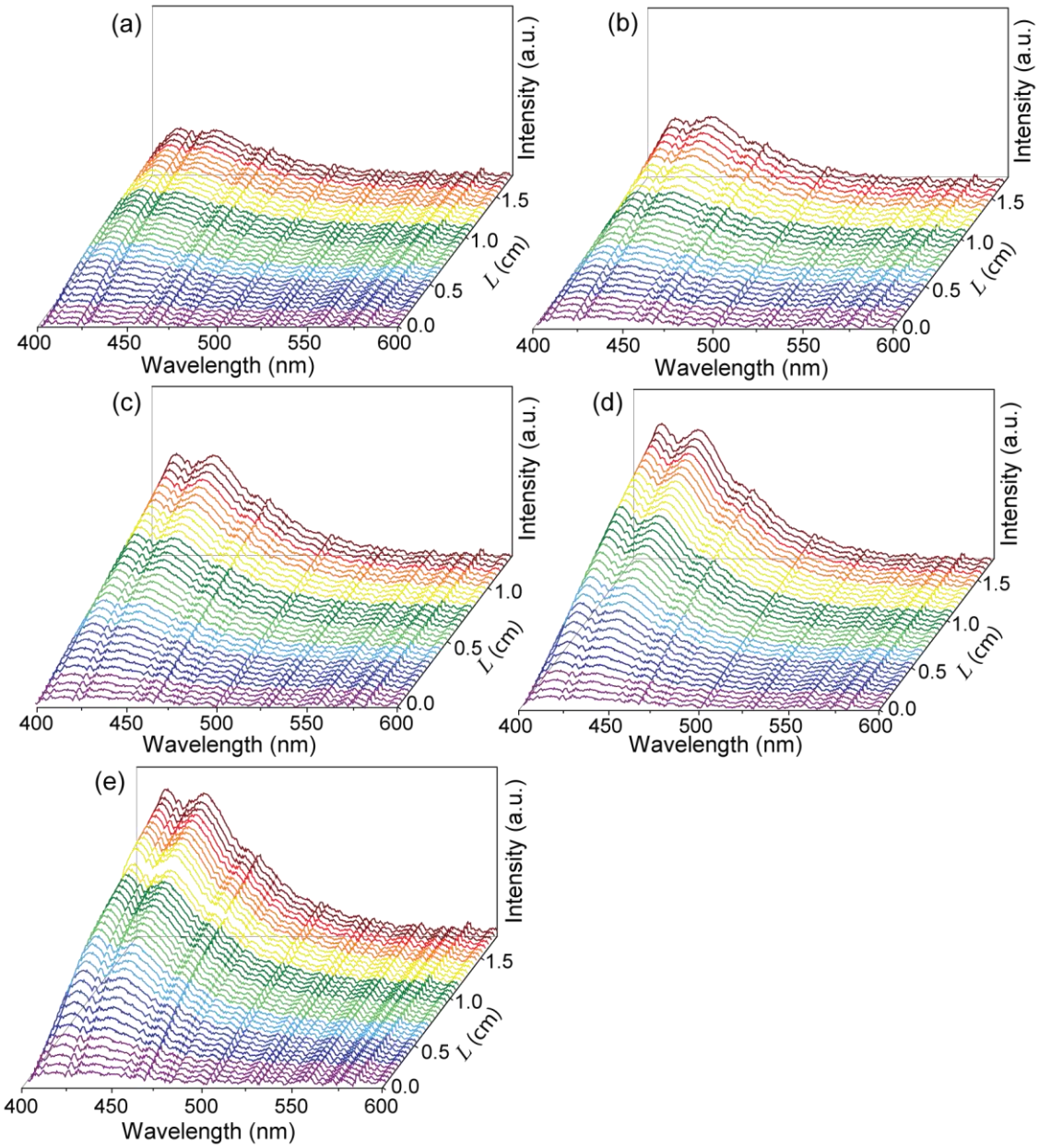

Figure 6.13 Emission spectra for different stripe lengths PBS2-M in the regions exposed to UV radiation with energy of (**a**) 30; (**b**) 60; (**c**) 80; (**d**) 100; (**e**) 120 μJ·pulse^{-1}.

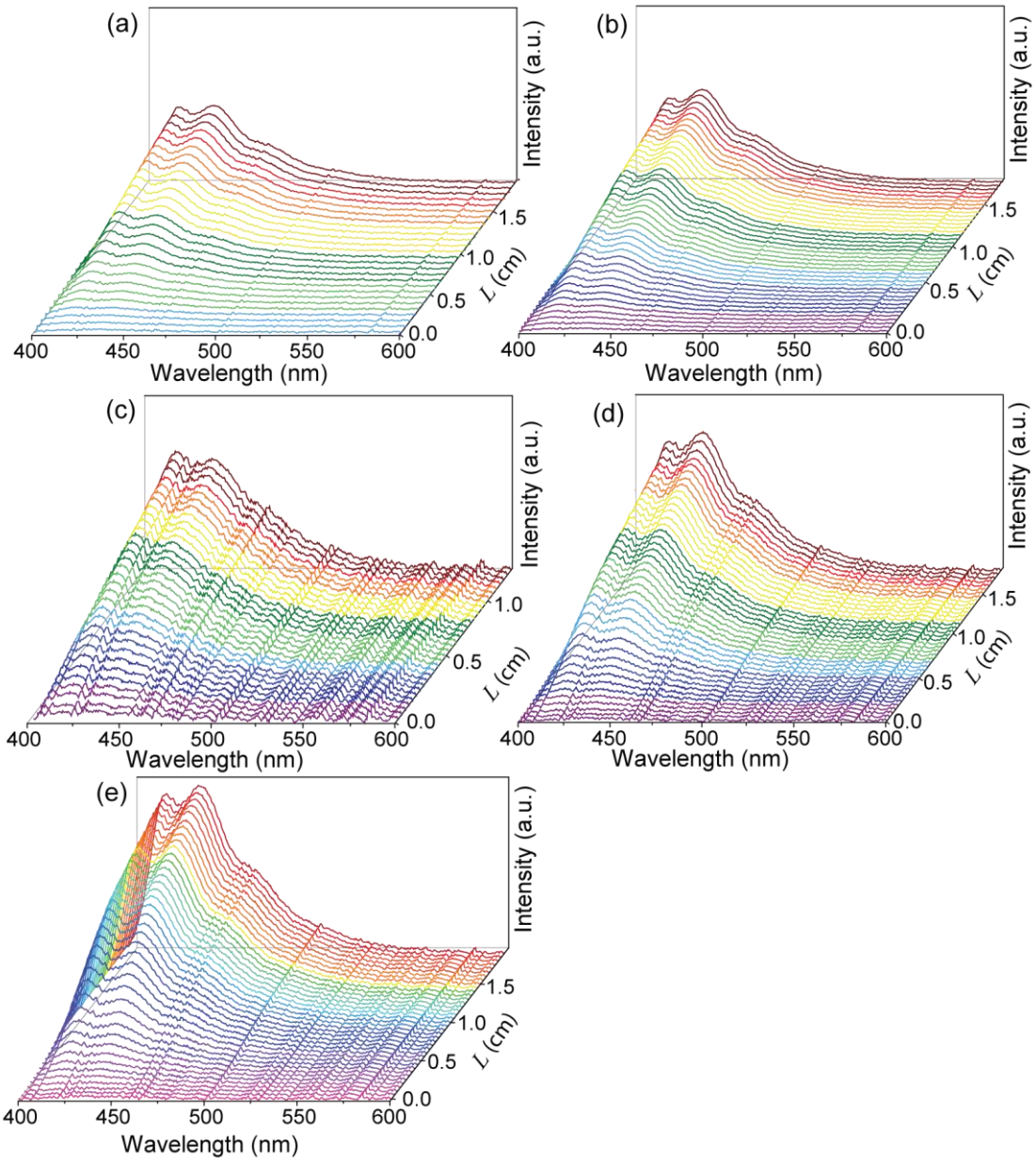

Figure 6.14 Emission spectra for different stripe lengths PBS3-M in the regions exposed to UV radiation with energy of (**a**) 30; (**b**) 60; (**c**) 80; (**d**) 100; (**e**) 120 μJ·pulse^{-1}.

Figure 6.15(a) shows the respective ASE integrated intensity versus the stripe length for the planar waveguides.

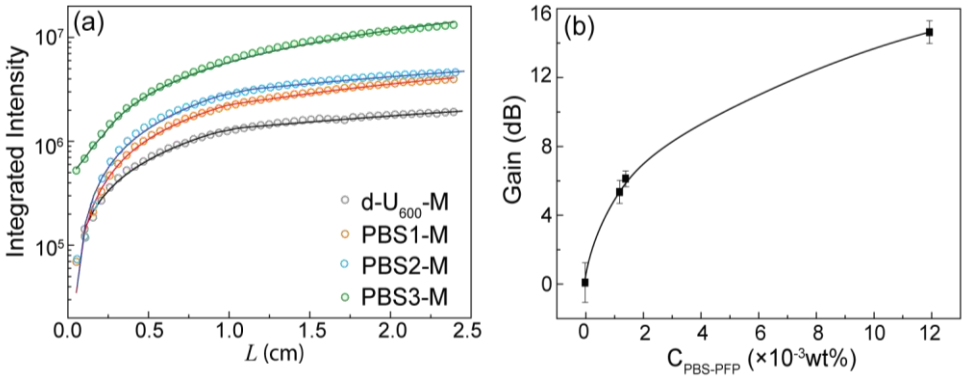

Figure 6.15 (**a**) Integrated ASE intensity as function of the stripe length for the planar waveguides. The lines are the data best fit (r^2>0.98). (**b**) Calculated optical gain coefficients as a function of PBS-PFP concentration ($C_{PBS\text{-}PFP}$, wt%) in the di-ureasil. The lines are visual guides.

An increase in the ASE emission with the excitation length is clearly observed. This behaviour can be described by a one dimensional optical amplifier rod, where the propagation equation for the ASE intensity, I_{ASE}, taking into account the gain saturation, can be written as [263]:

$$\frac{dI_{ASE}}{dz} = \frac{G.I_{ASE}}{1+\dfrac{I_{ASE}(z)}{I_{sat}}} + \left(A_{sp} \frac{N_0^*}{1+\dfrac{I_{ASE}(z)}{I_{sat}}} \times E_p \right) \times [\Omega / 4\pi]. \qquad (6.1)$$

where G is the optical gain coefficient, I_{sat} is the signal saturation intensity, A_{sp} is the spontaneous emission rate, N_0^* is the excited state population density and E_p is the energy of the emitted photon [263]. Ω is the solid angle defined by the output side of the amplifier and the slit on the sample surface, Figure 6.1, and for simplicity it is set to be constant [263]. The integration of Equation (6.1) leads to Equation (6.2), from which it is possible to extract the optical gain coefficient by the fitting to the experimental data.

$$I_{ASE} = \frac{\left(g_0 I_{sat} - J_{sp}\right)}{G} W\left(\frac{e^{g_0 z}}{GI_{sat} - J_{sp}} \left(J_{sp}\, e^{\frac{J_{sp}}{GI_{sat}-J_{sp}}} \right)^{1-\frac{J_{sp}}{GI_{sat}-J_{sp}}} \right) - \frac{J_{sp}}{G}. \qquad (6.2)$$

where $J_{sp} = \left(\dfrac{A_{sp} E_p \Omega N^*}{4\pi} \right)$ is the density of the spontaneous emission and W is the Lambert function. The gain values obtained for the planar waveguides based on the monoliths are represented in Figure 6.15(b), which show an increase of the optical gain values by increasing the polymer concentration in the di-ureasil. The maximum optical gain obtained was

15.0±0.2 dB for PBS3-M. Since, PBS1-M and PBS2-M have similar PBS-PFP concentration, the gain values are also similar, 5.5±0.2 dB and 6.1±0.2 dB, respectively.

Using the same approach, the optical gain coefficient was also calculated for the channel waveguides. Figure 6.16 shows the respective ASE integrated intensity versus the stripe length for the channel waveguides written on PBS1-M, PBS2-M, and PBS3-M.

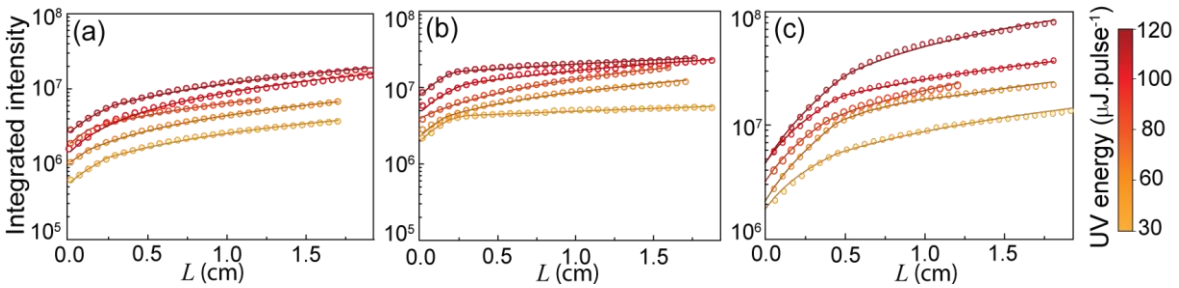

Figure 6.16 Integrated ASE intensity as function of the stripe length for the channel waveguides written on (**a**) PBS1-M, (**b**) PBS2-M, and (**c**) PBS3-M. The lines are the data best fit (r^2>0.98).

Figure 6.17 shows the optical gain values obtained for the channel waveguides, which reveals an increase in gain with the increase of Δn. The maximum gain obtained was ~34.0±0.2 dB for the channel with Δn=0.09 in PBS3-M. The gain increase in the channel waveguide samples results from the confinement of the radiation, and therefore by the increase of the population inversion. Concluding, similarly to the refractive index, the optical gain can also be defined through chemical (PBS-PFP doping) and physical (UV exposure) parameters.

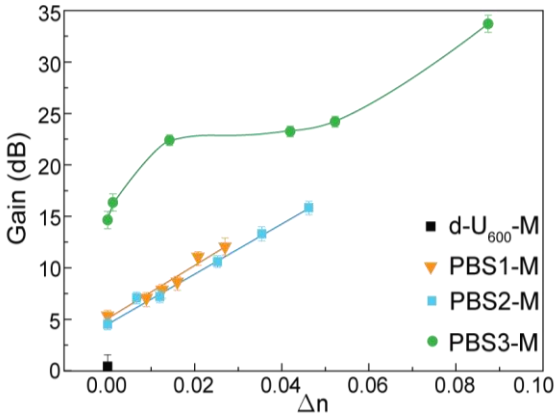

Figure 6.17 Optical gain coefficients as a function of refractive index contrast at 450 nm between the channel and planar waveguides regions. The lines are visual guides.

Furthermore, to assess the optical propagation and net gain in the channel waveguide, a probe optical signal (450 nm) was coupled to the channel input. Signal propagation through the waveguide was attained, and an optical fibre was aligned to the channel output extremity in order to measure the output emission spectra, using a spectrometer. Figure 6.18 shows the

spectra obtained at the output of the channel waveguides. The spectra were taken, independently, without pump excitation, and with UV excitation through an external perpendicular pump source placed above the channel waveguide, and a UV pump co-propagating with the probe optical signal. From the spectra, an intensity improvement was observed, when the waveguide was excited, especially for external perpendicular pumping.

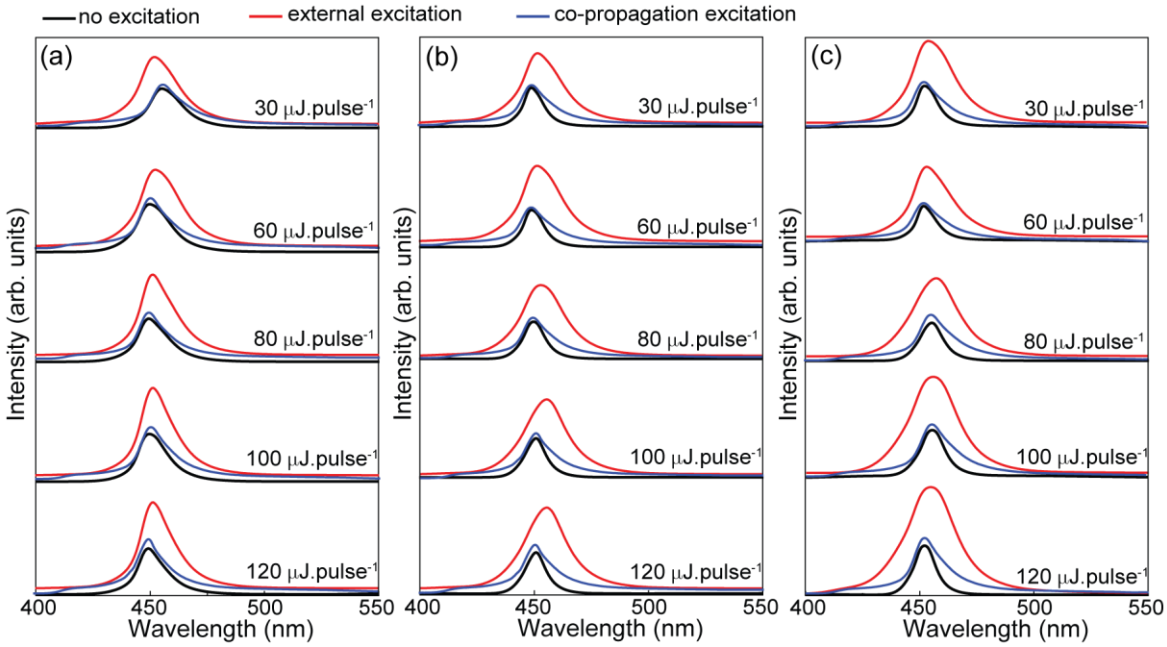

Figure 6.18 Spectra at the channel waveguides output written on the surface of (**a**) PBS1-M, (**b**) PBS2-M and (**c**) PBS3-M for external excitation (red line) and co-propagation excitation (blue line).

To further evaluate the channel waveguides, the net optical gain (in dB) was calculated. The probe optical signal was modulated in intensity with a square waveform (50 % duty cycle) at 200 Hz using a mechanical chopper. The output signal was detected by a photodiode connected to an oscilloscope. The signals transmitted in the channel waveguides are represented in Figure 6.19 without pumping, and with external perpendicular pumping and with co-propagation pumping. Again, an improvement in the intensity is observed when the waveguide is exposed to UV radiation, mainly when the excitation is external.

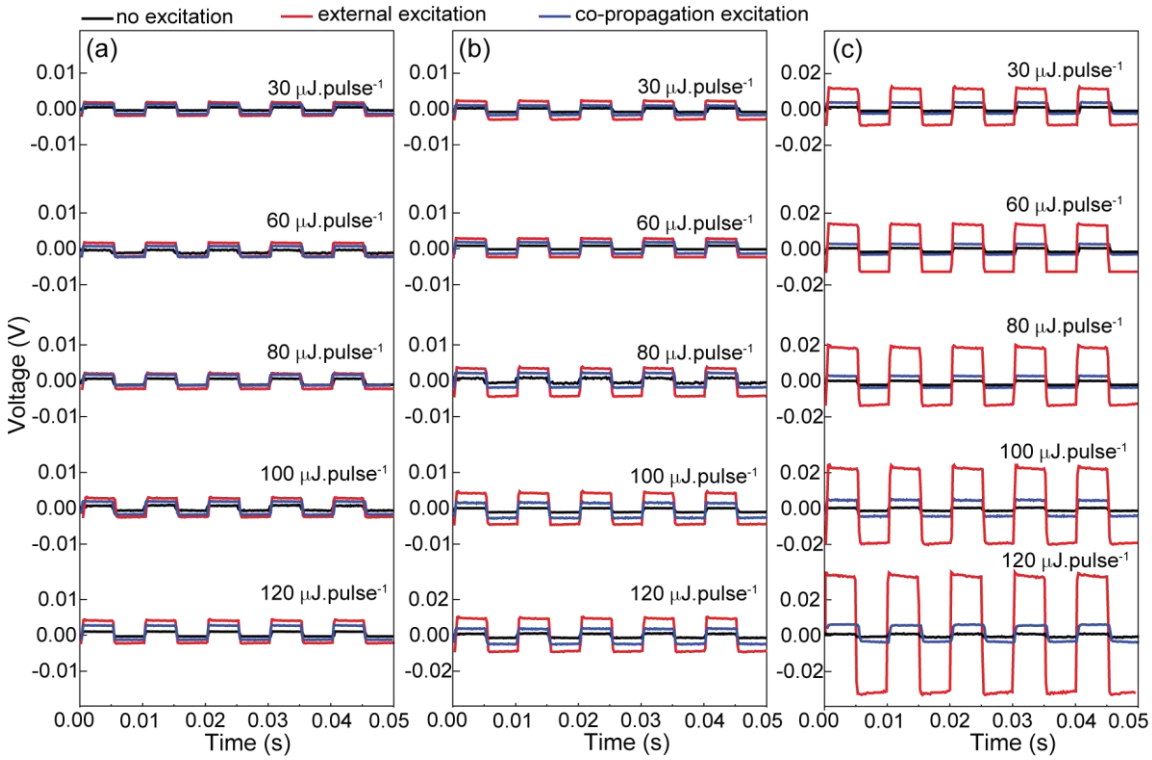

Figure 6.19 Optical signal at the channel waveguides output written on the surface of (**a**) PBS1-M, (**b**) PBS2-M, and (**c**) PBS3-M. The photodiode operates with an output capacitor, removing the DC component. External excitation (red line) and co-propagation excitation (blue line).

The net gain values were estimated from the ratio between the peak-to-peak voltages of the received signal with and without pumping, and are represented in Figure 6.20. Using the two pumping approaches, the maximum gain observed was in the waveguide with the higher refractive index contrast (Δn=0.09), yielding values of ~32 dB and ~16 dB, with external and with co-propagation pumping, respectively.

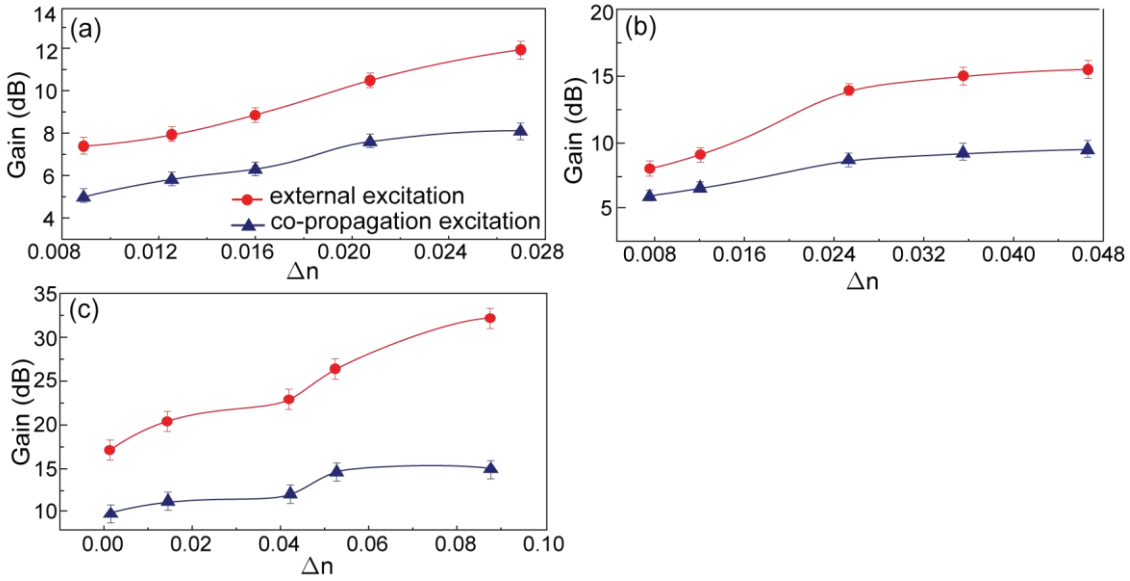

Figure 6.20 Net gain for each channel waveguide, for external excitation and co-propagation excitation. The lines are visual guides.

The gain efficiency ($\eta_G = \frac{G}{Pump}$) was calculated, in which ***Pump*** indicates either the pump signal energy density (η_G, $\mu J \cdot cm^{-2}$) or power density (η'_G, $kW \cdot cm^{-2}$), to enable a comparison with previous studies reported in the literature. In this work, the highest gain efficiency values, calculated through the energy density, were 0.73 ± 0.01 $cm \cdot \mu J^{-1}$ and 1.62 ± 0.02 $cm \cdot \mu J^{-1}$ for planar (PBS3-M) and channel waveguides (Δn=0.09 in PBS3-M), respectively. Larger values were only achieved for pure polydioctylfluorene (PFO) [277], which has a higher processing cost than the proposed PBS-PFP-di-ureasil hybrid. Comparing to other hybrid materials, the gain efficiency values obtained are among the best ones reported in the literature (Table 6.2). The gain efficiency was calculated from the power density, yielding values of 14.6 ± 0.2 $cm \cdot kW^{-1}$ and 32.5 ± 0.3 $cm \cdot kW^{-1}$ for the aforementioned planar and channel waveguides, respectively. Larger or similar values were only achieved previously for poly(9,9-dioctylfluorene-co-9,9-di(4-methoxy)phenylfluorene (F8DP) [278]. Nonetheless, the obtained values are among the best values reported in the literature for pure polymers (Table 6.2). As, the gain efficiency values are comparable to those previously reported for both pure conjugated polymers and hybrid materials, PBS-PFP-di-ureasils are a promising cost-effective solution for optical amplification in white light-emitting diodes for VLC.

Table 6.2 Excitation/emission wavelengths ($\lambda_{exc}/\lambda_{em}$), pump energy, pump power density, optical gain (G), and respective gain efficiency (η_G and η'_G) of selected polymer-based materials and organic-inorganic hybrids.

	Material	$\lambda_{exc}/\lambda_{em}$ (nm)	Pump		G (cm^{-1})	Gain efficiency		Ref
			energy ($\mu J \cdot cm^{-2}$)	power density ($kW \cdot cm^{-2}$)		η_G ($cm \cdot \mu J^{-1}$)	η'_G ($cm \cdot kW^{-1}$)	
Planar	d-U(600)/ PBS-PFP	365/450	4.8±0.5	0.24±0.02	3.5±0.1	0.73±0.01	14.6±0.2	this work
	PM 650-PMMA	532/620	-	23×10^3	12	-	5.2×10^{-4}	[279]
	fvin	532/640	413	-	50	0.12	-	[280]
	DCM-PMMA				40	0.10		[280]
	Coumarin-495	-/534	-	7×10^3	3.5	-	5.0×10^{-4}	[281]
	F8DP	355/452		0.6	66		110	[278]
	F8BT	440/576		2.8	22		7.8	
	Dow Red F	440/685			24		8.6	
	m-LPPP	490/-		22	50		2.3	[282]
	BuEH-PPV	435/562		1.2	18		15	[283]
				2.2	41		18.6	
				4.1	62		15.1	
	PFO	-/466	9	-	74	8.2	-	[277]
			1.3		10	7.7		
Channel	d-U(600)/ PBS-PFP	365/450	4.8±0.5	0.24±0.02	7.8±0.1	1.62±0.02	32.5±0.3	this work

PM 650-PMMA: pyrromethene 650 in poly-methyl methacrylate;
fvin: (4-di(4'-tert-butylbiphenyl-4-yl)amino-4'-dicyanovinylbenzene;
DCM: 4-dicyanomethylene-2-methyl-6-p-dimethylamino-styryl-4H-pyran;
F8BT: poly(9,9-dioctylfluorene-co-benzo-thiadiazole); m-LPPP: methyl-substituted conjugated laddertype poly(paraphenylene); BuEH-PPV: poly[2-butyl-5-(2'-ethyl-hexyl)-1,4-phenylenevinylene].

6.4 CONCLUSIONS

Planar and channel waveguides based on PBS-PFP doped within di-ureasil organic-inorganic hybrids were fabricated and optically characterized with the view of their potential application as optical amplifiers for VLC based on white LEDs. The incorporation of PBS-PFP into the hybrid host led to an enhanced emission in the blue spectral region (peaking around 390-550 nm), which overlaps with that of commercial solid-state lighting LEDs used for VLC. Moreover, the high absolute emission quantum yield values (~0.8) facilitate easy excitation of the waveguide using a UV emitting LED. The refractive index of the PBS-PFP-based di-ureasils can be facilely tuned through chemical (PBS-PFP doping) and physical (UV exposure) means. Spectroscopic ellipsometry demonstrated a maximum

refractive index variation of +0.02 upon doping with PBS-PFP, and +0.09 following UV exposure. This characteristic was exploited to pattern channel waveguides on the surface of PBS-PFP-di-ureasil monoliths using direct UV *laser* writing, and radiation confinement was attained.

The optical gain coefficient was measured using the VSL method, showing an increase in optical gain (4.7-15.0±0.2 dB) with the PBS-PFP concentration (1.2-12×10^{-3} wt%), and (15.0-34.0±0.2 dB) with the UV energy used to produce the channel waveguides (0-120 μJ·$pulse^{-1}$). To further evaluate the channel waveguides, the net gain was measured, using an optical signal peaking at 450 nm coupled in the input, transmitting bits when the waveguide was excited above the channel and in cross-section. An intensity improvement was observed when the waveguides were exposed to UV radiation. The maximum gain efficiency value observed in planar waveguides was 0.73±0.01 cm·μJ^{-1} (14.6±0.2 cm·kW^{-1}), which corresponds to the sample with highest PBS concentration (PBS3-M). In the channel waveguides, the highest gain efficiency obtained was 1.62±0.02 cm·μJ^{-1} (32.5±0.3 cm·kW^{-1}) for the channel with Δn=0.09 in PBS3-M when it was excited above the channel. These values are among the best known for conjugated polymers and hybrid materials. Larger values were only achieved for pure PFO, which has a higher processing cost than the hybrid material, showing the potential of the proposed material to be implemented as a cost-effective optical amplifier for VLC.

CHAPTER 7

LAB-ON-A-CHIP: BIOSENSOR

The development of portable low-cost PICs-based biosensors for lab-on-a-chip devices for real-time diagnosis is of great interest. In this chapter, it is presented the principle of operation and characterization of an optical biosensor based on a MZI to monitor the growing concentration of bacteria in a liquid medium. The device pattern was imprinted on transparent self-patternable organic-inorganic d-U_{600}Z40 hybrid films deposited in a silicon wafer substrate by direct UV *laser* writing, as described in Annex C. The sensor performance was evaluated using *Escherichia coli* (*E. coli*) cell growth in an aqueous medium, as an illustrative example. The measured sensitivity (2×10^{-4} RIU) and limit of detection (LOD=2.0 pg·mm^{-3}) are among the best values known for low refractive index contrast sensors. Therefore, the proposed biosensor constitutes a direct, compact, fast, and cost-effective solution for monitoring the concentration of lived-cells. These results led to the publication of one scientific contribution: A. R. N. Bastos, *et. al*, Sensors **18**, 840, 2018 [doi: 10.3390/s18030840].

7.1 INTRODUCTION

Due to the importance of highly sensitive biosensors, the production of precise and powerful analytical tools using biological sensing element is of great interest. Bacterial biosensors based on PICs have already been demonstrated [284–289], and among these, waveguide interferometer biosensors are advantageous combinations of evanescent field and optical phase difference measurement methods [57]. In this case, the exposure of the analyte in the waveguide affects its guiding properties (refractive index) [61]. The variation of the refractive index can be correlated with the concentration of the analyte and with the affinity constant of the interaction, resulting in a quantitative value of the interaction [61].

In this dissertation, the bacterial specimens' concentration in a fluid was monitor. In the field of pathogen detection, the most reported bacterial detection is made for *Legionella*, *Listeria*, *Salmonella*, *E. coli*, and *Campylobacter* [290]. *E. coli* naturally occurs in the intestinal tract of humans and warm-blooded animals, and consists of a diverse group of bacteria. Most *E. coli* strains are innocuous and are an actual integral and important part of a healthy intestinal tract. Nonetheless, some are pathogenic, and consequently, may cause disease, including severe diarrhea [291]. Featuring the development of low-cost and miniaturized biosensors with improved sensitivity and stability, a cost-effective and real-time biosensing technology based on a MZI structure was produced to monitor the concentration of *E. coli* cells in a liquid medium.

7.2 EXPERIMENTAL DETAILS

7.2.1 FABRICATION

The biosensor structure is analogous to the one used in the EO-MZI device (Figure 5.12), and it was patterned on the surface of a d-U_{600}Z40 film, Figure 7.1(a), as described in Annex C. After the patterning process, the silicon wafer substrate was cleaved to allow fibre butt coupling to the device, Figure 7.1(b). In order to establish a liquid container in one arm of the MZI, a mask of acrylate was used to establish a liquid container. The container aperture has a 5 mm length (L_{MZI}), thickness of ~62.5 μm, and width of 125 μm, and was produced by *laser* ablation of the acrylate mask in a glass substrate using an UV *laser*, operating at 300 Hz, with a pulse energy of 1.6 mJ·pulse^{-1} and translation velocity of 0.1×10^{-3} m·s^{-1}. After *laser* ablation, the container was removed from the glass substrate, aligned, and fixed into the optical chip, Figure 7.1(c).

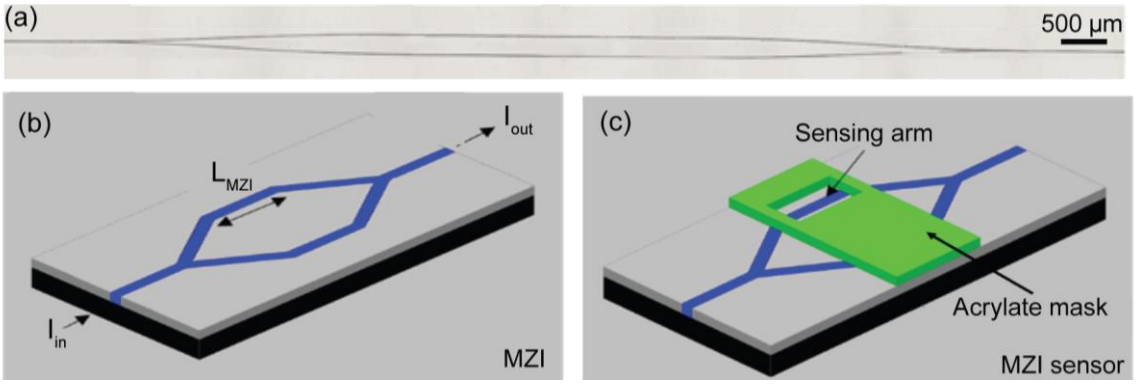

Figure 7.1 (**a**) Optical image showing the MZI structure patterned on the surface of the di-ureasil film. (**b-c**) Scheme of the bare biosensor, before and after the liquid container, respectively.

7.2.2 *E. COLI* CELL CULTURE AND REFRACTIVE INDEX MEASUREMENTS

Escherichia coli (ATCC 25922) was cultured aerobically in a *lysogeny* broth (LB) at 37 °C. After preparation, the growth medium was autoclaved at 121 °C for 20 min for sterilization. Subsequently, stationary suspensions of *E. coli* were prepared in a laminar air flow chamber. Proliferation was assessed spectrophotometrically by reading the media's optical density at 550 nm [292]. The *E. Coli* culture was conducted in collaboration with Doctor Nuno Silva, Principal Researcher at Physics Department and CICECO-Institute of Materials Aveiro from University of Aveiro, Doctor Marta Tacão, Post-Doctoral Research Fellow at Biology Department and CESAM from University of Aveiro, and Doctor João da Costa, Post-Doctoral Research Fellow at Chemistry Department and CESAM from University of Aveiro.

The refractive index measurements for all liquid media were carried out at 25 °C on an Abbe refractometer (Anton Paar, Abbemat 200) at a wavelength of 589 nm. A drop of *E. coli* suspension (0.2 mL) was placed on the refractometer and the measurements took place until complete evaporation was achieved.

7.2.3 OPTICAL CHARACTERIZATION

The scheme of the experimental set-up used to optically characterize the MZI optical sensor is displayed in Figure 7.2. The optical characterization intends to obtain the MZI sensor features and relates them to the refractive index of the *E. coli* solution. The optical signal source was a *laser* (Agere Systems, SL980S33C) peaking at 980 nm. The polarization selection was achieved through a polarization controller and a polarization beam splitter connected to the MZI sensor with a pigtailed single-mode polarization maintaining optical fibre (Thorlabs, P1-630PM-FC-1). The optical signal was injected by aligning the fibre on a fibre rotator (Thorlabs, HFR007) with a three-dimensional positioning system (Thorlabs, Nanomax-TS). The optical signal at the MZI sensor output was recovered with an identical process and the output optical signal was measured with an optical power meter (Noyes, OFM OPM4) with a resolution of 0.05 dB. Data acquisition was done with a sampling time of 0.5 s, beginning with the drop-dispensing process of the fluid containing LB medium and *E. coli* cells on the sensing arm. The transmission spectra of the MZI was also acquired with an optical spectrum analyser (OSA-EXFO, FTB-500), using an incident signal from an ASE source (Fitel). All optical measurements were independently performed 10 times to monitor the growth process for *E. coli* bacteria and guarantee the experimental repeatability.

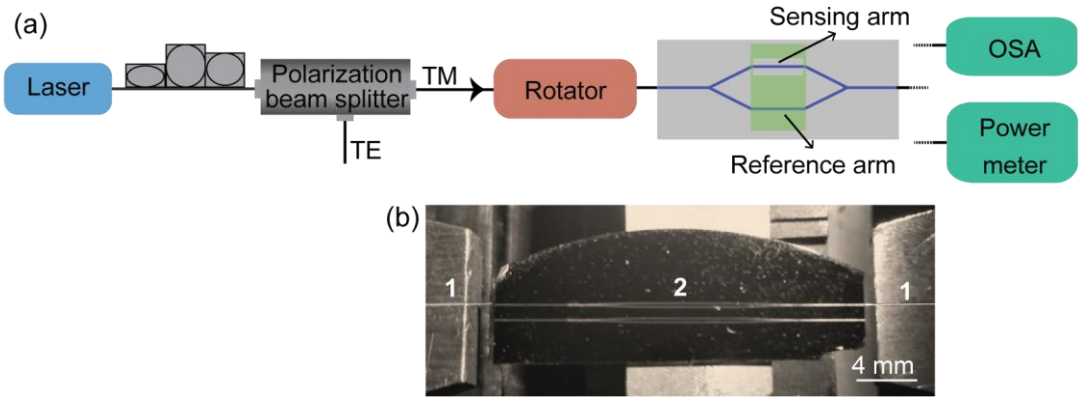

Figure 7.2 (**a**) Experimental set-up used for the optical measurements. (**b**) Photography of the alignment system used for the optical measurements of a MZI, where 1 are the optical fibres and 2 is the MZI patterned on the surface of a di-ureasil film.

7.3 PRINCIPLE OF OPERATION

As mentioned in Section 2.3.1 the optical losses (α) in the MZI is given by Equation (7.1)

$$\alpha(dB) = 10 \times \log_{10}\left(\frac{I_{out}}{I_{in}}\right) = 10 \times \log_{10}\left[\frac{1}{2}\left(1+\cos\left(\frac{2\pi.\Delta n_{RS}.L_{MZI}}{\lambda}\right)\right)\right] \quad (7.1)$$

where λ is the wavelength, L_{MZI} is the propagation length, and Δn_{RS} is the difference between the effective refractive index of the reference arm (n_R) and that of the sensing arm (n_S) [61]. The n_R value is constant since the waveguide medium will not change, including the superstrate, an acrylate mask with a refractive index of $1.4740 \pm (5 \times 10^{-4})$. The n_S values will show a temporal dependence because the superstrate of the sensor arm will be the fluid formed by the LB medium and *E. coli* cells, whose concentration will increase over time. Therefore, n_S will depend on the refractive index of the fluid (n_F). To estimate Δn_{RS}, for TE and TM polarizations, the embedded waveguide (three-dimensional) was modelled as an asymmetric slab waveguide (two-dimensional). This approximation is valid since the channel was patterned by UV direct *laser* writing, which induces a low refractive index increase ($\sim 10^{-3}$) [183] in the UV exposed region (channel region) compared with the non-exposed one. The waveguide propagation equation [121] was solved with an analytic method [293] for the interval $1.000 \leq n_F \leq 1.500$, Figure 7.3(a). Based on these results, α was calculated as a function of n_F using Equation (7.1), for TE and TM polarizations, Figure 7.3(b). Whereas the α values are almost constant for TE polarization, for TM polarization α reveals an asymptotic decay (~40 dB, when $n_F \approx 1.380$), ascribed to the increase of the evanescent field on the interface film/superstrate [294]. The MZI output is governed by a sinusoidal function,

revealing an asymptotic response when the cosine argument tends to $\pi+2k\pi$ (with k=0, 1, 2, …). Applying Equation (7.1), n_F was estimated for α values in TM polarization through:

$$n_F = -t \times \ln\left(\frac{\lambda}{2\pi L_{MZI} A} \operatorname{acos}\left(2\times 10^{\alpha/10} - 1\right) - y_0 \right). \tag{7.2}$$

where t, A, and y_0 are fit parameters of the exponential decay $\Delta n_{RS} = y_0 + A \times e^{n_F/t}$.

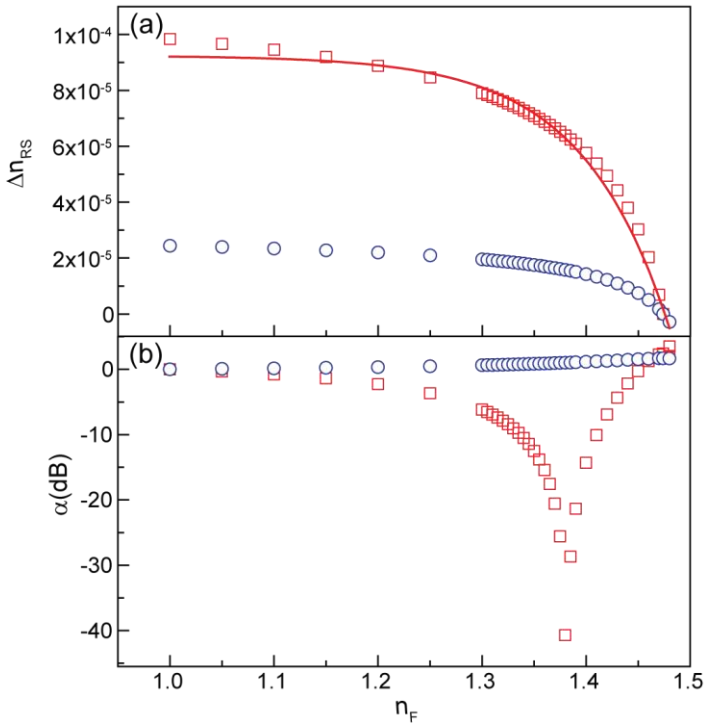

Figure 7.3 (**a**) Δn_{RS} and (**b**) α as a function of n_F for TE (○) and TM polarizations (□). The red line represents the data-best fit (r^2>0.99) for 1.000≤ n_F ≤1.500 (characteristic for air and *E. coli* cells [293]), using a single exponential decay ($\Delta n_{rs} = y_0 + A \times e^{n_F/t}$, with y_0=(9.3±0.1)×10⁻⁶, A=−1.9×10⁻¹² and t=(−8.40±0.04)×10⁻²).

The fluid was described by a mixture of two components (designated as A and B). During the measurement interval (~800 s), the number of *E. coli* living cells is constant, as the *E. coli* cell-cycle duplication period is ~1 hour [295,296]. Thus, n_F can be described by the Lorentz-Lorenz relation [297],

$$\frac{n_F^2 - 1}{n_F^2 + 2} = \phi_A \frac{n_A^2 - 1}{n_A^2 + 2} + \phi_B \frac{n_B^2 - 1}{n_B^2 + 2} \tag{7.3}$$

where ϕ_A and ϕ_B are the volume fractions of the two components, and n_A, n_B are the respective refractive indexes. Considering, that component A is the LB medium and B is the *E. coli* cells, the volume of *E. coli* cells in the fluid is defined by $V_{EC} = \phi_B \times V_{total}$. Therefore, the number of *E. coli* cells is $N = V_{EC} / V_{Cell}$, where V_{Total} and V_{Cell} are the volumes of the fluid and the

individual cell, respectively. The V_{Cell} can be approximately defined as a cylinder with a length of 2 μm and width of 1 μm, and the mass of each cell is 1 pg [298]. The *E. coli* cells concentration (C) can then be estimated by Equation (7.4).

$$C = \frac{\phi_B}{V_{cell}} \tag{7.4}$$

In order to evaluate the sensor performance, the error associated to the calculation of n_F was calculated through:

$$\Delta n_F = \left|\frac{\partial n_F}{\partial \alpha}\right| \Delta \mathrm{PM} = \frac{\Delta \mathrm{PM} \cdot \ln(10) \cdot t}{10 \cdot \mathrm{acos}(2 \cdot 10^{\alpha/10} - 1)} \sqrt{\frac{1}{10^{-\alpha/10} - 1}} \tag{7.5}$$

where ΔPM = 0.05 dB is the power meter measurement error.

Combing Equations (7.2, 3 and 5), the error in the concentration value (limit of detection, LOD) can be calculated through:

$$LOD = \frac{\Delta n_F}{V_{cell}} \frac{n_B^2 + 2}{n_B^2 - 1} \left[\frac{6 n_F}{(n_F^2 + 2)^2} - \phi_A \frac{n_A^2 - 1}{n_A^2 + 2} \right]. \tag{7.6}$$

7.4 Results and Discussion

Figure 7.4 shows the transmission spectrum of the MZI output, revealing a typical sinusoidal interference pattern, as described by Equation (7.1). After the *E. coli* based fluid spread in the sensing region, the transmission spectra revealed a red-shift that increased with time, Figure 7.4(b), which is related to the increase of n_F, as detailed below. Further evidences of the n_F temporal dependence can also be found through the study of the intensity ratio between I_{out} and I_{in} variation, which is a simpler methodology when compared with spectral analysis.

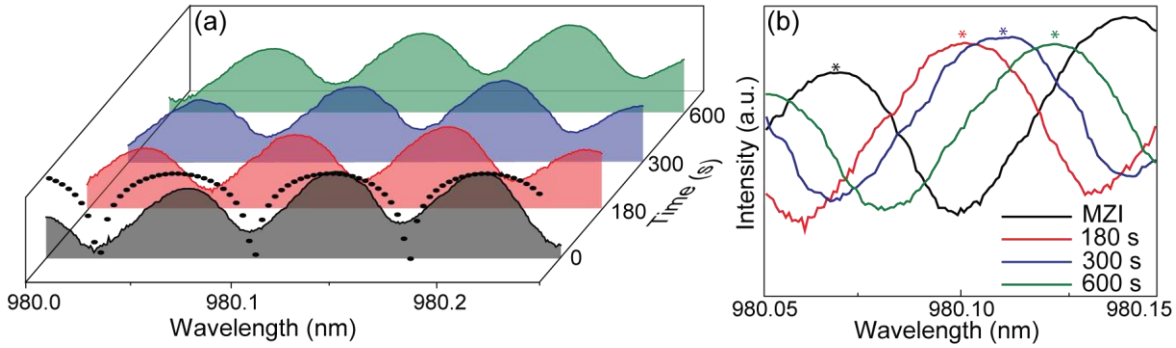

Figure 7.4 (**a**) Simulated (solid circles) and experimental transmission spectra of the MZI and the respective temporal dependence after the fluid spread in the sensing region for selected time intervals. (**b**) Magnification of the spectral region used to estimate n_F.

The optical loss α was measured for TM polarization, because α revealed an asymptotic decay with n_F for this polarization. Figure 7.5(a) shows the temporal evolution of the optical signal loss, after the spread of the fluid in the sensing region and signal stabilization ($\alpha \approx -10$ dB). During the measurements, the water from the LB medium evaporated, leading to an increase of *E. coli* concentration until the complete evaporation of water in the LB medium was achieved. During this process the fluid refractive index increased towards a final value that is closer to the *E. coli* refractive index. Evaluating α temporal dependence, a minimum value was observed at ~−23 dB, corresponding to the MZI asymptotic response that occurred for n_F=1.38 (represented in Figure 7.3(b)). The subsequent increase to ~−0.5 dB occurred for n_F>1.38. To guarantee a univocal sensor response, the asymptotic region must be towards higher n_F values; for instance, by tailoring the length of the sensing arm, if L_{MZI}=7 μm, the measurement range can be extended for $1.00 < n_F < 1.43$ [16].

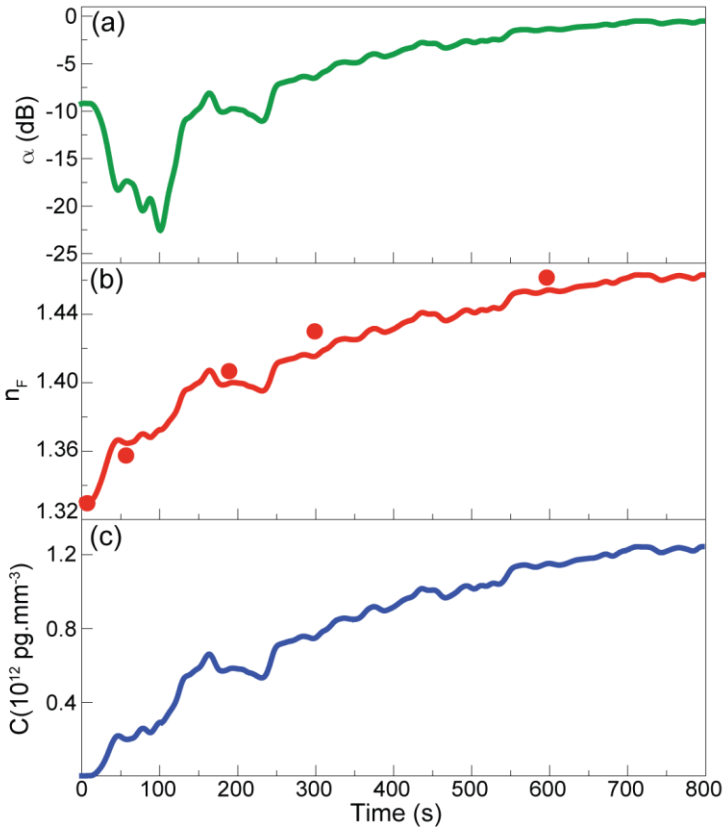

Figure 7.5 Temporal evolution of the (**a**) MZI sensor optical power loss, (**b**) n_F and of the (**c**) *E. coli* concentration. The solid circles in (**b**) correspond to the values estimated by the spectral shift analysis.

By analysing α and applying Equation (7.2), n_F was determined, Figure 7.5(b). The initial value of the fluid refractive index was $1.3310 \pm (2 \times 10^{-4})$, and during the water evaporation, n_F changed until a maximum value of $1.4632 \pm (2 \times 10^{-4})$ that was recorded at ~800 s. This n_F

variation can be rationalized through the calculation of weight average value between n_{EC} (~1.388) and n_{LB} (~1.330) [27,38]. In the beginning of the experiment, the main contribution for n_F derived from the water in the LB growth medium, and after the evaporation, the main contribution derived from the *E. coli* cells as well as fats and proteins left from the LB (n_{fats}=1.40–1.50, [39]), which led to a n_F value close to those of n_{EC} and n_{fats}. At t=100 s a n_F variation of $(+4.15\pm0.02)\times10^{-2}$ was observed, which closely matched the variation measured by the Abbe refractometer in the same conditions, $(+4.20\pm0.05)\times10^{-2}$, validating the results obtained by the MZI sensor. The n_F variation was also estimated through the transmission spectra in Figure 7.4. In particular, the temporal dependence of the peak position around 980 nm was used to obtain n_F through Equation (7.2). As illustrated in Figure 7.5(b) (solid circles) the estimated values are also in good agreement with those predicted by the intensity analysis. The error associated with these calculations is lower than 10^{-6} RIU, considering that the main error is the experimental optical spectral resolution (0.8 pm).

For biosensing, in particular to monitor the concentration growing of bacteria in a medium and estimate the sensor figures, the α temporal variation was used to calculate C through Equation (7.4), Figure 7.5(c). The initial concentration (C_0) was estimated as ~2.93×10^{9} cells·mL^{-1}, which is a typically reported value for *E. coli* after overnight growth in a rich medium, such as LB [27]. When the water evaporation occurred, C reached a stable value of ~1.23×10^{12} cells·mL^{-1}.

In order to evaluate the sensor performance, the refractive index sensitivity (Δn_F) was calculated, considering that the main error is associated with the estimation of α, which was assumed as the error of the optical power meter (0.05 dB), yielding to $\Delta n_F \leq 2\times10^{-4}$ RIU, which is the best value reported for low refractive index contrast biosensors. Larger or analogous values were only achieved for silicon-based devices, which use more complex and expensive photolithographic techniques compared with direct *laser* writing, Table 7.1. The RIU value is also comparable with the figure of merit known for a silicon-on-insulator MZI using the spectral shift methodology (e.g., RIU~10^{-4} estimated for a typical experimental spectral resolution of 10^{-11} m) [302]. Therefore, comparing the results with the figures of merit known for polymer-based sensors, whose Δn_F is larger (3×10^{-3} RIU) for a similar refractive index contrast [40]. Based on the estimated RIU values, a maximum LOD for the proposed sensor was calculated using Equation (7.6), yielding 2.0 pg·mm^{-3} (2.0×10^{3} cells·mL^{-1}), which is among the best values reported in the literature (Table 7.1).

Table 7.1 - Refractive index contrast, sensitivity (RIU) and limit of detection (LOD, pg·mm^{-3}) of selected optical biosensors using the intensity methodology. The method used to fabricate the sensor is also indicated.

Material	Method	Δn	RIU	LOD	Ref.
di-ureasil	Direct writing	10^{-3}	2×10^{-4}	2.0	this work
SiO_2		5×10^{-3}	1.5×10^{-4}	-	[304]
ORMOCER®	Photolithography	-	10^{-5}	2.4	[305]
Si-based		-	2×10^{-4}	-	[306]
SiN		-	3×10^{-3}	-	[307]
PDMS		-	-	2	[303]

ORMOCER®:Organic Modified Ceramic - Fraunhofer ISC; PDMS:Polydimethylsiloxane.

With a balance between the optimized measure window targeted to quantify the refractive index of biological fluids, sensitivity, and LOD, the proposed sensor is predicted to be able to measure and detect biological events such as bacterial growth [2,27,38] and haemoglobin concentrations [46], as well as monitor high cell density fermentation processes [47].

7.5 CONCLUSIONS

The design and experimental demonstration of a cost-effective optical biosensor for the determination of *E. coli* concentration, based on an MZI structure fabricated by *laser* direct writing on a self-patternable di-ureasil film was described. The sensor was designed using analytic models in order to establish the optical behaviour of the device, envisioning the desired application. The *E. coli* concentration was measured during an induced evaporation process of the medium from 2.93×10^{9} to ~1.23×10^{12} cells·mL^{-1} within a few minutes. The sensibility and LOD of the sensor were estimated to be 2×10^{-4} RIU and 2.0 pg·mm^{-3}, respectively, which are record values known for integrated optics-based solutions with low refractive index contrast. Featuring enhanced values, the sensor sensitivity and LOD can be easily improved ($\Delta n_F=2\times10^{-5}$ RIU and LOD=0.1 pg·mm^{-3}) by using a higher resolution power meter (e.g., 0.001 dB) or through spectral analysis ($\leq10^{-6}$ RIU), despite the higher cost. The use of such a simple design and the exploitation of a low contrast fabrication platform allowed the development of an optical biosensor with a relatively simple fabrication procedure and interrogation scheme, and without the drawback of the ambiguity on a broad measurement range ($1.00\leq n_F \leq1.38$) associated with high-resolution MZI-based sensors. Moreover, the optical biosensor can be tailored to specifically detect *E. coli* cells (or other biological agents) in a fluid, by simple coating the film of the MZI measuring arm, with a bio-recognition layer.

CHAPTER 8

CONCLUSIONS AND FUTURE WORK

In the area of green photonics, in particular optical communications and sensing fields, it is required to develop energy-efficient PICs featuring: low attenuation values in the NIR spectral region, refractive index similar to optical fibres, thermal stability, mechanical resistance, low energy consumption, reliability, repeatability and low-cost production. In what concerns optical communications, where the traffic demand has been increasing, the manufacturing of low-cost PICs seeks to revolutionize the speed and the capability of communications. For this, passive and active optical devices are indispensable. Passive devices are applied for a wide range of functionalities in optical systems, as control the propagation direction, and the optical signal properties (amplitude, phase and polarization). Contrarily to passive devices, the active ones require some type of external energy to perform their functions, as optical sources, amplifiers and detectors.

In this context, to produce passive optical components, in this dissertation, functionalized organic-inorganic hybrids, namely di-ureasils and tri-ureasils, were synthetized by the sol-gel method, and doped with different concentrations of ZPO-McOH (20-60 mol%). The resulting materials present transparency, homogeneity and optical quality (refractive index and attenuation coefficient) for PICs. The local structural features of these hybrids were discussed based on XRD, ^{29}Si and ^{13}C NMR, FT-IR, and FT-Raman measurements. It was concluded that the Si- and Zr-based networks are inter-constrained, with the Zr-based clusters embedded in the polymeric phase between the siliceous domain. Also, the individual order of the components based in Si and Zr were preserved with the doping. Through TGA and DSC, it was observed a thermal stability up to 150 °C, which meets the thermal standards for PICs.

Also, thermal stability improvements of ~16 % and ~38 % were observed by adding ZPO-McOH and for lower polymer molecular weight, respectively.

To analyse the optical properties of di-ureasils and tri-ureasils, a characterization was performed through UV-Vis-NIR spectroscopy, spectroscopic ellipsometry and prism coupling. In the relevant spectral region (1550 nm), the refractive index values are between 1.4981 and 1.5176, which are similar to the one in optical fibres reducing the insertion losses. The attenuation coefficient was around 1.2 and 2.3 $dB \cdot cm^{-1}$, that are reasonable values for low dimension circuits. In the UV spectral region, the materials present high absorption coefficients ($> 50\ dB \cdot cm^{-1}$), which allowed to use direct UV *laser* writing to induced polymerization and, consequently, locally change the refractive index ($\Delta n \sim 5 \times 10^{-3}$). Therefore, channel waveguides were patterned on the doped materials surface, supporting guided modes at 1550 nm.

Foreseen green photonic goals and exploiting the advantages of di-ureasil doped with 40 mol% ZPO-McOH for PICs, several passive optical devices were simulated and produced by direct UV *laser* writing to be applied in optical communications.

The effects of temperature and electric field in the doped di-ureasil were studied. Through prism coupling measurements, the TO coefficient was measured, yielding a value of $-(4.9 \pm 0.5) \times 10^{-4}\ °C^{-1}$, which is higher than the ones for polymers and silica materials. The electro-optic effect in di-ureasils was addressed envisioning the development of switching devices for coherent optical systems. Measurements were performed in a MZI patterned by direct *laser* writing on the d-U_{600}Z60 surface, yielding an EO coefficient of 39.9±0.5 pm/V and a V_π value of 2.9±0.3 V. These figures of merit resemble those reported for $LiNbO_3$ and silicon-based materials, highlighting the potential of di-ureasil as a low-cost solution for optical switching devices.

Taking advantage of the high TO coefficient of di-ureasils, an integrated thermally controlled wave plate was produced, where an Ag electrode was placed bellow the di-ureasil film to induce a temperature variation on the waveguide. A maximum phase shift of 54±2 ° was achieved (for a temperature variation of 3 °C achieved with 0.03 W), leading to a thermal linear retardation coefficient estimated of 17±1 °/°C, and a thermally induced birefringence variation of $(2.32 \pm 0.02) \times 10^{-5}$. The obtained values are higher than the ones reported for thermally induced birefringence of PMMA, demonstrating the feasibility of di-ureasils as cost-effective solutions for PCDs.

For coherent optical systems, a 90° hybrid coupler was produced, and incorporated with balanced photodiodes, resulting in an optical coherent receiver with capacity to extract the IQ phase components of an optical signal. The functionality of the PIC was tested through the demodulation of a 20 Gb/s QPSK transmission performed over 40 km G.652 and in back-to-back. The proposed 90° hybrid exhibited a phase deviation of 2 ° and an excess loss of 3.8±0.3 dB. An EVM minimum value of −19 dB was attained with a power penalty of 2.5 dB, relatively to back-to-back, for the HD-FEC limit (BER=3.8×10^{-3}). The comparison of those values with the ones attained for InP and silicon-based devices, showed the potential of integrated organic-inorganic hybrid to become key building blocks for PIC based demodulators. Moreover, the device operation bandwidth to demodulate the QPSK signal is 5 nm, which demonstrates the device capability to operate with other multi-level amplitude and phase shift keying modulation schemes, and with DWDM systems.

Envisioning the production of an active devices for VLC, namely an optical amplifier in the blue spectral region, planar and channel waveguides based on PBS-PFP doped within di-ureasils were fabricated and optically characterized. The incorporation of PBS-PFP into the hybrid host led to an enhanced emission in the blue spectral region (peaking around 390-550 nm) with high absolute emission quantum yield values (~ 0.8). The refractive index of the PBS-PFP-based di-ureasils was tuned through chemical and physical means, with a maximum variation of +0.02 upon doping with PBS-PFP, and +0.09 following UV exposure. The optical gain coefficient was measured using the VSL method, showing an increase in optical gain (4.7-15.0±0.2 dB) with the PBS-PFP concentration (1.2-12$\times10^{-3}$ wt%), and (15.0-34.0±0.2 dB) with the UV energy used to produce channel waveguides (0-120 μJ·pulse^{-1}). The maximum gain efficiency value attained in planar waveguides was 0.73±0.01 cm·μJ^{-1} (14.6±0.2 cm·kW^{-1}), and in channel waveguides was 1.62±0.02 cm·μJ^{-1} (32.5±0.3 cm·kW^{-1}), showing the potential of the proposed material to be implemented as a cost-effective optical amplifier for VLC based on white LEDs.

Regarding the sensing field, biosensors are highly useful for fast and sensitive pathogen detection. Therefore, taking advantage of di-ureasils materials, an optical biosensor for the determination of *E. coli* concentration by an interferometric methodology was fabricated and experimentally demonstrated. The analyte concentration was measured during an induced evaporation process of the medium from ~2.93×10^{9} to ~1.23×10^{12} cells·mL^{-1} within a few minutes. The measured sensitivity (2×10^{-4} RIU) and LOD (2.0 pg·mm^{-3}) are among the best values known for integrated optics-based solutions with low refractive index contrast,

demonstrating the feasibility of the proposed biosensor for a direct, compact, and low-cost solution for monitoring the concentration of lived-cells.

Concluding, distinct cost-effective PICs were produced and experimentally validated, demonstrating the organic-inorganic hybrids potential to produce low-cost and high efficiency optical components for optical communications and sensing applications, considering green photonics goals. The integration of these devices into a more complex optical architecture may be a step forward to manufactured optical components capable of breaking cost-performance barriers for the next generation of optical networks and sensing.

As future research, other solutions can still be suggested and addressed, involving new materials, PIC architectures and production methods. Resulting from the effort of this work, some research directions remain open:

- Develop PICs based on tri-ureasils organic-inorganic materials. As these materials showed refractive index values similar to the one in optical fibres, and lower attenuation coefficient comparing to di-ureasil, it is significant to verified if there is an improvement in the propagation losses.
- Test other methodologies for the polymerization, as a high-power UV lamp as a source for the PICs writing. Contrarily to the direct writing by UV *laser*, to pattern a device with a UV lamp an amplitude mask is required, nonetheless it has a low-cost and can be reutilize.
- Produce different PICs architectures: micro-rings resonators for tunable wavelength filtering or sensing, by changing its propagation properties using an external source (TO or EO effect) or by changing the superstrate environment, respectively; arrayed waveguide gratings that are capable of multiplexing a number of wavelengths into a single optical fibre, increasing the transmission capacity; combination of MMI couplers to generate several functionalities as phase demodulation; incorporate MZIs with phase shifters and polarization controllers to develop advanced modulators (M-PSK and M-QAM with polarization multiplexing).
- In the sensing area, a selective biosensor can be developed by coating the MZI measuring arm with a bio-recognition layer. This layer allows to specifically detect a biological agent in a liquid medium, due to its selective affinity to that specimen.

- Produce an optical amplifier based on the PBS-PFP-based di-ureasils and assess its performance in a VLC test-in-bed, showing the signal-to-noise improvement with this device in the VLC receiver.
- Develop new tests for EO switching devices to reinforce the materials potential in this field, namely analyse the MZI transmission spectra dependence with the applied voltage.

ANNEX A

LOCAL STRUCTURE, MORPHOLOGY AND THERMAL PROPERTIES CHARACTERIZATION: EXPERIMENTAL DETAILS

A.1 X-ray photoelectron spectroscopy (XPS)

The X-ray photoelectron spectra were carried out with a Physical Electronics PHI 5700 apparatus applying the non-monochromatic Mg-K_α line at 1253.6 eV, as the excitation source and the high resolution multi-region spectra were recorded with a pass energy of 23.5 eV. The binding energies were referenced to the C 1s peak at 284.8 eV. The measurements were performed in collaboration with Professor Doctor Enrique Rodríguez-Castellón from the Department of Inorganic Chemistry, Faculty of Sciences, University of Málaga, Málaga, Spain.

A.2 X-ray diffraction (XRD)

The X-ray diffractograms were acquired at room temperature in a diffractometer Philips X'Pert MPD. The samples were exposed to CuK_α radiation ($\lambda_{CuK\alpha}$=1.54 Å) in the angular range 1.05 °<2θ<50.00 °, with a resolution of $\Delta\theta=7\times10^{-4}$ rad, and an acquisition time of 35 seconds per point.

A.3 Nucleus magnetic resonance (NMR) spectroscopy

The nucleus magnetic resonance spectroscopy measurements using the magic angle spinning technique (MAS) of the atomic nucleus ^{29}Si, and the magic angle spinning in cross polarization (CP/MAS) of the atomic nucleus ^{13}C were performed in a Bruker Advance 400 (9.4T) spectrometer at 79.49 and 100.62 MHz, respectively. The chemical shift is express in ppm of tetramethylsilane. The ^{29}Si and ^{13}C NMR spectra were analysed to study the siliceous domains and the organic component of the selected hybrids, respectively. In the ^{29}Si NMR, the local environments around silicon atoms are identified with the notation T^m, where m (m=1, 2, 3) is the number of silicon atoms bonded to oxygen atom, in which the condensation degree (c) can be calculated from the following expression:

$$c=\frac{1}{3}(I_{T1}+2I_{T2}+3I_{T3}). \qquad \text{(A.1)}$$

where I_{T1}, I_{T2} and I_{T3} represent the relative percentage of the integrated areas of T^1, T^2 and T^3 environment, respectively, estimated by fitting the experimental spectra [156]. If it is observed

Q-type environments in the ^{29}Si NMR spectra, the c value is calculated from the following expression:

$$c = \frac{1}{3}(I_{T1} + 2I_{2T} + 3I_{T3}) + \frac{1}{4}(2I_{Q2} + 3I_{Q3} + 4I_{Q4}). \quad \text{(A.2)}$$

where I_{Q2}, I_{Q3} and I_{Q4} represent the relative percentage of the integrated areas of Q^2, Q^3 and Q^4 environment, respectively, estimated by fitting the experimental spectra [162]. The fit was performed through deconvolution of T^n and Q^n regions, using a sum of Gaussian functions. Considering the reported values for the chemical shift of each environment, the fit values for the peak position were constrained to [−54, −48] ppm for T^1, [−57, −60] ppm for T^2, and [−65, −68] ppm for T^3. As T^1 site corresponds to the border region of the material structure, it has a higher disorder, so its full width at half maximum was set to be ~1.5 higher than T^2 and T^3 sites [310].

A.4 Fourier-transform infrared spectroscopy (FT-IR)

The Fourier-transform infrared with attenuated total reflectance spectra were acquired at room temperature, using a Unicam FT-IR spectrophotometer. The spectra were collected over the range 4000-500 cm^{-1} by averaging 60 scans at a maximum resolution of 4 cm^{-1}.

A.5 Fourier transform Raman spectroscopy (FT-Raman)

The Fourier transform Raman spectra were recorded using a Bruker RFS 100 spectrometer, operating with a Nd:YAG *laser* excitation (1064 nm at 200 mW) by averaging 300 scans with a spectral resolution of 4 cm^{-1}, in a 180 ° configuration, between 0 and 4000 cm^{-1}.

A.6 Thermogravimetric analysis (TGA) and differential scanning calorimetry (DSC)

The thermogravimetric analysis was performed using a Shimadzu's TGA-50 analyser, with a heating velocity of 10 °C·min^{-1}, between 25 and 800 °C. A nitrogen flux of 110 mL·min^{-1} was used as a purge gas.

A.7 Scanning Electron Microscopy (SEM)

Scanning electron microscopy images were obtained with a field emission type microscope (Hitachi® SU-70) operating at 15.0 kV, in a secondary electron emission mode. The films were fixed on the SEM sample holder with a conductive adhesive (Nisshin® EMI) and the sample surface was cleaned with an air flux before coating process on a carbon vacuum evaporator

(Emitech® K950X). The conductive coating was performed with pure graphite rods with an evaporation time of 5 s.

A.8 Atomic Force Microscopy (AFM)

Atomic force microscopy were performed using a commercial NTEGRA Aura set-up (NT-MDT) in tapping mode using scans areas from 2×2 μm^2 to 6×6 μm^2. The scan rate was always kept at 0.5 Hz (tip velocity ranged from 2 to 6 $\mu m \cdot s^{-1}$). Silicon cantilevers (Nanosensors, PPP-NCHR) with the spring constant of 42 $N \cdot m^{-1}$ and tip radius less than 10 nm were used. The experimentally measured data were subjected to an average filter using an integration area of 10×10 pixels.

ANNEX B

OPTICAL CHARACTERIZATION: EXPERIMENTAL DETAILS

B.1 UV-Vis-NIR absorption spectroscopy

The absorbance spectra were recorded at room temperature, using a dual-beam spectrometer Lambda 950, (Perkin-Elmer) with a 150 mm diameter Spectralon integrating sphere or STD detector module over the scan range 200-1600 nm and a resolution of 2 nm. The absorption coefficient (Λ, cm^{-1}) was estimated for all the samples using the Lambert-Beer law, Equation (B.1).

$$\Lambda = \frac{A}{t'}. \tag{B.1}$$

where A and t' stand for the absorbance and optical path (film thickness in units of cm), respectively.

B.2 Prism coupling characterization

The prism coupling technique, originally proposed by Tien *et al.* [311], was implemented to determine the refractive index (n) and thickness (t) of thin films. This method is characterized by an optical signal coupled by a prism into a thin film (planar waveguide), Figure B.1. Changing the beam incident angle (ϕ_m, $m \in IN$ represents the guided mode) it is possible to excite several propagation modes in the film.

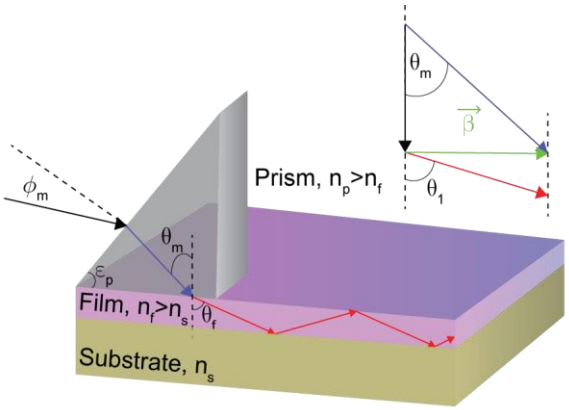

Figure B.1 Schematic representation of the prism coupling, where n_p, n_s, n_f and n_0 represent the refractive index values of the prism, substrate, film and air, respectively.

To verify coupling in the film, which leads to the existence of guided modes, the propagation constant parallel to the film surface (β) must be the same for the propagated wave in the prism and film:

$$\beta = n_p \sin(\theta_m) = n_f \sin(\theta_f). \tag{B.2}$$

where θ_m and θ_f are the angles that the beam does with the perpendicular of the film, in the prism and film, respectively. Applying the Snell law to the wave propagated in the prism:

$$N_m = n_p \sin\left[\arcsin\left(\frac{\sin(\phi_m)}{n_p}\right) + \varepsilon_p\right]. \tag{B.3}$$

where N_m is the effective refractive index in the m-mode, and ε_p is the prism angle [312], it is possible to obtain the effective refractive index through the measured parameter (ϕ_m) and the prism constants (n_p and ε_p). If two or more modes are identified, N_m values can relate to n_f and t, through the dispersion equation of a dielectric waveguide, Equation (B.4) [313].

$$k_0 t(n_{air} - N_m^2)^{1/2} = \Psi_m(n, N_m). \tag{B.4}$$

wherein,

$$\Psi_m(n, N_m) = m\pi + \Phi_0(n, m) + \Phi_2(n, m). \tag{B.5}$$

and

$$\Phi_j(n_f, N_m) = \arctan\left[\left(\frac{n_f}{n_j}\right)^{2p}\left(\frac{N_m^2 - n_j^2}{n_f^2 - N_m^2}\right)\right]^{1/2} \qquad j = 0, 2. \tag{B.6}$$

where k_0 is the vacuum wavenumber, Ψ_m, Φ_0 and Φ_2 are numerical functions of n, m and N_m. Therefore, a minimization routine of the difference between the members of Equation (B.4) allows to extract the values of n_f and t.

Using the prism coupling, it is also possible to determine the scattering attenuation through graphic analysis of the propagation losses in planar waveguides. The scattering losses have two contributions: extrinsic (due to particles and fissures) and intrinsic (due to composition and density fluctuations). To measure the attenuation, the propagation must be assured, and the scattering radiation intensity is monitored directly in the waveguide using an image system, obtaining the attenuation coefficient (α) through the mapping of the scattering light intensity, Equation (B.7):

$$I_1 = I_0 e^{-\alpha L}. \tag{B.7}$$

where I_1 is the scattering light intensity after a propagation length of L, and I_0 is the intensity at the initial point. Thus, through the scattering radiation intensity along the propagation in the waveguide, and fitting the experimental data to Equation (B.7), α can be easily determine with an error related to the fitting quality.

Experimental set-up

Three independent measurements of ϕ_m and m were performed for each sample in different locations in the thin film, in order to ensure the accuracy of the results. Figure B.2 represents the experimental set-up for the prism coupling measurements.

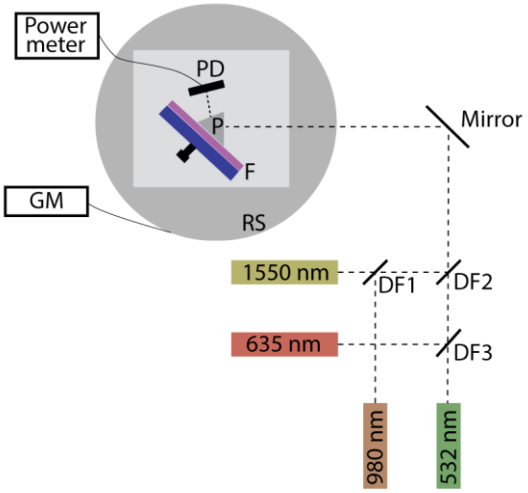

Figure B.2 Schematic representation of the prism coupling set-up. PD: photodiode; GM: goniometer; RS: rotation stage; DF: dichroic filter; P: prism; F: film.

The experimental set-up is characterized by four *lasers* (532 nm Roithner Lasertechnik GmbH RLDD532-3-3, 635 nm Stoker Yale RLDD532-3-3, 980 nm Thorlabs CPS980, 1550 nm Newport LPM1550-05E) coupled in the prism (Edmund Optics NT45-949, n=1.7434 at 1550 nm) which is located in a rotation stage (Newmark Systems Inc RT-5DR) with a resolution of 0.005 °. The film was pressed against the prism using a screw to adjust the pressure required to fix the film without damaging. The dichroic filters and mirror (Thorlabs PF10-03-G01) were used to guide the *laser* beam to the prism, DF1 (Thorlabs DMLP1180T) is transparent for 1550 nm and reflects at 980 nm, DF2 (Edmund Optics NT46-387) is transparent for the visible spectral range and reflects in the infrared, and DF3 (Andover Corporation 645FK84-25) is transparent for 532 nm and reflects at 635 nm. The system is also equipped with two photodiodes (Thorlabs, Si: FDS1010 and Ge: FDG1010) to detect visible and infrared spectral ranges, respectively, which are connected to a power meter. For each propagated mode in the film, the power meter measures a higher power, being possible

to determine with precision the angle for each mode. For the Equation (B.4) numerical solution, a MATLAB® routine was implemented, Figure B.3 shows the graphic user interface created. The input data in the interface are ϕ_m, m, wavelength, substrate and prism refractive index values, prism angle, initial values for the film refractive index and thickness, and the maximum number of interactions.

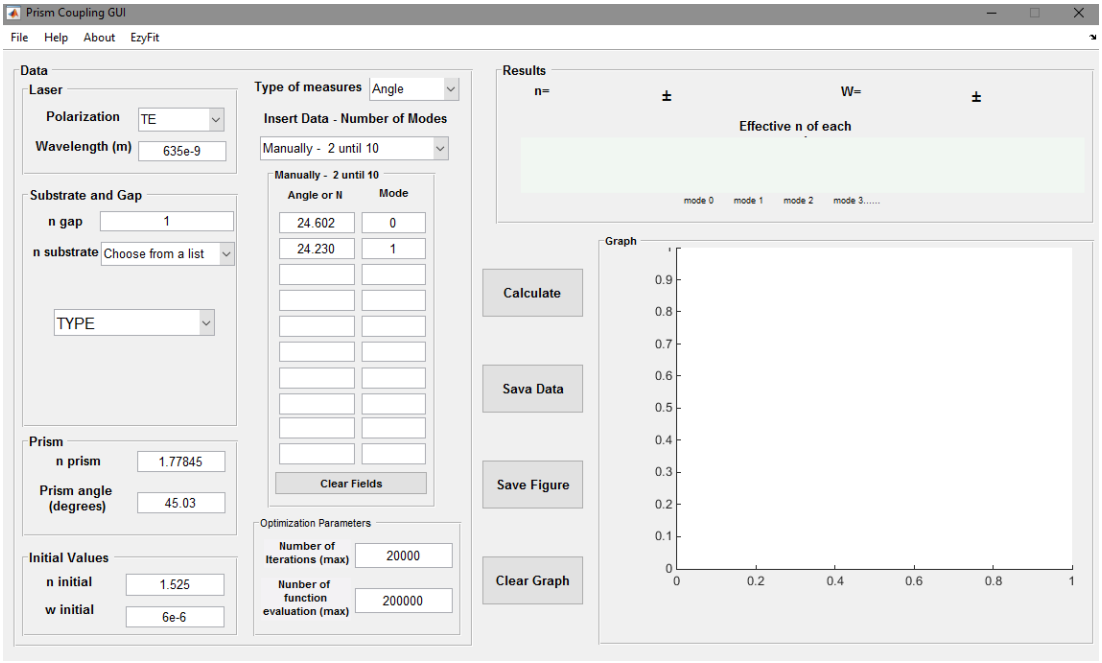

Figure B.3 Image of the graphic user interface for the prism coupling numerical method.

The computation principle of this program is to equalize the two components of Equation (B.4), and minimize the difference between them. For the error minimization, the Nelder-Mead algorithm [314] was implemented. The first part of the calculus is through the variation of the refractive index and thickness values for the experimental effective index values. In the second part, the program calculates the effective index for the theoretical values of refractive index and thickness, and change those values until the equation reach a minimum value. The difference between the theoretical and experimental effective index values allows to determine the error of each measurements through Equation (B.8).

$$n_e = \mathrm{STD}(n_{te} - n_{ee}). \tag{B.8}$$

where, n_e is the refractive index measurement error, STD is the standard deviation function, n_{te} and n_{ee} are the theoretical and experimental effective indexes, respectively.

To measure the attenuation coefficient, the experimental set-up in Figure B.4 was implemented. These measurements were performed using the same optical components of the prism coupling.

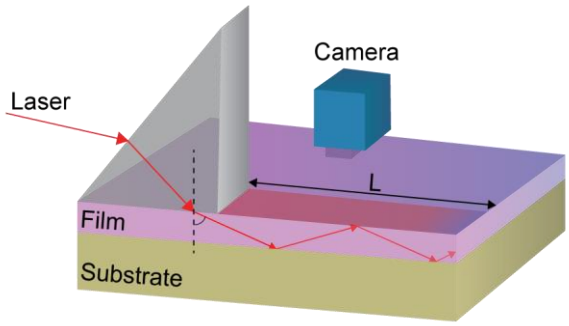

Figure B.4 Scheme of the experimental set-up to determine the scattering attenuation through graphic analysis.

B.3 Spectroscopic Ellipsometry

Spectroscopic ellipsometry is nowadays a standard optical technique for thin films characterization by analysing the change in polarized light upon reflection on a sample [315]. The advantages of this technique are the precision, reproducibility, high thickness sensibility, non-destructive, and no special sample preparation is required. The main disadvantage of ellipsometry is the indirect characterization required, leading to a difficult data analysis and the need to know some sample information [316].

Ellipsometry measures the change in the polarization state of a beam of light upon reflection from the sample. The state of polarization variation is characterized by the sample's morphological and optical features (thickness and refractive index). The experimental parameters measured by ellipsometry are Ψ and Δ, which represent the amplitude ratio and phase difference of the state of polarization, respectively, Figure B.5 [317]. The polarization state of the incident light can be decomposed into an *s* and a *p* component (*s*-component is oscillating parallel to the sample surface, and *p*-component is oscillating parallel to the plane of incidence). The intensity of the *s* and *p* component, after reflection, are denoted by r_s and r_p, also known as the complex Fresnel reflection coefficients. After reflection on the sample surface, there is a shift in the phase ($\Delta = \delta_{rp} - \delta_{rs}$) and a change in the relative amplitude of *p* and *s* components ($\tan\Psi = |r_p|/|r_s|$). Taking this into account, the fundamental equation of ellipsometry is written as:

$$\tan\Psi e^{i\Delta} = \frac{r_p}{r_s}. \qquad \text{(B.9)}$$

Since ellipsometry measured a ratio of two values (rather than the absolute value of either), it is robust, accurate (~Å) and reproducible.

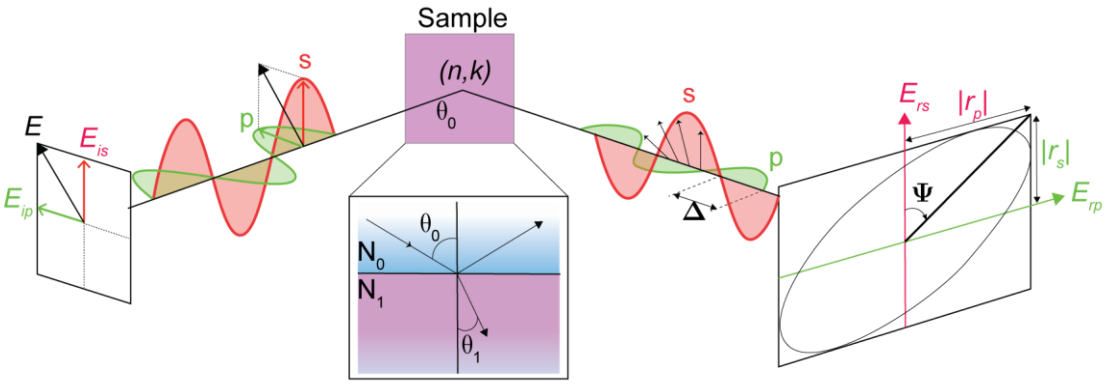

Figure B.5 Scheme of the ellipsometer operation.

Modern phase modulated ellipsometers measure the parameter values designated as I_s and I_c, being Ψ and Δ calculated using the appropriate formulation [318]:

$$\begin{cases} I_s = \sin(2\Psi)\sin(\Delta) \\ I_s = \sin(2\Psi)\cos(\Delta) \end{cases}. \tag{B.10}$$

A theoretical model of the sample structure must be employed to calculate I_s and I_c, leaving the parameters of interest (thickness and refractive index) as variables that are obtained, when the ellipsometric data generated by the model match the experimental one.

Experimental details

The spectroscopic ellipsometry measurements were performed using a Horiba Scientific AutoSE spectroscopic ellipsometer at an incidence angle of 69.8 °, with an average of 30 measurements per point, using a spot size of 250×250 μm^2. The data was fitted considering a layered structure model, Figure B.6. For the films deposited in borosilicate glass, the model consists of a three-layered system incorporating one layer for the substrate (borosilicate glass), the material under study layer and air as ambient medium. For films deposited in Si/SiO_2 substrate, the model consists of a four-layered system incorporating two layers for the oxidized silicon wafer substrate (Si and 1.00±0.05 μm of SiO_2), the material under study layer and air as ambient medium. The fitting was performed with the Simplex minimization algorithm, and the dispersion curves were determined using the Cauchy absorbent model, which expresses the refractive index (n) as a function of the wavelength (λ):

$$n(\lambda) = A + \frac{B \cdot 10^4}{\lambda^2} + \frac{C \cdot 10^9}{\lambda^4}. \tag{B.11}$$

where A is a dimensionless parameter, B (nm^2) parameter affect the curvature and amplitude of the dispersion curve in the visible spectral region, and C (nm^4) parameters affect the curvature and amplitude of the dispersion curve in the UV spectral region. The reported

values for the thickness and refractive index are the average of three measurements performed for each sample with a maximum standard deviation of 5 %. The films with thickness higher than 15 μm were considered as bulk, and the data were minimized using the direct inversion technique, using the above-mentioned Cauchy absorbent model.

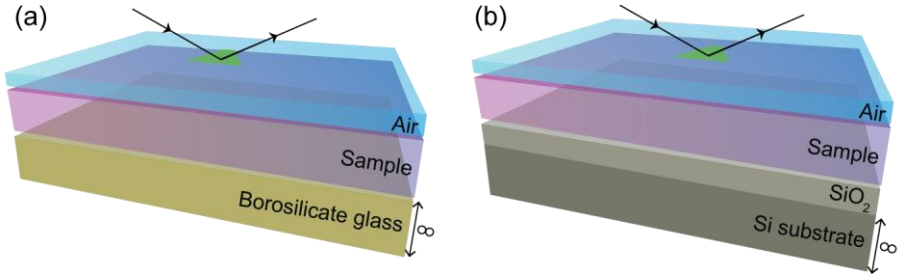

Figure B.6 Schematic representation of the layered structure model used for thin films deposited in (**a**) borosilicate glass and (**b**) Si/SiO_2 substrates. The green area corresponds to the measured spot.

B.4 Optical mode field characterization

The output waveguide mode field distribution was measured using a beam profile analyser (Newport, LPB-1) with a 10× microscope objective (Newport, M-10X), with a spatial resolution of 0.15 μm. The measurements were made with a fibre coupled *laser* emitting at 1550 nm (EXFO IQS-2400 WDM *Laser* Source) injected into the waveguide input using a positioning system (Thorlabs, Nanomax-TS). The optical signal at the output was aligned, using an identical positioning system, to the mentioned above microscope objective which focused the signal into the beam profile analyser. Figure B.7 illustrates the experimental set-up used for these measurements.

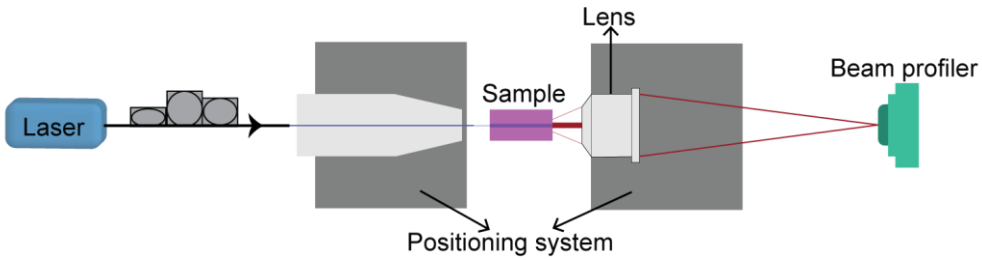

Figure B.7 Experimental set-up used to measure the optical mode field distribution at the sample output.

ANNEX C

DIRECT WRITING BY UV *LASER* SYSTEM: EXPERIMENTAL DETAILS

The writing system used to fabricate PICs based in organic-inorganic hybrids is composed by an UV pulsed excimer *laser* (KrF) (Coherent Bragg Star Industrial V2.0) emitting at 248 nm, with a pulse duration of 15 ns, repetition rate between 1 and 1000 Hz, and a maximum pulse energy of 16 mJ. The general view of the writing system is represented in Figure C.1(a).

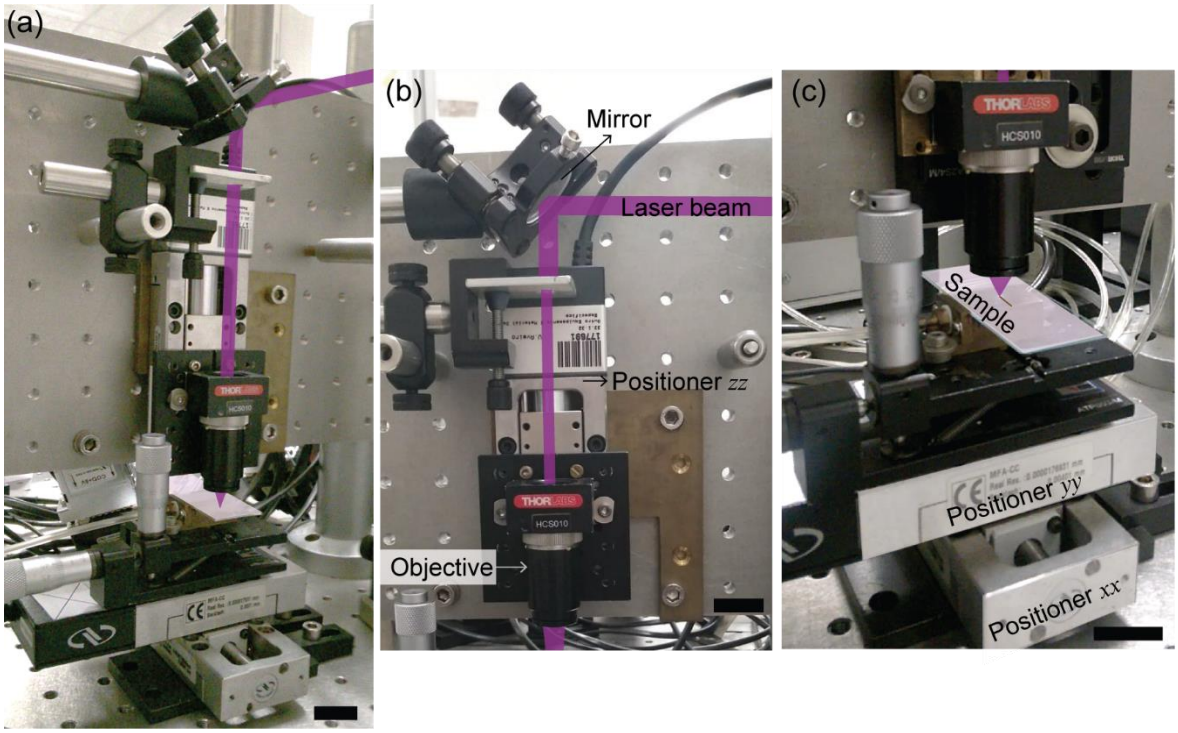

Figure C.1 Photos of the UV direct writing system (**a**) general view, (**b**) focusing system, and (**c**) translation stages (*xx*- and *yy*-directions). The scale bar corresponds to 2 cm.

As UV direct writing requires a small exposition area (<100×100 μm^2), the *laser* beam needed to be focus in the substrate. So, first the beam was forwarded through a mirror system (Linos Photonics-G340723000) to a focusing objective mounted vertically (Thorlabs-LMU-15X-248). To ensure that the *laser* beam fills the objective aperture, a circular slit (diameter of 10 mm) was placed before the objective. To control the distance between the objective and the substrate, and subsequently focus the beam, the objective was fixed into a *zz*-direction positioner (Newport-MFA–CC), Figure C.1(b).

To pattern the desired PIC design, the substrate position was displaced relatively to the *laser* beam, by two translation stages (*xx*- and *yy*-direction, Newport-MFA–CC), Figure C.1(c).

The substrate was fixed in those two positioners that will move according to the desired PIC design, with a maximum displacement of 25 mm, maximum speed of 2.5 $mm \cdot s^{-1}$, and a resolution of 17.5 nm. This system is computationally controlled with a motion controller (Newport-XPS) to properly adjust the drawing speed and the substrate position.

To control the two translation stages (*xx*- and *yy*-direction) in simultaneous, it is required to develop a trajectory file with the position, velocity and time values for a specific PIC design. These files were developed in MATLAB®, and uploaded in a LabVIEW™ application that controls the positioners and the UV *laser* operation parameters (frequency, energy and on/off time).

To pattern waveguides in the doped organic-inorganic hybrid film, the UV radiation energy should be between 2 and 4 $\mu J \cdot pulse^{-1}$ (controlled with neutral density filters placed before the circular slit) with a pulse frequency of 900 Hz, to prevent surface ablation. The translation stages (*xx*- and *yy*-direction) velocity was set to be 100 $\mu m \cdot s^{-1}$.

REFERENCES

[1] C. Yeh, Introduction, in: C.B.T.-A.P. Yeh (Ed.), Appl. Photonics, Elsevier, Boston, 1994: pp. 1–8. doi:10.1016/B978-0-08-049926-0.50005-8.

[2] D. Breuer, F. Geilhardt, R. Hülsermann, M. Kind, C. Lange, T. Monath, E. Weis, Opportunities for next-generation optical access, IEEE Commun. Mag. 49 (2011) 16–24. doi:10.1109/MCOM.2011.5706309.

[3] A.B. González, J. Pozo, The Biophotonics Revolution in Healthcare, Opt. Photonik. 12 (2017) 16–17. doi:10.1002/opph.201770306.

[4] A. Barrias, J. Casas, S. Villalba, A Review of Distributed Optical Fiber Sensors for Civil Engineering Applications, Sensors. 16 (2016) 748. doi:10.3390/s16050748.

[5] I.T. Ferguson, K.L. Yunghans, A. Ghods, V.G. Saravade, C. Zhou, A Review of the Physiological Aspects of Solid State Lighting, in: Light. Energy Environ., Optical Society of America, Boulder, Colorado, 2017: p. SW3C.3. doi:10.1364/SSL.2017.SW3C.3.

[6] A. Flores-Abad, O. Ma, K. Pham, S. Ulrich, A review of space robotics technologies for on-orbit servicing, Prog. Aerosp. Sci. 68 (2014) 1–26. doi:10.1016/j.paerosci.2014.03.002.

[7] Photonics21, Europe's age of light! How photonic will power growth and innovation, Photonics21 Vis. Pap. (2017). https://www.photonics21.org.

[8] Photonik, Branchenreport, Frankfurt am, 2013.

[9] F. Quan, Green photonics, J. Opt. 14 (2012) 024001. doi:10.1088/2040-8978/14/2/024001.

[10] V.L. Kalyani, C. Charan, Green Photonics – A Broad Overview and Future Aspects, J. Manag. Eng. Inf. Technol. 1 (2016) 9–14.

[11] E. Commission, 2030 climate & energy framework, Energy, Clim. Chang. Environ. (2014). https://ec.europa.eu/clima/policies/strategies/2030_en (accessed June 22, 2018).

[12] B. Jalali, S. Fathpour, K. Tsia, Green Silicon Photonics, Opt. Photonics News. 20 (2009) 18. doi:10.1364/OPN.20.6.000018.

[13] N. Anscombe, S. Eglash, New materials, new horizons, Nat. Photonics. 5 (2011) 274–274. doi:10.1038/nphoton.2011.65.

[14] B. Wessler, U. Tober, Green photonics: the role of photonics in sustainable product design, in: P. Ambs, D. Curticapean, C. Emmelmann, W. Knapp, Z.T. Kuznicki, P.P. Meyrueis (Eds.), 2011: p. 806515. doi:10.1117/12.882979.

[15] A. Amari, O.A. Dobre, R. Venkatesan, O.S.S. Kumar, P. Ciblat, Y. Jaouën, A Survey on Fiber Nonlinearity Compensation for 400 Gb/s and Beyond Optical Communication Systems, IEEE Commun. Surv. Tutorials. 19 (2017) 3097–3113. doi:10.1109/COMST.2017.2719958.

[16] S. Vigneshvar, C.C. Sudhakumari, B. Senthilkumaran, H. Prakash, Recent Advances in Biosensor Technology for Potential Applications - An Overview., Front. Bioeng. Biotechnol. 4 (2016) 11. doi:10.3389/fbioe.2016.00011.

[17] S.M. Yoo, S.Y. Lee, Optical Biosensors for the Detection of Pathogenic Microorganisms, Trends Biotechnol. 34 (2016) 7–25. doi:10.1016/j.tibtech.2015.09.012.

[18] C.M.S. Vicente, Híbridos orgânicos-inorgânicos para aplicações de baixo custo em ótica integrada, University of Aveiro, 2012.

[19] M.S. Erkllnç, D. Lavery, K. Shi, B.C. Thomsen, R.I. Killey, S.J. Savory, P. Bayvel, Bidirectional wavelength-division multiplexing transmission over installed fibre using a simplified optical coherent access transceiver, Nat. Commun. 8 (2017) 1–10. doi:10.1038/s41467-017-00875-z.

[20] J.J.V. Olmos, J. Sugawa, H. Ikeda, K. Sakamoto, GPON and lOG-EPON coexisting systems and filtering issues at the OLT, in: 16th Optoelectron. Commun. Conf., 2011: pp. 828–829.

[21] A. Shahpari, R.M. Ferreira, R.S. Luis, Z. Vujicic, F.P. Guiomar, J.D. Reis, A.L. Teixeira, Coherent Access: A Review, J. Light. Technol. 35 (2017) 1050–1058. doi:10.1109/JLT.2016.2623793.

[22] C. Laperle, M. Osullivan, Advances in high-speed DACs, ADCs, and DSP for optical coherent transceivers, J. Light. Technol. 32 (2014) 629–643. doi:10.1109/JLT.2013.2284134.

[23] G. Li, Recent advances in coherent optical communication, Adv. Opt. Photonics. 1 (2009) 279. doi:10.1364/AOP.1.000279.

[24] N. Cvijetic, Software-defined optical access networks for multiple broadband access solutions, in: 2013 18th Optoelectron. Commun. Conf. Held Jointly with 2013 Int. Conf. Photonics Switch., 2013: pp. 1–2.

[25] D. Hillerkuss, J. Leuthold, Software-Defined Transceivers in Dynamic Access Networks, J. Light. Technol. 34 (2016) 792–797. doi:10.1109/JLT.2015.2470089.

[26] K. Kikuchi, High Spectral Density Optical Communication Technologies, Springer Berlin Heidelberg, Berlin, Heidelberg, 2010. doi:10.1007/978-3-642-10419-0.

[27] M. Hernández, A. Arcia, R. Alvizu, M. Huerta, A review of XDMA-WDM-PON for Next Generation Optical Access Networks, in: 2012 Glob. Inf. Infrastruct. Netw. Symp., 2012: pp. 1–6. doi:10.1109/GIIS.2012.6466763.

[28] R. Alvizu, A. Arcia, M. Hernández, M. Huerta, T. Idelfonso, Hybrid WDM-XDM PON architectures for future proof access networks, 2012.

[29] H.S. Abbas, M.A. Gregory, The next generation of passive optical networks: A review, J. Netw. Comput. Appl. 67 (2016) 53–74. doi:10.1016/j.jnca.2016.02.015.

[30] I.A. Aboagye, F. Chen, Y. Cao, Performance Analysis of 112 Gb / s × 4-Channel WDM PDM-DQPSK Optical Label Switching System With Spectral Amplitude Code Labels, 7 (2017) 88–96. doi:10.1007/s13320-016-0345-5.

[31] E. Lach, W. Idler, Modulation formats for 100G and beyond, Opt. Fiber Technol. 17 (2011) 377–386. doi:10.1016/j.yofte.2011.07.012.

[32] M. Bass, Handbook of Optics, Volume II - Devices, Measurements, and Properties, Vasa. v (2004) 1–1496. doi:10.1017/CBO9781107415324.004.

[33] Z. Zhuang, S.W. Suh, J.S. Patel, Polarization controller using nematic liquid crystals., Opt. Lett. 24 (1999) 694–696. doi:10.1364/OL.24.000694.

[34] K. Liu, J. Shi, X. Chen, Linear polarization-state generator with high precision in periodically poled lithium niobate, Appl. Phys. Lett. 94 (2009) 101106. doi:10.1063/1.3097225.

[35] D.C. Zografopoulos, R. Asquini, E.E. Kriezis, a d'Alessandro, R. Beccherelli, Guided-wave liquid-crystal photonics., Lab Chip. 12 (2012) 3598–610. doi:10.1039/c2lc40514h.

[36] D. Dai, L. Liu, S. Gao, D.X. Xu, S. He, Polarization management for silicon photonic integrated circuits, Laser Photon. Rev. 7 (2013) 303–328. doi:10.1002/lpor.201200023.

[37] D.S. Millar, Digital Signal Processing for Coherent Optical Fibre Communications, Int. J. Adv. Stu. Hum. Soci. Scie. (2015) 133. http://discovery.ucl.ac.uk/1333248/1/1333248.pdf.

[38] E.L. Wooten, K.M. Kissa, A. Yi-Yan, E.J. Murphy, D. a. Lafaw, P.F. Hallemeier, D. Maack, D.V. Attanasio, D.J. Fritz, G.J. McBrien, D.E. Bossi, A review of lithium niobate modulators for fiber-optic communications systems, IEEE J. Sel. Top. Quantum Electron. 6 (2000) 69–82. doi:10.1109/2944.826874.

[39] M. Seimetz, C.-M. Weinert, Options, feasibility, and availability of 2 x 4 90° hybrids for coherent optical systems, J. Light. Technol. 24 (2006) 1317–1322. doi:10.1109/JLT.2005.863251.

[40] R.D. Group, 90-degree Hybrid Device Design for Coherent Optical Communication Systems, RSOFT Des. Gr. Rev. 10 (2011).

[41] D.R. Zimmerman, L.H. Spiekman, Amplifiers for the Masses: EDFA, EDWA, and SOA Amplets for Metro and Access Applications, J. Light. Technol. 22 (2004) 63–70. doi:10.1109/JLT.2003.822144.

[42] K.S. Abedin, T.F. Taunay, M. Fishteyn, D.J. DiGiovanni, V.R. Supradeepa, J.M. Fini, M.F. Yan, B. Zhu, E.M. Monberg, F. V Dimarcello, Cladding-pumped erbium-doped multicore fiber amplifier, Opt. Express. 20 (2012) 20191–20200. doi:10.1364/OE.20.020191.

[43] A.A. Fotiadi, Random lasers: An incoherent fibre laser, Nat. Photonics. 4 (2010) 204–205. doi:10.1038/nphoton.2010.76.

[44] Q.W. Niloy K. Dutta, Semiconductor Optical Amplifiers, World of Scientific Publishing Co. Lda., 2013.

[45] 陈伟 Wei Chen, 王科研 Keyan Wang, 孟洲 Zhou Meng, Stimulated Brillouin scattering effect on gain saturation of distributed fiber Raman amplifiers, Chinese Opt. Lett. 8 (2010) 365–367. doi:10.3788/m0000520100804.0365.

[46] J. Clark, G. Lanzani, Organic photonics for communications, Nat. Photonics. 4 (2010) 438–446. doi:10.1038/nphoton.2010.160.

[47] L. Grobe, A. Paraskevopoulos, J. Hilt, D. Schulz, F. Lassak, F. Hartlieb, C. Kottke, V. Jungnickel, K.-D. Langer, High-speed visible light communication systems, IEEE Commun. Mag. 51 (2013) 60–66. doi:10.1109/MCOM.2013.6685758.

[48] P. Das, B.Y. Kim, Y. Park, K.D. Kim, Color-independent VLC based on a color space without sending target color information, Opt. Commun. 286 (2013) 69–73. doi:10.1016/j.optcom.2012.07.083.

[49] S.T. Tan, X.W. Sun, H. V Demir, S.P. DenBaars, Advances in the LED Materials and Architectures for Energy-Saving Solid-State Lighting Toward “Lighting Revolution”, IEEE Photonics J. 4 (2012) 613–619. doi:10.1109/JPHOT.2012.2191276.

[50] X. Huang, Z. Wang, J. Shi, Y. Wang, N. Chi, 1.6 Gbit/s phosphorescent white LED based VLC transmission using a cascaded pre-equalization circuit and a differential outputs PIN receiver, Opt. Express. 23 (2015) 22034–22042. doi:10.1364/oe.23.022034.

[51] P.Y. Liu, L.K. Chin, W. Ser, T.C. Ayi, P.H. Yap, T. Bourouina, Y. Leprince-Wang, Real-Time measurement of single bacterium's refractive index using optofluidic immersion refractometry, in:

Procedia Eng., 2014: pp. 356–359. doi:10.1016/j.proeng.2014.11.743.

[52] A.L. Koch, Growth Measurement, in: Methods Gen. Mol. Microbiol. Third Ed., American Society of Microbiology, 2007. doi:10.1128/9781555817497.ch9.

[53] P. Vaiano, B. Carotenuto, M. Pisco, A. Ricciardi, G. Quero, M. Consales, A. Crescitelli, E. Esposito, A. Cusano, Lab on Fiber Technology for biological sensing applications, Laser Photon. Rev. 10 (2016) 922–961. doi:10.1002/lpor.201600111.

[54] A. Ricciardi, A. Crescitelli, P. Vaiano, G. Quero, M. Consales, M. Pisco, E. Esposito, A. Cusano, Lab-on-fiber technology: a new vision for chemical and biological sensing, Analyst. 140 (2015) 8068–8079. doi:10.1039/C5AN01241D.

[55] X. Fan, I.M. White, S.I. Shopova, H. Zhu, J.D. Suter, Y. Sun, Sensitive optical biosensors for unlabeled targets: A review, Anal. Chim. Acta. 620 (2008) 8–26. doi:10.1016/j.aca.2008.05.022.

[56] D. Dey, T. Goswami, Optical biosensors: A revolution towards quantum nanoscale electronics device fabrication, J. Biomed. Biotechnol. 2011 (2011) 7. doi:10.1155/2011/348218.

[57] P. Kozma, F. Kehl, E. Ehrentreich-Förster, C. Stamm, F.F. Bier, Integrated planar optical waveguide interferometer biosensors: A comparative review, Biosens. Bioelectron. 58 (2014) 287–307. doi:10.1016/j.bios.2014.02.049.

[58] A. Ksendzov, Y. Lin, Integrated optics ring-resonator sensors for protein detection., Opt. Lett. 30 (2005) 3344–3346. doi:10.1364/OL.30.003344.

[59] J. Dostálek, J. Tyroký, J. Homola, E. Brynda, M. Skalský, P. Nekvindová, J. Špirková, J. Škvor, J. Schröfel, Surface plasmon resonance biosensor based on integrated optical waveguide, Sensors Actuators, B Chem. 76 (2001) 8–12. doi:10.1016/S0925-4005(01)00559-7.

[60] B.J. Luff, R.D. Harris, J.S. Wilkinson, R. Wilson, D.J. Schiffrin, Integrated-optical directional coupler biosensor., Opt. Lett. 21 (1996) 618–620. doi:10.1364/OL.21.000618.

[61] M.C. Estevez, M. Alvarez, L.M. Lechuga, Integrated optical devices for lab-on-a-chip biosensing applications, Laser Photon. Rev. 6 (2012) 463–487. doi:10.1002/lpor.201100025.

[62] M.R.G. Maia, S. Marques, A.R.J. Cabrita, R.J. Wallace, G. Thompson, A.J.M. Fonseca, H.M. Oliveira, Simple and Versatile Turbidimetric Monitoring of Bacterial Growth in Liquid Cultures Using a Customized 3D Printed Culture Tube Holder and a Miniaturized Spectrophotometer: Application to Facultative and Strictly Anaerobic Bacteria, Front. Microbiol. 7 (2016) 1381. doi:10.3389/fmicb.2016.01381.

[63] Infinera, Photonic Integrated Circuits: A Technology and Application Prime, White Pap. (2005).

[64] I.P. Kaminow, Optical Integrated Circuits: A Personal Perspective, J. Light. Technol. 26 (2008) 994–1004. doi:10.1109/JLT.2008.922149.

[65] G.E. Moore, Cramming more components onto integrated circuits, Reprinted from Electronics, volume 38, number 8, April 19, 1965, pp.114 ff., IEEE Solid-State Circuits Soc. Newsl. 11 (2006) 33–35. doi:10.1109/N-SSC.2006.4785860.

[66] M. Smit, X. Leijtens, H. Ambrosius, E. Bente, J. van der Tol, B. Smalbrugge, T. de Vries, E.-J. Geluk, J. Bolk, R. van Veldhoven, L. Augustin, P. Thijs, D. D'Agostino, H. Rabbani, K. Lawniczuk, S. Stopinski, S. Tahvili, A. Corradi, E. Kleijn, D. Dzibrou, M. Felicetti, E. Bitincka, V. Moskalenko, J. Zhao, R. Santos, G. Gilardi, W. Yao, K. Williams, P. Stabile, P. Kuindersma, J. Pello, S. Bhat, Y. Jiao, D. Heiss, G. Roelkens, M. Wale, P. Firth, F. Soares, N. Grote, M. Schell, H. Debregeas, M. Achouche, J.-L. Gentner, A. Bakker, T. Korthorst, D. Gallagher, A. Dabbs, A. Melloni, F. Morichetti, D. Melati, A. Wonfor, R. Penty, R. Broeke, B. Musk, D. Robbins, An introduction to InP-based generic integration technology, Semicond. Sci. Technol. 29 (2014) 083001. doi:10.1088/0268-1242/29/8/083001.

[67] L.A. Coldren, S.W. Corzine, M.L. Mašanović, Diode Lasers and Photonic Integrated Circuits, Second, John Wiley & Sons, Inc., Hoboken, NJ, USA, 2012. doi:10.1002/9781118148167.

[68] K.J. Vahala, Optical microcavities, Nature. 424 (2003) 839. http://dx.doi.org/10.1038/nature01939.

[69] K. Williams, InP Integrated Photonics: State of the Art and Future Directions, in: Opt. Fiber Commun. Conf., OSA, Washington, D.C., 2017: p. M3B.5. doi:10.1364/OFC.2017.M3B.5.

[70] D. Thomson, A. Zilkie, J.E. Bowers, T. Komljenovic, G.T. Reed, L. Vivien, D. Marris-Morini, E. Cassan, L. Virot, J.-M. Fédéli, J.-M. Hartmann, J.H. Schmid, D.-X. Xu, F. Boeuf, P. O'Brien, G.Z. Mashanovich, M. Nedeljkovic, Roadmap on silicon photonics, J. Opt. 18 (2016) 073003. doi:10.1088/2040-8978/18/7/073003.

[71] X.J.M. Leijtens, B. Kuhlow, M.K. Smit, Arrayed waveguide gratings, Springer Ser. Opt. Sci. 123 (2006) 125–187. doi:10.1007/3-540-31770-8_5.

[72] T.M. Benson, S. V. Boriskina, P. Sewell, A. Vukovic, S.C. Greedy, A.I. Nosich, Micro/optical resonators for microlasers and integrated optoelectronics, in: Front. Planar Light. Circuit Technol., Kluwer Academic Publishers, Dordrecht, 2005: pp. 39–70. doi:10.1007/1-4020-4167-5_02.

[73] Y. Hida, Y. Hibino, H. Okazaki, Y. Ohmori, 10 m long silica-based waveguide with a loss of 1.7 dB/m, in: Integr. Photonics Res., OSA, Washington, D.C., 1995: p. IThC6. doi:10.1364/IPR.1995.IThC6.

[74] R. Nagarajan, C.H. Joyner, R.P. Schneider, J.S. Bostak, T. Butrie, A.G. Dentai, V.G. Dominic, P.W. Evans, M. Kato, M. Kauffman, D.J.H. Lambert, S.K. Mathis, A. Mathur, R.H. Miles, M.L. Mitchell, M.J. Missey, S. Murthy, A.C. Nilsson, F.H. Peters, S.C. Pennypacker, J.L. Pleumeekers, R.A. Salvatore, R.K. Schlenker, R.B. Taylor, Huan-Shang Tsai, M.F. Van Leeuwen, J. Webjorn, M. Ziari, D. Perkins, J. Singh, S.G. Grubb, M.S. Reffle, D.G. Mehuys, F.A. Kish, D.F. Welch, Large-scale photonic integrated circuits, IEEE J. Sel. Top. Quantum Electron. 11 (2005) 50–65. doi:10.1109/JSTQE.2004.841721.

[75] F. Boeuf, N. Vulliet, C. Baudot, S. Messaoudene, E. Baylac, S. Cremer, Challenges in Silicon Photonics Process Technology, in: 2017 Eur. Conf. Opt. Commun., IEEE, 2017: pp. 1–3. doi:10.1109/ECOC.2017.8346203.

[76] T. Komljenovic, M. Davenport, J. Hulme, A.Y. Liu, C.T. Santis, A. Spott, S. Srinivasan, E.J. Stanton, C. Zhang, J.E. Bowers, Heterogeneous Silicon Photonic Integrated Circuits, J. Light. Technol. 34 (2016) 20–35. doi:10.1109/JLT.2015.2465382.

[77] R.G.F. Baets, A.Z. Subramanian, S. Clemmen, B. Kuyken, P. Bienstman, N. Le Thomas, G. Roelkens, D. Van Thourhout, P. Helin, S. Severi, Silicon Photonics: Silicon Nitride Versus Silicon-on-insulator, in: Opt. Fiber Commun. Conf., OSA, Washington, D.C., 2016: p. Th3J.1. doi:10.1364/OFC.2016.Th3J.1.

[78] H. Venghaus, N. Grote, Fibre Optic Communication, Springer International Publishing, Cham, 2017. doi:10.1007/978-3-319-42367-8.

[79] A. Melloni, F. Morichetti, TriPleX: A new concept in optical waveguiding, Integr. Opt. (2007) 3–6. doi:10.1.1.655.8574.

[80] S. Zheng, H. Chen, A.W. Poon, Microring-Resonator Cross-Connect Filters in Silicon Nitride: Rib Waveguide Dimensions Dependence, IEEE J. Sel. Top. Quantum Electron. 12 (2006) 1380–1387. doi:10.1109/JSTQE.2006.883148.

[81] P. Muñoz, Towards fabless photonic integration, White Pap. VLC Photon (2012) 1–3.

[82] J.W. Kim, B. Chmielak, H. Lerch, U. Plachetka, Fabrication of photonic integrated circuits in silicon nitride using substrate conformal imprint lithography, Microelectron. Eng. 176 (2017) 11–14. doi:10.1016/j.mee.2017.01.008.

[83] B. Skubic, E. In De Betou, T. Ayhan, S. Dahlfort, Energy-efficient next-generation optical access networks, IEEE Commun. Mag. 50 (2012) 122–127. doi:10.1109/MCOM.2012.6122542.

[84] A. Ovsianikov, S. Passinger, R. Houbertz, B.N. Chichkov, Three Dimensional Material Processing with Femtosecond Lasers BT - Laser Ablation and its Applications, in: C. Phipps (Ed.), Springer US, Boston, MA, 2007: pp. 121–157. doi:10.1007/978-0-387-30453-3_6.

[85] R. Houbertz, G. Domann, C. Cronauer, A. Schmitt, H. Martin, J.-U. Park, L. Fröhlich, R. Buestrich, M. Popall, U. Streppel, P. Dannberg, C. Wächter, A. Bräuer, Inorganic–organic hybrid materials for application in optical devices, Thin Solid Films. 442 (2003) 194–200. doi:10.1016/S0040-6090(03)00982-9.

[86] R.A.S. Ferreira, C.D.S. Brites, C.M.S. Vicente, P.P. Lima, A.R.N. Bastos, P.G. Marques, M. Hiltunen, L.D. Carlos, P.S. André, Photonic-on-a-chip: a thermal actuated Mach-Zehnder interferometer and a molecular thermometer based on a single di-ureasil organic-inorganic hybrid, Laser Photon. Rev. 7 (2013) 1027–1035. doi:10.1002/lpor.201300080.

[87] K.B. Yoon, Low-loss multimode waveguides using organic-inorganic hybrid materials, Macromol. Res. 12 (2004) 290–292. doi:10.1007/BF03218402.

[88] R. Buestrich, F. Kahlenberg, M. Popall, P. Dannberg, R. Müller-Fiedler, O. Rösch, ORMOCER®s for Optical Interconnection Technology, J. Sol-Gel Sci. Technol. 20 (2001) 181–186. doi:10.1023/A:1008755607488.

[89] M. Yoshida, P.N. Prasad, Sol−Gel-Processed SiO2/TiO2/Poly(vinylpyrrolidone) Composite Materials for Optical Waveguides, Chem. Mater. 8 (1996) 235–241. doi:10.1021/cm950331o.

[90] A. Madani, H.R. Azarinia, Design and fabrication of all-polymeric photonic waveguides in optical integrated circuits, Opt. - Int. J. Light Electron Opt. 138 (2017) 33–39. doi:https://doi.org/10.1016/j.ijleo.2017.03.021.

[91] C. Molina, P.J. Moreira, R.R. Goncalves, R.A.S. Ferreira, Y. Messaddeq, S.J.L. Ribeiro, O. Soppera, A.P. Leite, P.V.S. Marques, V. de Zea Bermudez, L.D. Carlos, Planar and UV written channel optical waveguides prepared with siloxane-poly(oxyethylene)-zirconia organic-inorganic hybrids. Structure and optical properties, J. Mater. Chem. 15 (2005) 3937–3945. doi:10.1039/B505081M.

[92] C.M.S. Vicente, E. Pecoraro, R.A.S. Ferreira, P.S. André, R. Nogueira, Y. Messaddeq, S.J.L. Ribeiro, L.D. Carlos, Waveguides and gratings fabrication in zirconium-based organic/inorganic hybrids, J. Sol-Gel Sci. Technol. 48 (2008) 80–85. doi:10.1007/s10971-008-1775-3.

[93] K. Saravanamuttu, X.M. Du, S.I. Najafi, M.P. Andrews, Photoinduced structural relaxation and densification in sol-gel-derived nanocomposite thin fils: implications for integrtes optics device fabrication, Can. J. Chem. 76 (1998) 1717–1729. doi:10.1139/v98-176.

[94] X. Zhang, Z. Zhao, M. Qian, R. Yin, X. Zeng, P. Plante, Fabrication of Waveguide Splitters Using Sol-

Gel Hybrid Materials, in: Int. Top. Meet. Microw. Photonics, 2006: pp. 1–4. doi:10.1109/MWP.2006.346558.

[95] K. Abe, Y. Oizumi, T. Ishigure, Low-loss graded-index polymer crossed optical waveguide with high thermal resistance, Opt. Express. 26 (2018) 4512. doi:10.1364/OE.26.004512.

[96] H. Nawata, K. Ohmori, Organic-inorganic hybrid material for optical interconnects and application to optical coupling method, in: 2014 Int. Conf. Electron. Packag., IEEE, 2014: pp. 707–711. doi:10.1109/ICEP.2014.6826771.

[97] Y. Saito, K. Fukagata, T. Ishigure, Low-loss polymer optical waveguides with graded-index perfect circular cores for on-board interconnection, in: J.-E. Broquin, G. Nunzi Conti (Eds.), Integr. Opt. Devices, Mater. Technol. SPIE, 2016: p. 975005. doi:10.1117/12.2212135.

[98] P. Coudray, P. Etienne, Y. Moreau, J. Porque, S.I. Najafi, Sol-gel channel waveguide on silicon: fast direct imprinting and low cost fabrication, Opt. Commun. 143 (1997) 199–202. doi:https://doi.org/10.1016/S0030-4018(97)00445-8.

[99] X. Le Guével, S. Schutzmann, L. Stella, F. De Matteis, P. Prosposito, M. Casalboni, Effect of titania content on the optical properties of dye-doped hybrid sol–gel coatings, Opt. Mater. (Amst). 31 (2008) 451–454. doi:https://doi.org/10.1016/j.optmat.2008.06.009.

[100] E.J. Nassar, R.R. Gonçalves, M. Ferrari, Y. Messaddeq, S.J.L. Ribeiro, Titania-based organic–inorganic hybrid planar waveguides, J. Alloys Compd. 344 (2002) 221–225. doi:https://doi.org/10.1016/S0925-8388(02)00345-6.

[101] W.-S. Kim, J.-H. Lee, S.-Y. Shin, B.-S. Bae, Y.-C. Kim, Fabrication of ridge waveguides by UV embossing and stamping of sol-gel hybrid materials, IEEE Photonics Technol. Lett. 16 (2004) 1888–1890. doi:10.1109/LPT.2004.831053.

[102] E. Giorgetti, G. Margheri, S. Sottini, M. Casalboni, R. Senesi, M. Scarselli, R. Pizzoferrato, Dye-doped zirconia-based Ormosil planar waveguides: optical properties and surface morphology, J. Non. Cryst. Solids. 255 (1999) 193–198. doi:https://doi.org/10.1016/S0022-3093(99)00365-8.

[103] Y. Sorek, R. Reisfeld, I. Finkelstein, S. Ruschin, Sol-gel glass waveguides prepared at low temperature, Appl. Phys. Lett. 63 (1993) 3256–3258. doi:10.1063/1.110166.

[104] W. Que, X. Hu, X.L. Xia, L. Zhao, Photo-responsive properties of azobenzene small molecules in sol-gel hybrid TiO2/ormosil organic-inorganic matrices, Opt. Express. 15 (2007) 480–485. doi:10.1364/OE.15.000480.

[105] S.J.L. Ribeiro, Y. Messaddeq, R.R. Gonçalves, M. Ferrari, M. Montagna, M.A. Aegerter, Low optical loss planar waveguides prepared in an organic–inorganic hybrid system, Appl. Phys. Lett. 77 (2000) 3502–3504. doi:10.1063/1.1329159.

[106] C. Chen, Y. Yi, X. Wang, G. Xing, X. Sun, F. Wang, D. Zhang, Z. Shi, Z. Cui, Monolithic reconfigurable multi-functional waveguide modules for integrated optical network based on polymer photonic lightwave circuits, 2015 IEEE Int. Conf. Cyber Technol. Autom. Control Intell. Syst. IEEE-CYBER 2015. (2015) 709–714. doi:10.1109/CYBER.2015.7288028.

[107] Y. Gu, C. Chen, Y. Zheng, Z. Shi, X. Wang, Y. Yi, T. Jiang, X. Sun, F. Wang, Z. Cui, D. Zhang, Heat-induced multimode interference variable optical attenuator based on novel organic-inorganic hybrid materials, J. Opt. 17 (2015) 085802. doi:10.1088/2040-8978/17/8/085802.

[108] Y. Zou, L. Moreel, H. Lin, J. Zhou, L. Li, S. Danto, J.D. Musgraves, E. Koontz, K. Richardson, K.D. Dobson, R. Birkmire, J. Hu, Solution Processing and Resist-Free Nanoimprint Fabrication of Thin Film Chalcogenide Glass Devices: Inorganic-Organic Hybrid Photonic Integration, Adv. Opt. Mater. 2 (2014) 759–764. doi:10.1002/adom.201400068.

[109] L. Tian, Y. Sun, Y. Cao, Y. Yi, F. Wang, Y. Wu, D. Zhang, Polymer/Silica Hybrid Waveguide Bragg Grating Fabricated by UV-Photobleaching, IEEE Photonics Technol. Lett. 30 (2018) 603–606. doi:10.1109/LPT.2018.2805843.

[110] L. Liang, L. Qv, L. Zhang, C. Zheng, X. Sun, F. Wang, D. Zhang, Fabrication and characterization on an organic/inorganic 2×2 Mach–Zehnder interferometer thermo-optic switch, Photonics Nanostructures - Fundam. Appl. 12 (2014) 173–183. doi:10.1016/j.photonics.2013.12.001.

[111] C.M.S. Vicente, R. Venkatachaam, B.M. Ferreira, P.G. Marques, C.A.F. Marques, E. Pecoraro, L.D. Carlos, P.S. André, R.A.S. Ferreira, Thin film optimization design of organic-inorganic hybrids for waveguide high-rejection optical filters, Phys. Status Solidi - Rapid Res. Lett. 5 (2011) 280–282. doi:10.1002/pssr.201105283.

[112] P.G. Marques, A.R. Bastos, C.M.S. Vicente, E. Pecoraro, P.P. Lima, P.S. André, L.D. Carlos, R.A.S. Ferreira, Thermo-optical attenuator fabricated through direct UV laser writing in organic-inorganic hybrids, in: 2012 14th Int. Conf. Transparent Opt. Networks, 2012: pp. 1–4. doi:10.1109/ICTON.2012.6253722.

[113] D.C. Oliveira, A.G. Macedo, N.J.O. Silva, C. Molina, R.A.S. Ferreira, P.S. André, K. Dahmouche, V. de Zea Bermudez, Y. Messaddeq, S.J.L. Ribeiro, L.D. Carlos, Photopatternable Di-ureasil−Zirconium

Oxocluster Organic−Inorganic Hybrids As Cost Effective Integrated Optical Substrates, Chem. Mater. 20 (2008) 3696–3705. doi:10.1021/cm7031702.

[114] C.D.S. Brites, P.P. Lima, N.J.O. Silva, A. Millán, V.S. Amaral, F. Palacio, L.D. Carlos, A Luminescent Molecular Thermometer for Long-Term Absolute Temperature Measurements at the Nanoscale, Adv. Mater. 22 (2010) 4499–4504. doi:10.1002/adma.201001780.

[115] E. Pecoraro, S. García-Revilla, R.A.S. Ferreira, R. Balda, L.D. Carlos, J. Fernández, Real time random laser properties of Rhodamine-doped di-ureasil hybrids, Opt. Express. 18 (2010) 7470. doi:10.1364/OE.18.007470.

[116] S.E. Miller, Integrated Optics: An Introduction, Bell Syst. Tech. J. 48 (1969) 2059–2069. doi:10.1002/j.1538-7305.1969.tb01165.x.

[117] V. Passaro, C. Tullio, B. Troia, M. Notte, G. Giannoccaro, F. Leonardis, Recent Advances in Integrated Photonic Sensors, Sensors. 12 (2012) 15558–15598. doi:10.3390/s121115558.

[118] A. Kaźmierczak, S. Stopiński, A. Jusza, K. Anders, R. Piramidowicz, Sensing applications of photonic integrated circuits: ultra-compact optical transducers and interrogators, in: J. Dorosz, R.S. Romaniuk (Eds.), 17th Conf. Opt. Fibres Their Appl., 2017: p. 103250A. doi:10.1117/12.2271041.

[119] K. Okamoto, Beam propagation method, in: K.B.T.-F. of O.W. (Second E. Okamoto (Ed.), Fundam. Opt. Waveguides, Elsevier, Burlington, 2006: pp. 329–397. doi:10.1016/B978-012525096-2/50008-8.

[120] S.T. Chu, W.P. Huang, S.K. Chaudhuri, Simulation and analysis of waveguide based optical integrated circuits, Comput. Phys. Commun. 68 (1991) 451–484. doi:10.1016/0010-4655(91)90213-5.

[121] K. Okamoto, Fundamentals of Optical Waveguides, Elsevier, London, 2006. doi:10.1016/B978-012525096-2/50001-5.

[122] J.J. Gribble, J.M. Arnold, Beam propagation method and geometrical optics, IEE Proc. J - Optoelectron. 135 (1988) 343–348. doi:10.1049/ip-j:19880064.

[123] S.T. Chu, S.K. Chaudhuri, A finite-difference time-domain method for the design and analysis of guided-wave optical structures, J. Light. Technol. 7 (1989) 2033–2038. doi:10.1109/50.41625.

[124] M.D. Feit, J.A. Fleck, Computation of mode properties in optical fiber waveguides by a propagating beam method, Appl. Opt. 19 (1980) 1154–1164. doi:10.1364/AO.19.001154.

[125] C. Ma, E. Van Keuren, A simple three dimensional wide-angle beam propagation method, Opt. Express. 14 (2006) 4668–4674. doi:10.1364/OE.14.004668.

[126] P.L. Ho, Y.Y. Lu, A bidirectional beam propagation method for periodic waveguides, IEEE Photonics Technol. Lett. 14 (2002) 325–327. doi:10.1109/68.986801.

[127] L. Li, G. Nordin, J. English, J. Jiang, Small-area bends and beamsplitters for lowindex-contrast waveguides, Opt. Express. 11 (2003) 282. doi:10.1364/OE.11.000282.

[128] R.R.A. Syms, J.R. Cozens, Channel Waveguide Integrated Optics, in: Opt. Guid. Waves Devices, 1992.

[129] O. Soppera, P.J. Moreira, P.V.S. Marques, A.P. Leite, Influence of temperature and environment humidity on the transmission spectrum of sol–gel hybrid channel waveguides, Opt. Commun. 271 (2007) 430–435. doi:10.1016/j.optcom.2006.10.061.

[130] C. Urlacher, C.M. De Lucas, J. Mugnier, Chemical and physical aspects of sol—gel process for planar waveguides elaboration: application to zirconia waveguides, Synth. Met. 90 (1997) 199–204. doi:10.1016/S0379-6779(98)80007-6.

[131] J.M. Kahn, K.-P. Ho, Spectral Efficiency Limits and Modulation/Detection Techniques for DWDM Systems, IEEE J. Sel. Top. Quantum Electron. 10 (2004) 259–272. doi:10.1109/JSTQE.2004.826575.

[132] E. Ip, A.P.T. Lau, D.J.F. Barros, J.M. Kahn, Coherent detection in optical fiber systems, Opt. Express. 16 (2008) 753. doi:10.1364/OE.16.000753.

[133] J. Gao, H. Wu, Multi-function Mach-Zehnder modulator for pulse shaping and generation, Opt. Express. 24 (2016) 22239. doi:10.1364/OE.24.022239.

[134] H. Yamada, T. Chu, S. Ishida, Y. Arakawa, Optical directional coupler based on Si-wire waveguides, IEEE Photonics Technol. Lett. 17 (2005) 585–587. doi:10.1109/LPT.2004.840926.

[135] X. Chen, R.-D. Wen, S.-Y. Tseng, Analysis of optical directional couplers using shortcuts to adiabaticity, Light. Technol. 3. R. R. 16 (1998) 277–283. doi:10.1364/OE.24.018334.

[136] G. Agrawal, Fiber-Optic Communication Systems, 3rd ed., Wiley, 2002.

[137] G.P. Agrawal, Lightwave Technology: Components and Devices, John Wiley & Sons, Inc., Hoboken, NJ, USA, 2005. doi:10.1002/047174140X.fmatter.

[138] S.-H. Jeong, K. Morito, Compact optical 90 degrees hybrid employing a tapered 2x4 MMI coupler serially connected by a 2x2 MMI coupler., Opt. Express. 18 (2010) 4275–4288. doi:10.1364/OE.18.004275.

[139] Michael J. Connelly, Semiconductor Optical Amplifiers, Kluwer Academic Publishers, Boston, 2004. doi:10.1007/b101817.

[140] Gerd Keiser, Optical Communications Essentials, McGraw-Hill, 2003.

[141] S.-W. Chang, W.-C. Liao, Y.-M. Liao, H.-I. Lin, H.-Y. Lin, W.-J. Lin, S.-Y. Lin, P. Perumal, G. Haider,

C.-T. Tai, K.-C. Shen, C.-H. Chang, Y.-F. Huang, T.-Y. Lin, Y.-F. Chen, A White Random Laser, Sci. Rep. 8 (2018) 2720. doi:10.1038/s41598-018-21228-w.

[142] N.M. Lawandy, Coherent random lasing, Nat. Phys. 6 (2010) 246–248. doi:10.1038/nphys1644.

[143] H. Cao, Y.G. Zhao, S.T. Ho, E.W. Seelig, Q.H. Wang, R.P.H. Chang, Random Laser Action in Semiconductor Powder, Phys. Rev. Lett. 82 (1999) 2278–2281. doi:10.1103/PhysRevLett.82.2278.

[144] N.M. Lawandy, R.M. Balachandran, A.S.L. Gomes, E. Sauvain, Laser action in strongly scattering media, Nature. 368 (1994) 436–438. doi:10.1038/368436a0.

[145] R.C. Polson, Z.V. Vardeny, Random lasing in human tissues, Appl. Phys. Lett. 85 (2004) 1289–1291. doi:10.1063/1.1782259.

[146] C. Sanchez, P. Belleville, M. Popall, L. Nicole, Applications of advanced hybrid organic-inorganic nanomaterials: from laboratory to market, Chem. Soc. Rev. 40 (2011) 696–753. doi:10.1039/C0CS00136H.

[147] C. Brinker, G. Scherer, Sol-Gel Science: The Physics and Chemistry of Sol-Gel Processing, 1990.

[148] B.L. Cushing, V.L. Kolesnichenko, C.J. O'Connor, Recent Advances in the Liquid-Phase Syntheses of Inorganic Nanoparticles, Chem. Rev. 104 (2004) 3893–3946. doi:10.1021/cr030027b.

[149] R.A.S.F.L.D.C.V. de Z. Bermudez, Luminescent Organic–Inorganic Nanohybrids, in: Encycl. Nanosci. Nanotechnol., 2004: p. 719.

[150] M. Armand, V. de Zea Bermudez, C. Poinsignon, J.-Y. Sanchez, Proton conducting polymer, and application thereof as electrolyte in electrochemical devices, USA Patent, US5283310 A, 1994.

[151] E.A. Mikhalyova, A. V Yakovenko, M. Zeller, M.A. Kiskin, Y. V Kolomzarov, I.L. Eremenko, A.W. Addison, V. V Pavlishchuk, Manifestation of π–π Stacking Interactions in Luminescence Properties and Energy Transfer in Aromatically-Derived Tb, Eu and Gd Tris(pyrazolyl)borate Complexes, Inorg. Chem. 54 (2015) 3125–3133. doi:10.1021/ic502120g.

[152] C.R. Zamarreño, S. Lopez, M. Hernaez, I. Del Villar, I.R. Matias, F.J. Arregui, Optical Fiber Refractometers based on Indium Tin Oxide Coatings with Response in the Visible Spectral Region, Procedia Eng. 25 (2011) 499–502. doi:10.1016/j.proeng.2011.12.124.

[153] S.-J. Jiang, Z.-C. Jin, C.G. Granqvist, Low-refractive-index indium–tin–oxyfluoride thin films made by high-rate reactive dc magnetron sputtering, Appl. Opt. 27 (1988) 2847–2850. doi:10.1364/AO.27.002847.

[154] Schott, Nexterion catalogue, 2010. https://www.schott.com/d/nexterion/61d1ed78-3348-437f-8c1d-f68da893a91c/1.3/nexterion_product_catalogue_row_2010_1.pdf.

[155] N. Willis-Fox, A.-T. Marques, J. Arlt, U. Scherf, L.D. Carlos, H.D. Burrows, R.C. Evans, Synergistic photoluminescence enhancement in conjugated polymer-di-ureasil organic–inorganic composites, Chem. Sci. 6 (2015) 7227–7237. doi:10.1039/C5SC02409A.

[156] L. Fu, R.A.S. Ferreira, N.J.O. Silva, L.D. Carlos, V. de Zea Bermudez, J. Rocha, Photoluminescence and Quantum Yields of Urea and Urethane Cross-Linked Nanohybrids Derived from Carboxylic Acid Solvolysis, Chem. Mater. 16 (2004) 1507–1516. doi:10.1021/cm035028z.

[157] L.D. Carlos, V. de Zea Bermudez, R.A.S. Ferreira, L. Marques, M. Assunção, Sol−Gel Derived Urea Cross-Linked Organically Modified Silicates. 2. Blue-Light Emission, Chem. Mater. 11 (1999) 581–588. doi:10.1021/cm980373n.

[158] S.C. Moss, D. Adler, H. Fritzche, S. Ovshinsky, Physics of Disordered Materials, Springer US, Boston, MA, 1985. doi:10.1007/978-1-4613-2513-0.

[159] K. Dahmouche, C.V. Santilli, S.H. Pulcinelli, A.F. Craievich, Small-Angle X-ray Scattering Study of Sol−Gel-Derived Siloxane−PEG and Siloxane−PPG Hybrid Materials, J. Phys. Chem. B. 103 (1999) 4937–4942. doi:10.1021/jp984605h.

[160] G. Teufer, The crystal structure of tetragonal ZrO2, Acta Crystallogr. 15 (1962) 1187–1187. doi:10.1107/S0365110X62003114.

[161] L. Fu, R.A.S. Ferreira, A. Valente, J. Rocha, L.D. Carlos, Optically functional nanocomposites with poly(oxyethylene)-based di-ureasils and mesoporous MCM-41, Microporous Mesoporous Mater. 94 (2006) 185–192. doi:10.1016/j.micromeso.2006.03.041.

[162] R.F.P. Pereira, S.C. Nunes, G. Toquer, M.A. Cardoso, A.J.M. Valente, M.C. Ferro, M.M. Silva, L.D. Carlos, R.A.S. Ferreira, V. de Zea Bermudez, Novel Highly Luminescent Amine-Functionalized Bridged Silsesquioxanes, Front. Chem. 5 (2018) 1–15. doi:10.3389/fchem.2017.00131.

[163] R. Rondão, A.R. Frias, S.F.H. Correia, L. Fu, V. de Zea Bermudez, P.S. André, R.A.S. Ferreira, L.D. Carlos, High-Performance Near-Infrared Luminescent Solar Concentrators, ACS Appl. Mater. Interfaces. 9 (2017) 12540–12546. doi:10.1021/acsami.7b02700.

[164] V.T. Freitas, P.P. Lima, R.A.S. Ferreira, L.D. Carlos, E. Pecoraro, S.J.L. Ribeiro, V. De Zea Bermudez, Role of the reactive atmosphere during the sol-gel synthesis on the enhancing of the emission quantum yield of urea cross-linked tripodal siloxane-based hybrids, J. Sol-Gel Sci. Technol. 70 (2014) 227–235. doi:10.1007/s10971-013-3244-x.

[165] H. Sayilkan, Ş. Şsener, E. Şener, E. Arpaç, New metal alkoxides: Synthesis and hydrolysis-condensation reactions; some adsorption features of the hydrolysis-condensation products, J. Mater. Sci. 34 (1999) 5325–5330. doi:10.1023/A:1004701105573.

[166] R.M. Silverstein, G.C. Bassler, Spectrometric identification of organic compounds, J. Chem. Educ. 39 (1962) 546. doi:10.1021/ed039p546.

[167] D.J. Skrovanek, S.E. Howe, P.C. Painter, M.M. Coleman, Hydrogen bonding in polymers: infrared temperature studies of an amorphous polyamide, Macromolecules. 18 (1985) 1676–1683. doi:10.1021/ma00151a006.

[168] V. de Zea Bermudez, R.A.S. Ferreira, L.D. Carlos, C. Molina, K. Dahmouche, S.J.L. Ribeiro, Coordination of Eu3+ Ions in Siliceous Nanohybrids Containing Short Polyether Chains and Bridging Urea Cross-links, J. Phys. Chem. B. 105 (2001) 3378–3386. doi:10.1021/jp002665t.

[169] V.T. Freitas, P.P. Lima, R.A.S. Ferreira, E. Pecoraro, M. Fernandes, V. De Zea Bermudez, L.D. Carlos, Luminescent urea cross-linked tripodal siloxane-based hybrids, J. Sol-Gel Sci. Technol. 65 (2013) 83–92. doi:10.1007/s10971-012-2770-2.

[170] V.T. Freitas, P.P. Lima, V. De Zea Bermudez, R.A.S. Ferreira, L.D. Carlos, Boosting the emission quantum yield of urea cross-linked tripodal poly(oxypropylene)/siloxane hybrids through the variation of catalyst concentration, Eur. J. Inorg. Chem. (2012) 5390–5395. doi:10.1002/ejic.201200823.

[171] U. Schubert, E. Arpac, W. Glaubitt, A. Helmerich, C. Chau, Primary hydrolysis products of methacrylate-modified titanium and zirconium alkoxides, Chem. Mater. 4 (1992) 291–295. doi:10.1021/cm00020a014.

[172] M. Jansen, E. Guenther, Oxide Gels and Ceramics Prepared by a Nonhydrolytic Sol-Gel Process, Chem. Mater. 7 (1995) 2110–2114. doi:10.1021/cm00059a019.

[173] A.Z. Subramanian, P. Neutens, A. Dhakal, R. Jansen, T. Claes, X. Rottenberg, F. Peyskens, S. Selvaraja, P. Helin, B. Dubois, K. Leyssens, S. Severi, P. Deshpande, R. Baets, P. Van Dorpe, Low-Loss Singlemode PECVD silicon nitride photonic wire waveguides for 532-900 nm wavelength window fabricated within a CMOS pilot line, IEEE Photonics J. 5 (2013). doi:10.1109/JPHOT.2013.2292698.

[174] M.W. Urban, Fourier Transform Infrared and Fourier Transform Raman Spectroscopy of Polymers, in: Struct. Relations Polmers, 1993: pp. 3–40. doi:10.1021/ba-1993-0236.ch001.

[175] N.B. Colthup, L.H. Daly, S.E. Wiberley, PREFACE, in: Introd. to Infrared Raman Spectrosc., Thrid edit, Elsevier, San Diego, 1990: pp. xi–xii. doi:10.1016/B978-0-08-091740-5.50003-X.

[176] M.M. Nolasco, P.M. Vaz, V.T. Freitas, P.P. Lima, P.S. André, R.A.S. Ferreira, P.D. Vaz, P. Ribeiro-Claro, L.D. Carlos, Engineering highly efficient Eu(iii)-based tri-ureasil hybrids toward luminescent solar concentrators, J. Mater. Chem. A. 1 (2013) 7339. doi:10.1039/c3ta11463e.

[177] H. Ma, A.K.-Y. Jen, L.R. Dalton, Polymer-Based Optical Waveguides: Materials, Processing, and Devices, Adv. Mater. 14 (2002) 1339–1365. doi:10.1002/1521-4095(20021002)14:19<1339::AID-ADMA1339>3.0.CO;2-O.

[178] Telecordia, Generic Reliability Assurance Requirements for Passive Optical Components, 2010.

[179] Lionnel R. Xavier, Vasco R. Fernandes, C.M.S. Vicente, É. Pécoraro, L.D. Carlos, R.A.S. Ferreira, P.S. André, UV laser photofabrication of waveguide couplers using self-patterning organic-inorganic hybrids, Microw. Opt. Technol. Lett. 53 (2011) 2304–2307. doi:10.1002/mop.

[180] B.-S. Bae, Hybrid Nanocomposites for Nanotechnology: Electronic, Optical, Magnetic and Bio/Medical Applications, Springer, 2009.

[181] J.S. Weiner, D.A.B. Miller, D.S. Chemla, Quadratic electro-optic effect due to the quantum-confined Stark effect in quantum wells, Appl. Phys. Lett. 50 (1987) 842–844. doi:10.1063/1.98008.

[182] C. Vicente, P.G. Marques, E. Pecoraro, I. Bdikin, L.D. Carlos, P.S. Andre, R.A.S. Ferreira, Selective mode launching in multimode UV-patterned channel waveguide in organic-inorganic hybrids, in: Transparent Opt. Networks (ICTON), 2011 13th Int. Conf., 2011: pp. 1–4. doi:10.1109/ICTON.2011.5970889.

[183] V.R. Fernandes, C.M.S. Vicente, E. Pecoraro, D. Karpinsky, A.L. Kholkin, N. Wada, P.S. Andre, R.A.S. Ferreira, Determination of Refractive Index Contrast and Surface Contraction in Waveguide Channels Using Multiobjective Genetic Algorithm Applied to Spectroscopic Ellipsometry, Light. Technol. J. 29 (2011) 2971–2978. doi:10.1109/JLT.2011.2163924.

[184] B. Lebeau, P. Innocenzi, Hybrid materials for optics and photonics, Chem. Soc. Rev. 40 (2011) 886–906. doi:10.1039/C0CS00106F.

[185] C. Chen, X. Sun, F. Wang, F. Zhang, H. Wang, Z. Shi, Z. Cui, D. Zhang, Electro-Optic Modulator Based on Novel Organic-Inorganic Hybrid Nonlinear Optical Materials, Quantum Electron. IEEE J. 48 (2012) 61–66. doi:10.1109/JQE.2011.2179019.

[186] M.H. Ibrahim, A.S. Abdullah, A. Nawabjan, N.M. Kassim, A.B. Mohammad, A.S.M. Supa'at, A thermo-optic multimode interference switch structure based on vinyltriethoxysilane (VTES) hybrid organic–inorganic sol–gel, Opt. - Int. J. Light Electron Opt. 124 (2013) 1532–1535.

doi:http://dx.doi.org/10.1016/j.ijleo.2012.05.001.
[187] A. Moujoud, W.S. Kim, B.S. Bae, S.Y. Shin, Thermally stable optical characteristics of sol-gel hybrid material films, Appl. Phys. Lett. 88 (2006) 101916. doi:10.1063/1.2186111.
[188] F. Ay, A. Kocabas, C. Kocabas, A. Aydinli, S. Agan, Prism coupling technique investigation of elasto-optical properties of thin polymer films, J. Appl. Phys. 96 (2004) 7147. doi:10.1063/1.1812823.
[189] M.F. Hossain, H.P. Chan, M.A. Uddin, Study of optical anisotropies in benzocyclobutene thin films for the efficient design of optical waveguide devices, Opt. Express. 18 (2010) 8896. doi:10.1364/OE.18.008896.
[190] Z. Zhang, P. Zhao, P. Lin, F. Sun, Thermo-optic coefficients of polymers for optical waveguide applications, Polymer (Guildf). 47 (2006) 4893–4896. doi:10.1016/j.polymer.2006.05.035.
[191] J. Gosciniak, L. Markey, A. Dereux, S.I. Bozhevolnyi, Efficient thermo-optically controlled Mach-Zhender interferometers using dielectric-loaded plasmonic waveguides, Opt. Express. 20 (2012) 16300–16309. doi:10.1364/OE.20.016300.
[192] J. Chen, T. Zhang, J. Zhu, X. Zhang, J. Zhou, J. Fan, G. Hu, Low-loss planar optical waveguides fabricated from polycarbonate, Polym. Eng. Sci. 49 (2009) 2015–2019. doi:10.1002/pen.21441.
[193] K. Hassan, J.-C. Weeber, L. Markey, A. Dereux, A. Pitilakis, O. Tsilipakos, E.E. Kriezis, Thermo-optic plasmo-photonic mode interference switches based on dielectric loaded waveguides, Appl. Phys. Lett. 99 (2011) 241110. doi:10.1063/1.3670500.
[194] T. Watanabe, N. Ooba, S. Hayashida, T. Kurihara, S. Imamura, Polymeric optical waveguide circuits formed using silicone resin, Light. Technol. J. 16 (1998) 1049–1055. doi:10.1109/50.681462.
[195] K.K. Tung, W.H. Wong, E.Y.B. Pun, Polymeric optical waveguides using direct ultraviolet photolithography process, Appl. Phys. A. 80 (2005) 621–626. doi:10.1007/s00339-003-2248-8.
[196] M.F. Hossain, H.P. Chan, M.A. Uddin, Simultaneous measurement of thermo-optic and stress-optic coefficients of polymer thin films using prism coupler technique, Appl. Opt. 49 (2010) 403–408. doi:10.1364/AO.49.000403.
[197] L. Jinhua, Q. Fengxian, C. Guorong, G. Yijun, S. Qiang, Y. Dongya, G. Qing, Chiral Azo polyurethane(urea): Preparation, optical properties and low power consumption polymeric thermo-optic switch, J. Polym. Sci. Part B Polym. Phys. 49 (2011) 939–948. doi:10.1002/polb.22266.
[198] X. Li, Z. Cao, Q. Shen, Y. Yang, Influence of dopant concentration on thermo-optic properties of PMMA composite, Mater. Lett. 60 (2006) 1238–1241. doi:10.1016/j.matlet.2005.11.005.
[199] M. He, Y. Zhou, J. Dai, R. Liu, Y. Cui, T. Zhang, Synthesis and nonlinear optical properties of soluble fluorinated polyimides containing hetarylazo chromophores with large hyperpolarizability, Polymer (Guildf). 50 (2009) 3924–3931. doi:10.1016/j.polymer.2009.06.057.
[200] H.Y. Paul, Z. Zhiyi, R. Jacques, Compressed-gas-induced crystallization in tert-butyl poly(ether ether ketone), J. Polym. Sci. Part B Polym. Phys. 39 (2001) 1505–1512. doi:10.1002/polb.1122.
[201] T. Han, S. Madden, M. Zhang, R. Charters, B. Luther-Davies, Low loss high index contrast nanoimprinted polysiloxane waveguides, Opt. Express. 17 (2009) 2623–2630. doi:10.1364/OE.17.002623.
[202] X. Wang, L. Xu, D. Li, L. Liu, W. Wang, Thermo-optic properties of sol-gel-fabricated organic-inorganic hybrid waveguides, J. Appl. Phys. 94 (2003) 4228–4230. doi:10.1063/1.1604476.
[203] E.S. Kang, T.H. Lee, B.S. Bae, Measurement of the thermo-optic coefficients in sol-gel derived inorganic-organic hybrid material films, Appl. Phys. Lett. 81 (2002) 1438–1440. doi:10.1063/1.1501448.
[204] H. Zhang, J. Wang, L. Li, Y. Song, M. Zhao, X. Jian, Synthesis of liquid polysilisiquioxane resins and properties of cured films, Thin Solid Films. 517 (2008) 857–862. doi:10.1016/j.tsf.2008.05.056.
[205] M. Pokrass, Z. Burshtein, R. Gvishi, Thermo-optic coefficient in some hybrid organic/inorganic fast sol–gel glasses, Opt. Mater. (Amst). 32 (2010) 975–981. doi:10.1016/j.optmat.2010.01.038.
[206] J.C. Pincenti, S. Goel, D.L. Naylor, Thermally induced birefringence and stress in poly(methyl methacrylate) waveguides on oxidized silicon substrates, Appl. Opt. 32 (1993) 322–326. doi:10.1364/AO.32.000322.
[207] L. Shi, L. Tian, X. Chen, Electro-optic chirality control in MgO:PPLN, J. Appl. Phys. 112 (2012) 073103. doi:10.1063/1.4754861.
[208] M. Okuno, A. Sugita, K. Jinguji, M. Kawachi, Birefringence control of silica waveguides on Si and its application to a polarization-beam splitter/switch, J. Light. Technol. 12 (1994) 625–633. doi:10.1109/50.285356.
[209] B.R. Acharya, K.W. Baldwin, R.A. MacHarrie, J.A. Rogers, C.C. Huang, R. Pindak, In-fiber nematic liquid crystal optical modulator based on in-plane switching with microsecond response time, Appl. Phys. Lett. 81 (2002) 5243. doi:10.1063/1.1532532.
[210] J. Kim, S. Park, W. Chu, M. Oh, Integrated-optic polarization controllers incorporating polymer waveguide birefringence modulators., Opt. Express. 20 (2012) 12443–8. doi:10.1364/OE.20.012443.
[211] G. Raybon, A. Adamiecki, P.J. Winzer, S. Randel, L. Salamanca, A. Konczykowska, F. Jorge, J.Y. Dupuy,

L.L. Buhl, S. Chandrashekhar, C. Xie, S. Draving, M. Grove, K. Rush, R. Urbanke, High symbol rate coherent optical transmission systems: 80 and 107 Gbaud, J. Light. Technol. 32 (2014) 824–831. doi:10.1109/JLT.2013.2286963.

[212] S.J. Savory, Digital filters for coherent optical receivers, Opt. Express. 16 (2008) 804. doi:10.1364/OE.16.000804.

[213] M.G. Taylor, Phase Estimation Methods for Optical Coherent Detection Using Digital Signal Processing, J. Light. Technol. 27 (2009) 901–914. doi:10.1109/JLT.2008.927778.

[214] S.H. Jeong, K. Morito, Novel optical 90° hybrid consisting of a paired interference based 2x4 MMI coupler, a phase shifter and a 2x2 MMI coupler, J. Light. Technol. 28 (2010) 1323–1331. doi:10.1109/JLT.2010.2042278.

[215] P. Dong, C. Xie, L.L. Buhl, Monolithic coherent receiver based on 120-degree optical hybrids on silicon, Conf. Opt. Fiber Commun. Tech. Dig. Ser. 22 (2014) 2119–2125. doi:10.1109/OFC.2014.6887028.

[216] M. Kroh, J. Wang, A. Theurer, C. Zawadzki, D. Schmidt, R. Ludwig, M. Lauermann, A. Beling, A. Matiss, C. Schubert, A. Steffan, N. Keil, N. Grote, Coherent Receiver for 100G Ethernet Applications Based on Polymer Planar Lightwave Circuit, in: OSA (Ed.), 37th Eur. Conf. Expo. Opt. Commun., OSA, Washington, D.C., 2011: p. Tu.3.LeSaleve.2. doi:10.1364/ECOC.2011.Tu.3.LeSaleve.2.

[217] T. Richter, M. Kroh, J. Wang, A. Theurer, C. Zawadzki, Z. Zhang, N. Keil, A.G. Steffan, C. Schubert, Integrated Polarization-Diversity Coherent Receiver on Polymer PLC for QPSK and QAM signals, Opt. Fiber Commun. Conf. (2012) OW3G.1. doi:10.1364/OFC.2012.OW3G.1.

[218] J. Wang, M. Kroh, T. Richter, A. Theurer, A. Matiss, C. Zawadzki, Z. Zhang, C. Schubert, A. Steffan, N. Grote, N. Keil, Hybrid-integrated polarization diverse coherent receiver based on polymer PLC, IEEE Photonics Technol. Lett. 24 (2012) 1718–1721. doi:10.1109/LPT.2012.2213299.

[219] G.P. Agrawal, Optical Receivers, in: Fiber-Optic Commun. Syst., John Wiley & Sons, Inc., 2011: pp. 128–181. doi:10.1002/9780470918524.ch4.

[220] M. Aamer, N. Sotiropoulos, A. Brimont, J.-M. Fedeli, D. Marris-Morini, E. Cassan, L. Vivien, K. Ribaud, P. Grosse, J.M. Hartmann, D. Vermeulen, G. Roelkens, P. Sanchis, A. Hakansson, A Silicon Differential Receiver With Zero-Biased Balanced Detection for Access Networks, IEEE Photonics Technol. Lett. 25 (2013) 1207–1210. doi:10.1109/LPT.2013.2262931.

[221] J.-H. Kim, J.-S. Choe, K.-S. Choi, C.-J. Youn, D.-J. Kim, S.-H. Jang, Y.-H. Kwon, E.-S. Nam, Hybrid-integrated coherent receiver using silica-based planar lightwave circuit technology, Optoelectron. Mater. Devices VI, Asia Commun. Photonics, SPIE. 8308 (2011) 830824-830824–6. doi:10.1117/12.905571.

[222] R. Schmogrow, B. Nebendahl, M. Winter, A. Josten, D. Hillerkuss, S. Koenig, J. Meyer, M. Dreschmann, M. Huebner, C. Koos, J. Becker, W. Freude, J. Leuthold, Error Vector Magnitude as a Performance Measure for Advanced Modulation Formats, IEEE Photonics Technol. Lett. 24 (2012) 2198. doi:10.1109/lpt.2012.2219471.

[223] F. Chang, K. Onohara, T. Mizuochi, Forward error correction for 100 G transport networks, IEEE Commun. Mag. 48 (2010) S48–S55. doi:10.1109/MCOM.2010.5434378.

[224] A. Matiss, S. Bottacchi, J.K. Fischer, R. Ludwig, C.C. Leonhardt, C. Schmidt-Langhorst, C. Schubert, Performance of an integrated coherent receiver module for up to 160G DP-QPSK transmission systems, J. Light. Technol. 29 (2011) 1026–1032. doi:10.1109/JLT.2011.2109937.

[225] A. Beling, N. Ebel, A. Matiss, G. Unterbörsch, M. Nölle, J.K. Fischer, J. Hilt, L. Molle, C. Schubert, F. Verluise, L. Fulop, Fully-integrated polarization-diversity coherent receiver module for 100G DP-QPSK, Opt. Fiber Commun. Conf. (2011) 1–3. doi:10.1364/OFC.2011.OML5.

[226] V.E. Houtsma, N.N.G. Weimann, T.-C. Hu, R. Kopf, A. Tate, J. Frackoviak, R. Reyes, Y.-K.Y.-K. Chen, L. Zhang, C.R. Doerr, D.D.T. Neilson, L. Zhang, D.D.T. Neilson, Manufacturable monolithically integrated InP dual-port coherent receiver for 100G PDM-QPSK applications, Opt. Fiber Commun. Conf. Fiber Opt. Eng. Conf. 2011. (2011) 1–3. doi:10.1364/OFC.2011.OML2.

[227] M. Lauermann, C. Weimann, A. Knopf, W. Heni, R. Palmer, S. Koeber, D.L. Elder, W. Bogaerts, J. Leuthold, L.R. Dalton, C. Rembe, W. Freude, C. Koos, Integrated optical frequency shifter in silicon-organic hybrid (SOH) technology, Opt. Express. 24 (2016) 11694–11707. doi:10.1364/OE.24.011694.

[228] K. Liu, C.R. Ye, S. Khan, V.J. Sorger, Review and perspective on ultrafast wavelength-size electro-optic modulators, Laser Photon. Rev. 9 (2015) 172–194. doi:10.1002/lpor.201400219.

[229] P. Günter, ed., Nonlinear Optical Effects and Materials, Springer Berlin Heidelberg, Berlin, Heidelberg, 2000. doi:10.1007/978-3-540-49713-4.

[230] V. Katopodis, P. Groumas, Z. Zhang, R. Dinu, E. Miller, A. Konczykowska, J.-Y. Dupuy, A. Beretta, A. Dede, J.H. Choi, P. Harati, F. Jorge, V. Nodjiadjim, M. Riet, G. Cangini, A. Vannucci, N. Keil, H.-G. Bach, N. Grote, H. Avramopoulos, C. Kouloumentas, Polymer enabled 100Gbaud connectivity for datacom applications, Opt. Commun. 362 (2016) 13–21. doi:10.1016/j.optcom.2015.07.064.

[231] H. Zwickel, T. De Keulenaer, S. Wolf, C. Kieninger, Y. Kutuvantavida, M. Lauermann, M. Verplaetse, R. Pierco, R. Vaernewyck, A. Vyncke, X. Yin, G. Torfs, W. Freude, E. Mentovich, J. Bauwelinck, C. Koos,

100 Gbit/s Serial Transmission Using a Silicon-Organic Hybrid (SOH) Modulator and a Duobinary Driver IC, Opt. Fiber Commun. Conf. (2017) W4I.5. doi:10.1364/OFC.2017.W4I.5.

[232] B. Chmielak, M. Waldow, C. Matheisen, C. Ripperda, J. Bolten, T. Wahlbrink, M. Nagel, F. Merget, H. Kurz, Pockels effect based fully integrated, strained silicon electro-optic modulator, Opt. Express. 19 (2011) 17212. doi:10.1364/OE.19.017212.

[233] B.E. a Saleh, M.C. Teich, C.J. Wiley, Fundamentals of Photonics, in: Fundam. Photonics, 1991: pp. 696–736. doi:10.1002/0471213748.ch18.

[234] S. Wolf, H. Zwickel, C. Kieninger, Y. Kutuvantavida, M. Lauermann, J. Lutz, L. Altenhain, R. Schmid, W. Freude, C. Koos, S. Randel, Silicon-Organic Hybrid (SOH) IQ Modulator for 100 GBd 16QAM Operation, in: Opt. Fiber Commun. Conf. Postdeadline Pap., OSA, Washington, D.C., 2017: p. Th5C.1. doi:10.1364/OFC.2017.Th5C.1.

[235] C. Hoessbacher, A. Josten, B. Baeuerle, Y. Fedoryshyn, H. Hettrich, Y. Salamin, W. Heni, C. Haffner, R. Schmid, D. Elder, D. Hillerkuss, M. Moeller, L. Dalton, J. Leuthold, Broadband Plasmonic Modulator Enabling Single Carrier Operation Beyond 100 Gbit/s, in: Opt. Fiber Commun. Conf., OSA, Washington, D.C., 2017: p. W4I.6. doi:10.1364/OFC.2017.W4I.6.

[236] R.S. Weis, T.K. Gaylord, Lithium niobate: Summary of physical properties and crystal structure, Appl. Phys. A. 37 (1985) 191–203. doi:10.1007/BF00614817.

[237] H. Xu, X. Xiao, X. Li, Y. Hu, Z. Li, T. Chu, Y. Yu, J. Yu, High speed silicon Mach-Zehnder modulator based on interleaved PN junctions., Opt. Express. 20 (2012) 15093–9. doi:10.1364/OE.20.015093.

[238] P. Dong, L. Chen, Y. Chen, High-speed low-voltage single-drive push-pull silicon Mach-Zehnder modulators, Opt. Express. 20 (2012) 6163. doi:10.1364/OE.20.006163.

[239] K. Tsuzuki, T. Ishibashi, T. Ito, S. Oku, Y. Shibata, R. Iga, Y. Kondo, Y. Tohmori, 40 Gbit/s n–i–n InP Mach–Zehnder modulator with a voltage of 2.2 V, Electron. Lett. 39 (2003) 1464. doi:10.1049/el:20030939.

[240] P. Pust, P.J. Schmidt, W. Schnick, A revolution in lighting, Nat. Mater. 14 (2015) 454–458. doi:10.1038/nmat4270.

[241] S.R. Forrest, The path to ubiquitous and low-cost organic electronic appliances on plastic, Nature. 428 (2004) 911–918. doi:10.1038/nature02498.

[242] OLED Light, LG Disp. Co., Ltd. (2014). http://www.lgdisplay.com/eng/product/oled_light.jsp (accessed May 23, 2018).

[243] A new TV experience awakens, SONY Eur. Ltd. (2018). https://www.sony.co.uk/electronics/televisions/af8-series (accessed May 23, 2018).

[244] F. Hide, P. Kozodoy, S.P. DenBaars, A.J. Heeger, White light from InGaN/conjugated polymer hybrid light-emitting diodes, Appl. Phys. Lett. 70 (1997) 2664–2666. doi:10.1063/1.118989.

[245] M.T. Sajjad, P.P. Manousiadis, H. Chun, D.A. Vithanage, S. Rajbhandari, A.L. Kanibolotsky, G. Faulkner, D. O'Brien, P.J. Skabara, I.D.W. Samuel, G.A. Turnbull, Novel Fast Color-Converter for Visible Light Communication Using a Blend of Conjugated Polymers, ACS Photonics. 2 (2015) 194–199. doi:10.1021/ph500451y.

[246] D.A. Vithanage, A.L. Kanibolotsky, S. Rajbhandari, P.P. Manousiadis, M.T. Sajjad, H. Chun, G.E. Faulkner, D.C. O'Brien, P.J. Skabara, I.D.W. Samuel, G.A. Turnbull, Polymer colour converter with very high modulation bandwidth for visible light communications, J. Mater. Chem. C. 5 (2017) 8916–8920. doi:10.1039/C7TC03787B.

[247] H. Chun, S. Rajbhandari, G. Faulkner, D. O'Brien, Effectiveness of blue-filtering in WLED based indoor Visible light communication, in: 2014 3rd Int. Work. Opt. Wirel. Commun., 2014: pp. 60–64. doi:10.1109/IWOW.2014.6950777.

[248] M. Karl, J.M.E. Glackin, M. Schubert, N.M. Kronenberg, G.A. Turnbull, I.D.W. Samuel, M.C. Gather, Flexible and ultra-lightweight polymer membrane lasers, Nat. Commun. 9 (2018) 1525. doi:10.1038/s41467-018-03874-w.

[249] Y. Enami, C.T. Derose, D. Mathine, C. Loychik, C. Greenlee, R.A. Norwood, T.D. Kim, J. Luo, Y. Tian, A.K. Jen, N. Peyghambarian, Hybrid polymer / sol – gel waveguide modulators with exceptionally large electro – optic coefficients, Nat. Photonics. 1 (2007) 27–30. doi:10.1038/nphoton.2007.25.

[250] D. Amarasinghe, A. Ruseckas, G.A. Turnbull, I.D.W. Samuel, Organic Semiconductor Optical Amplifiers, Proc. IEEE. 97 (2009) 1637–1650. doi:10.1109/JPROC.2009.2023250.

[251] J. Clark, L. Bazzana, D.D.C. Bradley, J. Cabanillas-Gonzalez, G. Lanzani, D.G. Lidzey, J. Morgado, A. Nocivelli, W.C. Tsoi, T. Virgili, R. Xia, Blue polymer optical fiber amplifiers based on conjugated fluorene oligomers., J. Nanophotonics. 2 (2008) No pp. given. doi:10.1117/1.2902341.

[252] A. Dimali, R. Arvydas, V.A. E., T.G. A., S.I.D. W., High-Gain Broadband Solid-State Optical Amplifier using a Semiconducting Copolymer, Adv. Mater. 21 (2008) 107–110. doi:10.1002/adma.200801930.

[253] J.R.C. Smirnov, Q. Zhang, R. Wannemacher, L. Wu, S. Casado, R. Xia, I. Rodriguez, J. Cabanillas-González, Flexible all-polymer waveguide for low threshold amplified spontaneous emission, Sci. Rep. 6

(2016) 34565. doi:10.1038/srep34565.

[254] Y. Tamai, H. Ohkita, H. Benten, S. Ito, Exciton Diffusion in Conjugated Polymers: From Fundamental Understanding to Improvement in Photovoltaic Conversion Efficiency, J. Phys. Chem. Lett. 6 (2015) 3417–3428. doi:10.1021/acs.jpclett.5b01147.

[255] W. Niamh, K. Mario, A. Jochen, S. Ullrich, E.R. C., Tunable White-Light Emission from Conjugated Polymer-Di-Ureasil Materials, Adv. Funct. Mater. 26 (2015) 532–542. doi:10.1002/adfm.201504017.

[256] L.D. Carlos, R.A.S. Ferreira, R.N. Pereira, M. Assunção, V. de Zea Bermudez, White-Light Emission of Amine-Functionalized Organic/Inorganic Hybrids: Emitting Centers and Recombination Mechanisms, J. Phys. Chem. B. 108 (2004) 14924–14932. doi:10.1021/jp049052r.

[257] L. Fu, R.A.S. Ferreira, M. Fernandes, S.C. Nunes, V. de Zea Bermudez, G. Hungerford, J. Rocha, L.D. Carlos, Photoluminescence and quantum yields of organic/inorganic hybrids prepared through formic acid solvolysis, Opt. Mater. (Amst). 30 (2008) 1058–1064. doi:10.1016/j.optmat.2007.05.011.

[258] C.M.S. Vicente, P.P. Lima, V. de Zea Bermudez, L.D. Carlos, P.S. André, R.A.S. Ferreira, Fabrication of low-cost thermo-optic variable wave plate based on waveguides patterned on di-ureasil hybrids, Opt. Express. 22 (2014) 27159–68. doi:10.1364/OE.22.027159.

[259] K. Adarsh, M. Barry, C. Steve, E.R. C., Design and Response of High-Efficiency, Planar, Doped Luminescent Solar Concentrators Using Organic–Inorganic Di-Ureasil Waveguides, Adv. Opt. Mater. 4 (2015) 444–456. doi:10.1002/adom.201500412.

[260] I. Meazzini, C. Blayo, J. Arlt, A.-T. Marques, U. Scherf, H.D. Burrows, R.C. Evans, Ureasil organic–inorganic hybrids as photoactive waveguides for conjugated polyelectrolyte luminescent solar concentrators, Mater. Chem. Front. 1 (2017) 2271–2282. doi:10.1039/C7QM00264E.

[261] C.S.F. H., F.A. R., F. Lianshe, R. Raquel, P. Edison, R.S.J. L., A.P. S., F.R.A. S., C.L. D., Large-Area Tunable Visible-to-Near-Infrared Luminescent Solar Concentrators, Adv. Sustain. Syst. 0 (2018) 1800002. doi:10.1002/adsu.201800002.

[262] A.R. Frias, E. Pecoraro, S.F.H. Correia, L.M.G. Minas, A.R. Bastos, S. Garcia-Revilla, R. Balda, S.J.L. Ribeiro, P.S. Andre, L.D. Carlos, R.A.S. Ferreira, Sustainable luminescent solar concentrators based on organic-inorganic hybrids modified with chlorophyll, J. Mater. Chem. A. 6 (2018) 8712–8723. doi:10.1039/C8TA01712C.

[263] L. Dal Negro, P. Bettotti, M. Cazzanelli, D. Pacifici, L. Pavesi, Applicability conditions and experimental analysis of the variable stripe length method for gain measurements, Opt. Commun. 229 (2004) 337–348. doi:10.1016/j.optcom.2003.10.051.

[264] U. Scherf, E.J.W. List, Semiconducting Polyfluorenes—Towards Reliable Structure-Property Relationships, Adv. Mater. 14 (2002) 477–487. doi:10.1002/1521-4095(20020404)14:7<477::AID-ADMA477>3.0.CO;2-9.

[265] N.C. George, K.A. Denault, R. Seshadri, Phosphors for Solid-State White Lighting, Annu. Rev. Mater. Res. 43 (2013) 481–501. doi:10.1146/annurev-matsci-073012-125702.

[266] J. Graffion, A.M. Cojocariu, X. Cattoën, R.A.S. Ferreira, V.R. Fernandes, P.S. André, L.D. Carlos, M. Wong Chi Man, J.R. Bartlett, Luminescent coatings from bipyridine-based bridged silsesquioxanes containing Eu3+ and Tb3+ salts, J. Mater. Chem. 22 (2012) 13279. doi:10.1039/c2jm31289a.

[267] J. Graffion, X. Cattoën, M. Wong Chi Man, V.R. Fernandes, P.S. André, R.A.S. Ferreira, L.D. Carlos, Modulating the Photoluminescence of Bridged Silsesquioxanes Incorporating Eu 3+ -Complexed n , n '-Diureido-2,2'-bipyridine Isomers: Application for Luminescent Solar Concentrators, Chem. Mater. 23 (2011) 4773–4782. doi:10.1021/cm2019026.

[268] E. Pecoraro, R.A.S. Ferreira, C. Molina, S.J.L. Ribeiro, Y. Messsaddeq, L.D. Carlos, Photoluminescence of bulks and thin films of Eu3+-doped organic/inorganic hybrids, J. Alloys Compd. 451 (2008) 136–139. doi:10.1016/j.jallcom.2007.04.123.

[269] H.D. Burrows, V.M.M. Lobo, J. Pina, M.L. Ramos, J. Seixas de Melo, A.J.M. Valente, M.J. Tapia, S. Pradhan, U. Scherf, Fluorescence Enhancement of the Water- Soluble Poly{1,4-phenylene-[9,9-bis- (4-phenoxybutylsulfonate)]fluorene-2,7-diyl} Copolymer in n-Dodecylpentaoxyethylene Glycol Ether Micelles, Macromolecules. 37 (2004) 7425–7427. doi:10.1021/ma048780+.

[270] H.D. Burrows, M.J. Tapia, S.M. Fonseca, A.J.M. Valente, V.M.M. Lobo, L.L.G. Justino, S. Qiu, S. Pradhan, U. Scherf, N. Chattopadhyay, M. Knaapila, V.M. Garamus, Aqueous Solution Behavior of Anionic Fluorene-co-thiophene-Based Conjugated Polyelectrolytes, ACS Appl. Mater. Interfaces. 1 (2009) 864–874. doi:10.1021/am800267n.

[271] R.C. Evans, A.G. Macedo, S. Pradhan, U. Scherf, L.D. Carlos, H.D. Burrows, Fluorene based conjugated polyelectrolyte/silica nanocomposites: Charge-mediated phase aggregation at the organic-inorganic interface, Adv. Mater. 22 (2010) 3032–3037. doi:10.1002/adma.200904377.

[272] R.C. Evans, P.C. Marr, Chain confinement promotes β-phase formation in polyfluorene-based photoluminescent ionogels, Chem. Commun. 48 (2012) 3742–3744. doi:10.1039/c2cc18022g.

[273] M.C. Gonçalves, N.J.O. Silva, V. De Zea Bermudez, R.A.S. Ferreira, L.D. Carlos, K. Dahmouche, C. V. Santilli, D. Ostrovskii, I.C.C. Vilela, A.F. Craievich, Local structure and near-infrared emission features of neodymium-based amine functionalized organic/inorganic hybrids, J. Phys. Chem. B. 109 (2005) 20093–20104. doi:10.1021/jp052097n.

[274] H. Wu, X. Zhang, C. Guo, J. Xu, M. Wu, Q. Su, Three-band white light from InGaN-based blue LED chip precoated with Green/red phosphors, IEEE Photonics Technol. Lett. 17 (2005) 1160–1162. doi:10.1109/LPT.2005.846504.

[275] J. Yi, Q. Niu, W. Xu, L. Hao, L. Yang, L. Chi, Y. Fang, J. Huang, R. Xia, Significant Lowering Optical Loss of Electrodes via using Conjugated Polyelectrolytes Interlayer for Organic Laser in Electrically Driven Device Configuration, Sci. Rep. 6 (2016) 25810. doi:10.1038/srep25810.

[276] R.A.S. Ferreira, P.S. André, L.D. Carlos, Organic–inorganic hybrid materials towards passive and active architectures for the next generation of optical networks, Opt. Mater. (Amst). 32 (2010) 1397–1409. doi:10.1016/j.optmat.2010.06.019.

[277] G. Heliotis, D.D.C. Bradley, G.A. Turnbull, I.D.W. Samuel, Light amplification and gain in polyfluorene waveguides, Appl. Phys. Lett. 81 (2002) 415–417. doi:10.1063/1.1494473.

[278] R. Xia, G. Heliotis, Y. Hou, D.D.C. Bradley, Fluorene-based conjugated polymer optical gain media, Org. Electron. 4 (2003) 165–177. doi:10.1016/j.orgel.2003.08.009.

[279] S.Y. Lam, M.J. Damzen, Characterisation of solid-state dyes and their use as tunable laser amplifiers, Appl. Phys. B Lasers Opt. 77 (2003) 577–584. doi:10.1007/s00340-003-1285-5.

[280] H. Rabbani-Haghighi, Ś. Forget, Ś. Chńais, A. Siove, M.C. Castex, E. Ishow, Laser operation in nondoped thin films made of a small-molecule organic red-emitter, Appl. Phys. Lett. 95 (2009) 1–4. doi:10.1063/1.3182820.

[281] D. Mohan, A. Gaur, A.K. Sharma, R.D. Singh, Photoquenching in laser grade dyes: Part I, J. Lumin. 43 (1989) 363–368. doi:10.1016/0022-2313(89)90039-2.

[282] C. Zenz, W. Graupner, S. Tasch, G. Leising, K. Iskra, J. Flieser, T. Neger, Highly directional stimulated emission from a polymer waveguide, J. Appl. Phys. 84 (1998) 5445–5450. doi:10.1063/1.368858.

[283] M. McGehee, R. Gupta, S. Veenstra, E. Miller, M. Díaz-García, A. Heeger, Amplified spontaneous emission from photopumped films of a conjugated polymer, Phys. Rev. B. 58 (1998) 7035–7039. doi:10.1103/PhysRevB.58.7035.

[284] S. Zuppolini, G. Quero, M. Consales, L. Diodato, P. Vaiano, A. Venturelli, M. Santucci, F. Spyrakis, M.P. Costi, M. Giordano, A. Cutolo, A. Cusano, A. Borriello, Label-free fiber optic optrode for the detection of class C β-lactamases expressed by drug resistant bacteria, Biomed. Opt. Express. 8 (2017) 5191. doi:10.1364/BOE.8.005191.

[285] G. Quero, S. Zuppolini, M. Consales, L. Diodato, P. Vaiano, A. Venturelli, M. Santucci, F. Spyrakis, M.P. Costi, M. Giordano, A. Borriello, A. Cutolo, A. Cusano, Long period fiber grating working in reflection mode as valuable biosensing platform for the detection of drug resistant bacteria, Sensors Actuators B Chem. 230 (2016) 510–520. doi:10.1016/j.snb.2016.02.086.

[286] E. Brzozowska, M. Koba, M. Śmietana, S. Górska, M. Janik, A. Gamian, W.J. Bock, Label-free Gram-negative bacteria detection using bacteriophage-adhesin-coated long-period gratings, Biomed. Opt. Express. 7 (2016) 829. doi:10.1364/BOE.7.000829.

[287] S.-H. Ohk, A.K. Bhunia, Multiplex fiber optic biosensor for detection of Listeria monocytogenes, Escherichia coli O157:H7 and Salmonella enterica from ready-to-eat meat samples, Food Microbiol. 33 (2013) 166–171. doi:10.1016/j.fm.2012.09.013.

[288] D. V. Lim, Detection of microorganisms and toxins with evanescent wave fiber-optic biosensors, Proc. IEEE. 91 (2003) 902–907. doi:10.1109/JPROC.2003.813574.

[289] D. Ivnitski, Biosensors for detection of pathogenic bacteria, Biosens. Bioelectron. 14 (1999) 599–624. doi:10.1016/S0956-5663(99)00039-1.

[290] O. Lazcka, F.J. Del Campo, F.X. Muñoz, Pathogen detection: A perspective of traditional methods and biosensors, Biosens. Bioelectron. 22 (2007) 1205–1217. doi:10.1016/j.bios.2006.06.036.

[291] P.M. Griffin, R. V. Tauxe, The epidemiology of infections caused by Escherichia coli O157:H7, other enterohemorrhagic E. coli, and the associated hemolytic uremic syndrome., Epidemiol. Rev. 13 (1991) 60–98. doi:10.1093/oxfordjournals.epirev.a036079.

[292] R.B. Helling, C.N. Vargas, J. Adams, Evolution of Escherichia coli during growth in a constant environment., Genetics. 116 (1987) 349–358. doi:10.1111/j.1574-6968.1999.tb13521.x.

[293] I. Lumerical Solutions, Asymmetric slab dielectric waveguide, Lumerical Home Appl. (2017) Photonic Integrated Circuits. https://kb.lumerical.com/en/pic_passive_waveguides_asymmetric_slab_dielectric.html Acess date 2018-03-09 (accessed March 9, 2018).

[294] R.G. Heideman, R.P.H. Kooyman, J. Greve, Performance of a highly sensitive optical waveguide Mach-Zehnder interferometer immunosensor, Sensors Actuators B Chem. 10 (1993) 209–217.

doi:10.1016/0925-4005(93)87008-D.
[295] M.L. DePamphilis, S.D. Bell, Genome duplication, Garland Science, Taylor and Francis Group, New York, NY, 2011.
[296] H.J. Nielsen, B. Youngren, F.G. Hansen, S. Austin, Dynamics of Escherichia coli chromosome segregation during multifork replication, J. Bacteriol. 189 (2007) 8660–8666. doi:10.1128/JB.01212-07.
[297] H.A. Lorentz, The Theory of Electrons and Its Applications to the Phenomena of Light and Radiant Heat, Courier Corporation, New York, 1909.
[298] R. Phillips, J. Kondev, J. Theriot, H. Garcia, B. Chasan, Physical Biology of the Cell, Garland Science, Taylor and Francis Group, London, 2010. doi:10.1119/1.3459039.
[299] M.I. Zibaii, A. Kazemi, H. Latifi, M.K. Azar, S.M. Hosseini, M.H. Ghezelaiagh, Measuring bacterial growth by refractive index tapered fiber optic biosensor, J. Photochem. Photobiol. B Biol. 101 (2010) 313–320. doi:10.1016/j.jphotobiol.2010.07.017.
[300] H.-C. Ren, F. Vollmer, S. Arnold, A. Libchaber, High-Q microsphere biosensor - analysis for adsorption of rodlike bacteria., Opt. Express. 15 (2007) 17410–17423. doi:10.1364/OE.15.017410.
[301] P.-S. Liang, T.S. Park, J.-Y. Yoon, Rapid and reagentless detection of microbial contamination within meat utilizing a smartphone-based biosensor, Sci. Rep. 4 (2015) 5953. doi:10.1038/srep05953.
[302] K. Qin, S. Hu, S.T. Retterer, I.I. Kravchenko, S.M. Weiss, Slow light Mach–Zehnder interferometer as label-free biosensor with scalable sensitivity, Opt. Lett. 41 (2016) 753. doi:10.1364/OL.41.000753.
[303] M. Hofmann, Y. Xiao, S. Sherman, U. Gleissner, T. Schmidt, H. Zappe, Asymmetric Mach-Zehnder interferometers without an interaction window in polymer foils for refractive index sensing., Appl. Opt. 55 (2016) 1124–31. doi:10.1364/AO.55.001124.
[304] A. Crespi, Y. Gu, B. Ngamsom, H.J.W.M. Hoekstra, C. Dongre, M. Pollnau, R. Ramponi, H.H. van den Vlekkert, P. Watts, G. Cerullo, R. Osellame, Three-dimensional Mach-Zehnder interferometer in a microfluidic chip for spatially-resolved label-free detection, Lab Chip. 10 (2010) 1167–1173. doi:10.1039/B920062B.
[305] M. Wang, J. Hiltunen, C. Liedert, L. Hakalahti, R. Myllylä, An integrated young interferometer based on UV-imprinted polymer waveguides for label-free biosensing applications, J. Eur. Opt. Soc. 7 (2012). doi:10.2971/jeos.2012.12019.
[306] T. Schubert, N. Haase, H. Ktick, Refractive-index measurements using an integrated Mach-Zehnder interferometer, Sensors And Actuators. 60 (1997) 108–112. doi:10.1016/S0924-4247(97)01380-0.
[307] B.H. Schneider, J.G. Edwards, N.F. Hartman, Hartman interferometer: Versatile integrated optic sensor for label- free, real-time quantification of nucleic acids, proteins, and pathogens, Clin. Chem. 43 (1997) 1757–1763.
[308] O. Zhernovaya, O. Sydoruk, V. Tuchin, A. Douplik, The refractive index of human hemoglobin in the visible range, Phys. Med. Biol. 56 (2011) 4013–4021. doi:10.1088/0031-9155/56/13/017.
[309] J. Shiloach, R. Fass, Growing E. coli to high cell density - A historical perspective on method development, Biotechnol. Adv. 23 (2005) 345–357. doi:10.1016/j.biotechadv.2005.04.004.
[310] L.D. Carlos, R.A. Sá Ferreira, I. Orion, V. de Zea Bermudez, J. Rocha, Sol–gel derived nanocomposite hybrids for full colour displays, J. Lumin. 87–89 (2000) 702–705. doi:10.1016/S0022-2313(99)00366-X.
[311] P.K. Tien, R. Ulrich, Theory of Prism–Film Coupler and Thin-Film Light Guides, J. Opt. Soc. Am. 60 (1970) 1325. doi:10.1364/JOSA.60.001325.
[312] K. Ghawana, S. Singh, K.N. Tripathi, Determination of waveguide parameters of acrylonitrile-based polymer optical waveguides, J. Opt. 29 (1998) 265–267. doi:10.1088/0150-536X/29/4/003.
[313] R. Ulrich, R. Torge, Measurement of Thin Film Parameters with a Prism Coupler, Appl. Opt. 12 (1973) 2901. doi:10.1364/AO.12.002901.
[314] J.C. Lagarias, J.A. Reeds, M.H. Wright, P.E. Wright, Convergence Properties of the Nelder--Mead Simplex Method in Low Dimensions, SIAM J. Optim. 9 (1998) 112–147. doi:10.1137/S1052623496303470.
[315] M. Schubert, Infrared Ellipsometry on Semiconductor Layer Structures, Springer Berlin Heidelberg, Berlin, Heidelberg, 2005. doi:10.1007/b11964.
[316] D.E. Aspnes, Spectroscopic ellipsometry — Past, present, and future, Thin Solid Films. 571 (2014) 334–344. doi:10.1016/j.tsf.2014.03.056.
[317] H.G. Tompkins, E.A. Irene, C. Hill, N. Carolina, Handbook of Ellipsometry, Springer Berlin Heidelberg, 2005. doi:10.1007/3-540-27488-X.
[318] O. Acher, E. Bigan, B. Drévillon, Improvements of phase-modulated ellipsometry, Rev. Sci. Instrum. 60 (1989) 65–77. doi:10.1063/1.1140580.